

UNIVERSITY OF STRATHCLYDE

Department of Physics

**Hybrid materials integration of
wide-bandgap semiconductors for
chip-scale photonics**

by

Jack Andrew Smith



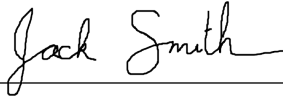
A thesis presented in fulfilment of the
requirements for the degree of
Doctor of Philosophy

December 2022

Declaration of Authorship

This thesis is the result of the author's original research. It has been composed by the author and has not been previously submitted for examination which has led to the award of a degree.

The copyright of this thesis belongs to the author under the terms of the United Kingdom Copyright Acts as qualified by University of Strathclyde Regulation 3.50. Due acknowledgement must always be made of the use of any material contained in, or derived from, this thesis.

Signed: 

Date: [30th January 2023](#)

Abstract

Presented in this thesis are efforts to develop a hybrid integrated optics platform consisting of the materials gallium nitride (GaN) and diamond. Wide-bandgap materials such as these are important for short wavelength (UV-visible) applications, or applications spanning broad bands of the electromagnetic spectrum. First, a passive GaN photonic chip was fabricated and characterised. Racetrack resonators featured low losses of 3.13 dB/cm and intrinsic quality (Q) factors of 1.22×10^5 were measured. A second chip featuring actively tunable devices using thermal micro-heaters featured a tuning efficiency of 11.658 pm/mW and a 3 dB full peak-switching bandwidth of 13.4 kHz. This is the first example of an actively tunable GaN micro-resonator. A high- Q diamond micro-disk resonator (intrinsic $Q = 1.6 \times 10^5$) was then integrated with the passive GaN chip using a micro-transfer printing technique. It was printed in series with a monolithic GaN micro-resonator, so that their respective performances could be measured effectively simultaneously. Finally, the performance of the hybrid wide-bandgap device for the application of photonic thermometry was examined. The high accuracies afforded by the dual-material device lead to a fivefold improvement in single-shot temperature errors over similar silicon devices.

Acknowledgements

I would like to thank my supervisor, Prof Michael Strain. To him I owe more than the completion of my PhD and the existence of this thesis. Firstly, his guidance throughout has been invaluable. More importantly, a genial atmosphere in which practically anything can be discussed means, by osmosis more than anything else, I believe I have developed as a researcher – both in knowledge and confidence. For this, I am hugely grateful.

I would also like to thank Prof Martin Dawson for his ever-insightful suggestions throughout my PhD, and Dr Benoit Guilhabert whose expertise over a wide range of topics certainly made life easier. Elsewhere in the Institute, I would like to thank Dr Yunzhou Cheng and Dr Enyuan Xie for their indispensable microfabrication know-how. For keeping the cleanroom running and enabling the success of not only my own, but many other projects, I am extremely thankful to Jim Sweeney and Dr Ian Watson. For their help and support I am thankful to Sharon Kelly and Lorraine Annand, without whom I (and many others in the Institute) would be interminably lost in administrative warrens.

A great deal of the work in this thesis would be impossible if it were not for the huge strides made by my predecessors in the group. I would therefore like to extend to Dr Paul Hill and Dr John McPhillimy a massive thank you. I trust, should they ever read this, that they can take pride in seeing how important their contributions to the group have been; and I hope they know how much I appreciated their advice. I am also grateful to Dr Charalambos Klitis and Dr Stuart May, who carried out all electron beam lithography patterning and additional facet polishing (featured in Chapter 3) at the James Watt Nanofabrication Centre. Their expertise enabled the devices presented throughout this work.

The pursuit of a PhD is unavoidably full of highs and lows, elation and stress. For giving me the energy to plod on and helping me find the enjoyment in work during those moments when nothing seemed to be working, I will forever be grateful to Dr José Carreira, and Dr Ruaridh Winstanley. My finishing the PhD in high spirits is in large part thanks to their friendship!

It would be remiss of me to neglect to thank Alex Munro, my high school physics teacher. The clarity of his explanations, the confidence that comes from complete ownership of

the subject material (the same confidence he would impart in his pupils), the joy of discovery and beauty in physics – these are all things I still remember from his lessons, and I am in no doubt here because of them.

Finally, I would like to thank my family and most of all my wife, Christine, for her love and support.

Contents

Declaration of Authorship	i
Abstract	ii
Acknowledgements	iii
List of Figures	viii
List of Tables	xv
1 Introduction	1
1.1 Motivation	1
1.2 The path to wide-bandgap integrated optics	2
1.2.1 Wide-bandgap materials	6
1.3 Materials	9
1.3.1 Gallium nitride	9
1.3.1.1 GaN properties pertinent to integrated optics applications	11
1.3.2 Diamond	13
1.3.2.1 Structure and growth	14
1.3.2.2 Substrates for diamond epitaxy	15
1.3.3 Hybrid integration of diamond and GaN	16
1.4 Microring resonator theory	17
1.4.1 Transfer matrix formulation	18
1.4.2 Coupling regimes	20
1.4.3 Q factor and other dispersion related parameters	21
1.4.4 Example parameter extraction using resonance fitting	24
1.4.5 Fano, asymmetric, and split resonances	25
1.5 Chapter summary	28
2 Passive GaN devices	40
2.1 Introduction	40
2.2 Optical simulations and chip design	43
2.2.1 Overview	43
2.2.2 Simulation software	43
2.2.3 Waveguide geometry	44
2.2.4 Mode profiles	45
2.2.5 Bend loss	46
2.2.6 Power cross-coupling	48

2.2.7	Design finalisation	50
2.3	Device fabrication and characterisation	52
2.3.1	Fabrication	52
2.3.2	Characterisation	54
2.4	Racetrack transmission results	54
2.4.1	Racetrack coupling	56
2.4.2	Racetrack loss	57
2.5	Microdisk transmission spectra	59
2.6	Summary	62
3	Tunable GaN microresonators	66
3.1	Introduction	66
3.1.1	Electro-optic tuning	68
3.1.2	Thermal tuning	68
3.2	Device fabrication and characterisation	70
3.2.1	Fabrication	70
3.2.2	Characterisation	73
3.3	Tuning results	74
3.3.1	Wavelength tuning	74
3.3.2	Coupling tuning	76
3.4	Bandwidth measurements	78
3.5	Summary	80
4	Hybrid integration of diamond with GaN PICs	85
4.1	Introduction	85
4.1.1	The case for hybrid integration	85
4.1.2	Diamond integration	87
4.2	Diamond disk fabrication	90
4.3	Hybrid integration by micro-transfer printing	92
4.3.1	Stamp preparation	92
4.3.2	Micro-transfer printing process	93
4.4	Results	95
4.4.1	Hybrid integration onto GaN PICs	95
4.4.2	Disk WGM considerations	97
4.4.3	Transmission measurements	101
4.5	Conclusion	103
5	High precision integrated photonic thermometry utilising a hybrid diamond on GaN chip	108
5.1	Introduction	108
5.1.1	The general case for chip-scale photonic thermometry	109
5.1.2	Device operation	111
5.1.3	Material considerations	112
5.1.4	Hybrid wide-bandgap photonic thermometry	112
5.2	Method	113
5.3	Results	114
5.3.1	Resonance position determination	114

5.3.2	Simultaneous thermal tuning and thermo-optic coefficient measurement	115
5.3.3	Single-shot temperature error	117
5.3.4	Stability measurements	120
5.4	Conclusion	123
6	Conclusion and outlook	127
6.1	Future work	128
A	Dielectric waveguide theory	131
A.1	General waveguide equation	131
A.1.1	The asymmetric planar slab	133

List of Figures

1.1	Colladon’s apparatus for demonstrating the guiding of light by total internal reflection along a cascading water stream. In this case an arc lamp is used instead of sunlight, as in his earlier demonstrations. <i>Adapted from: [7].</i>	3
1.2	(a) A 2 m rotating frame, on which parallel metal wires were mounted, thus acting as a polarisation filter for incident microwaves. (b) A triangular prism, filled with pitch or asphalt and weighing 450 kg, used for studying the refraction of microwaves. (c) Hertz’s spark-gap radio transmitter resonance curve. <i>Adapted from: [11].</i>	4
1.3	(a) Hollow metal RF waveguide [18]. (b) Single mode IR optical fibre, with the standard core diameter of 8 μm . (c) Silicon photonic wire waveguide, <i>Adapted from: [19]</i>	5
1.4	(a) An early integrated optical frequency multiplexer, where 6 GaAs-AlGaAs DFB diode lasers are monolithically integrated with passive AlGaAs waveguides which couple to a single optical fibre. <i>Adapted from: [24].</i> (b) Topics of publication in the ‘first’ 7 years of integrated optics, from 1969 to 1976 <i>Credit: [25]</i>	6
1.5	The operating wavelength ranges of various integrated optics applications from UV to IR. <i>Adapted from: [5]. OCT: optical coherence tomography.</i>	8
1.6	(a) Wurtzite GaN crystal structure. The unit cell is denoted by solid black lines, while the dashed lines help make clear the hexagonal symmetry present. <i>Adapted from: [75].</i> (b) Labels of the different planes in the wurtzite structure. (c) Orientation of c-plane GaN grown on c-plane sapphire (Al_2O_3), with their respective lattice constants labelled. <i>Adapted from: [76].</i>	10
1.7	SEM images of MOCVD GaN on (0001) sapphire, with (right) and without (left) a low temperature AlN buffer layer. <i>Adapted from: [81]</i>	11
1.8	(a) Carbon allotrope structures, and illustration of the energy activation barrier preventing the conversion of diamond to graphite. <i>Crystal structures adapted from: [111]</i> (b) Carbon P-T phase diagram. <i>Credit: [112]</i>	14
1.9	Repeated growth, lift-off, tiling, and re-growth steps to achieve large area free-standing diamond. <i>Credit: [118]</i>	16
1.10	(a) Finite-difference time domain simulations of a silicon microring resonator, radius 5 μm . A broadband pulse, centred on 1592.5 nm with a bandwidth of 2.5 nm, is injected into the bus waveguide (bottom left). The plots show the square magnitude electric field distributions 10,000 fs after simulation start, for four different wavelengths: from off-resonance (i), to on-resonance (iv). (b) Model transmission spectrum of a microring resonator, with terms labelled.	17

1.11	Model ring resonator with single evanescently coupled bus waveguide - a configuration known as an <i>all-pass</i> or <i>notch</i> filter.	19
1.12	(a) Resonant lineshapes, for a model resonator of fixed loss and varying r . The under-coupled case is both the narrowest and shallowest. The over-coupled case is broadest, and the critically-coupled case is deepest. (b) Extinction ratio (ER) and peak FWHM for a single resonance and increasing r/a . At $r/a = 1$, critical coupling is reached. (c) Effective phase delay for a small detuning around a resonance.	21
1.13	(a) GaN racetrack resonator transmission spectrum, displaying the effects of dispersion on the FSR. (b) Calculation of n_g from the FSRs extracted from the spectrum.	23
1.14	(a) High Q resonance, fitted with equation 1.7. (b) Power cross-couplings for increasing bus-ring separation gap, and three sets of waveguide widths. Narrower waveguides confine light less, and so couple more.	24
1.15	Extinction ratio and Q factor as functions of waveguide width. The red arrow indicates the position of the resonance in Figure 1.14 (a).	25
1.16	(a) Example Fano resonance in a silicon microring <i>Adapted from: [136]</i> , with additional schematic describing Fano interference in the transmission waveguide. (b) Asymmetric resonances plotted with the model provided in [137], which accounts for differences in supermode losses in the coupling section. (c) Example of asymmetric resonance splitting, with non-degenerate counter-propagating modes in the ring. (d) A resonance which is only moderately split, showing an effective flattening of the dip minimum level.	26
2.1	Previous GaN work. (a) Optical micrograph of an AWG based on GaN ridge waveguides on AlGaIn on sapphire [6]. (b) SEM of a GaN on sapphire grating coupler [7]. (c) SEM of a suspended GaN waveguide and PhC lattice [8]. (d) Optical micrograph of a portion of a GaN on sapphire directional coupler [9]. (e) SEM of the coupling region of a GaN on sapphire ring resonator [1]. (f) Optical micrograph of a GaN add-drop ring resonator used for SHG [10].	41
2.2	(a) Mode effective indices for TE (solid lines) and TM (dashed lines) polarisations for increasing waveguide width and fixed GaN height of 650 nm. The green bar indicates the target waveguide width. (b) The same, but for increasing waveguide height, with a starting point of 350 nm.	44
2.3	Normalised electric field profiles for the (a) TM_0 and (b) TE_0 modes. For each, vertical line profiles are taken through the centre point of the field intensity profile, and are plotted in (c).	45
2.4	(a) TM_0 mode in a straight waveguide section. (b) TM_0 mode in a curved waveguide section, with bend radius of 8 μm . (c) The same curved TM_0 mode, but on a logarithmic scale, showing the radiative loss of modal power from the guide. (d) Comparison of horizontal line profiles taken across the maxima of each mode, clearly showing a rightward shift for the bent waveguide.	47
2.5	Radiative bend loss as a function of bend radius, for wavelengths 1.51 μm and 1.64 μm and both polarisations.	48
2.6	Real parts of the dominant electric field components for the TE (a,b) and TM (c,d) supermodes, showing symmetric and anti-symmetric behaviour.	49

2.7	Plan views of the EME field intensity taken through a horizontal midpoint cross-section of adjacent GaN waveguides, separation 300 nm, for (a) TE and (b) TM polarisations. (c) Power in each waveguide as a function of propagation distance z , after injecting 1 unit of power into waveguide 1 at point $z = 0$, calculated both from the EME solver and FDE solver using equation 2.1.	50
2.8	GDS mask file for the GaN PIC, with details of three sections	51
2.9	Summary of the racetrack resonator dimensions.	51
2.10	Passive device fabrication. (a) The GaN roughness is first measured with AFM. (b) HSQ resist is spun and patterned with electron-beam lithography. (c) The GaN is dry etched in an inductively coupled plasma reactive ion etcher (ICP-RIE), with Ar/Cl ₂ chemistry. Residual HSQ is removed in a short buffered oxide wet etch, before the ends of the chip are cleaved to allow fibre butt-coupling to the waveguides.	52
2.11	Surface profilometer measurements on the (a) left and (b) right offcuts of the chip after cleaving. The total scan length is ~ 7.4 mm.	53
2.12	(a) Angled SEM image of waveguide facet, showing the expected thickness values for the GaN (~ 650 nm) and total step height (~ 1 μ m). Optical micrographs of (b) a racetrack resonator after the ICP step, (c) detail of the coupling section of a racetrack after the BOE step, and (d) a GaN disk. 53	
2.13	Schematic of the optical set-up used to characterise the device. Inset: Direct and false-colour images of single-mode output of waveguide. DUT: device under test, PBS: polarisation beam splitter, PD: photodetector.	54
2.14	(a) TE transmission, $L_c = 45$ μ m. (b) TM transmission, $L_c = 30$ μ m . . .	55
2.15	Highest loaded Q resonances for each polarisation. (a) TE, at 1558.8437 nm, FWHM = 53.6 pm, $Q = 2.91 \times 10^4$ (b) TM, at 1544.1192 nm, FWHM = 130.8 pm, $Q = 1.18 \times 10^4$	56
2.16	(a) Mean Q factors, showing a linear decrease with increasing coupling length. (b) TE resonance dip extinction values, with a cross section of line shapes around 1568 nm shown in (d), displaying maximum extinction for an intermediate value of coupling length. (c) Extracted mean TE power cross-coupling values, alongside a \sin^2 fit and the simulated values. . . .	57
2.17	(a) Distributed loss values extracted from the fits for each coupling length and polarisation, with mean values plotted as crosses. (b) Loss per racetrack round trip. (c) TE intrinsic Q factors for each coupling length. Inset: resonance which features the highest intrinsic Q factor measured. .	58
2.18	(a) Example TM microdisk transmission spectrum, radius 20 μ m, gap 200 nm. (b) Window of spectra highlighting three families of modes. (c) TE transmission spectrum, of the same disk. (d) Fast Fourier filtered spectrum, making the two families of modes more visible.	60
2.19	FDTD simulations of the field distributions within the GaN microdisk. A TE orientated source located inside the disk was used to excite the whispering gallery modes, and field distribution snapshots taken 5000 fs after simulation start. (a) The fundamental radial mode. (b) The first order radial mode.	61

3.1	(a) Model TM transmission spectra for two GaN ring resonators with different waveguide widths, showing the drastic difference in filtered wavelengths for a 10 nm width difference. (b) Example of a critically coupled resonance, where the fabricated device matches perfectly the as-designed values and the resonant wavelength is strongly filtered. (c) For a 10 nm width deviation, the same wavelength is allowed to pass almost completely.	67
3.2	Refractive index of thin-film GaN on sapphire, as a function of temperature and for different wavelengths. The bottom three data sets show linear increases with temperature. Credit: [18]	69
3.3	Tunable GaN resonator proces flow. (i) GaN on sapphire. (ii) Electron-beam lithography in HSQ resist. (iii) ICP-RIE etch in Ar/Cl ₂ chemistry. (iv) Cladding with HSQ, and conformal PECVD silica. (v) Electron-beam lithography in positive PMMA resist. (vi) Metal-deposition. (vii) Lift-off.	71
3.4	(a) Optical micrograph of a tunable GaN resonator. (b) SEM of a waveguide facet post-polishing, showing 890 nm of GaN with good sidewall verticality on 348 nm of AlN buffer layer. Dark streaks either side of the GaN are due to cracking in the HSQ after the PECVD deposition, which is performed at elevated temperatures.	72
3.5	Relevant dimensions of a tunable racetrack device, with coupling section cross-section shown.	72
3.6	Diagram and microscope image of the optical and electronic characterisation of the device. For simple tuning measurements, the 20 MHz function generator is replaced with a simple power supply. For bandwidth measurements, the function generator is used to supply a square wave input to the micro-heater.	73
3.7	(a) Current and (b) power plots for increasing voltage applied to the wavelength tuning micro-heater.	74
3.8	(a) Wavelength tuning of racetrack spectrum. (b) Detail of two nearby peaks.	75
3.9	Resonance wavelength of a selected peak against increasing micro-heater power.	75
3.10	(a) Q factor and (b) power cross-coupling coefficients for increasing micro-heater power. Calculated for the resonance at ~1588 nm.	76
3.11	(a) Current and (b) power plots for increasing voltage applied to coupler micro-heater.	76
3.12	Spectra taken for increasing voltages applied to the coupler micro-heater.	77
3.13	(a) Wavelength tuning. (b) Power cross-coupling, κ for increasing heater power.	77
3.14	The peak used as the optical switch for bandwidth measurements.	78
3.15	(a) Trace of the 0.5 Hz square wave input to the wavelength tuning micro-heater. (b) Trace of the modulated optical throughput incident on the detector.	78
3.16	Resonator thermal switching response time, with an inset detailing the fall time, which is 34 times shorter than the rise time.	79
3.17	(a) Trace of a 17 kHz square wave input to the micro-heaters. (b) Corresponding optical throughput trace.	79
3.18	Peak-to-peak amplitude, referenced against the initial low frequency value.	80

4.1	The hybrid integration of disparate elements, showing multiple pre-fabricated components integrated onto a single PIC.	86
4.2	(a) micro-LEDs transfer printed directly onto CMOS drive chip [8]. (b) Nanowire lasers printed so as to emit into polymer waveguides [10]. (c) A transfer printed germanium photodiode, coupled to a silicon waveguide [11]. (d) A transfer printed GaAs p-i-n photodiode array on SiN waveguides [12]. (e) A transfer printed quantum dot containing GaAs photonic crystal cavity, coupled to a silicon receiver waveguide [13].	88
4.3	GaP on diamond disk resonators, with NV centres contained in the diamond pillars beneath the GaP disks [23]. Ultra-high Q-factor (1×10^6) diamond rings patterned on SiO ₂ substrates [24]. A suspended array of tapered diamond waveguides, containing single photon source colour centres, pick-and-place integrated onto an AlN PIC [25].	89
4.4	(a) 3D Optical profile of a whole diamond platelet. (b) Line profile taken across the diagonal, showing a 4.6 μm thickness increase over 2.632 mm. (c) AFM scan of an as received diamond platelet, RMS roughness 1.49 nm, showing scarring from the CMP step. (d) A line profile, perpendicular to the scar orientation, showing these scratches are typically around 2 nm deep, and tens of nanometres wide.	90
4.5	(a) Diamond disk fabrication steps: (i) After cleaning and initial characterisation, the platelet is placed on a silicon carrier wafer. (ii) ICP etching in Ar/Cl ₂ to thin platelet. (iii) Transfer to a second silicon carrier, pre-patterned with alignment markers for electron-beam lithography in HSQ resist. (iv) An Ar/O ₂ etch down to the silicon transfers the pattern to the diamond. (b) Optical micrograph of a corner section of an as-received diamond, showing thin-film interference fringes due to the wedged thickness variation of the diamond. (c) Array of fully etched diamond disks, with a portion of partially etched platelet remaining in the bottom corner. Arrow indicates direction of increasing disk thickness.	91
4.6	Simplified process flow for stamp fabrication.	92
4.7	(a) The NLP 2000 tool used for transfer printing. (b) Detail of the essential components of the tool.	93
4.8	(a) Micro-transfer printing process: (i) Stamp compressed onto donor disk. (ii) The stage is quickly lowered, releasing the disk. The stamp relaxes, the pyramids decompress, and the stamp-disk contact area is reduced to the pyramid tip. (iii) Alignment over receiver waveguide. (iv) Disk compressed on top of waveguide. (v) Slow retraction of stage, printing the disk onto the waveguide. (b) Image taken during the alignment stage, with the body of the stamp delineated by the dashed square and a waveguide visible beneath. (c) Image taken after a disk is printed and stamp retracted.	94
4.9	(a) Optical micrograph of diamond disks and membrane on the air-clad GaN PIC. (b) SEM image of an earlier printing effort of (non-resonant) disks on GaN waveguides. (c) A diamond disk (bottom), and two AlGaAs disks (top), successively printed in an a small area. (d) Close up of the vertically coupled diamond disk (diameter: 25 μm). (e) Close up of the AlGaAs disks, one vertically coupled (diameter: 20 μm), one edge coupled (diameter: 10 μm). All scale bars: 50 μm	96

4.10	(a) Rigid diamond disk on a GaN waveguide, angled at 2.4299° . (b) The same, but simplified and at an exaggerated angle to highlight the similar triangles to the left of and above the GaN waveguide.	97
4.11	(a) Example radial potential of a WGM disk resonator. (b) $ E ^2$ for a model WGM resonator (refractive index = 2.4, radius = $2.5 \mu\text{m}$, $\lambda = 1600 \text{ nm}$) of decreasing azimuthal mode number. $m = 20$. (c) $m = 12$. (d) $m = 10$. Solid lines mark the boundary of the disk, dashed lines mark the circle defined by the caustic radius, and dotted lines mark the radiation boundary. 98	98
4.12	Transmission spectra, taken before and after printing, for both polarisations. 100	100
4.13	(a-f) Electric field distributions ($\lambda = 1550 \text{ nm}$) for the first six cross-sectional radial/axial modes of the diamond disk, labelled with their polarisation with respect to the plane of the disk. The modes are also labelled with their respective power coupling percentages from a GaN waveguide (not-pictured) beneath the disk edge.	101
4.14	(a) Highest loaded Q diamond resonance, at $\lambda = 1542.6089 \text{ nm}$, FWHM = 17.0 pm , $Q = 9.05 \times 10^4$, TE polarisation. (b) Deepest TE resonance, $\lambda = 1566.9018 \text{ nm}$, FWHM = 38.4 pm , $Q = 4.08 \times 10^4$. (c) Broadest TE resonance, $\lambda = 1591.5548 \text{ nm}$, FWHM = 227.6309 pm , $Q = 6.99 \times 10^3$	102
4.15	Diamond disk printed onto thermal tuners.	103
5.1	An example of high-level PIC implementation: a handheld multi-functional skin imaging device, capable of both OCT and epiluminescence microscopy, based on a $19.5 \times 1.1 \text{ mm}^2$ SOI PIC. <i>Adapted from [4]</i>	109
5.2	(a) Schematic of a compact, dual material photonic thermometer. (b) Resulting thermal red-shifting of their cascaded resonances, where resonator 2 has the greater thermo-optic coefficient, leading to $\Delta\lambda_2 > \Delta\lambda_1$	112
5.3	(a) Schematic and baffle enclosure erected around sample stage of fibre injection rig. (b) Hybrid diamond-GaN device.	113
5.4	(a) Lorentzian fitting and 95% confidence intervals of an example diamond peak at 1593.22 nm . (b) Detail around peak minimum. (c) The same peak, but with polynomial background correction. (d) Detail showing a much improved fit around peak centre.	115
5.5	(a) Thermally tuned cascaded diamond-GaN transmission spectrum. (b) Detail of nearby peaks.	116
5.6	Thermally induced peak position shifts, with linear fits, for the integrated diamond-GaN device. Each $\Delta\lambda/\lambda$ data point is an average over all peak shifts associated with that material.	116
5.7	(a) Standard error in each temperature shift measurement using the single GaN and diamond peaks shown in Figure 5.5. (b) Minimisation of error by averaging over an increasing number of peaks, taken for the second T_{setpoint} in (a).	119
5.8	(a) Correlation between mean diamond and GaN wavelength shifts. (b) Temperature response of the combined hybrid device, with error bars indicating the standard error in each temperature estimate.	120
5.9	Time trace acquisition method for stability measurement.	121
5.10	Time traces of voltage at the detector with the laser parked on the side of a resonance for each material, as well as the system throughput trace for comparison.	121

5.11	(a) FFT amplitude spectra of the side-of-peak time traces. (b) Allan variance plots for each trace. (c) Equivalent FFT spectra in temperature units. (d) Allan variance for the temperature traces.	122
6.1	(a) Plan view of the collection facet of a GaN slab waveguide (50 μm). (b) Attempted optical and electrical probing of tunable GaN resonators at 635 nm.	128
6.2	(a) TE mode of a single mode GaN partially etched waveguide. (b) On-going work on miniature photonic devices for membrane fabrication. . . .	129
A.1	Names of various waveguide geometries, where darker regions represent greater refractive indices. The direction of propagation is into the page. <i>Adapted from: [1]</i>	131
A.2	Transverse electric (TE) field solutions for an asymmetric slab waveguide, with line profiles and corresponding field patterns taken along the propagation length, z	134
A.3	Allowed propagation constants for the above geometry. Only two guided modes are supported at this wavelength.	136

List of Tables

1.1	UV-visible integrated optics state-of-the-art. Ring resonators are fully etched unless otherwise stated. Q_i : <i>intrinsic quality factor</i>	7
1.2	Some of the physical effects of each electric susceptibility component. . . .	12
1.3	Measurements of GaN's second order nonlinear susceptibility, all at telecomms wavelengths. OPO: optical parametric oscillation, MRR: micro-ring resonator, SHG: second harmonic generation.	13
2.1	Table of optical power confinement factors for two fundamental polarisations.	46
5.1	Thermo-optic coefficients calculated from the slopes of relative wavelength shift against temperature set-point.	117

For my wife.

Chapter 1

Introduction

1.1 Motivation

Integrated optics is the technology concerned with the manipulation of light on length scales commensurate with optical wavelengths. It is, in other words, aimed at fabricating photonic integrated circuits (PICs); with which some combination of generation, routing, modulation, and detection of optical signals can be performed on micron scales.

The historic focus of integrated optics has been telecommunications. Of particular importance is the chip-scale multiplexing of several wavelengths into fibre-optics for high-bandwidth, low-power communications. In this endeavour silicon PICs have been phenomenally successful, and they are now commercially available as fully packaged rack-mounted transceiver modules [1]. Recent demonstrations have shown data rates of 1.6 Tb/s for silicon photonic transmitters, and 800 Gb/s for a photonic engine (consisting of fully integrated on-chip control electronics and optics) [2]. For the world's power-hungry data centres, in which IP traffic is growing exponentially, PICs are becoming essential.

The success of PICs is not limited to this one field however, and is being replicated elsewhere. Increasingly, they are being implemented in diverse applications, from label-free biosensing [3] to quantum cloud computing [4]; each with their own disparate set of device requirements. Other new applications are emerging which require PICs operating at visible wavelengths where photon energies are greater than the bandgap of traditional materials like silicon, and are thus absorbed [5]. This is the impetus driving the development of new wide-bandgap material platforms, transparent from the UV, through visible, and out to IR wavelengths. Several concept proofs in various materials have been performed, but few are scalable in the same way as silicon – though silicon nitride has begun to address this.

Presented in this thesis are efforts to develop a wide-bandgap gallium nitride (GaN) on sapphire integrated optics platform: from the design, fabrication, and characterisation of low-loss waveguides to high-Q and electrically tunable microring resonators (crucial components of planar lightwave circuitry). Finally, since enhanced functionality often requires the hybrid integration of multiple materials on one PIC, after the development of the GaN platform itself, micro-transfer printing is used to integrate diamond microdisk resonators with the GaN. Experiments using the hybrid chip for highly accurate photonic thermometry show performance that significantly improves on the state-of-the-art.

The remainder of this chapter will provide a brief history of the field of integrated optics and provide an overview of the state-of-the-art for other wide-bandgap integrated optics materials. The general case for GaN and diamond is then made, before details of the growth and attractive properties of each are highlighted. Following this, the theory of optical microring resonators is explained, with details on how analysis of their transmission spectra will be performed throughout this thesis. Finally, the structure of the thesis and contributions of each chapter are outlined.

1.2 The path to wide-bandgap integrated optics

The transmission of light inside a guiding medium was first demonstrated in 1842 by Daniel Colladon, using nothing more than focused sunlight, a tank of water, and a valve producing a steady stream (Figure 1.1). By injecting light into the stream at a small angle, total internal reflection all along the ‘light pipe’ is achieved. Only if the stream is turbulent or obstructed in some way does the light it contains dramatically escape, illuminating an otherwise dark room [6]. Colladon described this demonstration as “*one of the most beautiful, and most curious experiments that one can perform in a course on optics.*” [7].

Total internal reflection had been studied since at least Kepler’s time, so in that sense Colladon’s demonstration was nothing extraordinary. The concept of confining light along some set path did however lead to a number of practical inventions in the late 19th century; such as glass rods used by surgeons and dentists to illuminate hard-to-reach places, without the significant excess heat generated by oil lamps or incandescent bulbs harming their patients [8].

The ray optics picture of transmission along a light pipe is sufficient as long as the cross-sectional size of guiding medium is large in comparison to the optical wavelength. In fact, this description was *all* that was available at the time. Maxwell’s electromagnetic field theory and conjecture that light is a transverse electromagnetic wave would not

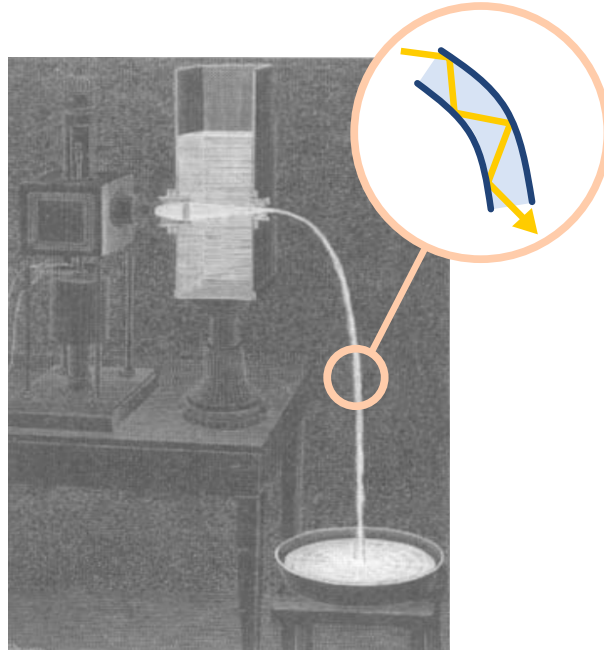


FIGURE 1.1: Colladon's apparatus for demonstrating the guiding of light by total internal reflection along a cascading water stream. In this case an arc lamp is used instead of sunlight, as in his earlier demonstrations. *Adapted from: [7].*

be developed until 1864 [9]; and not proven experimentally by Hertz until 1888, who was the first to produce and measure the properties of radio waves and microwaves [10]. Hertz was one of the few physicists in Europe who fully appreciated the importance of Maxwell's work over the more popular action-at-a-distance theories which postulated an infinite speed of light. With the apparatus in Figure 1.2 (a,b), he was able to study the polarisation and refraction of 66 cm microwaves [11]. Additionally, he was the first to measure electromagnetic resonance curves by tuning the length a receiver coil to be in resonance with a spark-gap radio transmitter – as in Figure 1.2 (c) [11].

Independently of Hertz, a self-taught electrical engineer and physicist named Oliver Heaviside would recast Maxwell's originally unwieldy electromagnetic theory, consisting of 20 equations and 20 variables, into the four succinct vector equations still in use today [12–14]. He would also be one of the earliest scientists to begin applying Maxwell's equations to the field of telecommunications [15]. Then, in 1897 Lord Rayleigh analysed the boundary-value problem of Maxwell's equations confined to hollow metal and dielectric waveguides, being the first to make the observations that will appear later in this thesis [16, 17]:

- Plane waves propagating in waveguides exist only as part of a set of normal modes – somewhat like the modes of vibration of a bounded two-dimensional membrane.

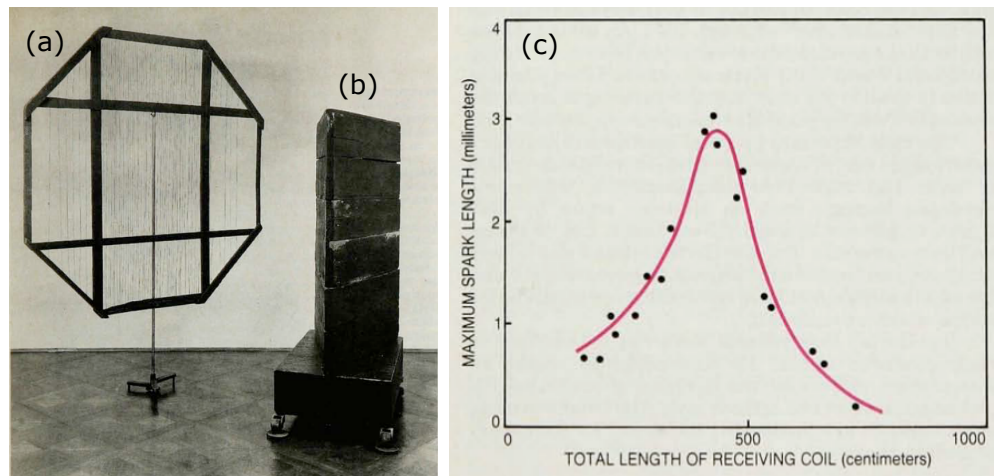


FIGURE 1.2: (a) A 2 m rotating frame, on which parallel metal wires were mounted, thus acting as a polarisation filter for incident microwaves. (b) A triangular prism, filled with pitch or asphalt and weighing 450 kg, used for studying the refraction of microwaves. (c) Hertz's spark-gap radio transmitter resonance curve. *Adapted from: [11].*

- Guided waves either have a longitudinal magnetic field component, or a longitudinal electric field component. In the former case, since the electric field is entirely transverse to the direction of propagation, this polarisation state is called transverse electric (TE). Similarly, the latter case is called transverse magnetic (TM).
- There exists a cut-off frequency (or wavelength), below (or above) which no propagating solutions exist. This cut-off is related to the dimensions and refractive index of the guiding medium.

For an explanation of dielectric waveguide theory, and analysis of the guided modes of a planar slab waveguide, refer to Appendix A. It would be another 40 years before these principles were put into practice with the simultaneous development by Southworth and Barrow of the hollow metal waveguide [17]. Low frequency radio waves were the first forms of electromagnetic plane waves that could be generated on demand, and their long wavelengths necessitated relatively large waveguides, like the one shown in Figure 1.3 (a). Once coherent laser sources became available [20, 21], the promise of high bandwidth long distance optical communication drove much research into optical cables made of glass. Initially propagation losses were prohibitively high (1000 dB/km), but in 1966 Kao and Hockham showed this was due to absorption by impurities in the glass, and the theoretical loss limit was far lower [22]. Naturally, shorter wavelengths require smaller guide dimensions for single-mode operation, as in Figure 1.3 (b), which depicts a modern single-mode IR fibre-optic cable, whose core has a diameter of 8 μm . As an aside, the concept of using modulated light instead of modulated electricity for communications was in fact one contemporary with the invention of the telephone itself. Alexander

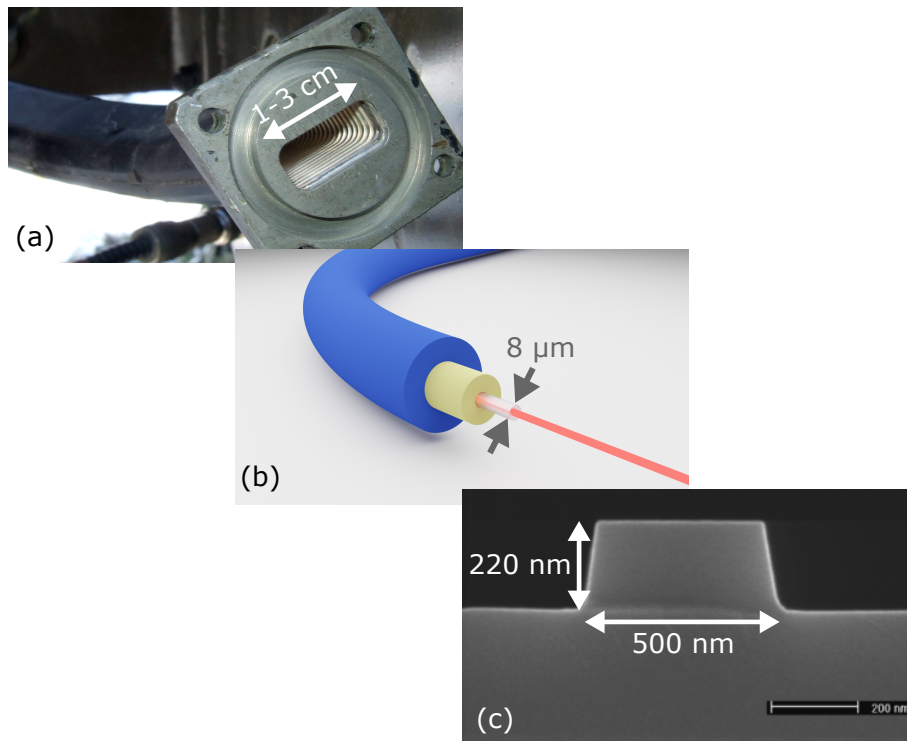


FIGURE 1.3: (a) Hollow metal RF waveguide [18]. (b) Single mode IR optical fibre, with the standard core diameter of $8\ \mu\text{m}$. (c) Silicon photonic wire waveguide, *Adapted from: [19]*

Graham Bell himself actually developed an early form of optical communication system in 1880 – the *photophone* – which used sunlight [23].

Finally, publishing in *The Bell System Technical Journal* in 1969, Miller proposed a “*a miniature form of laser beam circuitry*”, and further “*miniature forms for a laser, modulator, and hybrids.*” [26]. In the same journal issue, Marcatili comprehensively analysed rectangular dielectric waveguides, and showed how the optical coupling between two parallel guides can be used to form a 50:50 splitter, operating, for the first time, over microscopic dimensions [27]. The seminal work of Miller and Marcatili showed that the microfabrication technologies being developed for electronic integrated circuits (thin-film deposition, photolithography, dry etching, etc. [28]) could just as easily be applied to the fabrication of photonic integrated circuits (PICs), and the realisation of integrated waveguide lasers, phase modulators, optical filters, and couplers.

Several potential material platforms were explored for different applications and different wavelength ranges. A notable case was GaAs – an active material capable of lasing as well as passive waveguiding (Figure 1.4). Although intrinsically passive, silicon would eventually become the standard-bearer for integrated optics [29], because of its low losses, tight optical mode confinement, and CMOS fabrication compatibility [30]. A common

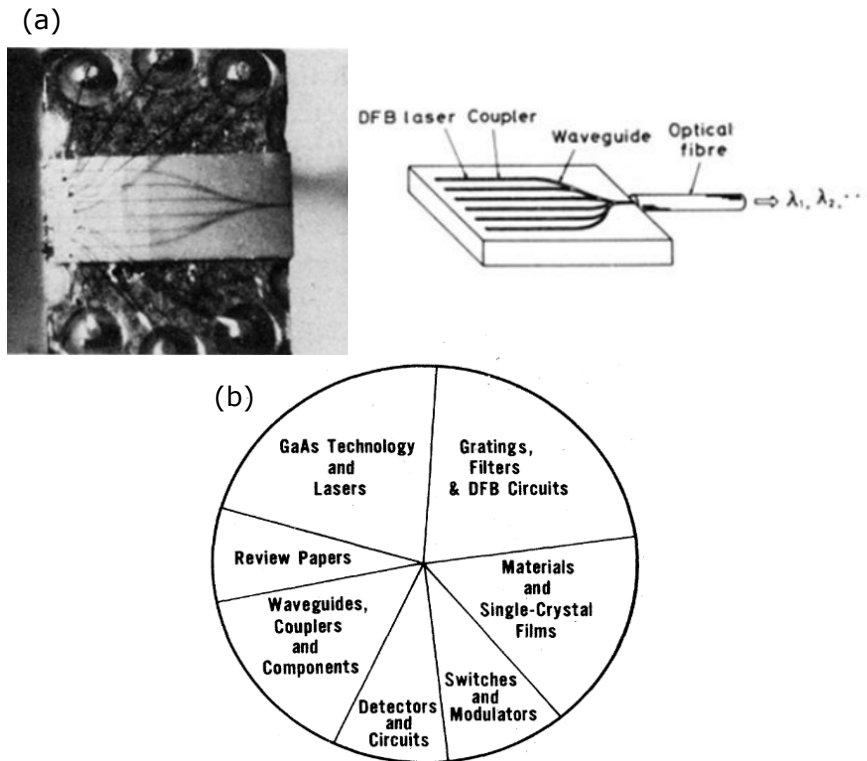


FIGURE 1.4: (a) An early integrated optical frequency multiplexer, where 6 GaAs-AlGaAs DFB diode lasers are monolithically integrated with passive AlGaAs waveguides which couple to a single optical fibre. *Adapted from: [24].* (b) Topics of publication in the ‘first’ 7 years of integrated optics, from 1969 to 1976 *Credit: [25]*

silicon waveguide cross section is shown in Figure 1.3 (c), which features a standard SOI silicon thickness of 220 nm [19].

1.2.1 Wide-bandgap materials

Early research efforts were predominantly focused on telecommunication applications operating in the near-IR wavelength range compatible with low loss fibre optic cables. Silicon has broadly excelled in this region of the electromagnetic spectrum. However, its relatively narrow bandgap (1.1 eV) precludes its usage for applications below around 1 μm , where there are now numerous applications that could benefit from chip-scale integration [5, 31]. This is driving the development of new wide-bandgap materials, whose transparency windows allow the extension of integrated optics into shorter wavelengths. These include: silicon nitride [32–34], aluminium nitride [35–37], aluminium oxide [38, 39], tantalum pentoxide [40, 41], titanium dioxide [42], silica [43], Hydex (doped silica) [44], polymers [45–48], silicon carbide [49, 50], lithium niobate [51], gallium phosphide [52], diamond [53–55], and gallium nitride [56–58].

Of these materials, the greatest interest has been given to silicon nitride (SiN), aluminium nitride (AlN), and lithium niobate (LiNbO₃, or simply LN). Fully fabricated SiN PICs can be sourced from commercial foundries [59]; or alternatively, large area wafers can be purchased for in-house fabrication. By utilising a photonic Damascene process in which the SiN waveguide core is not exposed to a dry-etch step [60], foundry-sourced waveguides feature some of the lowest losses in the field – on the order of 1 dB/m [61] (note the units of m^{-1}). However, SiN lacks a second order optical nonlinearity ($\chi^{(2)}$), meaning nonlinear applications are limited to those achievable with the much weaker third order nonlinearity ($\chi^{(3)}$) [62]. These terms will be explained in more detail later in this chapter.

Aluminium nitride is available in large area wafers. Unlike SiN, AlN has a moderate $\chi^{(2)}$, with which impressive nonlinear demonstrations, including highly efficient second harmonic generation [63], have been performed. Of the three, AlN has the widest bandgap (AlN: $E_g = 6.2$ eV, SiN: $E_g = 5.1$ eV, LN: $E_g = 3.7$ eV), and as such it has the greatest operational transparency window. In demonstration of this, resonator quality factors exceeding 2×10^4 have been measured at wavelengths of just 369.5 nm [36]. Propagation losses as low as 3 dB/cm have been measured at 635 nm [64].

Finally, LN possesses the greatest $\chi^{(2)}$ – approximately 30 times larger than AlN [51]. This makes it the pre-eminent material for many nonlinear processes, such as the rapid modulation (500 GHz) of optical signals using electro-optic switching [70]. The etching of waveguides in LN is made difficult by the non-volatility of its etch products in typical dry-etch gases such as chlorine, fluorine, and oxygen. Besides raising the issue of redepositing etchants onto devices and etch-chamber walls, this also tends to mean

TABLE 1.1: UV-visible integrated optics state-of-the-art. Ring resonators are fully etched unless otherwise stated. Q_i : *intrinsic quality factor*.

Device	Dimensions (μm) $w \times h, r$	λ (nm)	Q_i ($\times 10^3$)	Loss (dB/cm)
AlN ring [36]	$0.25 \times 0.2, 40$	369.5	20	-
AlN ring [65]	$1 \times 0.55, 60$	532	147	7.3
AlN ring [36]	$0.45 \times 0.2, 50$	638	170	-
AlN ridge [64]	3×0.8	520 (635)	-	13 (3)
SiN ridge [66]	0.7×0.1	660	-	0.51
SiN ridge [67]	0.4 (0.7) $\times 0.23$	532	-	3 (1)
SiN ridge [68]	10×0.25	632-780	-	0.1-0.2
SiN disk [69]	$- \times 0.203, 20$	652-660	3400	-
LN rib ring [51]	$0.48 \times 0.18/0.12, 100$	637	11000	0.06
Al ₂ O ₃ ridge [38]	0.6×0.1	371	-	2.89
Al ₂ O ₃ ring [38]	$0.5 \times 0.1, 90$	405	470	2.6

dry-etch waveguides can only be fabricated with very physical etch processes (i.e. sputtering with argon) [71]. Despite this, with recipe optimisation, propagation losses of just 0.06 dB/cm have been reported at 637 nm [51]. Table 1.1 gives an overview of the state-of-the-art in the field.

The question of which material, if any, will come to dominate short wavelengths in the same way silicon has dominated longer wavelengths likely has no simple answer. It is worth noting that even silicon, lacking its own efficient optical source, requires heterogeneous integration with other active materials to achieve fully integrated devices for telecommunication applications [72, 73]. In a similar fashion, other applications across the electromagnetic spectrum often require sets of properties not found in a single material (and which may indeed be mutually exclusive in some cases). To overcome this, the hybridisation of multiple materials presents an excellent route toward utilising complementary properties on a single photonic chip – just as has been the case for silicon. This is discussed in more detail in subsequent chapters.

Figure 1.5 shows the operating bandwidths of some integrated optics applications, and how wide-bandgap materials are necessary to access technologies at shorter wavelengths. Although all quite distinct topics, the general motivations for integrating these applications on a photonic chip are: improvements in stability, resilience from environmental changes, and eventually, improved economy – resulting from the drastic reduction in

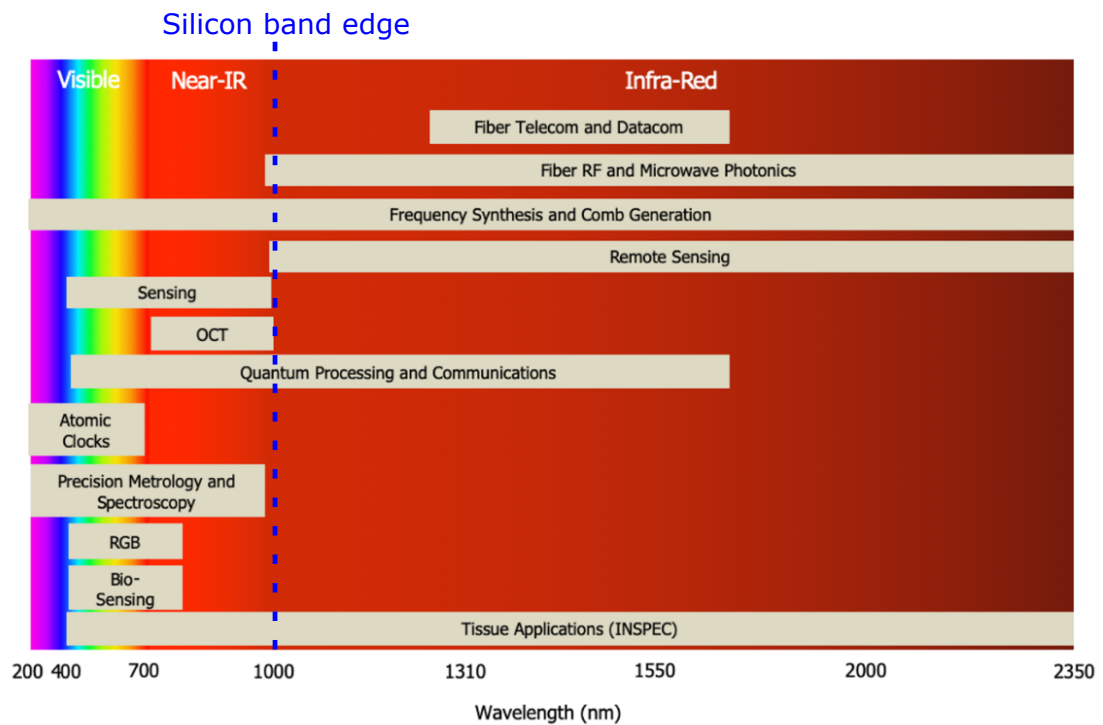


FIGURE 1.5: The operating wavelength ranges of various integrated optics applications from UV to IR. Adapted from: [5]. OCT: optical coherence tomography.

device footprint when compared with bench-top or rack-mounted equivalents. These arguments would be familiar to Miller, and indeed appear in some form in his original 1969 paper; but they take on a heightened significance when some of the new quantum applications specifically require long-term stability and isolation from decoherence mechanisms as a requisite for successful operation [74]. Transparency over a wide wavelength range is also necessary for a number of nonlinear processes, such as frequency conversion utilising second harmonic generation from 1560 nm to 780 nm in a GaN microresonator, for example [56].

Given their broad transparency ranges and complementary properties, the materials used in this thesis are GaN and diamond. Diamond possesses a number of superlative thermal and optical properties, but utilising them in a scalable way is difficult because of limitations in the growth of the material best suited for integrated optics applications (i.e. large area wafers, on low index substrates). GaN meanwhile is commercially available in large areas and can be grown on sapphire. It has the additional benefit of a moderate $\chi^{(2)}$ nonlinearity (whose magnitude lies between AlN and LN). These factors are discussed in greater detail in the following sections.

1.3 Materials

1.3.1 Gallium nitride

It is difficult to overstate the importance of group III-nitrides such as GaN. Used in the fabrication of light emitting diodes (LEDs), GaN has revolutionised lighting systems across the world by plugging a gap in the electromagnetic spectrum for semiconductors emitting blue wavelengths. In combination with long pre-existing red and green LEDs, highly efficient white LEDs – and all the benefits thereof – were then possible [77].

Shown in Figure 1.6 are the unit cell and crystallographic planes of GaN, which under normal conditions crystallises in the hexagonal wurtzite structure. GaN is commonly grown by metalorganic vapour phase epitaxy (MOVPE) or hydride vapour phase epitaxy (HVPE) on sapphire substrates, but can also be grown on Si or SiC [78]. GaN grown on c-plane sapphire has a polarity that is either parallel or anti-parallel with the [0001] direction as drawn in Figure 1.6(a,b). This polarity is often termed either Ga-polar or N-polar GaN, depending respectively on whether growth proceeds with the as-drawn [0001] or $[000\bar{1}]$ directions normal to the surface of the sapphire [79]. Transparent deep into the UV, stable at the high temperatures associated with MOVPE, and readily available in good quality, large area templates, sapphire is in some respects an excellent substrate for GaN heteroepitaxy. However, a 16% lattice constant mismatch (reduced from 33% by

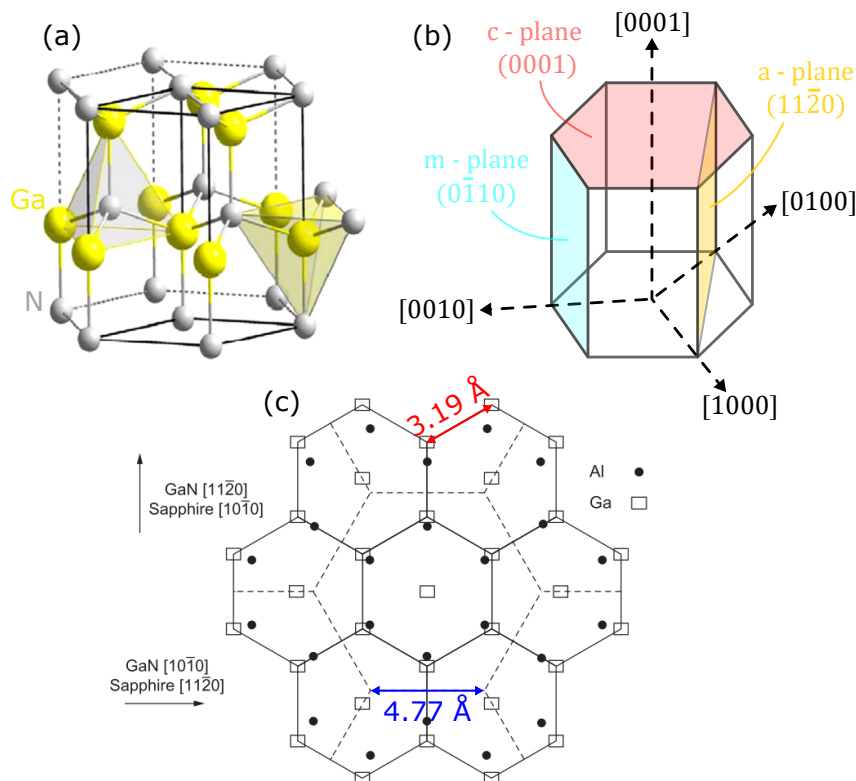


FIGURE 1.6: (a) Wurtzite GaN crystal structure. The unit cell is denoted by solid black lines, while the dashed lines help make clear the hexagonal symmetry present. *Adapted from: [75].* (b) Labels of the different planes in the wurtzite structure. (c) Orientation of c-plane GaN grown on c-plane sapphire (Al_2O_3), with their respective lattice constants labelled. *Adapted from: [76].*

a 30° rotation of the GaN unit cell, as in Figure 1.6 (c)), and a 39% thermal expansion coefficient mismatch, both significantly hinder the growth of quality GaN films. Another result of the rotation of the nitride's unit cell when grown on *c*-plane sapphire is the misalignment of their natural cleavage planes. For larger devices such as GaN laser diodes, the lack of mirror quality laser facet definition is a serious issue [80]. However, the fabrication of micron scale waveguide devices is still possible, at the cost of increased insertion losses. In any case, polishing of facets as in Chapter 3 may ameliorate this issue.

In 1986, Amano *et al.* discovered that the growth of smooth, optically flat, crack free GaN, could be achieved if a buffer layer of aluminium nitride (AlN) is first deposited on the sapphire at low temperatures [82]. The “low-temperature deposited buffer layer technology” is still in use today; or variations thereof. All-GaN layer structures are also possible with the low temperature deposition of a buffer layer of GaN [83]. For either method dislocation densities are relatively high, with values of 10^8 cm^{-2} commonly reported. Scanning electron microscope (SEM) images of GaN growth following Amano's

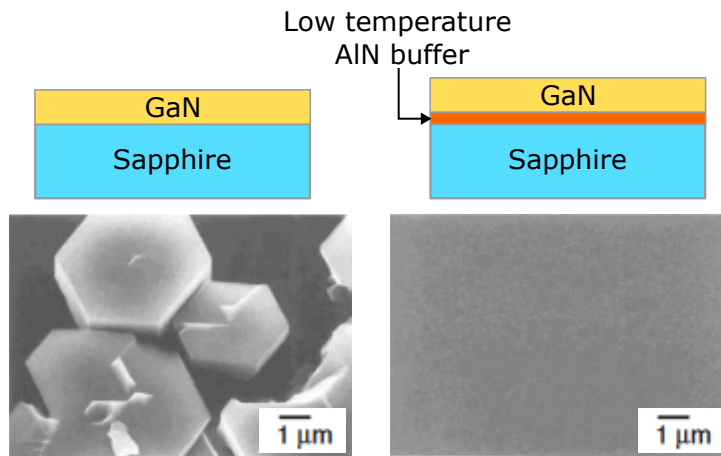


FIGURE 1.7: SEM images of MOCVD GaN on (0001) sapphire, with (right) and without (left) a low temperature AlN buffer layer. Adapted from: [81]

two step method (600 °C AlN deposition, 1000 °C GaN deposition) are shown in Figure 1.7. It is quite clear that GaN grown without a buffer layer is completely unsuitable for the fabrication of optoelectronic devices, let alone micron scale waveguides.

1.3.1.1 GaN properties pertinent to integrated optics applications

For applications in integrated optics GaN has a number of attractive properties. First, it is broadly transparent; from 365 nm to 7 μm [84], though theoretically extending out to 13.6 μm [85]. It has a wide bandgap of 3.4 eV, limiting two photon absorption. Its stiff wurtzite structure, comprised of strongly ionic bonds, makes it capable of handling high temperatures and high optical powers without damage. As seen above, it can be grown on a low-index substrate such as sapphire ($n \sim 1.76$), and given its own relatively high refractive index ($n \sim 2.39$), this leads to good optical confinement in the GaN layer, even if there is an intermediate AlN buffer layer ($n \sim 2.16$). The process of fabricating waveguides in GaN also benefits from the relative maturity of the technologies and recipes developed for optoelectronic devices such as micro-LEDs. Particular examples include reactive ion etching (RIE) in Ar/Cl₂ or Ar/Cl₂/BCl₃ plasmas [86, 87].

The final property that makes GaN interesting, particularly for integrated nonlinear optics, is its lack of inversion symmetry. This means the crystal structure has no centre of symmetry, through which reflections would otherwise map points onto identical points. Non-centrosymmetry is a requisite for second-order nonlinear processes, such as linear electro-optic tuning, second harmonic generation and sum/difference-frequency conversion. Without going into details beyond the scope of this discussion, the time-varying polarisation (or net dipole moment per unit volume), $\mathbf{P}(t)$, can be written as the following power series with respect to an incident electric field $\mathbf{E}(t)$:

TABLE 1.2: Some of the physical effects of each electric susceptibility component.

Term	Effects
$Re(\chi^{(1)})$	Dispersion, birefringence, linear refractive index $n = \sqrt{1 + \chi^{(1)}}$
$Im(\chi^{(1)})$	Linear absorption, gain
$Re(\chi^{(2)})$	Pockels effect, electro-optic tuning, three-wave mixing, second harmonic generation, frequency conversion, optical parametric oscillation
$Im(\chi^{(2)})$	0, always
$Re(\chi^{(3)})$	Kerr effect, four-wave mixing, third harmonic generation, frequency conversion
$Im(\chi^{(3)})$	Raman scattering, two photon absorption

$$\mathbf{P}(t) = \varepsilon_0 \chi \mathbf{E}(t) = \varepsilon_0 \left(\chi^{(1)} \mathbf{E}(t) + \chi^{(2)} \mathbf{E}^2(t) + \chi^{(3)} \mathbf{E}^3(t) + \dots \right), \quad (1.1)$$

where $\chi^{(n)}$ is referred to as the n^{th} order susceptibility and ε_0 is the vacuum permittivity. This time varying polarisation can then act as a source for new components of the electromagnetic field, according to Larmor's theorem [62]. Susceptibilities are complex numbers, whose real and imaginary components (related to each other through the Kramers-Krönig relations) are responsible for the dielectric properties of the material, and in turn to that material's response to incident electric fields. Imaginary components are responsible for dissipative processes that involve energy exchange with the material (eg. inelastic Raman scattering). For reference, the effect of each component is collated in Table 1.2.

All materials have $\chi^{(1)}$ and $\chi^{(3)}$ nonlinearities, but only non-centrosymmetric ones have $\chi^{(2)}$. Second-order materials, which thus provide access to the lowest order of nonlinear processes, are thus of huge importance. In the field of GaN integrated optics, there have been demonstrations of four-wave mixing in waveguides [88], as well as microring-resonance enhanced parametric oscillation [89] and second harmonic generation [56]. These results, in combination with studies on bulk material, allow us to glean a picture of GaN's place in the gamut of nonlinear optics materials. However, since nonlinear susceptibilities are often extracted from the conversion efficiencies of the interacting fields (e.g. the efficiency of converting an input power to output second harmonic power), which are themselves subject to numerous other factors, direct comparison can be difficult [90]. Nevertheless, some GaN nonlinear susceptibilities from literature are shown in Table 1.3.

GaN is on the same order, though moderately less than lithium niobate, which in similar SHG measurements has $\chi^{(2)} = 41.7$ pm/V [94]. However, GaN has the advantage of a broader transparency range, and thus the potential for generating wavelengths in

TABLE 1.3: Measurements of GaN’s second order nonlinear susceptibility, all at telecomms wavelengths. OPO: optical parametric oscillation, MRR: micro-ring resonator, SHG: second harmonic generation.

Source	Comments	Value
Xiong 2011 [56]	SHG in MRR	$\chi^{(2)} = 16 \pm 7 \text{ pm/V}$
Zheng 2022 [89]	OPO in MRR	$\chi^{(2)} = -9 \text{ pm/V}$
Zhang 1998 [91]	Maker-fringe measurements [92] on GaN:Mg films	$\chi^{(2)} = -16.5 \text{ pm/V}$
Abe 2015 [93]	Maker-fringe measurements on bulk GaN	$\chi^{(2)} = -3.8 \pm 0.2 \text{ pm/V}$

the near UV to far-IR by nonlinear frequency conversion [85]. Furthermore, lithium niobate’s remarkable nonlinear properties also make it strongly photorefractive, meaning its refractive index changes under illumination. The photorefractive effect cannot be described by $\chi^{(n)}$ for any n , and it is independent of intensity, meaning it can be strong even at low powers [62]. This effect is severe enough to impede device performance in cavity enhanced nonlinear processes, though schemes for mitigating its effects have been developed [95]. GaN compares favourably to other III-nitrides such as AlN, for which SHG-based extractions of $\chi^{(2)}$ have yielded 4.7 pm/V [96].

1.3.2 Diamond

Diamond’s excellent mechanical, chemical, and electronic properties are well known, and in many cases make it the best-in-class material for related applications. For integrated optics the properties of central interest are its wide-bandgap (5.5 eV), broad transparency window (from 225 nm out to far IR), high refractive index ($n = 2.4$), exceptional Raman gain coefficient (10 cm/GW [97]), and superlative temperature handling abilities, stemming from its low thermo-optic coefficient, low thermal expansion, and unmatched thermal conductivity of 2000 W/m·K. This has led to diamond’s extensive use as a heatspreader for high power vertical-external-cavity surface-emitting lasers [98] and high power GaN-diamond transistors [99]; as well as monolithic [100] or integrated Raman lasers [97].

For quantum applications, diamond is host to hundreds of optically active atomic scale defects, or *colour centres*. Many of these defects – notably the nitrogen vacancy (NV) and silicon vacancy (SiV) centres – are on-demand optically addressable single photon sources that can operate at room temperatures. Such defects are extremely useful resources in optical quantum computing [101–103], communications [104–106] and in the case of the NV centre, magnetometry [107–110].

1.3.2.1 Structure and growth

Diamond is tetrahedrally bonded carbon; forming a crystal structure most easily thought of as two intersecting face-centred cubic lattices offset by $\frac{1}{4}$ the unit cell in each direction. It is a monatomic analogue of the zinc-blende structure (in which GaN may also crystallise, under special conditions), and is thus centro-symmetric, having $\chi^{(2)} = 0$. Under normal temperatures and pressures graphite is the more stable allotrope of carbon, having a standard enthalpy 2.9 kJ/mol below diamond's [113]. Diamond therefore owes its existence to an extremely large activation barrier which prevents its spontaneous conversion back to the energetically favourable graphite phase (Figure 1.8 (a)). Once formed, diamond is thus kinetically stable, though not thermodynamically stable.

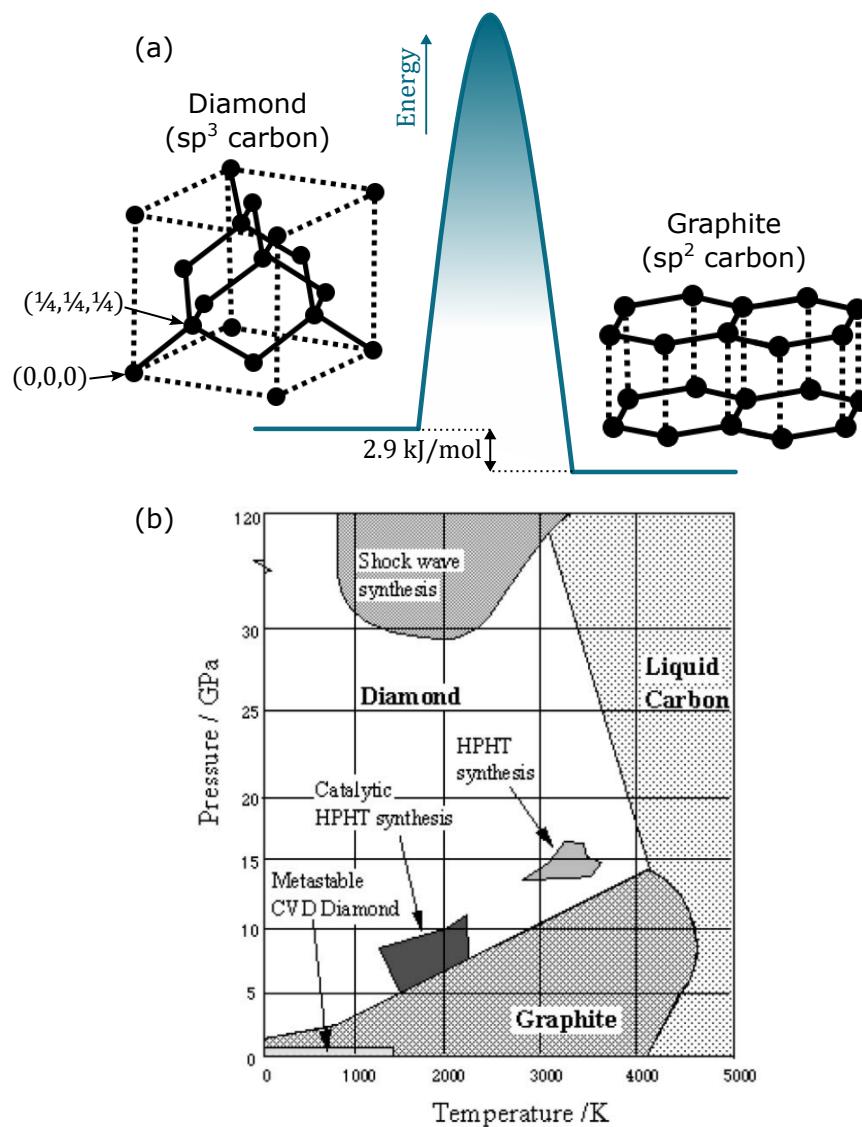


FIGURE 1.8: (a) Carbon allotrope structures, and illustration of the energy activation barrier preventing the conversion of diamond to graphite. *Crystal structures adapted from: [111]* (b) Carbon P-T phase diagram. *Credit: [112]*

This presents an interesting challenge when trying to grow diamond. There are two primary methods: high pressure high temperature (HPHT) synthesis, and chemical vapour deposition (CVD). In HPHT, diamond seed crystals, graphite (or other high purity carbon source), and a metal catalyst are placed in a hydraulic press designed to mimic the extreme conditions under which natural diamonds form underground – tens of thousands of atmospheres and temperatures around 2000 K [113]. Besides the expense of maintaining such extreme conditions, this method of growth is more suited to the production of artificial gemstones, and not to the formation of a thin-film of material useful for photonics applications.

By comparison, CVD operates at low temperatures and pressures. The P-T phase diagram shown in Figure 1.8 (b) delineates the conditions under which HPHT and CVD operate. Purely thermodynamic considerations suggest that the pressures and temperatures associated with CVD growth should lead to graphite only. The success of CVD therefore rests on a complex chemical and physical process – a detailed understanding of which is relatively new [114]. It is now understood that hydrogen is the most important element in the gas phase, primarily because it etches sp^2 bonded carbon (graphite) much faster than sp^3 carbon (diamond). In this way, the diamond lattice is slowly assembled, as graphitic carbon atoms are continuously etched and returned to the gas phase [113, 115].

1.3.2.2 Substrates for diamond epitaxy

Substrates for diamond heteroepitaxy are fairly limited. Although inexpensive, nucleation on silicon substrates is difficult and usually requires either scratching the surface with a diamond-grit abrasive; or utilising bias enhanced nucleation (BEN), whereby the substrate platen is negatively biased in order to bombard the substrate with positive ions, subplanting it with carbon containing species [115, 116]. The largest area and highest quality single crystal diamond grown by this method has been on single crystal iridium (on yttria stabilised zirconia, on silicon) [117]. However, the scalability of this method is limited by the extremely high cost of the substrate materials.

This leaves diamond homoepitaxy. Optical quality single crystal diamonds are regularly grown by homoepitaxy on pre-existing single crystals (themselves grown by CVD or HPHT). However, this limits the achievable size of the diamond to not much larger than the seed crystal. There are methods around this, such as the one shown in Figure 1.9. Several smaller suitable diamond ‘clones’ may be carefully tiled together, effectively forming a larger area substrate for subsequent diamond homoepitaxy. After growth,

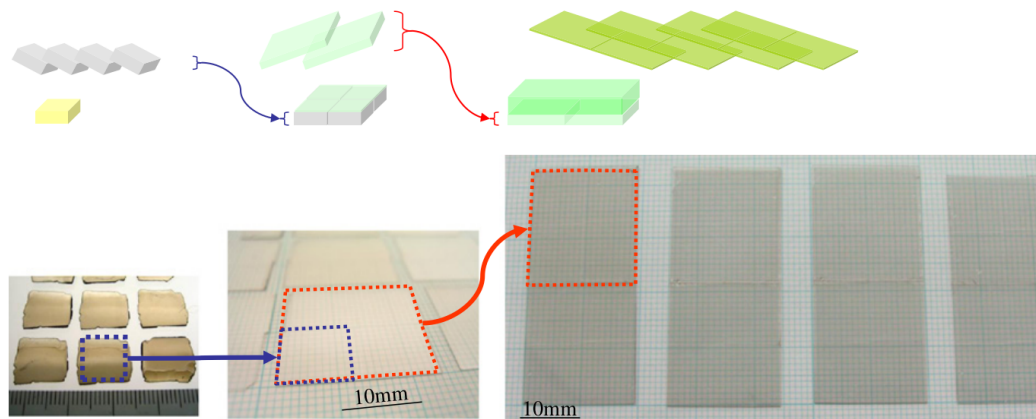


FIGURE 1.9: Repeated growth, lift-off, tiling, and re-growth steps to achieve large area free-standing diamond. *Credit: [118]*

sub-surface damage at a controlled depth, induced either by a powerful laser or ion-bombardment, can then be selectively chemically etched, lifting-off the new diamond. After polishing, the process can be repeated, until relatively large area diamonds result [118]. The success of this method relies on how well aligned each diamond clone is in the greater structure, as misalignment leads to strong variations in the diamond morphology.

While impressive and promising, these endeavours in growth serve to highlight that the kind of material of most use for planar lightwave circuitry (e.g. large lateral dimensions, single-mode thickness, low refractive index substrate) simply does not yet exist. Silicon on insulator is available in 200 mm wafers, GaN on sapphire in 2-4" templates, and single-crystal diamond only as free-standing plates *mm* in size. Furthermore, since they are lifted-off and polished from their growth substrate (as in the above tiling method), they are typically only available in thicknesses of several tens of microns – much too thick for single mode operation at optical wavelengths [119].

1.3.3 Hybrid integration of diamond and GaN

An extremely promising and increasingly widespread method to circumvent the above difficulties with diamond growth is to first fabricate small diamond components, before integrating them with another material platform which does not suffer the same issues. That platform should be commercially available in larger areas, and possess properties not intrinsic to the diamond that may enhance device functionality (e.g. second-order optical nonlinearities).

In the remainder of this thesis, the platform investigated is GaN on sapphire, and the integration method is micro-transfer printing. GaN is an excellent host platform for diamond because of their similar refractive indices – easing phase-matching requirements

between optical modes in each material and reducing interfacial scattering losses. Both indices are around 2.4 at 637 nm, which incidentally, is the zero-phonon line emission wavelength of diamond's NV centre [104]. Additionally, GaN can be fabricated on much larger scales than *mm*-sized diamond platelets, and possesses the second-order nonlinearity which is lacking in diamond.

1.4 Microring resonator theory

Microring resonators are a fundamental component of integrated optical platforms and allow measurement of key performance parameters such as waveguide loss and dispersion. They are employed in a range of measurements in the following chapters, and so are treated in some detail here.

Waveguides forming closed loops – usually taking the form of rings, disks, or racetracks – constitute a class of optical microresonators used extensively in integrated optics. If a whole number of wavelengths fit into the optical path length of the loop, or:

$$\lambda_{res} = \frac{n_{eff}(\lambda)L}{m}, \quad m = 1, 2, 3, \dots \quad (1.2)$$

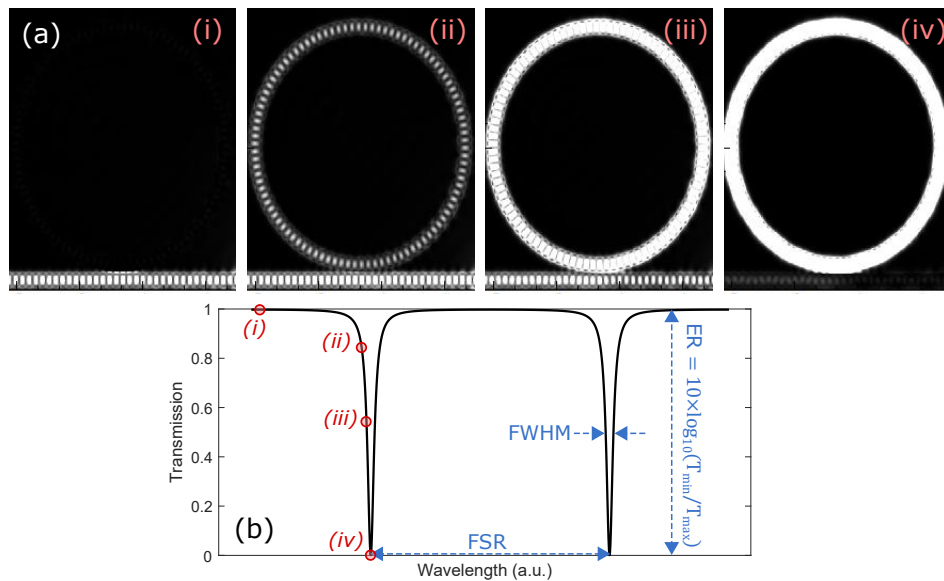


FIGURE 1.10: (a) Finite-difference time domain simulations of a silicon microring resonator, radius 5 μm . A broadband pulse, centred on 1592.5 nm with a bandwidth of 2.5 nm, is injected into the bus waveguide (bottom left). The plots show the square magnitude electric field distributions 10,000 fs after simulation start, for four different wavelengths: from off-resonance (i), to on-resonance (iv). (b) Model transmission spectrum of a microring resonator, with terms labelled.

then the microresonator is said to be on resonance. $n_{eff}(\lambda)$ is the effective index of the circulating mode, and L is the physical cavity length. Not to be confused with the cross-sectional waveguide mode of effective index n_{eff} is the *azimuthal* ring mode, described simply with the azimuthal mode number m . Coherent light at the resonance wavelength λ_{res} constructively interferes inside the loop, leading to a significant build-up of optical intensity (Figure 1.10 (a-iv)). This effect is used to enhance their efficiency as integrated lasers [120], and the efficiency of other nonlinear processes such as second harmonic generation [121, 122] or photon-pair generation by four wave mixing [123]. In addition, the sensitive wavelength dependence offered by these microresonators makes them well suited to applications as wavelength filters [124], frequency combs [125], intensity modulators [126], phase modulators [127], wavelength division (de)multiplexers [128], and sensors (of anything that should shift n_{eff} or L) [129]. Figure 1.10 (a) shows the simulated field distribution of a waveguide-coupled silicon microring resonator for four different wavelengths, while Figure 1.10 (b) shows where these wavelengths might lie on a model transmission spectrum; as well as showing the free spectral range (FSR), full width half maximum (FWHM), and extinction ratio (ER).

1.4.1 Transfer matrix formulation

Consider a single waveguide ring adjacent to a straight bus waveguide, as in Figure 1.11. The bus is situated close enough to the ring that optical power can evanescently couple between the two. This configuration is known as an *all-pass* or *notch* filter, and will feature heavily in subsequent chapters. The transmission characteristics of the resonator are most commonly described in the transfer matrix formalism [130]. The four complex mode amplitudes $E_{i1}, E_{i2}, E_{t1}, E_{t2}$ are normalised, so that their squared magnitudes correspond to the modal power, and E_{i1} is set to equal 1 so that 1 unit of power is injected into the system at time zero. They are also harmonic in time, oscillating according to $\exp(i\omega t)$, where $\omega = 2\pi\nu$ is the angular frequency. They interact in the coupling region according to [131]:

$$\begin{pmatrix} E_{t1} \\ E_{t2} \end{pmatrix} = \begin{pmatrix} r & k \\ -k^* & r^* \end{pmatrix} \begin{pmatrix} E_{i1} \\ E_{i2} \end{pmatrix} \quad (1.3)$$

where r and k are the complex coupling coefficients, denoting the self-coupling and cross-coupling respectively. The coupling matrix determinant is equal 1, meaning power is preserved in the coupling region:

$$|r|^2 + |k|^2 = 1 \quad (1.4)$$

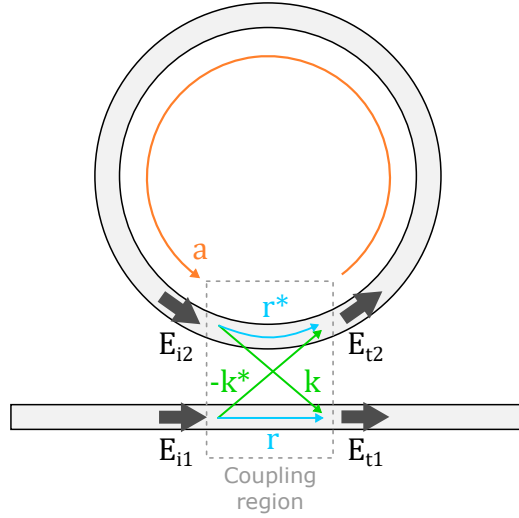


FIGURE 1.11: Model ring resonator with single evanescently coupled bus waveguide - a configuration known as an *all-pass* or *notch* filter.

Thus $|r|^2$ and $|k|^2$ represent the power splitting ratios, and $|k|^2$ – usually replaced with the Greek letter κ – is the power cross-coupling from bus waveguide to the ring.

The field E_{i2} is simply the field E_{t2} after one round trip of the ring, or:

$$E_{i2} = a e^{i\phi} E_{t2} \quad (1.5)$$

where a is the single pass attenuation coefficient, making a^2 the single pass power transmission factor. For a lossless ring, $a = 1$. ϕ is the phase accumulation in a single round trip of the ring, given by:

$$\phi = \beta L = \frac{2\pi}{\lambda} n_{eff}(\lambda) L, \quad (1.6)$$

where β is the propagation constant of the circulating mode. Equations 1.3 and 1.5 are enough to calculate expressions for the power in the ring and the power transmitted in the bus waveguide, the latter of which we are most interested in. We find that the transmission function of the notch filter, T_n , is:

$$T_n = |E_{t1}|^2 = \frac{a^2 + r^2 - 2ra \cos(\phi)}{1 + (ra)^2 - 2ra \cos(\phi)}, \quad (1.7)$$

and resonances occur for $\phi = 0, 2\pi, 4\pi, \dots$

It is also possible to calculate the effective phase delay added by the ring [30]:

$$\varphi = \pi + \phi + \arctan\left(\frac{r\sin(\phi)}{a - r\cos(\phi)}\right) + \arctan\left(\frac{r\sin(\phi)}{1 - r\cos(\phi)}\right), \quad (1.8)$$

which is valid over a small detuning region around the resonance position. Before continuing, some caveats need to be introduced. First, the assumption that the coupling is lossless could lead to artificially narrowed resonances since the FWHM decreases as loss decreases. Thus, to keep the width correct these losses are included in the a term. When discussing resonator losses, we are thus referring to a *distributed loss*, which is simply derived from a^2 and is expressed in units of dB/cm . Contributions to the distributed loss include sidewall scattering, material absorption, coupler-section scattering, and radiative (bend) loss intrinsic to the microring itself. The distributed loss is necessarily higher than the propagation loss of an equivalent waveguide, or indeed the intrinsic loss of an uncoupled and isolated ring.

Second, note that a and r enter equation 1.7 symmetrically, meaning they can be freely swapped without changing the output of the function. Thus, when fitting data with a and r as free variables, care must be taken to ascribe the correct physical meaning to each. To do so requires the parameterisation of one or the other (e.g. varying the coupling by increasing the gap between ring and bus), so that trends across several devices can be examined. Alternatively, since longer wavelengths are confined less for a given geometry, they have greater cross-coupling fractions and it may be possible to examine trends in a transmission wavelength sweep of a single device [132].

1.4.2 Coupling regimes

A ring resonator's performance is strongly dependent upon the fraction of power coupled from bus to ring. In the above description, this depends on the parameters a and r , where r is related to the *power* cross-coupling κ through $\kappa = 1 - r^2$. If $r < a$ the ring is over-coupled and if $r > a$ the ring is under-coupled. If $r = a$, then the ring is critically coupled, and at this point the transmission drops to zero. The difference in resulting lineshapes is demonstrated in Figure 1.12 (a), which for a fixed $a = 0.9$, plots three model resonances of varying r . In Figure 1.12 (b), the ER and FWHM of a model resonance are plotted as a function of the ratio r/a (equal to 1 at critical coupling). Note how on the under-coupling side of critical coupling the extinction very quickly tends to 0 dB, while for over-coupling the extinction is non-zero for a much larger range of coupling values. The FWHM meanwhile monotonically decreases with cross-coupling. Finally, the effective phase delay, calculated for increasing r values, is plotted in Figure 1.12 (c). In the over-coupled regime, there is a continuous positive increase in the phase added by temporary storage of light in the ring. At critical coupling, there is an abrupt π

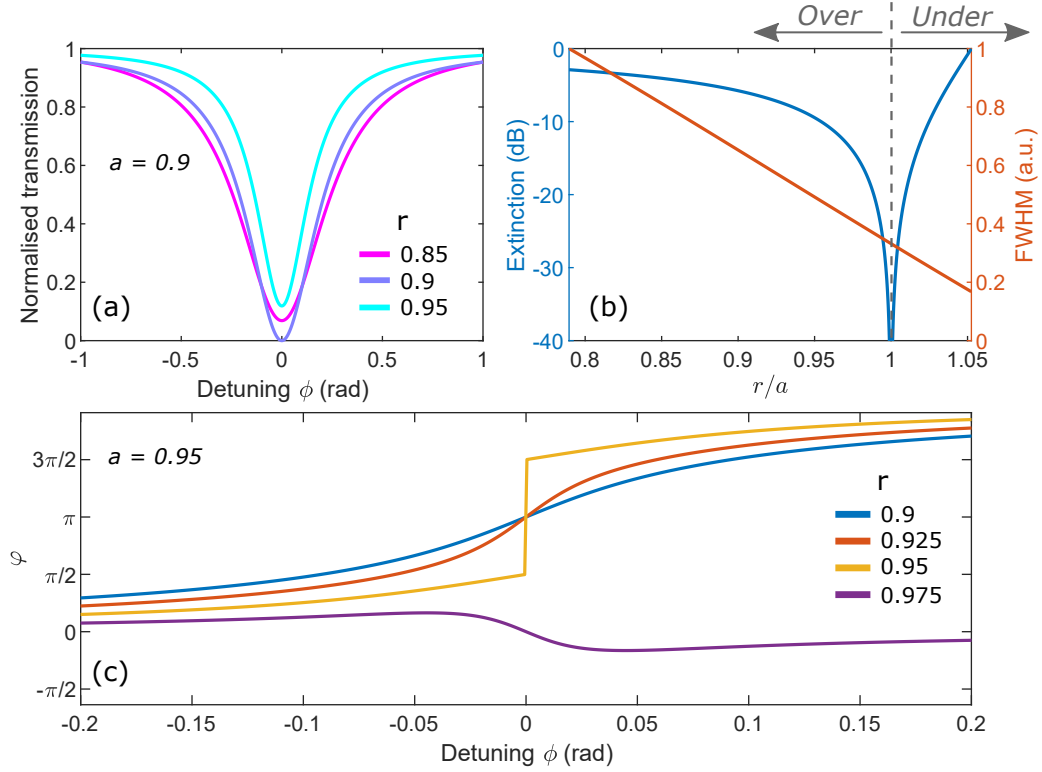


FIGURE 1.12: (a) Resonant lineshapes, for a model resonator of fixed loss and varying r . The under-coupled case is both the narrowest and shallowest. The over-coupled case is broadest, and the critically-coupled case is deepest. (b) Extinction ratio (ER) and peak FWHM for a single resonance and increasing r/a . At $r/a = 1$, critical coupling is reached. (c) Effective phase delay for a small detuning around a resonance.

phase shift which leads to perfect destructive interference of the ring out-coupled and bus self-coupled light, which in turn is why the transmission drops to zero when $r = a$. An under-coupled ring actually decreases the phase-shift around the resonance.

1.4.3 Q factor and other dispersion related parameters

Physically, the quality (Q) factor of a microresonator is the number of oscillations of the field in the loop before cavity loss attenuates the optical energy to $1/e$ of its initial value. It is given by:

$$Q = \frac{\lambda_{res}}{FWHM}, \quad (1.9)$$

From equation 1.7, an expression for the FWHM can be found in terms of the loss and power-coupling terms [30]:

$$FWHM = \frac{(1 - ra)\lambda_{res}^2}{\pi n_g L \sqrt{ra}}, \quad (1.10)$$

Then, the Q factor can be expressed as:

$$Q = \frac{\pi n_g L \sqrt{ra}}{\lambda_{res}(1 - ra)}, \quad (1.11)$$

where n_g is the *group refractive index*, to be defined shortly.

Since the Q factor includes loss to the coupler, it must necessarily be lower than the intrinsic Q factor of an identical, but isolated resonator. Thus, there is a distinction between the *loaded* and unloaded (or *intrinsic*) Q factors. There is a simple relationship between the two, which also includes the on-resonance normalised transmission, T [36]:

$$Q_{intrinsic} = \frac{2Q_{loaded}}{1 \pm \sqrt{T}} \quad (1.12)$$

The summation is taken in the denominator in the case of under-coupling, and subtraction in the case of over-coupling. Unless otherwise stated, in the rest of this thesis ‘Q factor’ is understood to refer to loaded Q factor.

Finally, the free spectral range (FSR), which is simply the inter-peak spacing, is given by [131]:

$$FSR = \frac{\lambda^2}{n_g L} \quad (1.13)$$

Instead of the effective index, the preceding equations have used the group index, n_g . While the effective index describes the phase velocity, v_p , of a plane wave in a waveguide according to: $n_{eff} = c/v_p$, the group index describes the group velocity, v_g , of the envelope around a propagating pulse: $n_g = c/v_g$. Since waveguides are inherently dispersive media (stemming both from the the constituent material’s chromatic dispersion and independent waveguide geometry dispersion effects), it is important to include the group index in the previous equations. The group index is defined by the following [131]:

$$n_g = n_{eff} - \lambda \frac{dn_{eff}}{d\lambda} \quad (1.14)$$

To see the effect of waveguide dispersion, consider the transmission spectrum shown in Figure 1.13 (a); taken for a GaN racetrack resonator (discussed in greater detail in Chapter 2). In this case, if the mean FSR of the first four resonances (solid red lines) is projected across the entire spectrum (dotted red lines), the expected peak positions quickly fall behind the actual peak positions. The reason for this is waveguide dispersion.

In Figure 1.13 (b) the FSR, plotted for a centre wavelength between the two peaks of interest, is seen to increase with wavelength. By simple rearrangement of equation 1.13, these values can be used to plot the group index, also shown in Figure 1.13 (b). Waveguide dispersion is usually quantified with the dispersion parameter, D , which describes the spreading in time of a pulse at a given wavelength, for a given length of propagation, and so has units $ps/(nm \times km)$. It is given by [133]:

$$D = -\frac{\lambda}{c} \frac{d^2 n_{eff}}{d\lambda^2} = \frac{1}{c} \frac{dn_g}{d\lambda} \quad (1.15)$$

Since n_{eff} is not easily accessible, we can more easily calculate D by using the slope of the group index n_g (calculated simply from equation 1.13) with respect to wavelength. Figure 1.13 (c) plots D calculated with this method, and compares it with values extracted from finite difference simulations. Since the extracted slope of n_g strongly depends on how well the measured values conform to a low order polynomial fit (usually of order 3), the relative agreement between the measured and simulated values is reassuring. The GaN is displaying *anomalous dispersion*, whereby $D > 0$. The opposite case is termed *normal dispersion*, and is more common among strongly confined optical modes

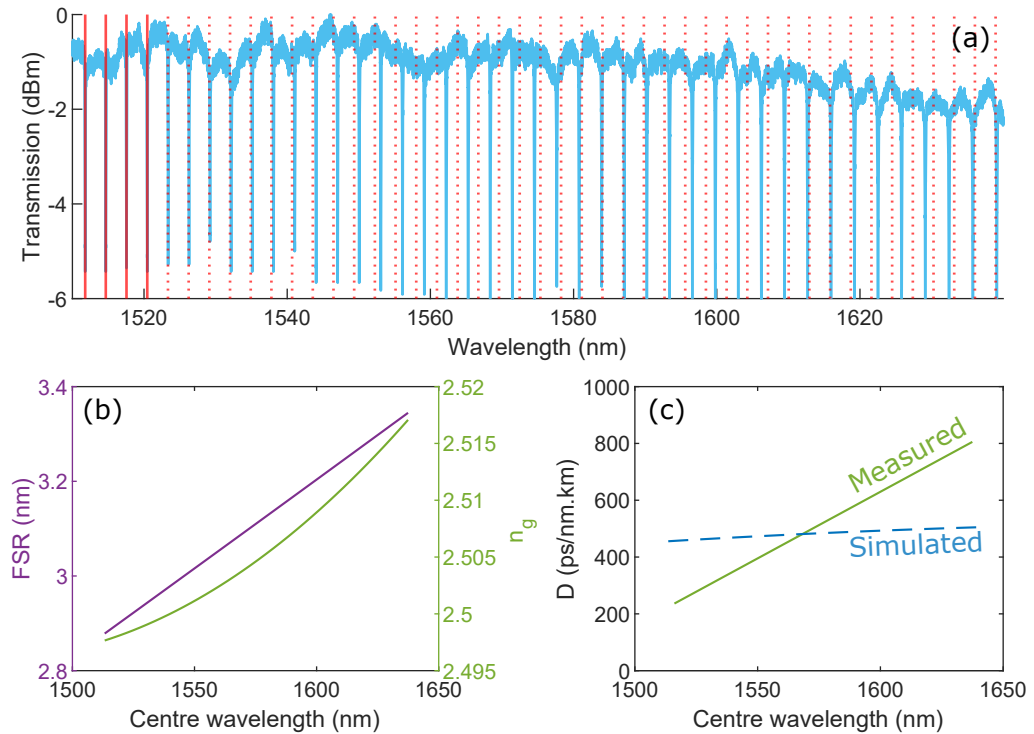


FIGURE 1.13: (a) GaN racetrack resonator transmission spectrum, displaying the effects of dispersion on the FSR. (b) Calculation of n_g from the FSRs extracted from the spectrum.

and shorter wavelengths, wherein waveguide geometric dispersion effects are more severe [134].

1.4.4 Example parameter extraction using resonance fitting

Resonance lineshapes are Lorentzian, and may in the first instance be fitted with Lorentzian functions. Indeed, to simplify the extraction of accurate centre wavelength positions stymied by off-resonance asymmetry, this method is used later in Chapter 6. However, equation 1.7 is also regularly used, both in this thesis and widely in literature, since it conveniently provides information on resonator loss and coupling. It does not include dispersion, so the process for fitting is usually to define a small dispersion-free window around a resonance. The data in that window are then normalised so that equation 1.7 can be fitted – describing well the the transmitted light in a small region of phase/wavelength detuning around the resonance.

The distributed loss and power cross-coupling can be extracted from the values a and r , for which the (non-linear least squares) fit converges. This analysis remains valid in even the most extreme cases: with short wavelengths, extremely narrow resonances and exponential trends in cross-coupling. For example, consider the resonance in Figure 1.14 (a) – a measurement on a proprietary commercial silicon nitride platform. The resonant wavelength is 635.5426 nm and the FWHM is just 0.43 pm, giving a loaded Q factor of 1.49×10^6 . The free parameters in the fit are found to be 0.99974 and 0.99649 (though we do not yet know for certain which is a and which is r).

Given the peak’s narrow width and relatively poor extinction, it is likely under-coupled, and thus the smaller of the two fit parameters must be equal to a . This is confirmed

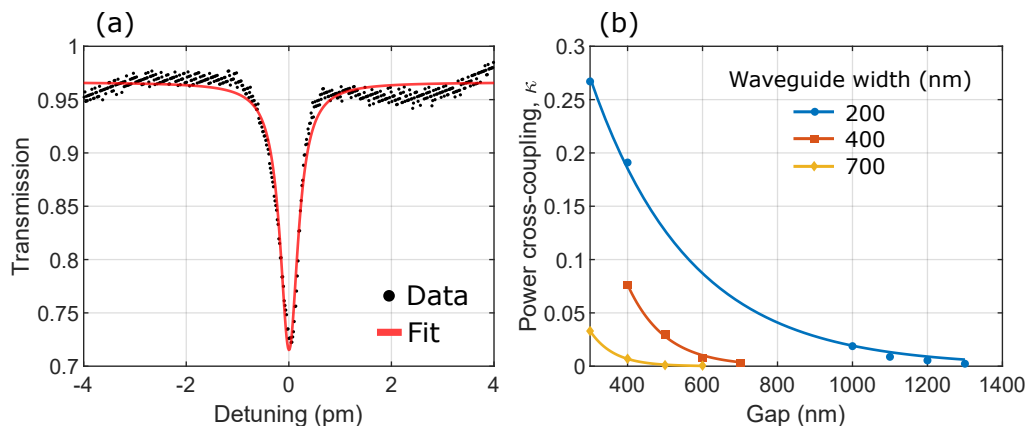


FIGURE 1.14: (a) High Q resonance, fitted with equation 1.7. (b) Power cross-couplings for increasing bus-ring separation gap, and three sets of waveguide widths. Narrower waveguides confine light less, and so couple more.

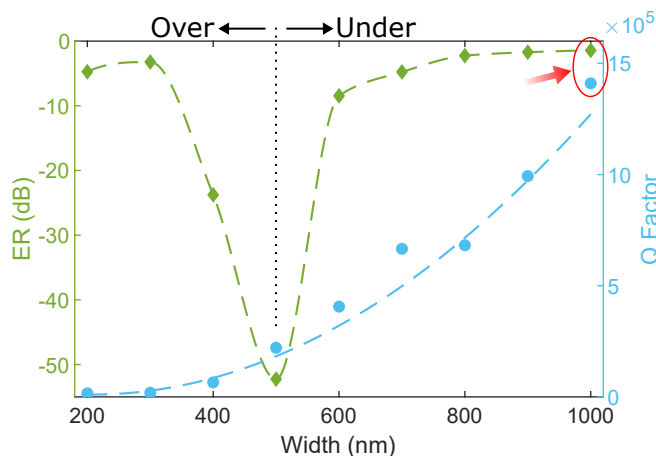


FIGURE 1.15: Extinction ratio and Q factor as functions of waveguide width. The red arrow indicates the position of the resonance in Figure 1.14 (a).

by the peak's location on the curves plotted in Figure 1.15, which shows the ER and Q factor for rings of varying waveguide width. For a fixed wavelength, a decrease in width pushes the confined mode towards cut-off, reducing confinement and increasing cross-coupling. Therefore, in Figure 1.15, to the left of the critically coupled (maximum extinction) position at 500 nm, the resonances are over-coupled, and to the right they are under-coupled. This is corroborated by the monotonic increase in Q factor for increasing waveguide width (decreasing cross-coupling). Knowledge of a and r allows us to plot the extracted power cross-coupling fractions, this time as functions of increasing gap between bus and ring. They closely agree with exponential fits (Figure 1.14 (b)), as expected given the exponential dependency of the evanescent waves in the coupling region between bus and ring.

By inspecting trends in FWHM and ER, neither of which depend on the fitting, we can be sure we are subsequently assigning the correct meaning to each of the fit parameters. This is especially important when characterising a new material platform, for which the expected losses and couplings may not be known (although numerical simulations may help with the latter). It is also particularly important for low loss resonances that may be near critical coupling, as in the above. If however there is a large discrepancy between the extracted fit parameters, it is often self-evident which corresponds to loss and which to coupling, by comparison with coupling simulations or reasonable justifications of extracted loss values.

1.4.5 Fano, asymmetric, and split resonances

We have so far described the response of an ideal microring resonator whose resonance lineshapes are Lorentzian. Other lineshapes are possible, each stemming from a different

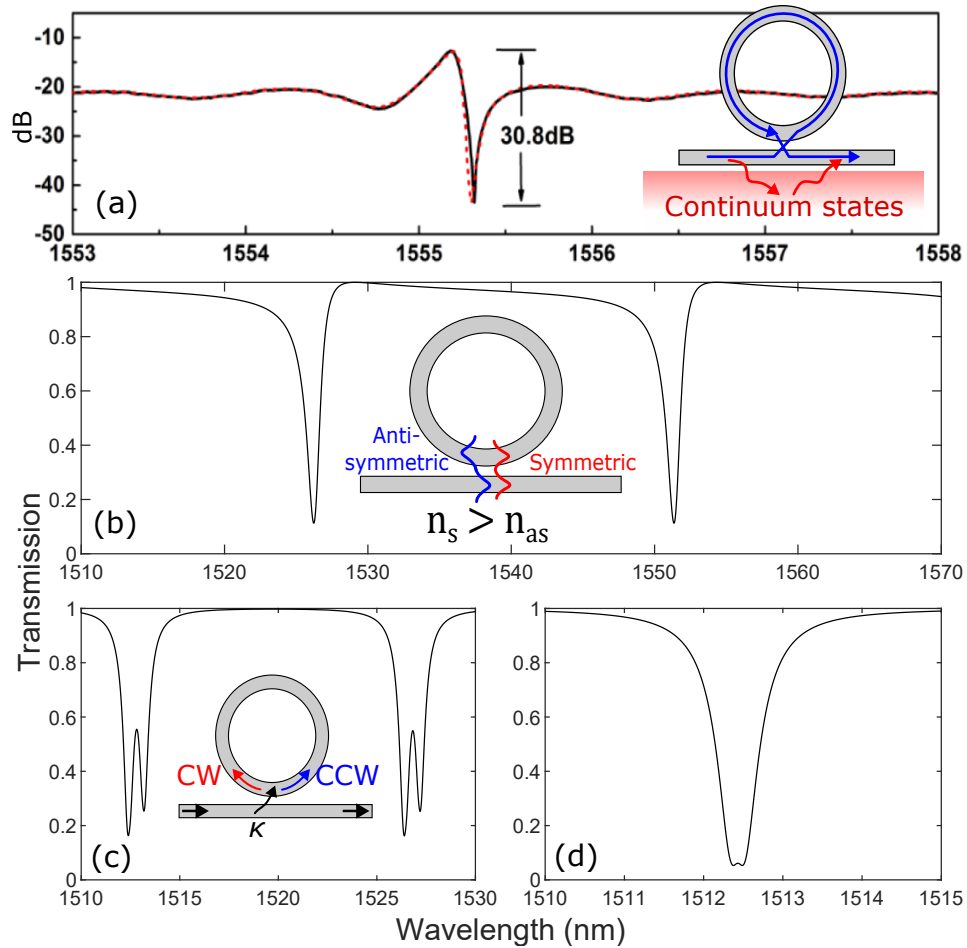


FIGURE 1.16: (a) Example Fano resonance in a silicon microring *Adapted from: [136]*, with additional schematic describing Fano interference in the transmission waveguide. (b) Asymmetric resonances plotted with the model provided in [137], which accounts for differences in supermode losses in the coupling section. (c) Example of asymmetric resonance splitting, with non-degenerate counter-propagating modes in the ring. (d) A resonance which is only moderately split, showing an effective flattening of the dip minimum level.

physical deviation from this ideal case. Normally considered deleterious – the result of fabrication errors – some of these lineshapes may have their own advantages because of enhanced wavelength sensitivity and extinction ratios [135]. Whether to target a specific application, or just to understand why a device isn't performing as expected, it is important to appreciate where these deviations from the ideal lineshape come from. Note, these lineshapes are not the result of low frequency modulations in the off-resonance transmitted light, which may be coming from Fabry-Perot resonances in the bus waveguide or broadband scattering from defects along the propagation length; but are instead fundamentally different from normal behaviour as described above.

Fano resonances occur as the result of interference between discrete energy states and a continuum of states, and as such are historically the domain of atomic physics [138].

The typical asymmetric Fano lineshape has also been observed (or engineered) in resonant photonic systems such as ring resonators (as in Figure 1.16 (a)) [135, 136], generic waveguide coupled cavities [139, 140], and metamaterials [141]. Here, the discrete energy states are replaced with classical resonant modes – commonly the azimuthal modes of a microring. Interference in the transmission line then occurs between an indirect resonance-assisted pathway, and a direct pathway progressing via a continuum band of non-resonant states [142]. In this sense, the typical Lorentzian lineshape described previously is in fact a special case of the more general case which includes Fano resonances [143]. The relative coupling strengths between the direct and indirect pathways are what determines the direction and magnitude of the asymmetry in the resonance.

Another source of asymmetry, previously studied for the case of fibre based rings, stems from the dissimilar modal losses of the symmetric and anti-symmetric supermodes in the coupling section (Figure 1.16 (b)) [137]. For a description of waveguide coupling, and explanations of these supermodes, see Chapter 2. Youngquist *et al.* used these two supermodes as a basis for an equivalent derivation of the transmission function of a ring resonator [137]. Although describing macroscale loops of fibre, their description should remain valid for integrated devices where bus and ring have similar cross sections and are single mode. Since the symmetric supermode has a higher effective index, it is more confined and should be attenuated less. Asymmetry is then a natural result of their model, and if the two modes are given the same loss, Lorentzian lineshapes are recovered.

The most prevalent deviation from a single Lorentzian lineshape is a double Lorentzian, as in Figures 1.16 (c,d). With power entering the bus waveguide from the left, the ring as drawn in Figure 1.16 (c) will never have its backward (clockwise, CW) propagating mode excited. All of the power from the bus will couple to the forward (counter-clockwise, CCW) mode. For a perfect ring the CW and CCW modes are uncoupled and degenerate, i.e. they have the same resonant wavelength. If some scattering mechanism (usually sidewall roughness) is present, optical power can couple from one mode to the other, though they may still be degenerate. Counter-directional coupling leads to a build-up of power in the CW mode, and in turn to a new basis set of system eigenmodes: the two travelling CW and CCW waves, as well as new symmetric and anti-symmetric standing wave linear combinations of these [144]. These modes are not degenerate, and so the single Lorentzian splits in two. There are several physical contributions to resonance splitting, and they are generally wavelength dependent – meaning one resonance may exhibit it while the next does not. The primary source, especially for rings with high index contrast, is sidewall roughness [145, 146], but it has also been shown that perturbations caused by the presence of the coupling section itself contribute to backscattering [144]. This means that the coupling length and gap can potentially

be engineered to ameliorate (or induce, if desired) resonance splitting. Finally, if the splitting is very slight, as in Figure 1.16 (d), the resonance may appear as more of a narrowband-stop filter.

1.5 Chapter summary

This chapter gave a brief historical overview of integrated optics: from Colladon's early demonstration of total internal reflection along a jet of water, to the inception of planar lightwave circuitry with Miller's influential 1969 paper. The recent increase in demand for wide-bandgap material platforms was elucidated, alongside a list of several potential material platforms. An overview of the materials used later in this thesis was given, with attention given to challenges in the growth of the kind of material suited for integrated optics. The necessary theory of ring resonators was built up from the transfer matrix formalism, and important expressions for the transmission function and Q factor of an all-pass filter were given.

Chapter 2 details the simulation, design, fabrication, and optical characterisation of GaN on sapphire racetrack and disk resonators, edge coupled to bus waveguides. Although the simulations are for GaN on sapphire specifically, some more general details into the numerical simulation of waveguides are given. A detailed analysis of the resonator loss and coupling, as functions of varying racetrack parameters, is also presented.

Chapter 3 progresses to present, for the first time, electrically tunable GaN racetrack resonators. After giving the motivation for fabricating actively tunable microresonators, the tuning efficiencies and bandwidths of GaN racetracks are examined in detail.

Following these chapters which focus on the development of the GaN platform itself, chapter 4 presents the topic of hybrid integration, highlighting the benefits of assembling a chip to use the complementary properties of multiple materials, and giving some examples from literature. The fabrication and assembly of diamond microdisk resonators is presented, alongside the optical characterisation of a novel hybrid diamond-on-GaN chip.

Finally, chapter 5 details a potential application for the hybrid, wide-bandgap, diamond-on-GaN device, in photonic thermometry. A brief overview of the history of electrical resistance thermometry is made, culminating in recent attempts to advance the technology with photonic measurements of temperature. The theory of a dual-material photonic thermometer is presented, and a resulting fivefold reduction in temperature measurement error of the hybrid device in comparison with similar silicon based devices is shown.

References

- [1] Yufei Liu, Shuxiao Wang, Jiayao Wang, Xinyu Li, Mingbin Yu, and Yan Cai. Silicon photonic transceivers in the field of optical communication. *Nano Communication Networks*, 31:100379, mar 2022.
- [2] Saeed Fatholouloumi, David Hui, Susheel Jadhav, Jian Chen, Kimchau Nguyen, M. N. Sakib, Z. Li, Hari Mahalingam, Siamak Amiralizadeh, Nelson N. Tang, Harinadh Potluri, Mohammad Montazeri, Harel Frish, Reece A. Defrees, Christopher Seibert, Alexander Krichevsky, Jonathan K. Doylend, John Heck, R. Venables, A. Dahal, A. Awujoola, A. Vardapetyan, Guneet Kaur, Min Cen, Vishnu Kulkarni, Syed S. Islam, R. L. Spreitzer, S. Garag, A. C. Alduino, R. K. Chiou, L. Kamyab, S. Gupta, B. Xie, R. S. Appleton, S. Hollingsworth, S. McCargar, Y. Akulova, K. M. Brown, R. Jones, Daniel Zhu, Thomas Liljeberg, and Ling Liao. 1.6 Tbps Silicon Photonics Integrated Circuit and 800 Gbps Photonic Engine for Switch Co-Packaging Demonstration. *Journal of Lightwave Technology*, 39(4):1155–1161, 2021.
- [3] Patrick Steglich, Giulia Lecci, and Andreas Mai. Surface Plasmon Resonance (SPR) Spectroscopy and Photonic Integrated Circuit (PIC) Biosensors: A Comparative Review. *Sensors*, 22(8):2901, apr 2022.
- [4] Vikas Hassija, Vinay Chamola, Vikas Saxena, Vaibhav Chanana, Prakhar Parashari, Shahid Mumtaz, and Mohsen Guizani. Present landscape of quantum computing. *IET Quantum Communication*, 1(2):42–48, dec 2020.
- [5] Daniel J. Blumenthal. Photonic integration for UV to IR applications. *APL Photonics*, 5(2), feb 2020.
- [6] D Colladon. On the reflections of a ray of light inside a parabolic liquid stream. *Comptes Rendus*, 15:800–802, 1842.
- [7] Jeff Hecht. Illuminating the Origin of Light Guiding. *Optics and Photonics News*, pages 26–30, 1999.
- [8] Jeff Hecht. *City of Light: The Story of Fiber Optics*. Oxford University Press, 2004.
- [9] James Clerk Maxwell. VIII. A dynamical theory of the electromagnetic field. *Philosophical Transactions of the Royal Society of London*, 155:459–512, dec 1865.
- [10] H Hertz. On the Finite Velocity of Propagation of Electromagnetic Action. *Wiedemann's Ann.*, 34:551, 1888.
- [11] Joseph F Mulligan. Heinrich hertz and the development of physics. *Physics Today*, 42(3):50–57, 1989.
- [12] Dipak L. Sengupta and Tapan K. Sarkar. Maxwell, Hertz, the Maxwellians, and the early history of electromagnetic waves. *IEEE Antennas and Propagation Magazine*, 45(2):13–19, apr 2003.
- [13] Bruce J. Hunt. Oliver Heaviside: A first-rate oddity. *Physics Today*, 65(11):48–54, nov 2012.
- [14] Christopher Donaghy-Spargo and Alex Yakovlev. Oliver Heaviside's electromagnetic theory. *Philosophical Transactions of the Royal Society A: Mathematical, Physical and Engineering Sciences*, 376(2134), dec 2018.

- [15] Oliver Heaviside. Electromagnetic Theory Vol. I. *The Electrician Publishing*, 1893.
- [16] Lord Rayleigh. On the passage of electric waves through tubes, or the vibrations of dielectric cylinders. *The London, Edinburgh, and Dublin Philosophical Magazine and Journal of Science*, 43(261):125–132, 1897.
- [17] Karle S. Packard. The Origin of Waveguides: A Case of Multiple Rediscovery. *IEEE Transactions on Microwave Theory and Techniques*, 32(9):961–969, 1984.
- [18] <https://commons.wikimedia.org/wiki/File:WaveguideJ-Band.png> Date Accessed: 2022-04-15.
- [19] Shankar Kumar Selvaraja, Patrick Jaenen, Wim Bogaerts, Dries Van Thourhout, Pieter Dumon, and Roel Baets. Fabrication of photonic wire and crystal circuits in silicon-on-insulator using 193-nm optical lithography. *Journal of Lightwave Technology*, 27(18):4076–4083, sep 2009.
- [20] A. L. Schawlow and C. H. Townes. Infrared and Optical Masers. *Physical Review*, 112(6):1940, dec 1958.
- [21] T. H. Maiman. Stimulated Optical Radiation in Ruby. *Nature*, 187:493–494, 1960.
- [22] K C Kao and G A Hockham. Dielectric-fibre surface waveguides for optical frequencies. *Proceedings of the IEE*, 113(7):1151–1158, 1966.
- [23] Alexander Graham Bell. The photophone. *Journal of the Franklin Institute*, 110(4):237–248, 1880.
- [24] K. Aiki, M. Nakamura, and J. Umeda. A Frequency-Multiplexing Light Source with Monolithically Integrated Distributed-Feedback Diode Lasers. *IEEE Journal of Quantum Electronics*, 13(4):220–223, 1977.
- [25] P K Tien. Integrated optics and new wave phenomena in optical wave guides. *Reviews of Modern Physics*, 49(2):361–408, 1977.
- [26] Stewart E. Miller. Integrated optics: An introduction. *Bell System Technical Journal*, 48(7):2059–2069, 1969.
- [27] E. A. J. Marcatili. Dielectric rectangular waveguide and directional coupler for integrated optics. *Bell System Technical Journal*, 48(7):2071–2102, 1969.
- [28] R. G. Poulsen. PLASMA ETCHING IN INTEGRATED CIRCUIT MANUFACTURE - A REVIEW. In *J Vac Sci Technol*, volume 14, pages 266–274. American Vacuum Society AVS, jun 1976.
- [29] R. A. Soref and J. P. Lorenzo. Single-crystal silicon: a new material for 1.3 and 1.6 μm integrated-optical components. *Electronics Letters*, 21(21):953–954, 1985.
- [30] W. Bogaerts, P. De Heyn, T. Van Vaerenbergh, K. De Vos, S. Kumar Selvaraja, T. Claes, P. Dumon, P. Bienstman, D. Van Thourhout, and R. Baets. Silicon microring resonators. *Laser and Photonics Reviews*, 6(1):47–73, jan 2012.
- [31] Andrea M. Armani, Jinghan He, Hong Chen, Jingan Zhou, Yuji Zhao, Jin Hu, Constantine Sideris, Yingmu Zhang, Andre Kovach, and Mark C. Harrison. Nonlinear nanophotonic devices in the ultraviolet to visible wavelength range, sep 2020.

- [32] Marco A.G. Porcel, Alberto Hinojosa, Hilde Jans, Andim Stassen, Jeroen Goyvaerts, Douwe Geuzebroek, Michael Geiselmann, Carlos Dominguez, and Iñigo Artundo. [INVITED] Silicon nitride photonic integration for visible light applications. *Optics & Laser Technology*, 112:299–306, apr 2019.
- [33] Martin Hubert Peter Pfeiffer, Clemens Herkommer, Junqiu Liu, Tiago Morais, Michael Zervas, Michael Geiselmann, and Tobias J. Kippenberg. Photonic damascene process for low-loss, high-confinement silicon nitride waveguides. *IEEE Journal of Selected Topics in Quantum Electronics*, 24(4), jul 2018.
- [34] Haolan Zhao, Bart Kuyken, Stéphane Clemmen, François Leo, Ananth Subramanian, Ashim Dhakal, Philippe Helin, Simone Severi, Edouard Brainis, Gunther Roelkens, and Roel Baets. Visible-to-near-infrared octave spanning supercontinuum generation in a silicon nitride waveguide. *Optics Letters*, 40(10):2177, may 2015.
- [35] Chi Xiong, Wolfram H.P. Pernice, and Hong X. Tang. Low-loss, silicon integrated, aluminum nitride photonic circuits and their use for electro-optic signal processing. *Nano Letters*, 12(7):3562–3568, jul 2012.
- [36] Tsung Ju Lu, Michael Fanto, Hyeonrak Choi, Paul Thomas, Jeffrey Steidle, Sara Mouradian, Wei Kong, Di Zhu, Hyowon Moon, Karl K. Berggren, Jeehwan Kim, Mohammad Soitani, Stefan Preble, and Dirk Englund. Aluminum nitride integrated photonics platform for the ultraviolet to visible spectrum. *Optics express*, 26(9):11147, 2018.
- [37] Hong Chen, Jingan Zhou, Dongying Li, Dongyu Chen, Abhinav K. Vinod, Houqiang Fu, Xuanqi Huang, Tsung Han Yang, Jossue A. Montes, Kai Fu, Chen Yang, Cun Zheng Ning, Chee Wei Wong, Andrea M. Armani, and Yuji Zhao. Supercontinuum Generation in High Order Waveguide Mode with near-Visible Pumping Using Aluminum Nitride Waveguides. *ACS Photonics*, 8(5):1344–1352, may 2021.
- [38] Gavin N West, William Loh, Dave Kharas, Cheryl Sorace-Agaskar, Karan K. Mehta, Jeremy Sage, John Chiaverini, and Rajeev J. Ram. Low-loss integrated photonics for the blue and ultraviolet regime. *APL Photonics*, 4(2):26101, 2019.
- [39] Cheryl Sorace-Agaskar, Dave Kharas, Siva Yegnanarayanan, Ryan T. Maxson, Gavin N. West, William Loh, Suraj Bramhavar, Rajeev J. Ram, John Chiaverini, Jeremy Sage, and Paul Juodawlkis. Versatile Silicon Nitride and Alumina Integrated Photonic Platforms for the Ultraviolet to Short-Wave Infrared. *IEEE Journal of Selected Topics in Quantum Electronics*, 25(5), sep 2019.
- [40] Michael Belt, Michael L. Davenport, John E. Bowers, and Daniel J. Blumenthal. Ultra-low-loss Ta₂O₅-core/SiO₂-clad planar waveguides on Si substrates. *Optica*, 4(5):532, 2017.
- [41] Ranran Fan, Chung-Lun Wu, Yuan-Yao Lin, Chin-Yu Liu, Pin-Shuo Hwang, Chao-Wei Liu, Junpeng Qiao, Min-Hsiung Shih, Yung-Jr Hung, Yi-Jen Chiu, Ann-Kuo Chu, and Chao-Kuei Lee. Visible to near-infrared octave spanning supercontinuum generation in tantalum pentoxide (Ta₂O₅) air-cladding waveguide. *Optics Letters*, 44(6):1512, mar 2019.
- [42] Jennifer T. Choy, Jonathan D. B. Bradley, Parag B. Deotare, Ian B. Burgess, Christopher C. Evans, Eric Mazur, and Marko Lončar. Integrated TiO₂ resonators for visible photonics. *Optics Letters*, 37(4):539, feb 2012.

- [43] Ki Youl Yang, Dong Yoon Oh, Seung Hoon Lee, Qi Fan Yang, Xu Yi, Boqiang Shen, Heming Wang, and Kerry Vahala. Bridging ultrahigh-Q devices and photonic circuits. *Nature Photonics*, 12(5):297–302, mar 2018.
- [44] David J. Moss, Roberto Morandotti, Alexander L. Gaeta, and Michal Lipson. New CMOS-compatible platforms based on silicon nitride and Hydex for nonlinear optics, jul 2013.
- [45] Lianchao ShangGuan, Daming Zhang, Tong Zhang, Ru Cheng, Jihou Wang, Chunxue Wang, Fei Wang, Seng Tiong Ho, Changming Chen, and Teng Fei. Functionalized polymer waveguide optical switching devices integrated with visible optical amplifiers based on an organic gain material. *Dyes and Pigments*, 176:108210, may 2020.
- [46] Ruidong Xia, George Heliotis, and Donal D.C. Bradley. Fluorene-based polymer gain media for solid-state laser emission across the full visible spectrum. *Applied Physics Letters*, 82(21):3599–3601, may 2003.
- [47] Masatoshi Yonemura, Akari Kawasaki, Satoru Kato, Manabu Kagami, and Yukitoshi Inui. Polymer waveguide module for visible wavelength division multiplexing plastic optical fiber communication. *Optics Letters*, 30(17):2206, sep 2005.
- [48] Marianne Hiltunen, Jussi Hiltunen, Petri Stenberg, Jarno Petäjä, Esa Heinonen, Pasi Vahimaa, and Pentti Karioja. Polymeric slot waveguide at visible wavelength. *Optics Letters*, 37(21):4449, nov 2012.
- [49] Tianren Fan, Xi Wu, Ali A. Eftekhari, Matteo Bosi, Hesam Moradinejad, Eric V. Woods, and Ali Adibi. High-quality integrated microdisk resonators in the visible-to-near-infrared wavelength range on a 3C-silicon carbide-on-insulator platform. *Optics Letters*, 45(1):153, jan 2020.
- [50] Charles Babin, Rainer Stöhr, Naoya Morioka, Tobias Linkewitz, Timo Steidl, Raphael Wörnle, Di Liu, Erik Hesselmeier, Vadim Vorobyov, Andrej Denisenko, Mario Hentschel, Christian Gobert, Patrick Berwian, Georgy V. Astakhov, Wolfgang Knolle, Sridhar Majety, Pranta Saha, Marina Radulaski, Nguyen Tien Son, Jawad Ul-Hassan, Florian Kaiser, and Jörg Wrachtrup. Fabrication and nanophotonic waveguide integration of silicon carbide colour centres with preserved spin-optical coherence. *Nature Materials*, 21(1):67–73, nov 2022.
- [51] Boris Desiatov, Amirhassan Shams-Ansari, Mian Zhang, Cheng Wang, and Marko Lončar. Ultra-low-loss integrated visible photonics using thin-film lithium niobate. *Optica*, 6(3):380, mar 2019.
- [52] Dalziel J. Wilson, Katharina Schneider, Simon Hönl, Miles Anderson, Yannick Baumgartner, Lukas Czornomaz, Tobias J. Kippenberg, and Paul Seidler. Integrated gallium phosphide nonlinear photonics. *Nature Photonics*, 14(1):57–62, jan 2020.
- [53] Belén Sotillo, Vibhav Bharadwaj, John Patrick Hadden, Stefano Rampini, Andrea Chiappini, Toney T. Fernandez, Cristina Armellini, Ali Serpengüzel, Maurizio Ferrari, Paul E. Barclay, Roberta Ramponi, and Shane M. Eaton. Visible to infrared diamond photonics enabled by focused femtosecond laser pulses. *Micromachines*, 8(2):60, feb 2017.
- [54] Benjamin Feigel, David Castelló-Lurbe, Hugo Thienpont, and Nathalie Vermeulen. Opportunities for visible supercontinuum light generation in integrated diamond waveguides. *Optics Letters*, 42(19):3804, oct 2017.

- [55] Pawel Latawiec, Vivek Venkataraman, Amirhassan Shams-Ansari, Matthew Markham, and Marko Lončar. Integrated diamond Raman laser pumped in the near-visible. *Optics Letters*, 43(2):318, jan 2018.
- [56] Chi Xiong, Wolfram Pernice, Kevin K. Ryu, Carsten Schuck, King Y. Fong, Tomas Palacios, and Hong X. Tang. Integrated GaN photonic circuits on silicon (100) for second harmonic generation. *Optics Express*, 19(11):10462, 2011.
- [57] Alexander W. Bruch, Chi Xiong, Benjamin Leung, Menno Poot, Jung Han, and Hong X. Tang. Broadband nanophotonic waveguides and resonators based on epitaxial GaN thin films. *Applied Physics Letters*, 107(14), 2015.
- [58] Hong Chen, Houqiang Fu, Xuanqi Huang, Xiaodong Zhang, Tsung-han Yang, Jossue A Montes, Izak Baranowski, and Yuji Zhao. Low loss GaN waveguides at the visible spectral wavelengths for integrated photonics applications. *Optics Express*, 25(25):31758, dec 2017.
- [59] Pascual Muñoz, Gloria Micó, Luis A. Bru, Daniel Pastor, Daniel Pérez, José David Doménech, Juan Fernández, Rocío Baños, Bernardo Gargallo, Rubén Alemany, Ana M. Sánchez, Josep M. Cirera, Roser Mas, and Carlos Domínguez. Silicon nitride photonic integration platforms for visible, near-infrared and mid-infrared applications. *Sensors (Switzerland)*, 17(9):2088, sep 2017.
- [60] Martin Hubert Peter Pfeiffer, Clemens Herkommer, Junqiu Liu, Tiago Morais, Michael Zervas, Michael Geiselmann, and Tobias J. Kippenberg. Photonic damascene process for low-loss, high-confinement silicon nitride waveguides. *IEEE Journal of Selected Topics in Quantum Electronics*, 24(4), jul 2018.
- [61] Junqiu Liu, Guan hao Huang, Rui Ning Wang, Jijun He, Arslan S. Raja, Tianyi Liu, Nils J. Engels, and Tobias J. Kippenberg. High-yield, wafer-scale fabrication of ultralow-loss, dispersion-engineered silicon nitride photonic circuits. *Nature Communications*, 12(1), dec 2021.
- [62] Robert W. Boyd. *Nonlinear Optics*. Academic Press, fourth edition, 2020.
- [63] Alexander W. Bruch, Xianwen Liu, Xiang Guo, Joshua B. Surya, Zheng Gong, Liang Zhang, Junxi Wang, Jianchang Yan, and Hong X. Tang. 17 000%/W second-harmonic conversion efficiency in single-crystalline aluminum nitride microresonators. *Applied Physics Letters*, 113(13):131102, sep 2018.
- [64] Hojoong Jung and Hong X. Tang. Aluminum nitride as nonlinear optical material for on-chip frequency comb generation and frequency conversion. *Nanophotonics*, 5(2):263–271, jun 2016.
- [65] Walter Shin, Yi Sun, Mohammad Soltani, and Zetian Mi. Demonstration of green and UV wavelength high Q aluminum nitride on sapphire microring resonators integrated with microheaters. *Applied Physics Letters*, 118(21), may 2021.
- [66] Sebastian Romero-García, Florian Merget, Frank Zhong, Hod Finkelstein, and Jeremy Witzens. Silicon nitride CMOS-compatible platform for integrated photonics applications at visible wavelengths. *Optics Express*, 21(12):14036, jun 2013.
- [67] A. Z. Subramanian, P. Neutens, A. Dhakal, R. Jansen, T. Claes, X. Rottenberg, F. Peyskens, S. Selvaraja, P. Helin, B. Dubois, K. Leyssens, S. Severi, P. Deshpande, R. Baets, and P. Van Dorpe. Low-Loss Singlemode PECVD silicon nitride photonic wire waveguides for 532-900 nm wavelength window fabricated within a CMOS pilot line. *IEEE Photonics Journal*, 5(6), dec 2013.

- [68] N. Daldosso, M. Melchiorri, F. Riboli, F. Sbrana, L. Pavesi, G. Pucker, C. Kompocholis, M. Crivellari, P. Bellutti, and A. Lui. Fabrication and optical characterization of thin two-dimensional Si 3N4 waveguides. *Materials Science in Semiconductor Processing*, 7(4-6):453–458, jan 2004.
- [69] Ehsan Shah Hosseini, Siva Yegnanarayanan, Amir H. Atabaki, Mohammad Soltani, and Ali Adibi. High quality planar silicon nitride microdisk resonators for integrated photonics in the visible wavelength range. *Optics Express*, 17(17):14543, aug 2009.
- [70] Andrew J Mercante, Shouyuan Shi, Peng Yao, Linli Xie, Robert M Weikle, and Dennis W Prather. Thin film lithium niobate electro-optic modulator with terahertz operating bandwidth. *Optics Express*, 26(11):14810, 2018.
- [71] Mian Zhang, Cheng Wang, Rebecca Cheng, Amirhassan Shams-Ansari, and Marko Loncar. Monolithic ultra-high-Q lithium niobate microring resonator. *Optica*, 4(12):1536–1537, dec 2017.
- [72] Zhechao Wang, Amin Abbasi, Utsav Dave, Andreas De Groote, Sulakshna Kumari, Bernadette Kunert, Clement Merckling, Marianna Pantouvaki, Yuting Shi, Bin Tian, Kasper Van Gasse, Jochem Verbist, Ruijun Wang, Weiqiang Xie, Jing Zhang, Yunpeng Zhu, Johan Bauwelinx, Xin Yin, Zeger Hens, Joris Van Campenhout, Bart Kuyken, Roel Baets, Geert Morthier, Dries Van Thourhout, and Gunther Roelkens. Novel Light Source Integration Approaches for Silicon Photonics. *Laser and Photonics Reviews*, 11(4):1–21, 2017.
- [73] Alexander W. Fang, Hyundai Park, Oded Cohen, Richard Jones, Mario J. Paniccia, and John E. Bowers. Electrically pumped hybrid AlGaInAs-silicon evanescent laser. *Optics Express*, 14(20):9203, oct 2006.
- [74] M. G. Thompson, A. Politi, J. C.F. Matthews, and J. L. O’Brien. Integrated waveguide circuits for optical quantum computing. *IET Circuits, Devices and Systems*, 5(2):94–102, mar 2011.
- [75] Thobeka Kente and Sabelo Dalton Mhlanga. Gallium nitride nanostructures: Synthesis, characterization and applications. *Journal of Crystal Growth*, 444:55–72, jun 2016.
- [76] Ishwara Bhat. Physical properties of gallium nitride and related III-V nitrides. In *Wide Bandgap Semiconductor Power Devices: Materials, Physics, Design, and Applications*, pages 43–77. Elsevier, jan 2018.
- [77] S. P. Denbaars. Gallium-nitride-based materials for blue to ultraviolet optoelectronics devices. *Proceedings of the IEEE*, 85(11):1740–1749, 1997.
- [78] L. Liu and J. H. Edgar. Substrates for gallium nitride epitaxy, apr 2002.
- [79] E S Hellman. The polarity of GaN: A critical review, 1998.
- [80] William A. Melton and Jacques I. Pankove. GaN growth on sapphire. *Journal of Crystal Growth*, 178(1-2):168–173, 1997.
- [81] Hiroshi Amano. Growth of GaN on sapphire via low-temperature deposited buffer layer and realization of p-type GaN by Mg doping followed by low-energy electron beam irradiation. *International Journal of Modern Physics B*, 29(32):1133, oct 2015.
- [82] H. Amano, N. Sawaki, I. Akasaki, and Y. Toyoda. Metalorganic vapor phase epitaxial growth of a high quality GaN film using an AlN buffer layer. *Applied Physics Letters*, 48(5):353–355, aug 1986.

- [83] S. Nakamura, T. Mukai, and M. Senoh. In situ monitoring and Hall measurements of GaN grown with GaN buffer layers. *Journal of Applied Physics*, 71(11):5543–5549, aug 1992.
- [84] Jennifer Hite, Mark Twigg, Michael Mastro, Jaime Freitas, Jerry Meyer, Igor Vurgaftman, Shawn O'Connor, Nicholas Condon, Fritz Kub, Steven Bowman, and Charles Eddy. Development of periodically oriented gallium nitride for non-linear optics [Invited]. *Optical Materials Express*, 2(9):1203, sep 2012.
- [85] Aref Chowdhury, Hock M. Ng, Manish Bhardwaj, and Nils G. Weimann. Second-harmonic generation in periodically poled GaN. *Applied Physics Letters*, 83(6):1077–1079, aug 2003.
- [86] S. J. Pearton, R. J. Shul, and Fan Ren. A review of dry etching of GaN and related materials, 2000.
- [87] Stephen J. Pearton, Erica A. Douglas, Randy J. Shul, and Fan Ren. Plasma etching of wide bandgap and ultrawide bandgap semiconductors. *Journal of Vacuum Science & Technology A*, 38(2):020802, jan 2020.
- [88] Dvir Munk, Moshe Katzman, Ohad Westreich, Moran Bin Nun, Yedidya Lior, Noam Sicon, Yossi Paltiel, and Avi Zadok. Four-wave mixing and nonlinear parameter measurement in a gallium-nitride ridge waveguide. *Optical Materials Express*, 8(1):66, jan 2018.
- [89] Yanzhen Zheng, Changzheng Sun, Bing Xiong, Lai Wang, Zhibiao Hao, Jian Wang, Yanjun Han, Hongtao Li, Jiadong Yu, and Yi Luo. Integrated Gallium Nitride Nonlinear Photonics. *Laser and Photonics Reviews*, 16(1):2100071, jan 2022.
- [90] Ichiro Shoji, Takashi Kondo, Ayako Kitamoto, Masayuki Shirane, and Ryoichi Ito. Absolute scale of second-order nonlinear-optical coefficients. *Journal of the Optical Society of America B*, 14(9):2268, 1997.
- [91] H. Y. Zhang, X. H. He, Y. H. Shih, M. Schurman, Z. C. Feng, and R. A. Stall. Study of nonlinear optical effects in GaN:Mg epitaxial film. *Applied Physics Letters*, 69(20):2953–2955, jun 1996.
- [92] J. Jerphagnon and S. K. Kurtz. Maker fringes: A detailed comparison of theory and experiment for isotropic and uniaxial crystals. *Journal of Applied Physics*, 41(4):1667–1681, 1970.
- [93] Makoto Abe, Hiroaki Sato, Jun Suda, Masashi Yoshimura, Yasuo Kitaoka, Yusuke Mori, Ichiro Shoji, and Takashi Kondo. Accurate Measurement of Nonlinear Optical Coefficients of Gallium Nitride. 2015.
- [94] Cheng Wang, Michael J Burek, Zin Lin, Haig A Atikian, Vivek Venkataraman, I-Chun Huang, Peter Stark, and Marko Lončar. Integrated high quality factor lithium niobate microdisk resonators. *Optics Express*, 22(25):30924, 2014.
- [95] Yuntao Xu, Mohan Shen, Juanjuan Lu, Joshua B. Surya, Ayed Al Sayem, and Hong X. Tang. Mitigating photorefractive effect in thin-film lithium niobate microring resonators. *Optics Express*, 29(4):5497, feb 2021.
- [96] W. H.P. Pernice, C. Xiong, C. Schuck, and H. X. Tang. Second harmonic generation in phase matched aluminum nitride waveguides and micro-ring resonators. *Applied Physics Letters*, 100(22):223501, may 2012.
- [97] Pawel Latawiec, Vivek Venkataraman, Michael J. Burek, Birgit J. M. Hausmann, Irfan Bulu, and Marko Lončar. On-chip diamond Raman laser. *Optica*, 2(11):924, nov 2015.

- [98] Alan J. Kemp, Gareth J. Valentine, John Mark Hopkins, Jennifer E. Hastie, Scott A. Smith, Stephane Calvez, Martin D. Dawson, and David Burns. Thermal management in vertical-external-cavity surface-emitting lasers: Finite-element analysis of a heatspreader approach. *IEEE Journal of Quantum Electronics*, 41(2):148–155, feb 2005.
- [99] M. Y. Chernykh, A. A. Andreev, I. S. Ezubchenko, I. A. Chernykh, I. O. Mayboroda, E. M. Kolobkova, Yu V Khrapovitskaya, J. V. Grishchenko, P. A. Perminov, V. S. Sedov, A. K. Martyanov, A. S. Altakhov, M. S. Komlenok, V. P. Pashinin, A. G. Sinogeykin, V. I. Konov, and M. L. Zanaevskii. GaN-based heterostructures with CVD diamond heat sinks: A new fabrication approach towards efficient electronic devices. *Applied Materials Today*, 26:101338, mar 2022.
- [100] Sean Reilly, Vasili G. Savitski, Hangyu Liu, Erdan Gu, Martin D. Dawson, and Alan J. Kemp. Monolithic diamond Raman laser. *Optics Letters*, 40(6):930, mar 2015.
- [101] Jeremy L. O’Brien. Optical quantum computing. *Science*, 318(5856):1567–1570, dec 2007.
- [102] Steven Praver and Igor Aharonovich. *Quantum Information Processing with Diamond: Principles and Applications*. 2014.
- [103] Sébastien Pezzagna and Jan Meijer. Quantum computer based on color centers in diamond. *Applied Physics Reviews*, 8(1):011308, feb 2021.
- [104] Lilian Childress and Ronald Hanson. Diamond NV centers for quantum computing and quantum networks. *MRS Bulletin*, 38(2):134–138, feb 2013.
- [105] B. Hensen, H. Bernien, A. E. Dreaú, A. Reiserer, N. Kalb, M. S. Blok, J. Ruitenbergh, R. F.L. Vermeulen, R. N. Schouten, C. Abellán, W. Amaya, V. Pruneri, M. W. Mitchell, M. Markham, D. J. Twitchen, D. Elkouss, S. Wehner, T. H. Taminiu, and R. Hanson. Loophole-free Bell inequality violation using electron spins separated by 1.3 kilometres. *Nature*, 526(7575):682–686, oct 2015.
- [106] Nicolás Lo Piparo, Mohsen Razavi, and William J. Munro. Measurement-device-independent quantum key distribution with nitrogen vacancy centers in diamond. *Physical Review A*, 95(2):022338, feb 2017.
- [107] Sungkun Hong, Michael S. Grinolds, Linh M. Pham, David Le Sage, Lan Luan, Ronald L. Walsworth, and Amir Yacoby. Nanoscale magnetometry with NV centers in diamond. *MRS Bulletin*, 38(2):155–161, feb 2013.
- [108] Akihiro Kuwahata, Takahiro Kitaizumi, Kota Saichi, Takumi Sato, Ryuji Igarashi, Takeshi Ohshima, Yuta Masuyama, Takayuki Iwasaki, Mutsuko Hatano, Fedor Jelezko, Moriaki Kusakabe, Takashi Yatsui, and Masaki Sekino. Magnetometer with nitrogen-vacancy center in a bulk diamond for detecting magnetic nanoparticles in biomedical applications. *Scientific Reports*, 10(1):1–9, feb 2020.
- [109] Mohamed I. Ibrahim, Christopher Foy, Dirk R. Englund, and Ruonan Han. High-scalability CMOS quantum magnetometer with spin-state excitation and detection of diamond color centers. *IEEE Journal of Solid-State Circuits*, 56(3):1001–1014, mar 2021.
- [110] Felix M. Stürner, Andreas Brenneis, Thomas Buck, Julian Kassel, Robert Rölver, Tino Fuchs, Anton Savitsky, Dieter Suter, Jens Grimmel, Stefan Hengesbach, Michael Förtsch, Kazuo Nakamura,

- Hitoshi Sumiya, Shinobu Onoda, Junichi Isoya, and Fedor Jelezko. Integrated and Portable Magnetometer Based on Nitrogen-Vacancy Ensembles in Diamond. *Advanced Quantum Technologies*, 4(4):2000111, apr 2021.
- [111] https://commons.wikimedia.org/wiki/File:Allotropes_Of_Carbon.png Date Accessed 2022-05-27.
- [112] Sergio Ferro. Synthesis of diamond. *Journal of Materials Chemistry*, 12(10):2843–2855, oct 2002.
- [113] Paul W. May. Diamond thin films: A 21st-century material. *Philosophical Transactions of the Royal Society A: Mathematical, Physical and Engineering Sciences*, 358(1766):473–495, 2000.
- [114] Peter K. Bachmann, Hans Juergen Hagemann, Hartmut Lade, Dieter Leers, Frederike Picht, Detlef U. Wiechert, and Howard Wilson. Diamond chemical vapor deposition: gas compositions and film properties. In *Materials Research Society Symposium - Proceedings*, volume 339, pages 267–277. Cambridge University Press, 1994.
- [115] Makoto Kasu. Diamond epitaxy: Basics and applications, jun 2016.
- [116] Jean Charles Arnault, Samuel Saada, and Victor Ralchenko. Chemical Vapor Deposition Single-Crystal Diamond: A Review, jan 2022.
- [117] Matthias Schreck, Stefan Gsell, Rosaria Brescia, and Martin Fischer. Ion bombardment induced buried lateral growth: The key mechanism for the synthesis of single crystal diamond wafers. *Scientific Reports*, 7, mar 2017.
- [118] Hideaki Yamada, Akiyoshi Chayahara, Yoshiaki Mokuno, Nobuteru Tsubouchi, and Shin Ichi Shikata. Uniform growth and repeatable fabrication of inch-sized wafers of a single-crystal diamond. *Diamond and Related Materials*, 33:27–31, mar 2013.
- [119] Ye Tao and Christian Degen. Facile fabrication of single-crystal-diamond nanostructures with ultrahigh aspect ratio. *Advanced Materials*, 25(29):3962–3967, aug 2013.
- [120] Yiyun Zhang, Xuhui Zhang, Kwai Hei Li, Yuk Fai Cheung, Cong Feng, and Hoi Wai Choi. Advances in III-nitride semiconductor microdisk lasers. *Physica Status Solidi (A) Applications and Materials Science*, 212(5):960–973, 2015.
- [121] Alexander W. Bruch, Xianwen Liu, Xiang Guo, Joshua B. Surya, Zheng Gong, Liang Zhang, Junxi Wang, Jianchang Yan, and Hong X. Tang. 17 000%/W second-harmonic conversion efficiency in single-crystalline aluminum nitride microresonators. *Applied Physics Letters*, 113(13):131102, sep 2018.
- [122] Xiang Guo, Chang-Ling Zou, and Hong X. Tang. Second-harmonic generation in aluminum nitride microrings with 2500%/W conversion efficiency. *Optica*, 3(10):1126, oct 2016.
- [123] J. W. Silverstone, R. Santagati, D. Bonneau, M. J. Strain, M. Sorel, J. L. O’Brien, and M. G. Thompson. Qubit entanglement between ring-resonator photon-pair sources on a silicon chip. *Nature Communications*, 6, aug 2015.
- [124] Douwe H. Geuzebroek and Alfred Driessen. Ring-resonator-based wavelength filters. *Springer Series in Optical Sciences*, 123:341–379, 2006.
- [125] Weiqiang Wang, Leiran Wang, and Wenfu Zhang. Advances in soliton microcomb generation. *Advanced Photonics*, 2(3), 2020.

- [126] Lin Zhang, Yunchu Li, Jeng Yuan Yang, Muping Song, Raymond G. Beausoleil, and Alan E. Willner. Silicon-based microring resonator modulators for intensity modulation. *IEEE Journal on Selected Topics in Quantum Electronics*, 16(1):149–158, jan 2010.
- [127] Guozhen Liang, Heqing Huang, Aseema Mohanty, Min Chul Shin, Xingchen Ji, Michael Joseph Carter, Sajjan Shrestha, Michal Lipson, and Nanfang Yu. Robust, efficient, micrometre-scale phase modulators at visible wavelengths. *Nature Photonics*, 15(12):908–913, dec 2021.
- [128] Sasikanth Manipatruni, Long Chen, and Michal Lipson. 50 Gbit/s wavelength division multiplexing using silicon microring modulators. *IEEE International Conference on Group IV Photonics GFP*, pages 244–246, 2009.
- [129] Jeremy Witzens and Michael Hochberg. Optical detection of target molecule induced aggregation of nanoparticles by means of high-Q resonators. *Optics Express*, 19(8):7034, 2011.
- [130] A Yariv. Universal relations for coupling of optical power between microresonators and dielectric waveguides. *Electronics Letters*, 36(4):321–322, 2000.
- [131] Dominik Gerhard Rabus and Cinzia Sada. *Integrated Ring Resonators: A Compendium*, volume 127. Springer Series in Optical Sciences 127, 2 edition, 2020.
- [132] W. R. McKinnon, D. X. Xu, C. Storey, E. Post, A. Densmore, A. Del age, P. Waldron, J. H. Schmid, and S. Janz. Extracting coupling and loss coefficients from a ring resonator. *Optics Express*, 17(21):18971, oct 2009.
- [133] FG Smith, TA King, and D Wilkins. *Optics and Photonics: An Introduction*. Wiley, 2007.
- [134] Seung Hoon Lee, Dong Yoon Oh, Qi Fan Yang, Boqiang Shen, Heming Wang, Ki Youl Yang, Yu Hung Lai, Xu Yi, Xinbai Li, and Kerry Vahala. Towards visible soliton microcomb generation. *Nature Communications*, 8(1):1–8, nov 2017.
- [135] Fang Chen, Huafeng Zhang, Lihui Sun, Jijun Li, and Chunchao Yu. Temperature tunable Fano resonance based on ring resonator side coupled with a MIM waveguide. *Optics and Laser Technology*, 116:293–299, aug 2019.
- [136] Guolin Zhao, Ting Zhao, Huifu Xiao, Zilong Liu, Guipeng Liu, Jianhong Yang, Zhaoyu Ren, Jintao Bai, and Yonghui Tian. Tunable Fano resonances based on microring resonator with feedback coupled waveguide. *Optics Express*, 24(18):20187, sep 2016.
- [137] Robert C. Youngquist, Loren F. Stokes, and Herbert J. Shaw. Effects of Normal Mode Loss in Dielectric Waveguide Directional Couplers and Interferometers. *IEEE Journal of Quantum Electronics*, 19(12):1888–1896, 1983.
- [138] Andrey E. Miroshnichenko, Sergej Flach, and Yuri S. Kivshar. Fano resonances in nanoscale structures. *Reviews of Modern Physics*, 82(3):2257–2298, aug 2010.
- [139] Shanhui Fan. Sharp asymmetric line shapes in side-coupled waveguide-cavity systems. *Applied Physics Letters*, 80(6):908–910, feb 2002.
- [140] Yun-Feng Xiao, Venkat Gaddam, and Lan Yang. Coupled optical microcavities: an enhanced refractometric sensing configuration. *Optics Express*, 16(17):12538, aug 2008.

-
- [141] Xiaodong Yang, Mingbin Yu, Dim Lee Kwong, and Chee Wei Wong. All-optical analog to electromagnetically induced transparency in multiple coupled photonic crystal cavities. *Physical Review Letters*, 102(17), 2009.
- [142] Jae Woong Yoon and Robert Magnusson. Fano resonance formula for lossy two-port systems. *Optics Express*, 21(15):17751, jul 2013.
- [143] Mikhail F. Limonov, Mikhail V. Rybin, Alexander N. Poddubny, and Yuri S. Kivshar. Fano resonances in photonics. *Nature Photonics*, 11(9):543–554, sep 2017.
- [144] Ang Li, Thomas Van Vaerenbergh, Peter De Heyn, Peter Bienstman, and Wim Bogaerts. Backscattering in silicon microring resonators: A quantitative analysis. *Laser and Photonics Reviews*, 10(3):420–431, may 2016.
- [145] Brent E. Little, Juha-Pekka Laine, and Sai T. Chu. Surface-roughness-induced contradirectional coupling in ring and disk resonators. *Optics Letters*, 22(1):4, jan 1997.
- [146] Francesco Morichetti, Antonio Canciamilla, and Andrea Melloni. Statistics of backscattering in optical waveguides. *Optics Letters*, 35(11):1777, jun 2010.

Chapter 2

Passive GaN devices

Having explained the motivation behind using GaN as a material platform for PICs in general, this chapter details the specific design, fabrication, and characterisation of key passive GaN devices. Waveguides, racetrack resonators and disk resonators (both evanescently coupled to adjacent waveguides) are fabricated on a single chip, and like many first fabrication runs, various aspects of the geometry of these devices is varied. The values chosen for the parameterisation of, for example, the coupling length between a bus waveguide and an adjacent resonator, are drawn from a parameter space guided by numerical simulations. These simulations are also detailed in the following sections. The fabrication steps are then highlighted before detailed analyses of the transmission spectra are presented. Intrinsic Q factors and distributed loss values measured here are comparable to current state of the art values [1–3].

2.1 Introduction

Despite GaN’s promising properties, to date there have been comparatively few examples of GaN PICs or the components thereof (e.g. waveguides, resonators). This seems largely due to the fact that research into the fabrication of these devices has been occurring concurrently with more fundamental research into the growth of the necessary high quality material. Even with the two-step heteroepitaxy process outlined in the previous chapter, the large area growth of thin, single-mode thickness GaN remains challenging [4, 5], and wafers often need to be polished back. Although polishing tends to reduce the surface roughness, it can also scratch the GaN because the material is so hard. Furthermore, polishing usually imparts thickness variations across the template. Scratches may reduce device yield, while uncontrolled thickness variations will alter the effective index of guided modes from their desired values.

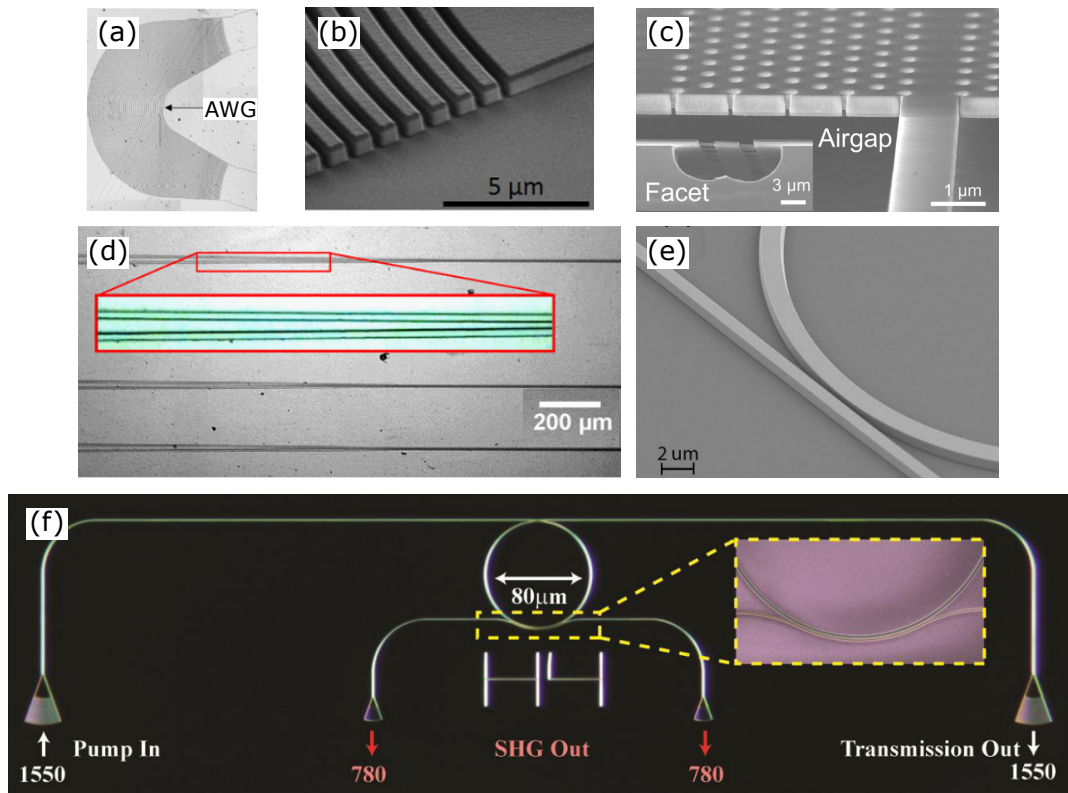


FIGURE 2.1: Previous GaN work. (a) Optical micrograph of an AWG based on GaN ridge waveguides on AlGaIn on sapphire [6]. (b) SEM of a GaN on sapphire grating coupler [7]. (c) SEM of a suspended GaN waveguide and PhC lattice [8]. (d) Optical micrograph of a portion of a GaN on sapphire directional coupler [9]. (e) SEM of the coupling region of a GaN on sapphire ring resonator [1]. (f) Optical micrograph of a GaN add-drop ring resonator used for SHG [10].

Figure 2.1(a) shows an early effort in GaN integrated optics microfabrication – a series of closely spaced ridge waveguides (of dimension $3 \times 3 \mu\text{m}$) forming an arrayed waveguide grating (AWG): essentially the integrated optics equivalent of a diffraction grating, used in (de)multiplexing [6]. Figure 2.1(b) shows an SEM of a GaN grating coupler, used for vertically coupling light into waveguides ($1 \times 0.65 \mu\text{m}$) [7]. Figure 2.1(c) shows a suspended GaN photonic crystal (PhC) waveguide, with air holes underetched in the silicon substrate [8]. Figure 2.1(d) shows a portion of a GaN directional coupler used to measure the quantum interference of two single photons [9]. Figure 2.1(e) shows the coupling section of a high Q GaN ring resonator ($Q_{int} = 1.37 \times 10^5$ at 1556 nm), of dimensions $1.25 \times 0.7 \mu\text{m}$ [1]. Finally, Figure 2.1(f) shows a doubly resonant GaN add-drop ring resonator used to convert 1550 nm pump light to its second harmonic at 775 nm [10].

GaN on sapphire is a desirable layer structure for integrated optics because of the high refractive index contrast between the GaN and sapphire (~ 0.62 at 635 nm, ~ 0.57 at 1.5 μm). High index contrasts lead to tight mode confinement in the waveguiding layer,

which in turn allows for smaller bend radii and thus more devices in a smaller area on chip. Furthermore, nonlinear applications benefit from the field intensity enhancement which stems from the strong confinement of optical radiation in the waveguide. This permits lower optical pump powers and reduces the required interaction length for such nonlinear effects [11]. Record loss values at IR wavelengths for rib (partially etched) and ridge (fully etched) waveguides are 1 dB/cm and 2.4 dB/cm, respectively [2, 3]. The low losses in the first case can be attributed firstly to partially etched waveguides being intrinsically less lossy, and secondly to the large cross-sectional dimensions of the guide: $10 \times 1.5 \mu\text{m}$. This means the guided mode tends to have only a small overlap with the sidewalls, and therefore any roughness induced losses. Similarly, low losses for the fully etched ridge waveguide ($1.2 \times 1.5 \mu\text{m}$) are attributed to low sidewall roughness achieved by an optimised dry etch process.

Silicon is another widely used substrate for the epitaxial growth of GaN. For applications in integrated optics, the subsequent underetching or removal of the silicon is required (e.g. Figure 2.1(c)) because its large refractive index (~ 3.48 at $1.5 \mu\text{m}$) precludes waveguiding in the GaN. Furthermore, silicon absorbs light at wavelengths below $1 \mu\text{m}$. After the removal of the silicon, the resulting suspended devices will be largely or completely air-clad, giving them an even greater index contrast than sapphire. This improves mode confinement, but also worsens scattering losses from sidewall roughness; which is proportional to the index contrast squared [12]. Both photonic crystal cavities (PhCCs) and evanescently coupled disks have been realised in this fashion, with demonstrations of second harmonic generation in both [13–15]. Although the underside roughness of the underetched GaN is reported to be on par with the top surface roughness - both with an r.m.s. value $< 1.5 \text{ nm}$ over a $500 \times 500 \text{ nm}^2$ area [8] - these devices exhibit high propagation losses of 10-12 dB/mm, leading to PhCC Q factors of just 2200 in the NIR [16]. Even the highest reported Q factor for a single resonance of a suspended PhCC of 3.4×10^4 featured high propagation losses of 11 dB/mm [17]. The fabrication of suspended structures comes with its own challenges. Firstly, since waveguiding in the GaN can only occur in areas that have been underetched completely, device areas are either limited in size or require numerous tether structures. These tethers add significant scattering losses to the suspended waveguides, with values as high as 3.5 dB/tether reported [17].

In this chapter, the simulation, fabrication, and characterisation of GaN on sapphire devices will be demonstrated. The material used in the following consists of $\sim 650 \text{ nm}$ of c-plane unintentionally doped HVPE GaN, grown on $\sim 430 \mu\text{m}$ sapphire with a $\sim 350 \text{ nm}$ buffer layer of crystalline AlN. It was grown by Kyma Technologies, who also polished the GaN back to $< 1 \mu\text{m}$ from its growth thickness. Devices were left air-clad to facilitate easy coupling to printed diamond components in later chapters.

2.2 Optical simulations and chip design

2.2.1 Overview

There are a number of key parameters that need to be calculated before the first chip is fabricated. The first of these is the desired waveguide width for single-mode operation (the waveguide height is not considered a free parameter, and is instead set by the as-received thickness of the GaN layer). The radiative bend loss must also be estimated, so that this additional form of loss can be avoided by designing waveguide bends to have radii sufficiently larger than the cut-off value. Finally, the power cross-coupling between two adjacent waveguides must be calculated. This is usually important for the design of directional couplers, where an arbitrary amount of optical power can be routed from one waveguide to another (assuming they are identical [18]) simply by choosing an appropriate coupling length for a given gap. While we neglect directional couplers here, the dynamics of power coupling between waveguides is still important for the evanescent coupling of light from a bus waveguide to a racetrack resonator, particularly when it comes to benchmarking the power cross-coupling fractions extracted experimentally with those suggested by simulations.

2.2.2 Simulation software

Commercial software (Ansys' Lumerical MODE) was used for the simulations presented here; both the primary finite difference eigenmode (FDE) solver and eigenmode expansion (EME) solvers. FDE is a full-vectorial Maxwell's equations solver, based on a method by Zhu and Brown [19]. The cross-sectional device geometry is decomposed into a mesh which is used to construct a matrix formulation of Maxwell's equations. Finding the supported modes of the structure then involves solving the eigenvalue problem of these matrices (whose eigenvalues are the modal propagation constants, β). The spatial mode profiles, loss, and effective indices (n_{eff}) can then be found. EME is effectively an extension of the FDE solver to a third dimension in which the mode is propagating. Here, the three-dimensional device structure is split into several cells, each a cross-section of the device at that point along the length. The modes at each cell interface are calculated as above, before scattering matrices are found by matching tangential electric \mathbf{E} and magnetic \mathbf{H} field components at the cell interfaces. The scattering matrices are then used to propagate an input field across the entire device.

2.2.3 Waveguide geometry

FDE simulations of a GaN waveguide were carried out. The geometry is set up as in Figure 2.2, with a 350 nm layer of AlN between the sapphire and GaN. All simulations make use of frequency dependent refractive index data for the GaN [20], AlN [21], and sapphire [22]; and unless otherwise stated, the simulation wavelength was 1.55 μm , which is the centre wavelength of the majority of wavelength transmission sweeps taken experimentally.

First, the width of the waveguide was swept for a fixed height of 1 μm (650 nm GaN, 350 nm AlN). As the width increases, more modes are accommodated in the waveguide. Their effective refractive indices are plotted in Figure 2.2(a), where solid lines represent TE modes, dashed lines represent TM, and only the fundamental TE/TM modes have been labelled for clarity. Although the waveguide height can be reduced by dry-etching, this would be an undesirable additional fabrication step. There is far greater control over the width parameter (as long as the chosen value is sufficiently greater than the resolution of the lithography method used), and so Figure 2.2(a) was used to determine the desired waveguide width. A target width of 1 μm is found to easily support a single TE and TM mode. Although strictly speaking other modes are present, they are found

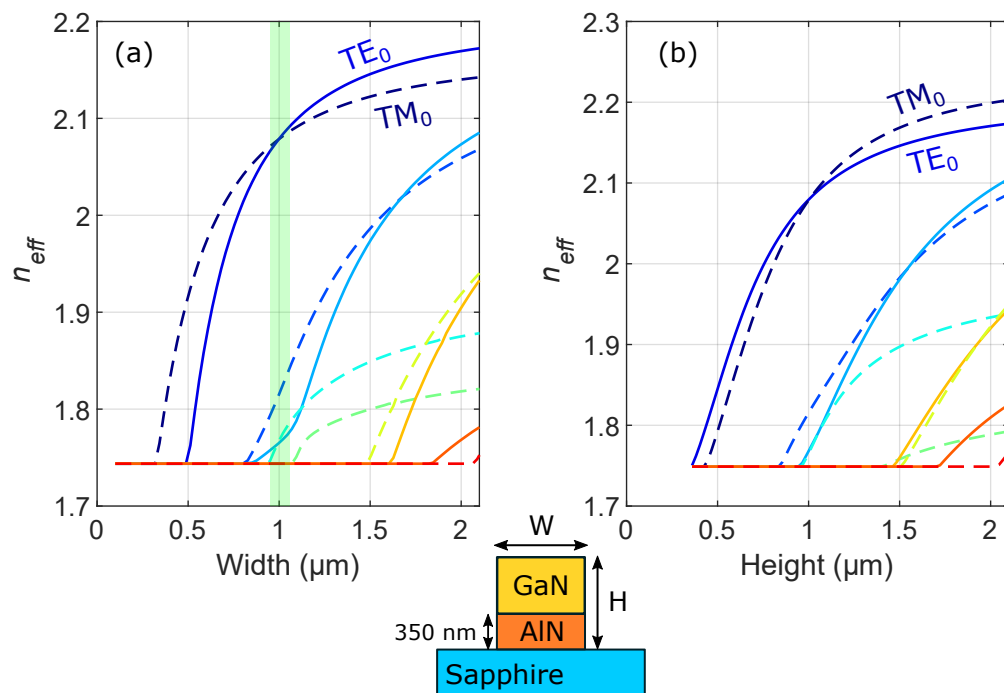


FIGURE 2.2: (a) Mode effective indices for TE (solid lines) and TM (dashed lines) polarisations for increasing waveguide width and fixed GaN height of 650 nm. The green bar indicates the target waveguide width. (b) The same, but for increasing waveguide height, with a starting point of 350 nm.

to have n_{eff} close to that of the slab-mode, i.e. the solution that corresponds to guiding in the substrate. The slab-mode effective index is found to be $n_{eff} = 1.7437$, and modes whose n_{eff} approach this value suffer from increasingly poor confinement and high substrate leakage losses (see Appendix A), such that they are effectively screened out when the device is fabricated. A thickness sweep for the target width of $1 \mu\text{m}$ is then performed, with results plotted in Figure 2.2(b). Small deviations from the nominal total height of $1 \mu\text{m}$ do not introduce extra modes, but naturally, larger increases do. For example, an increase of 500 nm in the height introduces a second set of TE and TM modes with $n_{eff} \sim 1.99$. This is noteworthy because it is indeed possible for the CMP process to impart such a thickness variation across the wafer, and even across the relatively small area of the chip.

2.2.4 Mode profiles

The fundamental mode profiles for the two polarisations are shown in Figure 2.3. Their effective indices are similar, but no scattering from one polarisation to another was observed experimentally. Since the two modes are approximately phase-matched (by virtue of having similar effective indices) this suggests that the waveguides instead lack

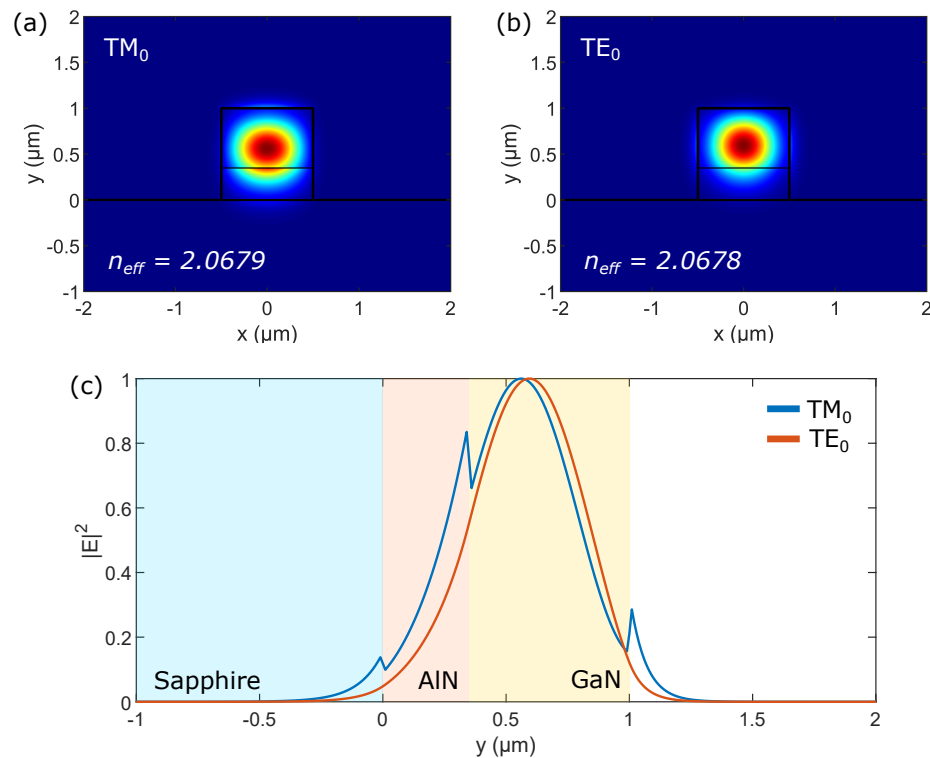


FIGURE 2.3: Normalised electric field profiles for the (a) TM_0 and (b) TE_0 modes. For each, vertical line profiles are taken through the centre point of the field intensity profile, and are plotted in (c).

a strong coupling mechanism to transfer power from one mode to the other [18]. The usual mechanism for this coupling is scattering from sidewall roughness, and since this was not observed, this suggests the GaN sidewalls were fairly smooth.

Although similar in their effective indices, the differing polarisations give the modes quite distinct spatial profiles. The TM_0 mode, which has a dominant E_y electric field component and zero E_x component, is characterised by strong discontinuities in the vertical direction. Conversely, the TE_0 mode has dominant E_x and zero E_y components, and is characterised by discontinuities in the horizontal direction. Such discontinuities are typical for TM and TE modes respectively, and are a consequence of the requirement that the normal component of the electric displacement $\mathbf{D} = \varepsilon\mathbf{E}$ be continuous at dielectric interfaces [23]. A comparison of the two vertical profiles is shown in Figure 2.3(c), and because $E_y = 0$ for TE_0 , there are no discontinuities in this direction, with the result that there is less modal power in the AlN buffer layer for this polarisation. The mode confinements can be quantified by calculating what percentage of the integrated intensities in Figures 2.3(a,b) overlap with each material, with results tabulated in Table 2.1.

TABLE 2.1: Table of optical power confinement factors for two fundamental polarisations.

Mode	GaN %	AlN %	Sapphire %
TM_0	87.92	12.00	0.08
TE_0	92.59	7.37	0.04

An improvement of nearly 5% is observed in the confinement to the GaN layer for the TE_0 mode. Also, much less of the power overlaps with the AlN buffer layer, where the material quality is presumed to be worse, with defects and dislocations adding more scattering loss.

2.2.5 Bend loss

Curved waveguides are inherently leaky [24, 25], meaning there is an unavoidable amount of optical loss when using bent waveguides to redirect light around a PIC. The minimisation of this loss is of key importance when designing PICs, and particularly when fabricating high Q ring or disk resonators. Marcatili showed the fundamental mechanism for this loss to be coupling or tunnelling to outwardly propagating radiation modes [26], and analytical solutions for the case of asymmetric slab waveguides have since been developed [27–29]. The common method is to solve Maxwell’s equations under a conformal transformation that maps a curved waveguide with curved boundary conditions in one coordinate system to a straight waveguide with straight boundaries in another

coordinate system [28]. Doing so requires the replacement of the step index profile that defines the waveguide structure with a graded index profile that captures the radial dependence of the effective index and propagation constant of the mode. This is the method used by Lumerical's numerical FDE solver.

Figure 2.4(a-c) demonstrates the effect on the TM_0 mode profile after an example bend with radius of $8\ \mu\text{m}$ is introduced. Comparing the modes and their line profiles in

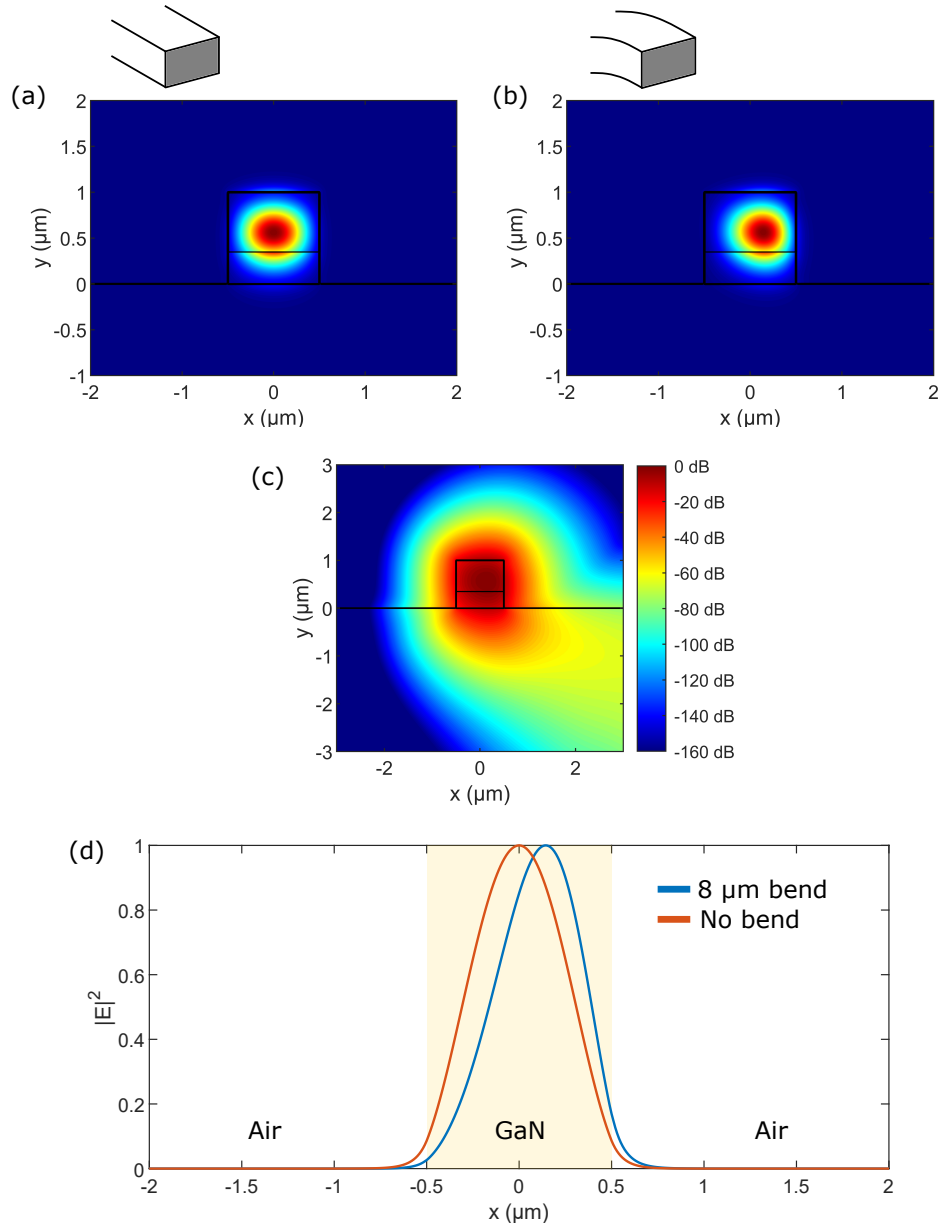


FIGURE 2.4: (a) TM_0 mode in a straight waveguide section. (b) TM_0 mode in a curved waveguide section, with bend radius of $8\ \mu\text{m}$. (c) The same curved TM_0 mode, but on a logarithmic scale, showing the radiative loss of modal power from the guide. (d) Comparison of horizontal line profiles taken across the maxima of each mode, clearly showing a rightward shift for the bent waveguide.

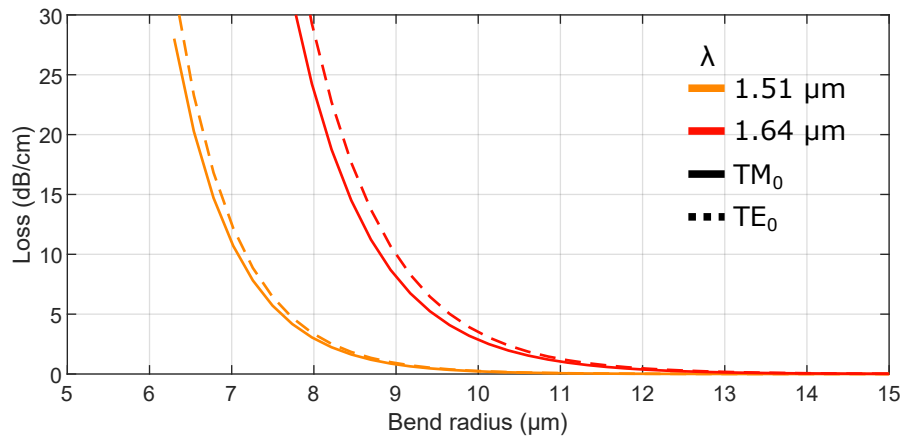


FIGURE 2.5: Radiative bend loss as a function of bend radius, for wavelengths 1.51 μm and 1.64 μm and both polarisations.

Figure 2.4(d), the bend pushes the mode outwards - such that scattering losses against sidewall roughness may increase, and coupling to radiation modes is made easier.

The radiation loss can be quantified if perfectly matched layers are used as boundary conditions for the simulation window. Light that escapes the waveguide can then be absorbed at the edges of the simulation span, and for a bent waveguide lacking any other loss mechanism, this loss is equal to the radiative bend loss. With this method, the bend radius is varied and loss is measured for each polarisation, with results plotted in Figure 2.5. The simulation is carried out for a wavelengths of 1.51 μm and 1.64 μm , since these values cover the entire measurement bandwidth of the devices.

As expected, the TE_0 mode is more lossy for a given radius than the TM_0 mode. Critical bend radii of 10 - 13 μm are observed, below which bend losses rapidly increase. Therefore, a standard value of 30 μm is chosen for all waveguide bends - offering a good balance between saving space on chip, and being far away from the cut-off radius, in a region where bend loss is a negligible addition to the waveguide propagation loss.

2.2.6 Power cross-coupling

The final set of simulations involves calculating the power coupled between adjacent GaN waveguides. The exchange of power between waveguides is formally known as *directional coupling*, and can be examined either by means of coupled-mode theory, or equivalently, by considering the propagation of the supermodes of the dual-waveguide system [18]. FDE simulations of identical GaN waveguides, separated by a 300 nm gap, show four guided modes. This gap is chosen as it is a reasonable value that can be repeated during the lithography step of the fabrication.

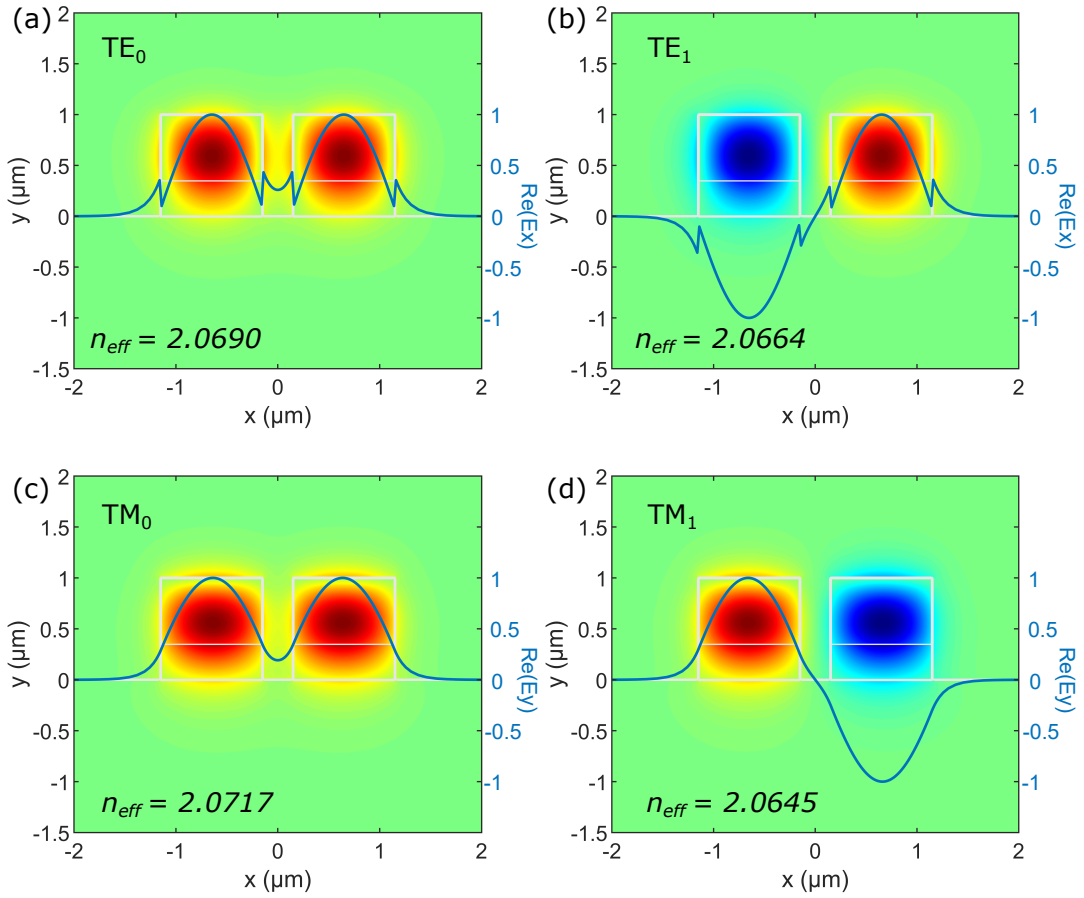


FIGURE 2.6: Real parts of the dominant electric field components for the TE (a,b) and TM (c,d) supermodes, showing symmetric and anti-symmetric behaviour.

If the non-zero $Re(E_{x,y})$ component is plotted for TE and TM polarisations, as in Figure 2.6, a set of symmetric and anti-symmetric solutions is revealed for each polarisation. These four supermodes make up a basis set of eigenmodes, and the supermode profile at any point along the propagation length is simply a linear combination of these modes [18]. Consider just one polarisation, and note that due to confinement considerations, the symmetric mode always has a greater effective index (and thus greater propagation constant) than the anti-symmetric mode. Thus, as light travels down the waveguides, oscillating in time with angular frequency ω , the admixture of the two modes leads to a beating of power back and forth between the guides. Complete power transfer occurs in one *beat length*. For identical guides, the amount of power in waveguide 2, P_2 , after injecting power P_1 into waveguide 1, is simply given by [18]:

$$P_2(z) = P_1 \sin^2 \left(\frac{\pi z \Delta n}{\lambda} \right), \quad (2.1)$$

where Δn is the difference between the symmetric and anti-symmetric effective indices.

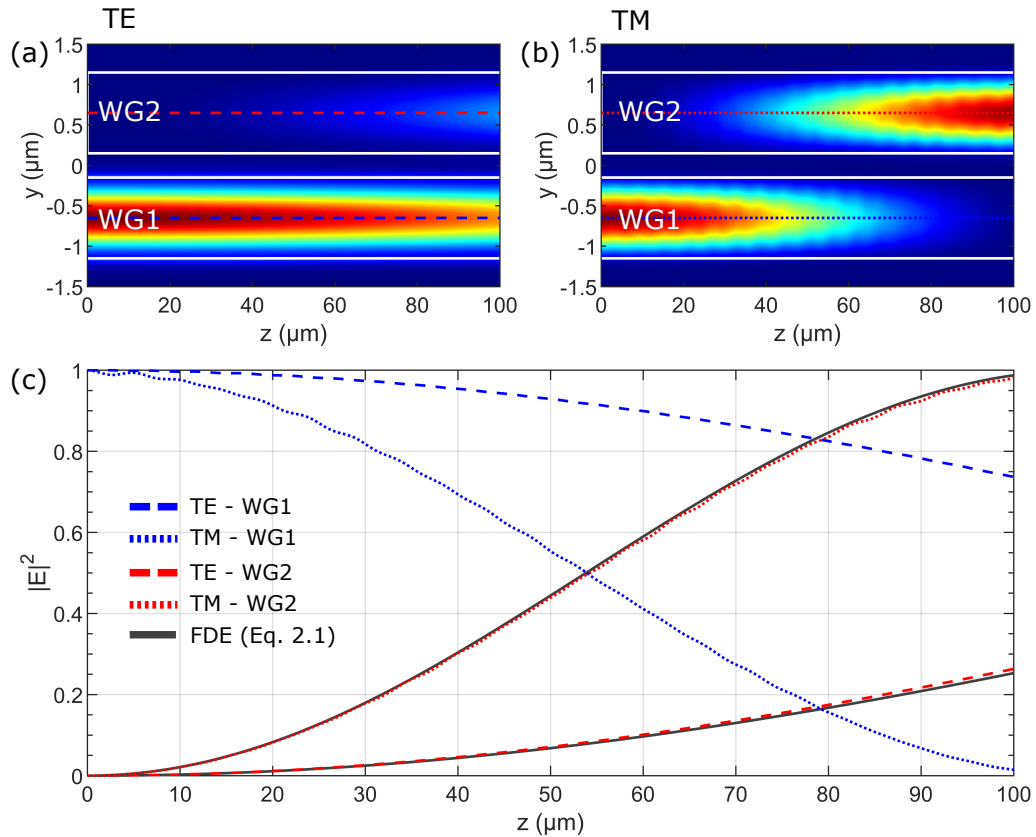


FIGURE 2.7: Plan views of the EME field intensity taken through a horizontal midpoint cross-section of adjacent GaN waveguides, separation 300 nm, for (a) TE and (b) TM polarisations. (c) Power in each waveguide as a function of propagation distance z , after injecting 1 unit of power into waveguide 1 at point $z = 0$, calculated both from the EME solver and FDE solver using equation 2.1.

The calculated values from equation 2.1 are plotted alongside values extracted from EME coupling simulations in Figure 2.7. Also shown are plan views of the cross-sectional intensity profiles in the coupled guides. Power transfer per unit of coupling length is greater for the TM mode, largely due to the greater index difference Δn for this set of modes than for the TE modes. Indeed, the calculated power coupling values, which rely on this Δn , are in close agreement with the EME simulation values, shown in Figure 2.7(c).

2.2.7 Design finalisation

For the first round of fabrication, we are primarily interested in benchmarking waveguide loss, power cross-coupling, and high Q devices. To that end, the final chip design, shown in Figure 2.8, is broken into sections containing devices with varying parameters. There are cutbacks, where the only parameter changing is the total length; meaning the total insertion loss is nominally a function of propagation loss only. Unfortunately,

these devices were destroyed during the cleaving process. A range of point coupled disk resonators, where both the radius of the disk and the coupling gap are varied, are also included. Since disks have only one etched sidewall (as opposed to a ring or racetrack's 'inside' and 'outside' sidewalls), they are potentially high Q.

There are racetracks with varying coupling lengths L_c and constant coupling gaps, allowing us to measure the power cross-coupling by fitting their resonances. The dimensions are summarised in Figure 2.9, and the coupling length is varied simply by increasing the horizontal offset of the racetrack with respect to the bus waveguide. The power coupled to the resonator is made a function of coupling length instead of coupling gap because, as shown above, the coupling is a \sin^2 function of length. By contrast, coupling is an

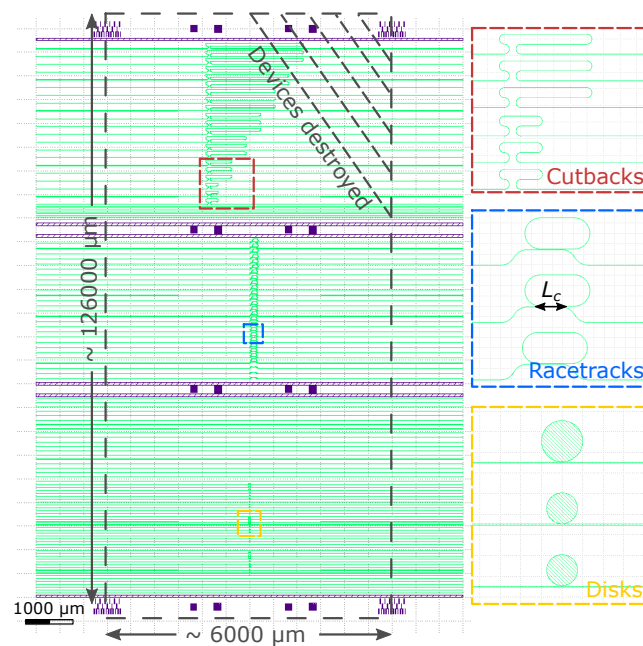


FIGURE 2.8: GDS mask file for the GaN PIC, with details of three sections

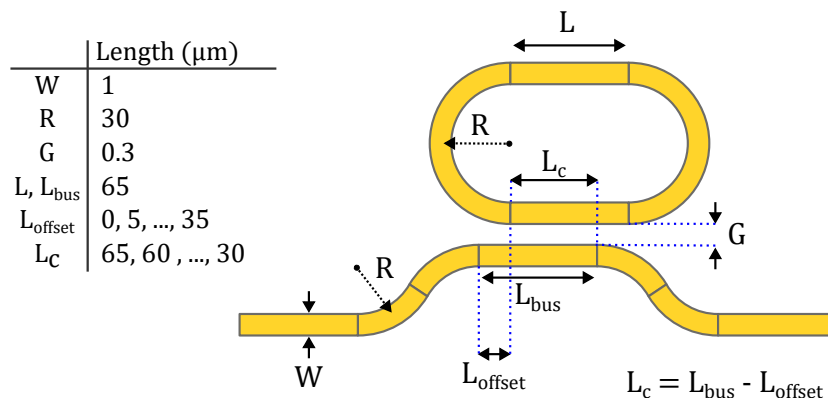


FIGURE 2.9: Summary of the racetrack resonator dimensions.

exponential function of gap, relying as it does on the overlap of exponentially decaying evanescent fields. When fabrication tolerances are also taken into consideration, it is generally easier to avoid parameterisations of the coupling gap where possible. The coupling length is varied from 30 μm to 65 μm , offering approximately 2% - 10% power cross-coupling for the TE mode (Figure 2.7(c)). Recall that resonators of moderate to high Q factors have single-pass amplitude transmission values, a , approaching 1. Thus only a small fraction of cross-coupled power, κ , is required to satisfy the condition for critical coupling, i.e. that the loss in the ring equals the coupled power: $1 - a^2 = \kappa$.

Finally, 2° half angle inverse tapers are used to expand the waveguide to a width of 2 μm at the edges of the pattern, easing mode matching with the lensed fibre used to butt-couple light into the waveguides.

2.3 Device fabrication and characterisation

2.3.1 Fabrication

The device fabrication is outlined in Figure 2.10. The surface roughness of the GaN was first measured by atomic force microscopy (AFM), and over an area of $2.5 \times 3 \mu\text{m}^2$ an RMS roughness value of $0.41 \pm 0.06 \text{ nm}$ was obtained. Hydrogen silsesquioxane (HSQ) resist was then spun on the GaN, before being patterned with electron-beam lithography.

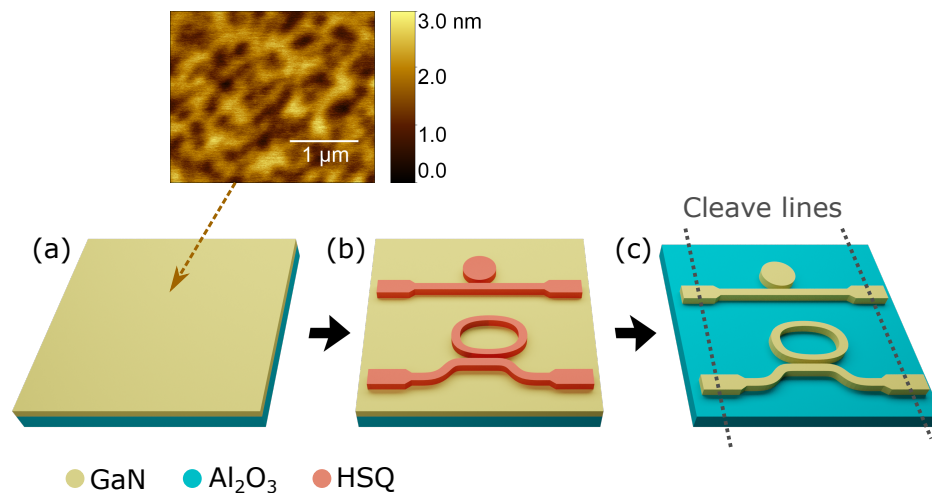


FIGURE 2.10: Passive device fabrication. (a) The GaN roughness is first measured with AFM. (b) HSQ resist is spun and patterned with electron-beam lithography. (c) The GaN is dry etched in an inductively coupled plasma reactive ion etcher (ICP-RIE), with Ar/Cl₂ chemistry. Residual HSQ is removed in a short buffered oxide wet etch, before the ends of the chip are cleaved to allow fibre butt-coupling to the waveguides.

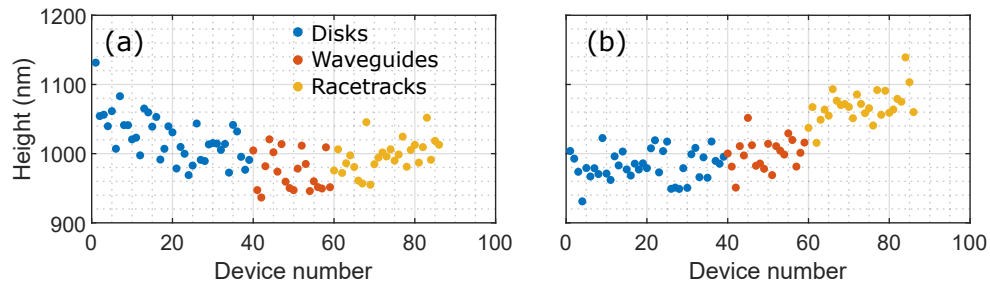


FIGURE 2.11: Surface profilometer measurements on the (a) left and (b) right offcuts of the chip after cleaving. The total scan length is ~ 7.4 mm.

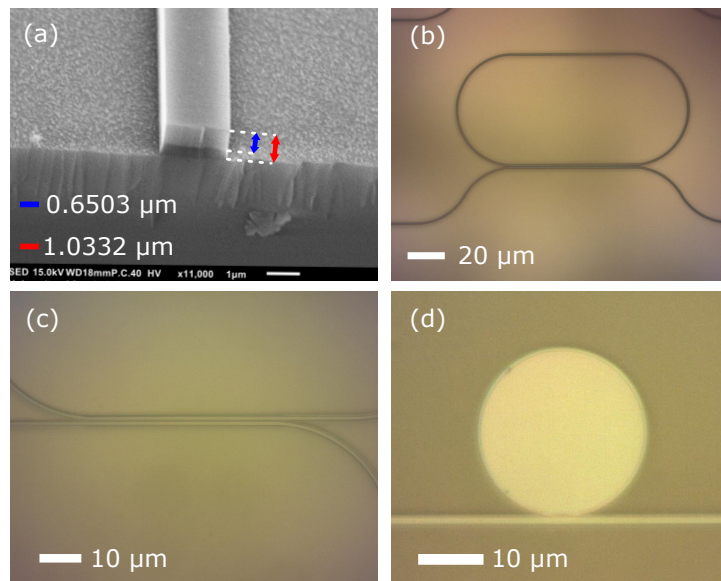


FIGURE 2.12: (a) Angled SEM image of waveguide facet, showing the expected thickness values for the GaN (~ 650 nm) and total step height ($\sim 1 \mu\text{m}$). Optical micrographs of (b) a racetrack resonator after the ICP step, (c) detail of the coupling section of a racetrack after the BOE step, and (d) a GaN disk.

Upon electron-beam exposure and development, cross-linked HSQ forms an SiO_2 -like hard mask. Transfer of the mask pattern to the GaN was achieved with an Ar/Cl_2 etch down to the sapphire in an ICP-RIE, in a recipe with the following conditions: Ar 10 sccm, Cl_2 30 sccm, coil power 400 W, platen power 200 W, and pressure 20 mTorr. Residual HSQ was removed in a short buffered oxide solution wet etch. A thick layer of photoresist was then spun on the chip to protect the devices during the final cleaving step. A diamond-tipped scribe was used to score the underside of the sapphire, easing mechanical cleaving of the end portions of the chip and allowing for fibre-coupling to the exposed waveguide facets. The protective resist was then removed with a solvent clean.

Surface profilometer measurements (Figure 2.11) on the chip offcuts after the cleave show slight waveguide height variations across the chip, where the full scan length between device numbers 1 and 86 was 7.4 mm. Mean thickness values for the left and right

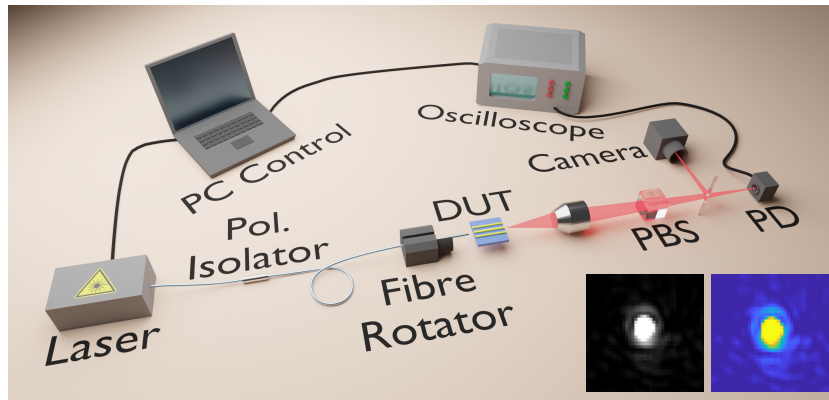


FIGURE 2.13: Schematic of the optical set-up used to characterise the device. Inset: Direct and false-colour images of single-mode output of waveguide. DUT: device under test, PBS: polarisation beam splitter, PD: photodetector.

offcuts are $1.003 \mu\text{m}$ and $1.014 \mu\text{m}$, respectively, indicating good uniformity across the chip, centred around the target thickness of $1 \mu\text{m}$. An SEM image of a waveguide end facet (Figure 2.12(a)) confirms this value, which based on the contrast difference in the image, breaks down to $\sim 650 \text{ nm}$ of GaN and $\sim 350 \text{ nm}$ of AlN.

2.3.2 Characterisation

Transmission spectra are taken with the optical set-up shown in Figure 2.13. The fibre output from a tuneable Agilent 81640A laser source is passed through an in-line polarisation isolator, before coupling to a polarisation-maintaining lensed fibre. The lensed fibre is used to focus the light down to a spot size (approximate radius: $1.5 \mu\text{m}$) that makes efficient mode matching with the waveguides possible - compensating for the disparity between single-mode fibre core diameter and waveguide dimensions. Light transmitted through the device is collected by a microscope objective, passed through a polarisation beam splitter (PBS), and focused onto a detector and CCD camera via a beam splitter. The injection fibre and PBS are both mounted in rotating holders, providing a means to inject and collect either TE or TM polarised modes. Transmission spectra are constructed by synchronously running a wavelength sweep on the laser and a time trace of the detector voltage with an oscilloscope.

2.4 Racetrack transmission results

Figure 2.14 compares the normalised transmission spectra of two racetracks, considered to be representative of the general performance trends for each polarisation. Each show free spectral ranges of $\sim 3.1 \text{ nm}$, and group indices of ~ 2.5 . For TE injection, the

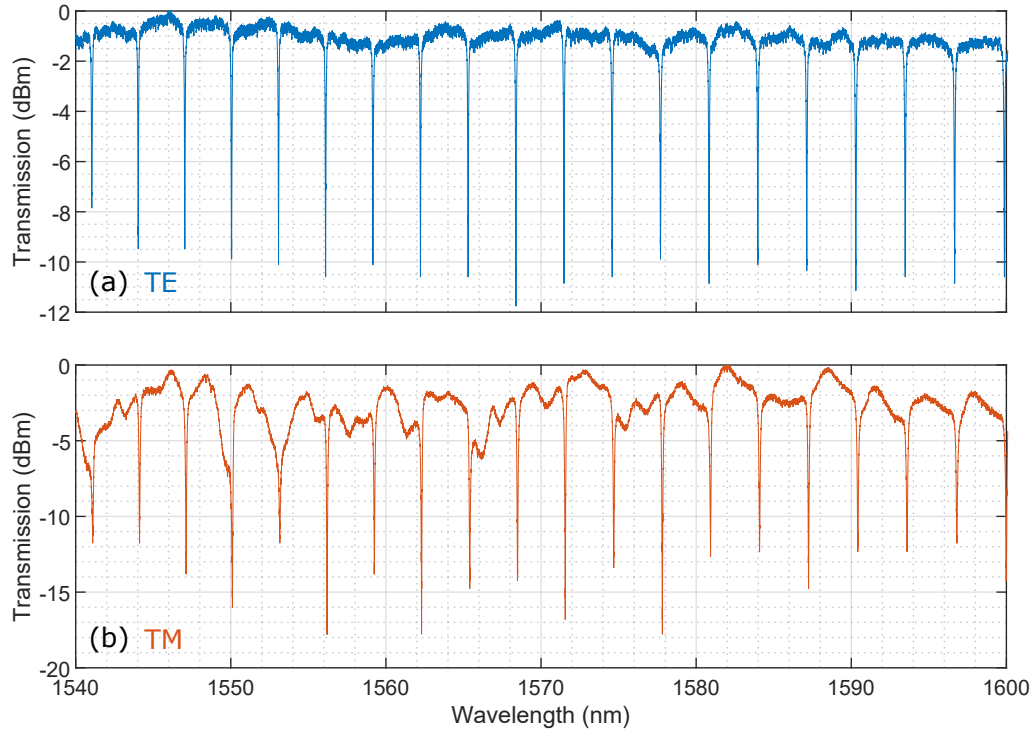


FIGURE 2.14: (a) TE transmission, $L_c = 45 \mu\text{m}$. (b) TM transmission, $L_c = 30 \mu\text{m}$

characteristics of a resonance are fairly consistent across the measured range, with an almost flat off-resonance throughput. Conversely, the TM injected racetracks suffer from a low frequency modulation of the off-resonance transmission, as well as inconsistent resonance line shapes.

A more detailed understanding is gained by fitting resonances with the following equation [23] (derived in the previous chapter):

$$T_n = \frac{r^2 + a^2 - 2racos(\phi)}{1 + (ra)^2 - 2racos(\phi)}, \quad (2.2)$$

where r is the self-coupling coefficient, a is the single-pass field amplitude transmission, and ϕ is the phase-accumulation in the resonator, given by $\phi = \beta L$ where β is the propagation constant and L is the cavity length. The highest loaded Q factor resonances for each polarisation are shown in Figure 2.15, with values of 2.91×10^4 and 1.18×10^4 for the TE and TM modes respectively. Over two nominally identical resonators, and 37 measurable resonances, the mean loaded Q factor for TE injection was 2.6×10^4 . For TM injection, there were only 13 resonances of three identical resonators for which the off-resonant throughput signal did not irrevocably distort the fit; and over these 13 resonances a mean loaded Q factor of 1.19×10^4 was measured. The difference in peak linewidth (and thus Q factor) is to be expected given the above simulations, which show

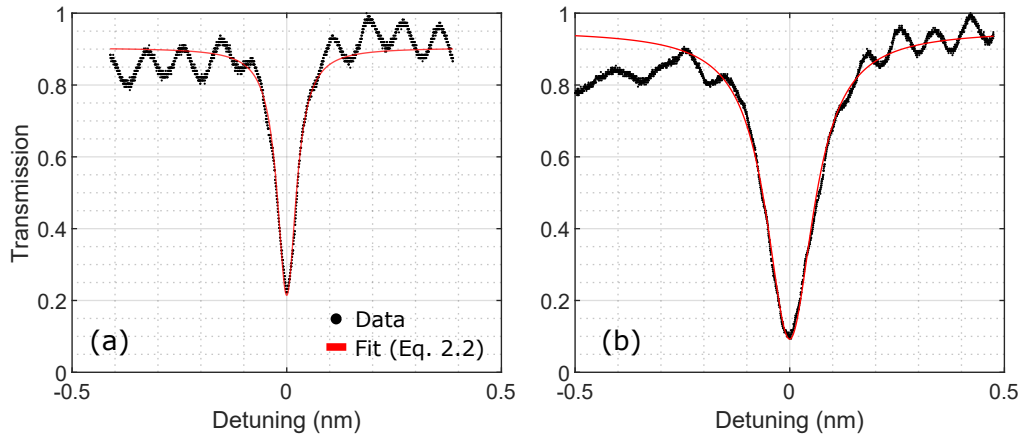


FIGURE 2.15: Highest loaded Q resonances for each polarisation. (a) TE, at 1558.8437 nm, FWHM = 53.6 pm, $Q = 2.91 \times 10^4$ (b) TM, at 1544.1192 nm, FWHM = 130.8 pm, $Q = 1.18 \times 10^4$.

power cross-coupling for the TM mode is much greater. It follows that these devices will likely be over-coupled, and the coupling loss contribution to the resonant linewidth broadening will be greater, reducing the Q factor.

Recall, the fitting terms governing loss and coupling (a and r) enter equation 2.2 symmetrically, meaning they can be freely swapped without changing the resultant T_n . Therefore, in cases where devices are near to or at critical-coupling, that is where $r = a$, care must be taken to disentangle the two and assign the correct physical meaning to each. This can be done either by investigating how these parameters (particularly the cross-coupling $\kappa = 1 - r^2$) vary with wavelength, or by an independent measurement determining one or the other [30]. In the present case, the two will be functions of coupling length, and trends in the peak FWHM and extinction values will reveal which resonators are under-coupled ($r > a$), over-coupled ($r < a$), or critically-coupled ($r = a$).

2.4.1 Racetrack coupling

First, note in Figure 2.16(a) that as the coupling length decreases, the resonant linewidth monotonically decreases - evident in the increase in Q factor. Further discussion is limited to the case of TE injection, where in Figures 2.16(b,d), a clear turning point in peak extinction values is observed. Starting from a coupling length of 60 μm , the devices are clearly over-coupled - with resonance dips characterised by broad, shallow line shapes. As the coupling decreases, the resonators approach critical coupling at around 45 μm , where dips have the best extinction and an intermediate linewidth. A further decrease in coupling leads to under-coupled resonances, which have the narrowest peaks and shallow resonances. Mean power cross-coupling fractions are plotted in Figure 2.16(c).

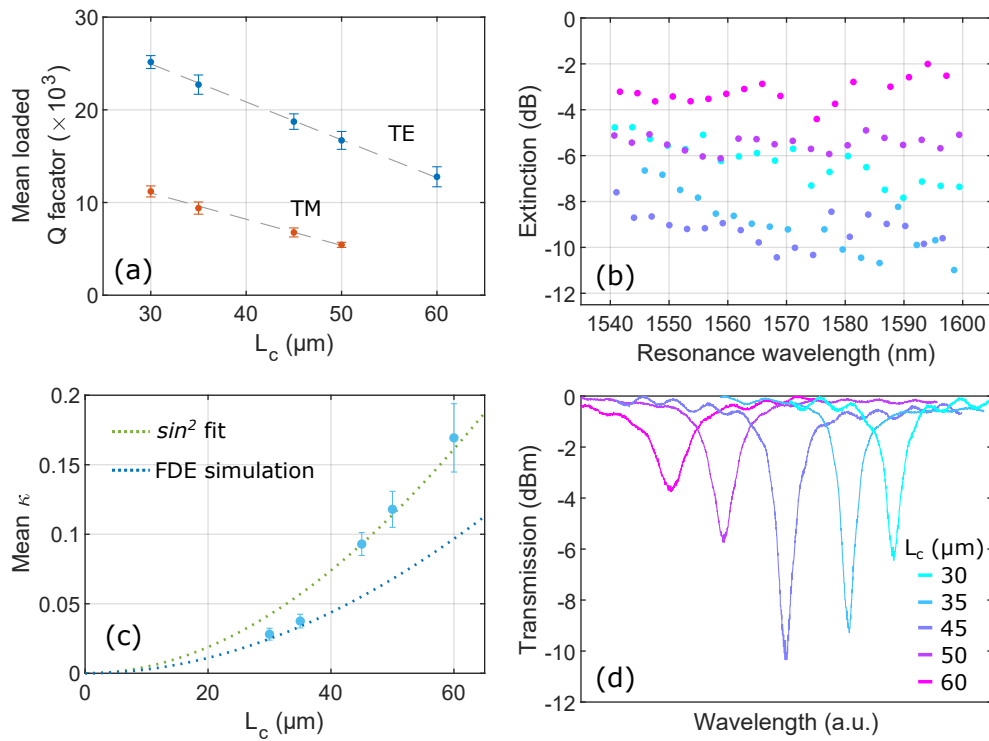


FIGURE 2.16: (a) Mean Q factors, showing a linear decrease with increasing coupling length. (b) TE resonance dip extinction values, with a cross section of line shapes around 1568 nm shown in (d), displaying maximum extinction for an intermediate value of coupling length. (c) Extracted mean TE power cross-coupling values, alongside a \sin^2 fit and the simulated values.

We note that the simulation underestimates these values for larger coupling lengths, which are nonetheless well modelled by fitting them with equation 2.1 with Δn as a free parameter, found to equal 3.4×10^{-3} - an increase from the previously simulated value of 2.6×10^{-3} . This difference can be explained by fabrication differences across the chip, and the potential for overexposure in the coupling region to leave behind GaN which enhances the coupling between bus and racetrack - particularly for devices with longer coupler lengths. For example, if the coupling gap is reduced by just 20 nm, from 300 nm to 280 nm, simulations show Δn increases to 3.1×10^{-3} .

2.4.2 Racetrack loss

The distributed loss values for each polarisation are plotted in Figure 2.17(a), and in Figure 2.17 (b) is the same, but expressed as a loss per round trip of the cavity. In the derivation of equation 2.2, additional coupling losses are contained within the parameter a , and so the distributed loss values are necessarily higher than the equivalent waveguide propagation loss. We would therefore expect the distributed loss to decrease with decreasing coupling length since for shorter lengths the influence of the coupling

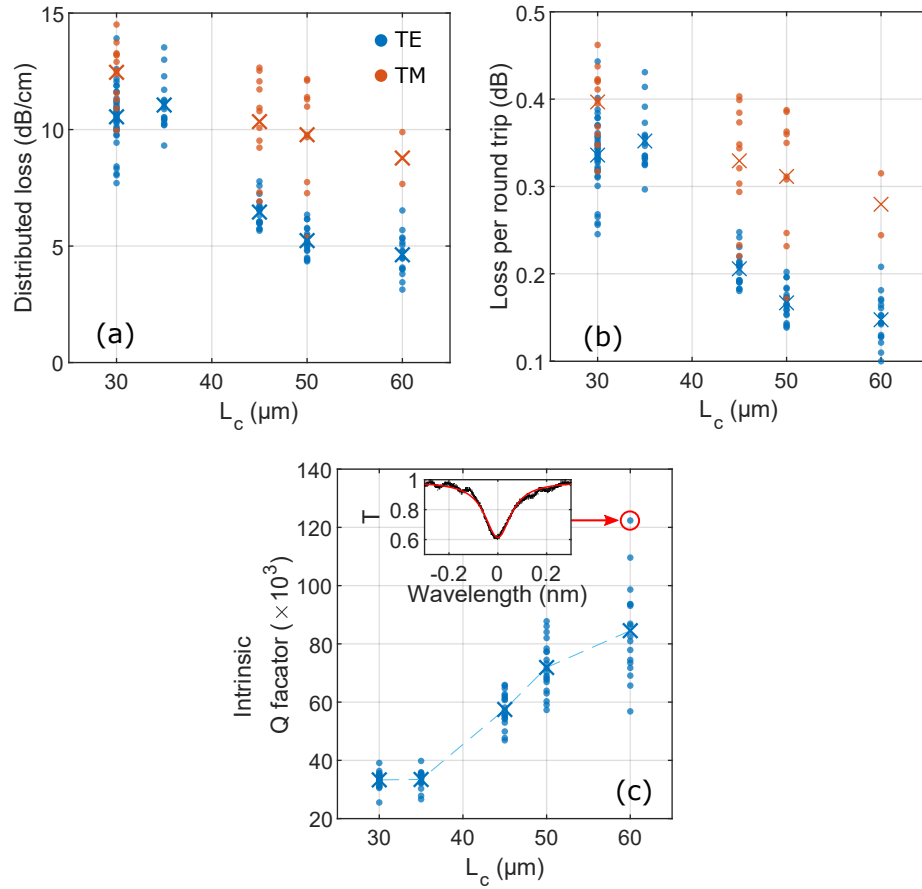


FIGURE 2.17: (a) Distributed loss values extracted from the fits for each coupling length and polarisation, with mean values plotted as crosses. (b) Loss per racetrack round trip. (c) TE intrinsic Q factors for each coupling length. Inset: resonance which features the highest intrinsic Q factor measured.

section should diminish. Instead, the observed increase suggests that any losses due to the coupler are outweighed by other loss mechanisms – differences in the GaN material quality, or lithography, across the chip perhaps.

The TM mode is lossier than the TE mode, which based on the confinement factors in table 2.1, suggests that light scattering and absorption from defects and dislocations in the buffer layer for the TM mode is a greater source of loss than any sidewall scattering for the TE mode. *Chen et al.* showed that for low powers and wavelengths greater than 800 nm, free carrier absorption can add 1-3 dB/cm to the propagation loss [2]. This is because III-nitrides grown on sapphire are intrinsically n-type doped, with GaN’s carrier density ($10^{15} - 10^{17} \text{ cm}^{-3}$) significantly larger than other materials (Silicon: 10^{10} cm^{-3} , GaAs: 10^6 cm^{-3} , InP: 10^7 cm^{-3}) [2]. Unfortunately, free carrier loss is proportional to the carrier density, and inversely proportional to the carrier mobility - which is itself decreased by the high density of dislocations that arise from the lattice mismatch between

GaN (or AlN) and sapphire. However, the material used here was specifically grown to be semi-insulating, which should ameliorate the amount of free carrier loss.

Indeed, for 17 measured TE resonances at $L_c = 60 \mu m$, a mean value of 4.63 dB/cm is measured, with a minimum value of 3.13 dB/cm, which despite being a distributed loss with additional loss mechanisms, is close to the state of the art *propagation losses* for GaN ridge waveguides of 2.4 dB/cm [2].

The intrinsic Q factor, Q_{int} , is calculated with the following [31]:

$$Q_{int} = \frac{2Q}{1 \pm \sqrt{T}}, \quad (2.3)$$

where Q is the loaded Q factor and T is the normalised on-resonance transmitted power. For under-coupling (over-coupling) the summation (subtraction) is taken in the denominator. Corresponding to the low distributed losses, we calculate a peak intrinsic Q factor of 1.22×10^5 and a mean value of 8.4×10^4 over the same 17 resonances as above. The peak intrinsic Q factor measured here is similar to the current highest literature value for GaN (1.37×10^5 [1]), despite our devices being left air-clad and thus more susceptible to sidewall scattering losses, while the devices in [1] are clad by atomic layer deposition with Al_2O_3 . The spread of intrinsic Q factors across the chip also serves to highlight there may be a difference in the GaN material quality or microfabrication process across the chip.

2.5 Microdisk transmission spectra

GaN microdisk resonators were also fabricated. Such devices are commonly used as integrated UV whispering gallery mode (WGM) lasers – though not strictly in the present case of undoped material. They are often fabricated and characterised in isolation [32, 33], or coupled to bus waveguides [15, 34]. Here, a range of disks were coupled via point coupling sections to bus waveguides (as in Figure 2.12(d)), and transmission spectra were taken as above. Two example spectra are shown in Figure 2.18.

For all disks and both polarisations, all resonances were relatively narrow and suffered from poor extinctions, characteristic of under-coupling. Under-coupling is especially likely because of the short interaction length between bus and disk in the point coupling section. The TE spectrum shown in Figure 2.18(c) was the only spectrum for that polarisation for which resonances were visible, suggesting all others were so under-coupled as to be essentially indistinguishable from background throughput intensity. This is also why in the TE case only two families of modes are visible, while the TM spectrum shows

coupling to three modes. To make the TE resonances clearer, Figure 2.19(d) replots the TE spectrum after a fast Fourier transform was used to isolate and remove the low frequency modulation of the spectrum.

A ring or racetrack – being nothing more than a waveguide wrapped back on itself – can be designed to support a single family of well spaced resonances whose azimuthal mode number decreases with wavelength, simply by making the waveguide single-mode. While a microdisk of the same thickness may also support a single *vertically* confined mode, the lack of an internal confining dielectric interface means several *radial* modes can exist. For a detailed explanation of this, see Chapter 4. Looking for a self-repeating pattern of resonances, it is possible to identify these mode families, which for convenience have been labelled with coloured arrows in Figure 2.19(b,d). A single colour of arrow corresponds to

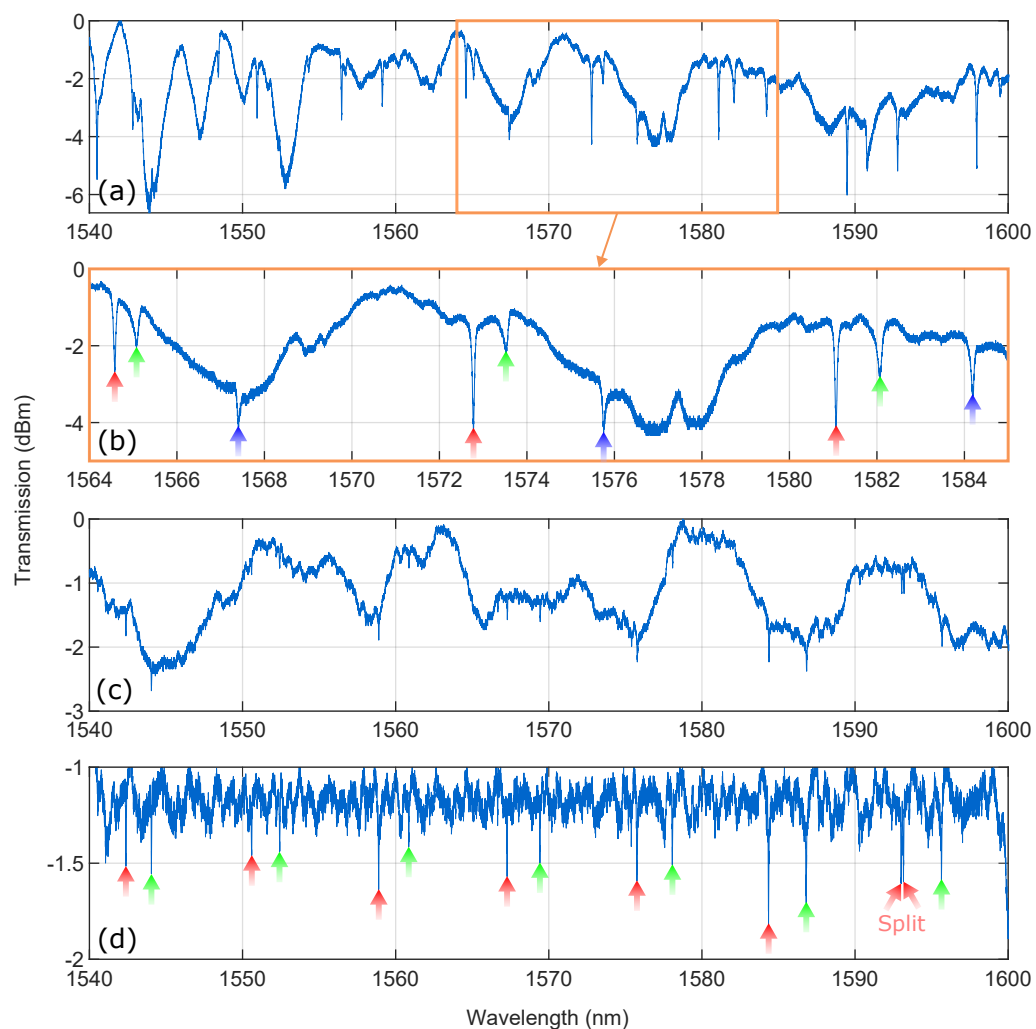


FIGURE 2.18: (a) Example TM microdisk transmission spectrum, radius 20 μm , gap 200 nm. (b) Window of spectra highlighting three families of modes. (c) TE transmission spectrum, of the same disk. (d) Fast Fourier filtered spectrum, making the two families of modes more visible.

one radial mode, while repetitions of that arrow with increasing wavelength correspond to decreasing azimuthal mode number, m .

The square magnitude electric field distributions of two such TE polarised radial modes are shown in Figure 2.19, with (a) being the fundamental, and (b) being the first order. Since the central lobes (and power distribution) move inwards with increasing radial mode number, we expect these modes to be coupled to by a smaller fraction than the fundamental radial mode. We might then ascribe the red and green labelled resonances in Figure 2.19(d) to the fundamental and first order radial modes respectively, since a cursory inspection of the spectrum shows the green resonances are narrower and shallower (i.e. *more* under-coupled). Indeed, the red resonances are 24.5% broader, and 19% deeper than the green resonances on average. This is reflected in differences in their average power cross-couplings: 0.075% and 0.048% for the red and green labelled peaks respectively, extracted from resonances fits on the unfiltered spectrum of Figure 2.18(c).

From the free spectral ranges of each mode family, the group index can also be calculated. In the TM case, the red, green, and blue arrows denote modes with group indices of 2.39, 2.32, and 2.35 respectively; while for TE, the red and green modes are 2.32 and 2.30 respectively. No value exceeds the group index recorded for the racetracks previously, which given a decreasing effective index with wavelength, indicates the disks are slightly less dispersive.

Across all disks, a peak TE Q factor of 4.38×10^4 was measured. Since the disks are in general so under-coupled, their intrinsic Q factors are not much larger than their loaded Q factors, with a peak Q_{int} of 4.45×10^4 noted, corresponding to a low loss of 7.9 dB/cm for the TE case. For the TM measurement on the same disk, the peak Q_{int} is lower, at

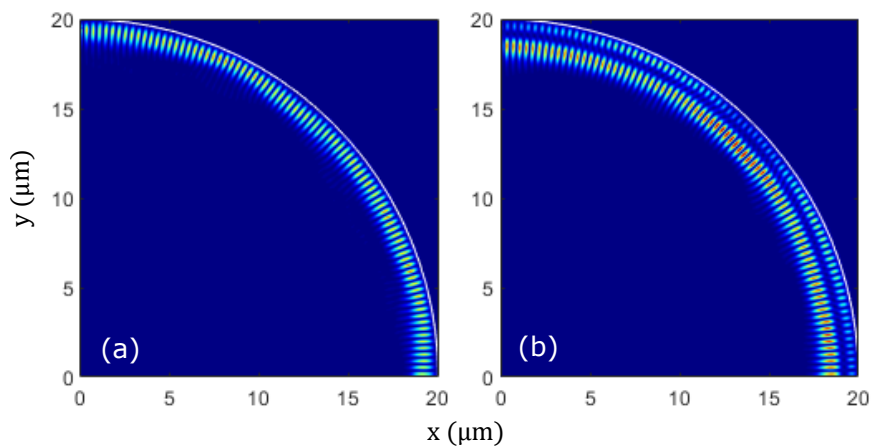


FIGURE 2.19: FDTD simulations of the field distributions within the GaN microdisk. A TE orientated source located inside the disk was used to excite the whispering gallery modes, and field distribution snapshots taken 5000 fs after simulation start. (a) The fundamental radial mode. (b) The first order radial mode.

2.66×10^4 ; with a loss of 13.8 dB/cm. This reflects the general racetrack performance where the TM mode, which has a greater overlap with the AlN buffer layer exhibits higher losses.

Finally, note how these spectra, and even the TM racetrack spectrum presented previously (Figure 2.14(b)), display an obvious low frequency modulation of the background optical throughput. A possible explanation for this is wavelength dependent scattering loss in the coupler sections. Such a loss would be more prominent for strongly coupled resonators (as in the TM racetrack case), and certainly more prominent for disks with nominally small coupling gaps like here – even in the TE case. To alleviate this issue, the coupling gap could be increased. If this leads to resonances too under-coupled, this can be combated by wrapping the bus waveguide around a portion of the disk – in the commonly implemented pulley configuration [35].

2.6 Summary

In summary, this chapter presented the fabrication and characterisation of GaN resonator devices. The devices were designed in accordance to numerical simulations, also detailed in the above. Transmission spectra reveal high Q racetrack resonators, with intrinsic Q factors (122,000) and losses (3.13 dB/cm) at the current state of the art for GaN on sapphire. GaN WGM disk resonators, which are often fabricated in isolation for use as laser sources, were here fabricated with evanescently coupled bus waveguides. To the best of our knowledge, their loaded Q factors exceed the state of the art – which is of the order of 1×10^3 [36, 37]. High Q factors are desirable for WGM lasers, because the increased build up of optical radiation in the cavity greatly reduces the effective lasing threshold. However, it should be noted that our material, being non-intentionally doped and consisting of a single GaN layer on AlN, lacks additional loss mechanisms (scattering and absorption), which are present in those lasing GaN heterostructure disks presented in literature.

References

- [1] Erik Stassen, Minhao Pu, Elizaveta Semenova, Evgeniy Zavarin, Wsevolod Lundin, and Kresten Yvind. High-confinement gallium nitride-on-sapphire waveguides for integrated nonlinear photonics. *Optics Letters*, 44(5):1064, 2019.
- [2] Hong Chen, Houqiang Fu, Xuanqi Huang, Xiaodong Zhang, Tsung-Han Yang, Jossue A. Montes, Izak Baranowski, and Yuji Zhao. Low loss GaN waveguides at the visible spectral wavelengths for integrated photonics applications. *Optics Express*, 25(25):31758, 2017.
- [3] Ohad Westreich, Mordechai Katz, Yossi Paltiel, Orna Ternyak, and Noam Sicon. Low propagation loss in GaN/AlGaIn-based ridge waveguides. *Physica Status Solidi (A) Applications and Materials Science*, 212(5):1043–1048, 2015.
- [4] Dirk Ehrentraut and Zlatko Sitar. Advances in Bulk Crystal Growth of AlN and GaN. *MRS Bulletin*, 34(4):259–265, 2009.
- [5] M. Bockowski. Review: Bulk growth of gallium nitride: challenges and difficulties. In *Crystal Research and Technology*, volume 42, pages 1162–1175. John Wiley & Sons, Ltd, dec 2007.
- [6] R. Hui, Y. Wan, J. Li, S. X. Jin, J. Y. Lin, and H. X. Jiang. III-nitride-based planar lightwave circuits for optical communications. *Optics InfoBase Conference Papers*, 5(1):4–6, 2005.
- [7] Alexander W. Bruch, Chi Xiong, Benjamin Leung, Menno Poot, Jung Han, and Hong X. Tang. Broadband nanophotonic waveguides and resonators based on epitaxial GaN thin films. *Applied Physics Letters*, 107(14), 2015.
- [8] N. Vico Triviño, U. Dharanipathy, J. F. Carlin, Z. Diao, R. Houdré, and N. Grandjean. Integrated photonics on silicon with wide bandgap GaN semiconductor. *Applied Physics Letters*, 102(8), 2013.
- [9] Yanfeng Zhang, Loyd McKnight, Erman Engin, Ian M. Watson, Martin J. Cryan, Erdan Gu, Mark G. Thompson, Stephane Calvez, Jeremy L. O’Brien, and Martin D. Dawson. GaN directional couplers for integrated quantum photonics. *Applied Physics Letters*, 99(16):2009–2012, 2011.
- [10] Chi Xiong, Wolfram Pernice, Kevin K. Ryu, Carsten Schuck, King Y. Fong, Tomas Palacios, and Hong X. Tang. Integrated GaN photonic circuits on silicon (100) for second harmonic generation. *Optics Express*, 19(11):10462, 2011.
- [11] S. M. Hendrickson, A. C. Foster, R. M. Camacho, and B. D. Clader. Integrated nonlinear photonics: emerging applications and ongoing challenges [Invited]. *Journal of the Optical Society of America B*, 31(12):3193, dec 2014.
- [12] F P Payne and J. P.R. Lacey. A theoretical analysis of scattering loss from planar optical waveguides. *Optical and Quantum Electronics*, 26(10):977–986, 1994.
- [13] Y. Zeng, I. Roland, X. Checoury, Z. Han, M. El Kurdi, S. Sauvage, B. Gayral, C. Brimont, T. Guillet, M. Mexis, F. Semond, and P. Boucaud. Resonant second harmonic generation in a gallium nitride two-dimensional photonic crystal on silicon. *Applied Physics Letters*, 106(8):081105, feb 2015.
- [14] I. Roland, M. Gromovyi, Y. Zeng, M. El Kurdi, S. Sauvage, C. Brimont, T. Guillet, B. Gayral, F. Semond, J. Y. Duboz, M. De Micheli, X. Checoury, and P. Boucaud. Phase-matched second harmonic generation with on-chip GaN-on-Si microdisks. *Scientific Reports*, 6(July):1–8, 2016.

- [15] I. Roland, Y. Zeng, X. Checoury, M. El Kurdi, S. Sauvage, C. Brimont, T. Guillet, B. Gayral, M. Gromovyi, J. Y. Duboz, F. Semond, M. P. de Micheli, and P. Boucaud. Near-infrared III-nitride-on-silicon nanophotonic platform with microdisk resonators. *Optics Express*, 24(9):9602, may 2016.
- [16] U. Dharanipathy, N. Vico Triviño, C. Yan, Z. Diao, J.-F. Carlin, N. Grandjean, and R. Houdré. Near-infrared characterization of gallium nitride photonic-crystal waveguides and cavities. *Optics Letters*, 37(22):4588, 2012.
- [17] I. Roland, Y. Zeng, Z. Han, X. Checoury, C. Blin, M. El Kurdi, A. Ghrib, S. Sauvage, B. Gayral, C. Brimont, T. Guillet, F. Semond, and P. Boucaud. Near-infrared gallium nitride two-dimensional photonic crystal platform on silicon. *Applied Physics Letters*, 105(1):011104, jul 2014.
- [18] Amnon Yariv. *Optical Electronics*. Saunders College Publishing, 1991.
- [19] Zhaoming Zhu and Thomas Brown. Full-vectorial finite-difference analysis of microstructured optical fibers. *Optics Express*, 10(17):853, aug 2002.
- [20] A. S. Barker and M. Ilegems. Infrared lattice vibrations and free-electron dispersion in GaN. *Physical Review B*, 7(2):743–750, jan 1973.
- [21] J. Pastrňák and L. Roskocová. Refraction Index Measurements on AlN Single Crystals. *physica status solidi (b)*, 14(1):K5–K8, jan 1966.
- [22] Irving H. Malitson. Refraction and Dispersion of Synthetic Sapphire. *Journal of the Optical Society of America*, 52(12):1377, dec 1962.
- [23] W. Bogaerts, P. de Heyn, T. van Vaerenbergh, K. de Vos, S. Kumar Selvaraja, T. Claes, P. Dumon, P. Bienstman, D. van Thourhout, and R. Baets. Silicon microring resonators. *Laser and Photonics Reviews*, 6(1):47–73, jan 2012.
- [24] John Heebner, Rohit Grover, and Tarek Ibrahim. Optical microresonator theory. *Springer Series in Optical Sciences*, 138:71–103, 2008.
- [25] Allan W. Snyder and John D. Love. Tunnelling leaky modes on optical waveguides. *Optics Communications*, 12(3):326–328, nov 1974.
- [26] E. A.J. Marcatili. Bends in Optical Dielectric Guides. *Bell System Technical Journal*, 48(7):2103–2132, 1969.
- [27] D. Marcuse. Bending Losses of the Asymmetric Slab Waveguide. *Bell System Technical Journal*, 50(8):2551–2563, 1971.
- [28] Mordehai Heiblum and Jay H. Harris. Analysis of Curved Optical Waveguides by Conformal Transformation. *IEEE Journal of Quantum Electronics*, 11(2):75–83, 1975.
- [29] D. Marcuse. Bend Loss of Slab and Fiber Modes Computed with Diffraction Theory, 1993.
- [30] W. R. McKinnon, D. X. Xu, C. Storey, E. Post, A. Densmore, A. Delâge, P. Waldron, J. H. Schmid, and S. Janz. Extracting coupling and loss coefficients from a ring resonator. *Optics Express*, 17(21):18971, 2009.
- [31] Steven A. Miller, Mengjie Yu, Xingchen Ji, Austin G. Griffith, Jaime Cardenas, Alexander L. Gaeta, and Michal Lipson. Low-loss silicon platform for broadband mid-infrared photonics, mar 2017.

-
- [32] Gangyi Zhu, Jiaping Li, Nan Zhang, Xin Li, Jun Dai, Qiannan Cui, Qinghai Song, Chunxiang Xu, and Yongjin Wang. Whispering-Gallery Mode Lasing in a Floating GaN Microdisk with a Vertical Slit. *Scientific Reports*, 10(1):1–7, dec 2020.
- [33] Chap Hang To, Wai Yuen Fu, Kwai Hei Li, Yuk Fai Cheung, and Hoi Wai Choi. GaN microdisk with direct coupled waveguide for unidirectional whispering-gallery mode emission. *Optics Letters*, 45(4):791, feb 2020.
- [34] Farsane Tabataba-Vakili, Blandine Alloing, Benjamin Damilano, Hassen Souissi, Christelle Bri-mont, Laetitia Doyennette, Thierry Guillet, Xavier Checoury, Moustafa E.L. Kurdi, Sébastien Chenot, Eric Frayssinet, Jean Yves Duboz, Fabrice Semond, Bruno Gayral, and Philippe Boucaud. Monolithic integration of ultraviolet microdisk lasers into photonic circuits in a III-nitride on silicon platform. *arXiv*, 45(15):1–5, 2020.
- [35] Ehsan Shah Hosseini, Siva Yegnanarayanan, Amir Hossein Atabaki, Mohammad Soltani, and Ali Adibi. Systematic design and fabrication of high-Q single-mode pulley-coupled planar silicon nitride microdisk resonators at visible wavelengths. *Optics Express*, 18(3):2127, feb 2010.
- [36] Hyeonjun Baek, Chul Ho Lee, Kunook Chung, and Gyu Chul Yi. Epitaxial GaN microdisk lasers grown on graphene microdots. *Nano Letters*, 13(6):2782–2785, jun 2013.
- [37] Gangyi Zhu, Jiaping Li, Nan Zhang, Xin Li, Jun Dai, Qiannan Cui, Qinghai Song, Chunxiang Xu, and Yongjin Wang. Whispering-Gallery Mode Lasing in a Floating GaN Microdisk with a Vertical Slit. *Scientific Reports*, 10(1):1–7, jan 2020.

Chapter 3

Tunable GaN microresonators

In this chapter, electrically actuated tunable GaN racetrack resonators are presented. Integrated micro-heaters are used to red-shift the resonance wavelength of the racetrack. The fabrication and characterisation of these devices is detailed, with transmission and bandwidth measurements presented. To the best of our knowledge, the work presented here is the first example of a tunable GaN micro-resonator.

3.1 Introduction

In the previous chapter, passive GaN micro-resonators were presented. The periodic wavelength filtering offered by these optical micro-cavities is set by the effective index and path length of the circulating mode, with no way to tune the wavelength response post-fabrication. For many applications this is a serious limitation to device functionality, especially since the effective index (and to a lesser extent the path length) are sensitive to a number of environmental conditions such as temperature, humidity, surface adsorption, and device cladding variations. Furthermore, fabrication discrepancies can drastically alter the wavelengths filtered by the micro-resonator. For example, the effective index is acutely sensitive to the waveguide width, and for a model GaN micro-ring resonator (radius 20 μm), simulations show that a decrease in width of just 10 nm is enough to shift resonances by several line-widths (Figure 3.1 (a)). In an all-pass configuration, this difference would mean wavelengths which should be strongly filtered (Figure 3.1 (b)) are instead allowed to pass almost completely (Figure 3.1 (c)).

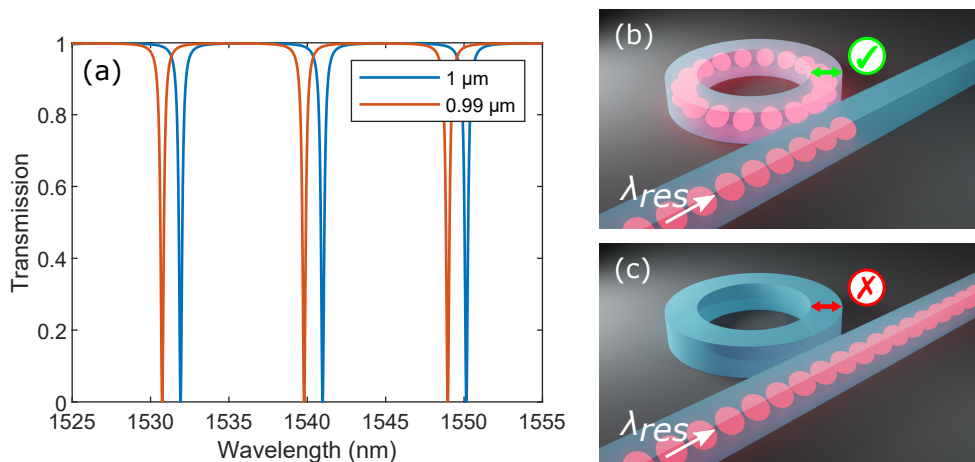


FIGURE 3.1: (a) Model TM transmission spectra for two GaN ring resonators with different waveguide widths, showing the drastic difference in filtered wavelengths for a 10 nm width difference. (b) Example of a critically coupled resonance, where the fabricated device matches perfectly the as-designed values and the resonant wavelength is strongly filtered. (c) For a 10 nm width deviation, the same wavelength is allowed to pass almost completely.

Actively tunable micro-resonators are thus required to bring the wavelength dependence of a device into line with its as-designed value. Depending on the material platform in question, resonance *trimming* may also be possible, whereby a permanent change is induced post-fabrication (usually in the device cladding), which fixes the effective index at the correct value. Examples for silicon photonics include the photo-oxidation of a polymer cladding [1], or the introduction of stress in a buried oxide layer [2].

Besides correcting for fabrication inconsistencies or environmentally induced drifts, the ability to actively control a resonator's transmission and reflection characteristics opens up important applications in signal modulation, switching, and routing. Tunable micro-cavities (particularly those with small mode volumes) are also attractive for collecting and enhancing the single-photon emissions of diamond's colour centres, which can be spectrally broad at room temperatures. Thus, tuning a resonator into spectral overlap with the zero-phonon line (ZPL) of a coupled emitter's spectrum is necessary to maximize the Purcell enhancement factor and increase the rate of generation of indistinguishable ZPL photons over those emitted at longer wavelengths through the phonon sidebands [3, 4]. However, the integration of diamond, which lacks a strong intrinsic tuning mechanism, with another photonic platform which does not, is an ongoing topic of research. In the next chapter, the hybridisation of diamond and GaN photonics will be elucidated. In this chapter, the fabrication and testing of tunable GaN racetrack resonators will be presented.

The figures of merit for a tunable micro-resonator are the tuning speed, range, and efficiency, quoted as either the power needed to tune a resonance over one FSR (W/FSR)

or the wavelength shift per unit of power (pm/mW). Several tuning mechanisms exist, including thermal [5], electro-optic [6], carrier density manipulation [7], strain [8], and microelectromechanical [9]. Of course, not all methods are applicable to all materials, and so discussion will be limited to the two methods most applicable to GaN photonics: thermal and electro-optic.

3.1.1 Electro-optic tuning

Linear electro-optic tuning only applies to non-centrosymmetric materials. This includes the semiconductors GaN, GaAs, CdTe, and ZnTe; crystals like LiNbO₃, LiTaO₃, BaTiO₃, and KDP [6, 10]; and some poled polymers containing specifically engineered organic chromophore molecules [11]. As mentioned in Chapter 2, non-centrosymmetric materials lack inversion symmetry, meaning it is possible to achieve strong and effectively instantaneous material polarisation responses to incident DC or low-frequency electric fields. The refractive index, which relates to the polarisation through the non-linear susceptibility, χ , can thus be tuned (in linear proportion) to an incident electric field. This is also known as the *Pockels effect*, and is distinct from the *Kerr effect*, where the refractive index change is proportional to the *square* of the electric field. Recall from Chapter 1 that the Kerr effect is a $\chi^{(3)}$ process, while the Pockels effect is $\chi^{(2)}$. Consequently, the Kerr effect is weaker than the Pockels effect, but applies to all materials - not just non-centrosymmetric ones.

Relying on the material's polarisation response, electro-optic tuning is typically more efficient [12, 13] and faster than thermal tuning, with modulation bandwidths of tens of GHz [14, 15], extending to hundreds of GHz for some poled polymers [16] or for LiNbO₃ where index matching between optical and modulating RF fields is achieved [17]. The strength of the electro-optic effect is governed by the direction of the incident electric field relative to the crystallographic directions corresponding to the non-zero elements of the electro-optic tensor. Different crystal structures will have different non-zero elements, and this is an important consideration when designing integrated electro-optic modulators.

3.1.2 Thermal tuning

For thermal tuning, a current is passed through resistive micro-heaters located in close proximity to the waveguide. Joule heating raises the temperature, T , of the waveguide, changing its refractive index; which at constant pressure, changes according to the material's thermo-optic coefficient, dn/dT . The change in index alters the resonance condition, and thus the wavelength of a resonance is shifted. Materials with positive

thermo-optic coefficients display red-shifting of resonances. There are some materials which possess negative thermo-optic coefficients, and so experience blue-shifting of resonances in response to temperature increases [19–21]. In general, materials with low melting points and high thermal expansion coefficients tend to have negative thermo-optic coefficients, whereas crystalline materials with high melting points and low thermal expansion coefficients have positive thermo-optic coefficients [22]. Thus, with the exception of many polymer waveguides, for the materials widely used in integrated optics a resonator’s response to temperature is dominated by a positive effective index shift, and not by any increase in cavity length due to thermal expansion, resulting in the following simple expression for the wavelength shift [23]:

$$\frac{d\lambda}{dT} = \frac{dn}{dT} \frac{\lambda_0}{n_g}, \quad (3.1)$$

where n_g is the group index, and λ_0 is the initial wavelength.

The thermo-optic coefficient is itself a function of both temperature and wavelength – through the wavelength dependent refractive index, n . Fortunately, any second-order polynomial behaviour only manifests itself at high temperatures, or at wavelengths operating near the material’s band-gap. For example, evaluations of the refractive index and thermo-optic coefficient of thin-film GaN on sapphire (GaN thickness: $5.18\mu\text{m}$) undertaken by *Watanabe et al.* only showed a nonlinear increase in refractive index for wavelengths below 500 nm, and elevated temperatures [18], as shown in Figure 3.2.

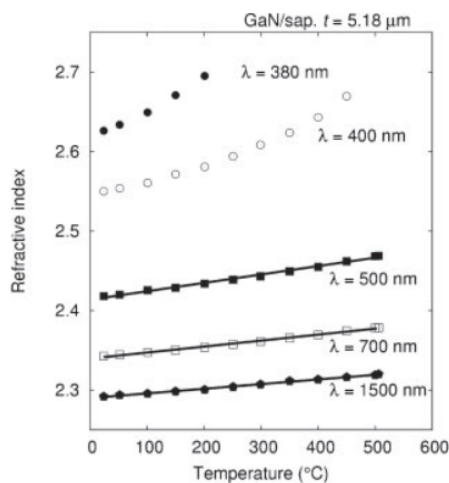


FIGURE 3.2: Refractive index of thin-film GaN on sapphire, as a function of temperature and for different wavelengths. The bottom three data sets show linear increases with temperature. Credit: [18]

Thermal tuning is simple to implement and unlike electro-optic tuning, works for all materials and crystallographic orientations - as long as there is enough cladding to isolate the mode from any optical loss due to the metal heating elements. Simulations show that a conformal cladding thickness of 600 nm should result in losses less than 0.05 dB/cm for the GaN waveguides presented here. However, the most commonly used cladding material, silicon dioxide, has a small thermal conductivity (just 1.38 W/m·K) [24], which limits the achievable modulation rates of these devices. The amount of heat actually reaching the waveguide is small, which has the benefit of limiting thermal crosstalk between devices, but the drawback of lowering the efficiency [25]. In any case, these problems can be mitigated by improved heater design, or by the local removal of portions of the silica cladding, with efficiencies of 2.4 mW/FSR reported [26] for silicon micro-rings.

While it is in principle possible to tune a GaN resonator with the electro-optic effect, in the following we use thermal tuning. Thermal tuning is still a widely implemented and important tuning mechanism, especially since at time of writing there have been no demonstrations of an actively tunable GaN resonator. It should be noted however that future work on an electro-optic GaN resonator would be an important advancement.

3.2 Device fabrication and characterisation

3.2.1 Fabrication

The GaN material used was a second wafer from Kyma Technologies, similar to that used in the previous chapter. The device fabrication is outlined in Figure 3.3. Steps (i) to (iii) are identical to those in the previous chapter, involving the fabrication of passive racetrack structures with the use of electron-beam lithography in HSQ resist, and ICP-RIE dry etching in Ar/Cl₂. The additional steps start with the cladding of the device with spin-on glass (HSQ), and PECVD SiO₂. The two layers are visible in the SEM image in Figure 3.4 (b). This bi-layer is used as the HSQ first planarises the sample surface, to help with subsequent deposition of metal contacts. Being a denser layer, the PECVD prevents pin holes in the cladding, and removes the potential for shorting between contacts.

Positive resist (PMMA) was then spun on the sample in preparation for patterning, metal deposition and lift-off. Figure 3.3 (vi-vii) represents a simplification of this process, which actually involves two metal deposition steps - one for the high resistance nickel chrome (NiCr) alloy heating elements, and another for the low resistance gold (Au) contact pads and tracks. NiCr is a common metal alloy used for resistive micro-heaters,

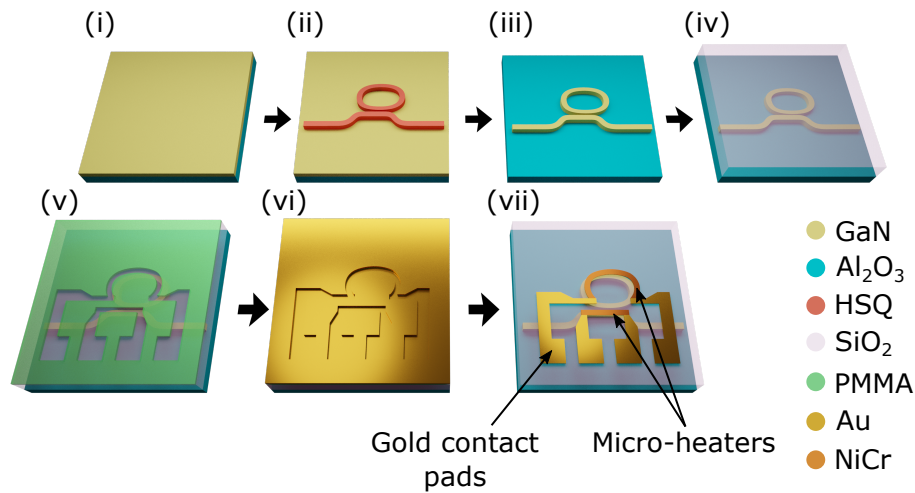


FIGURE 3.3: Tunable GaN resonator proces flow. (i) GaN on sapphire. (ii) Electron-beam lithography in HSQ resist. (iii) ICP-RIE etch in Ar/Cl₂ chemistry. (iv) Cladding with HSQ, and conformal PECVD silica. (v) Electron-beam lithography in positive PMMA resist. (vi) Metal-deposition. (vii) Lift-off.

because its base resistivity ($1.1 \times 10^{-6} \Omega m$) is an order of magnitude greater than other heating metals [27]. Two micro-heaters are included in the design. One was situated directly atop a portion of the racetrack resonator, used to tune its resonance condition. The second was situated atop the coupling bus waveguide, with a 500 nm offset away from the resonator, in a configuration similar to that found in *Orlandi et al.* [28]. The purpose of this offset was to induce a temperature (and thus index) differential between bus and resonator waveguides. By introducing a controllable phase mismatch between the two modes of the evanescent coupler, the coupling coefficient, κ , can be made tunable. Unfortunately, these devices showed no tuning of the coupling, and instead only showed parasitic tuning of the resonance condition. Clearly, optimisation of these heaters is needed (particularly their offset with respect to the underlying waveguide), to reproduce the results found in *Orlandi et al.*

Unlike the passive chip in the previous chapter, this chip underwent an additional end-facet polishing step because of the poor quality of the initial mechanical cleave. Recall, consistent cleaving of GaN on sapphire is made difficult by a 30° rotation of the GaN crystal planes with respect to the same directions in the sapphire. This rotation acts to reduce the lattice constant mismatch from 30% to 15% [29]. Proper nitridation, graded AlGa_xN_{1-x}, or AlN buffer layers can also help reduce this mismatch, but even with these mitigations, the cleavage planes of the GaN and sapphire are misaligned [29]. While the cleaving dynamics are largely governed by the sapphire because it is so much thicker than the thin film GaN, the GaN facet orientation and quality can still suffer because of this misalignment. This chip in particular had prohibitively high insertion losses after

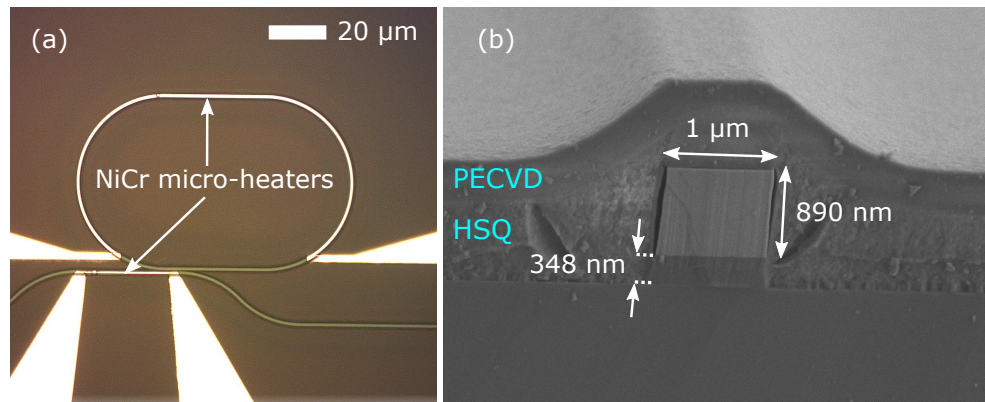


FIGURE 3.4: (a) Optical micrograph of a tunable GaN resonator. (b) SEM of a waveguide facet post-polishing, showing 890 nm of GaN with good sidewall verticality on 348 nm of AlN buffer layer. Dark streaks either side of the GaN are due to cracking in the HSQ after the PECVD deposition, which is performed at elevated temperatures.

the cleave, and so a polishing step was undertaken to improve optical coupling to the chip. After the polishing step, burnt portions of protective photoresist remained on some portions of the edge of the chip, but despite this an overall improvement in the coupling was observed.

Figure 3.4 (a) shows an optical micrograph of an example device, with the heating elements labelled, and Figure 3.4 (b) is an SEM of a successful GaN facet cleave, with waveguide dimensions labelled and a clear separation between the spin-on HSQ and PECVD deposited silica cladding. For a summary of the device dimensions see Figure 3.5. Similar to the racetracks in the previous chapter, resonators with a range of lateral offsets relative to the bus waveguide are included. The range of effective coupling lengths varies from 5 μm to 35 μm . These coupling lengths are shorter than those used

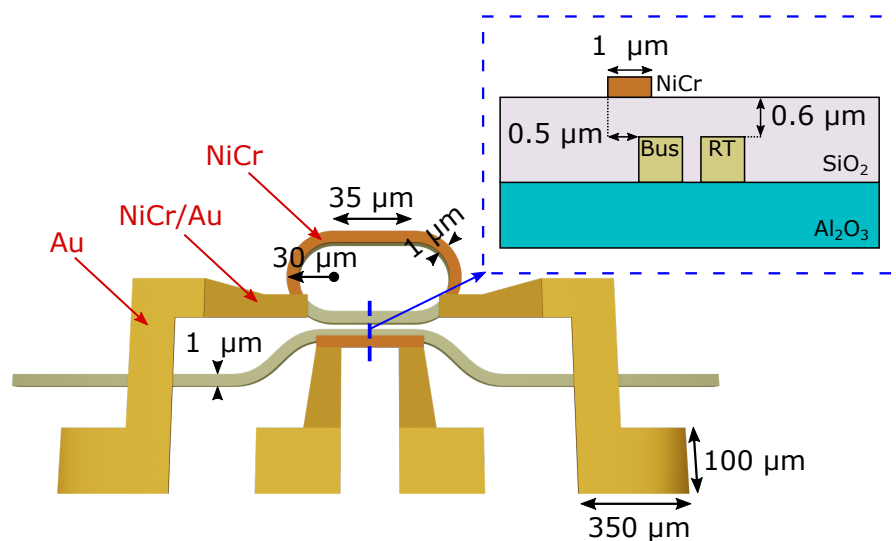


FIGURE 3.5: Relevant dimensions of a tunable racetrack device, with coupling section cross-section shown.

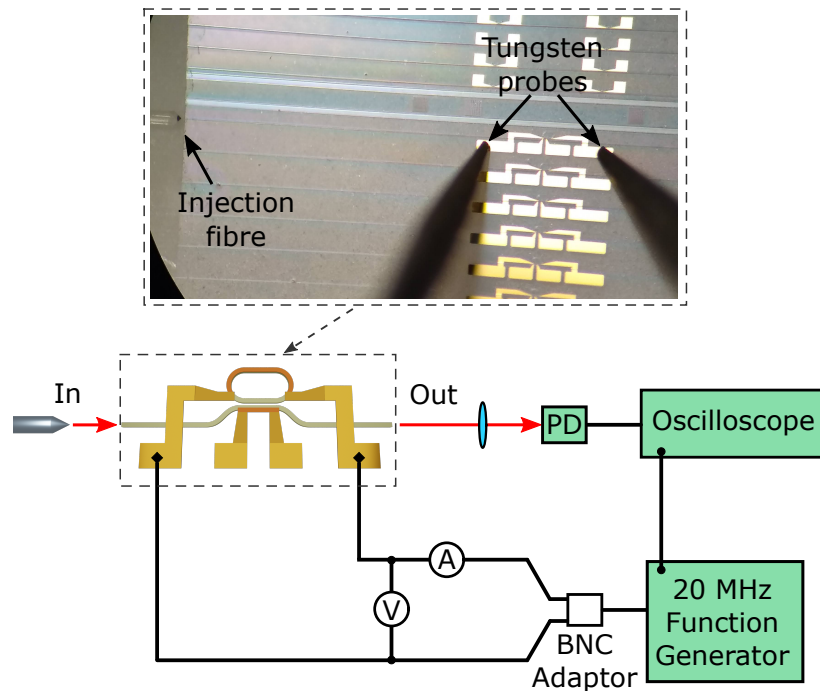


FIGURE 3.6: Diagram and microscope image of the optical and electronic characterisation of the device. For simple tuning measurements, the 20 MHz function generator is replaced with a simple power supply. For bandwidth measurements, the function generator is used to supply a square wave input to the micro-heater.

for the previous chip, since that chip was unclad and this chip is clad with silica. The cladding decreases the refractive index contrast between the GaN and its surroundings, decreasing its confinement and increasing the power cross-coupling between bus and racetrack. Thus, for the same coupling gap, to target critically coupled devices a shorter range of coupling lengths is required. Despite this, the devices presented here are over-coupled, unlike the previous unclad devices which showed a clear transition between under and over-coupling for the range of coupling lengths targeted.

3.2.2 Characterisation

The device is optically characterised with the same end-fire fibre injection rig as that used in the previous chapter. In addition, tungsten probes are used to contact the gold pads to pass an electrical current through the micro-heaters, as shown in Figure 3.6. For basic tuning measurements, the 20 MHz function generator shown in Figure 3.6 is replaced with a simple power supply. The function generator is used in subsequent bandwidth measurements to provide a square wave input to the micro-heater. An auxiliary output is sent to the oscilloscope, which is used to record both the modulated optical throughput from the photodetector, and the input modulating electrical signal.

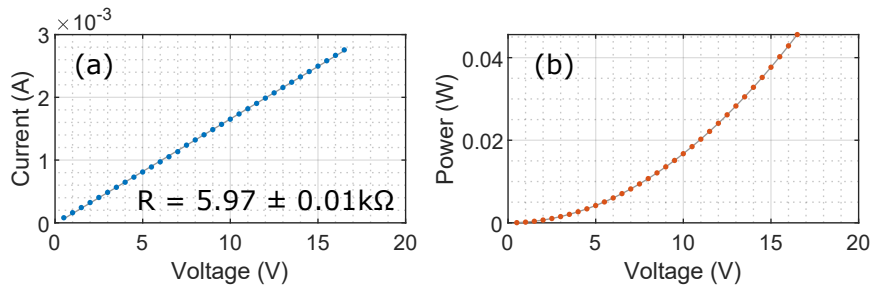


FIGURE 3.7: (a) Current and (b) power plots for increasing voltage applied to the wavelength tuning micro-heater.

The heater resistance is simply found from Ohm's law and a straight line fit of the drawn current against the supplied voltage, shown in Figure 3.7 (a). From the slope, equal to R^{-1} , a resistance of 5.97 k Ω is calculated. The upper limit for the power dissipated in the resistive micro-heater can then be calculated simply from Joule's Law, and is plotted in Figure 3.7 (b).

3.3 Tuning results

3.3.1 Wavelength tuning

The tuning of a racetrack transmission spectrum is shown in Figure 3.8, where the voltage applied to the micro-heater was incremented in steps of 0.5 V up to a final value of 16.5 V. The racetrack FSR is 3.99 nm, and the 16.5 V difference between first and final spectrum gives a tuning range of 0.53 nm. Taking $\Delta\lambda = 0.53 \text{ nm}$ and equation 3.1, the maximum temperature increase in the racetrack guide is estimated to be 13.9 K.

The resonance wavelengths are then extracted from peak fits using the same method as the previous chapter, and are plotted against the power dissipated in the heater (Figure 3.9). A clear linear trend with respect to heater power is observed, from which tuning efficiencies of 11.66 pm/mW, or 342 mW/FSR, are calculated. Since the thermo-optic coefficient of GaN ($6 \times 10^{-5} \text{ K}^{-1}$ [18]) is approximately three times smaller than that of silicon ($1.8 \times 10^{-4} \text{ K}^{-1}$ [30]), it is natural that the tuning efficiencies found here are smaller than most silicon resonators. However, in a comparison which excludes those state of the art devices with removed areas of cladding or substrate, our devices perform broadly as expected, given the ratio of thermo-optic coefficients. Similar silicon devices have tuning efficiencies in the range of $\sim 100 \text{ mW/FSR}$ [23, 31–34], which is a little over three times better than the above value of 342.3 mW/FSR. Compared to other less mature integrated optics platforms our device performs rather well, with recent efforts in

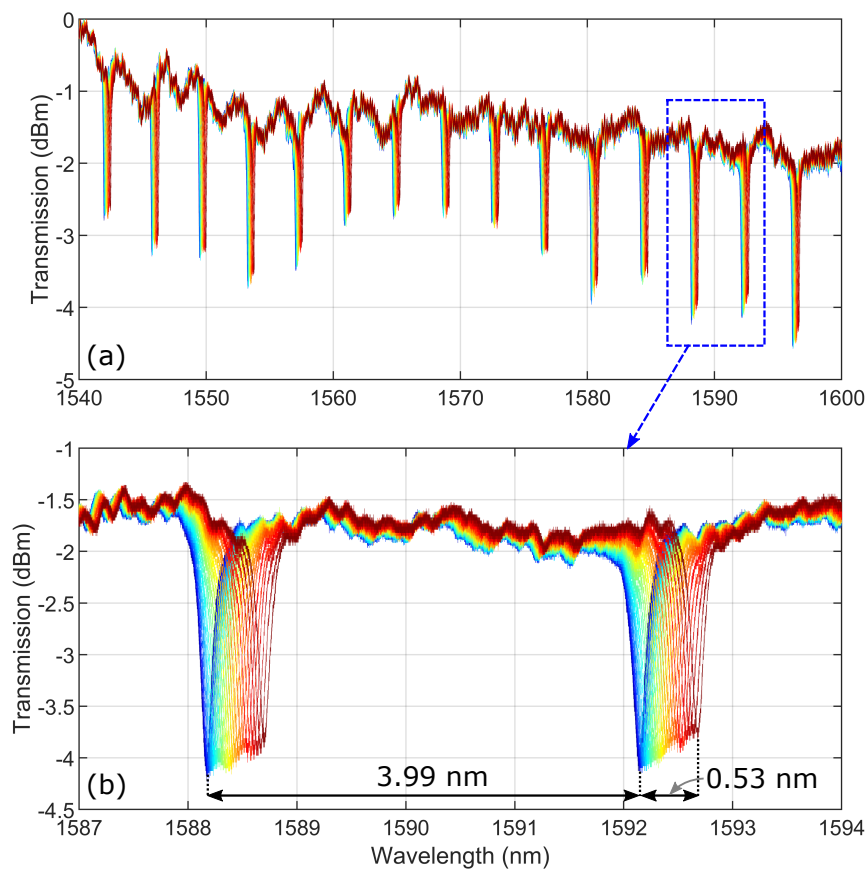


FIGURE 3.8: (a) Wavelength tuning of racetrack spectrum. (b) Detail of two nearby peaks.

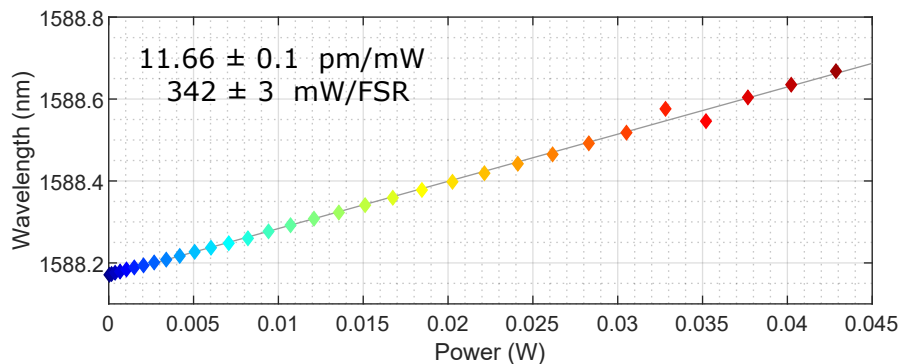


FIGURE 3.9: Resonance wavelength of a selected peak against increasing micro-heater power.

lithium niobate achieving only 1.219 pm/mW (without cladding or substrate removal) [35]; and similar aluminium nitride rings achieving only 2.879 pm/mW [36].

It is evident in the spectrum of Figure 3.8 that the tuners are not only changing the resonance position, but are also reducing the extinction - implying an increase in loss or cross-coupling, κ . Unwanted altering of the lineshape is common, with a notable example being doped silicon rings tuned by carrier injection in a p-i-n junction, whose intrinsic

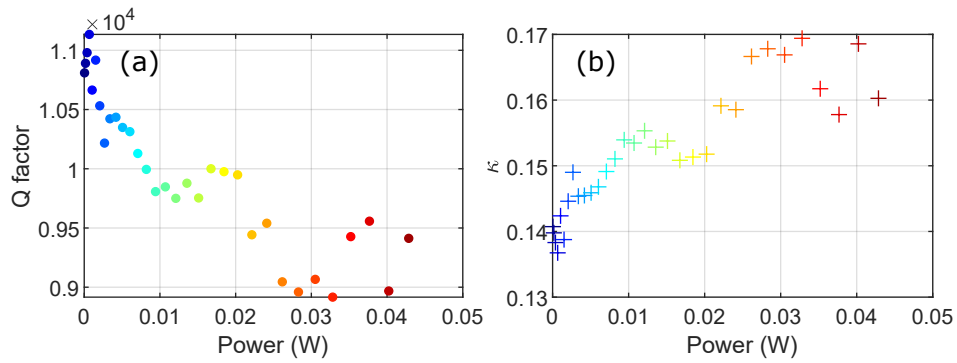


FIGURE 3.10: (a) Q factor and (b) power cross-coupling coefficients for increasing micro-heater power. Calculated for the resonance at ~ 1588 nm.

zone is located in the waveguide core. The increase in carriers in the waveguide not only tunes the resonant wavelengths by action of an effective index shift, but also increases the absorption, and therefore loss, in the ring. In the present case, since there is no obvious mechanism by which the optical loss can so strongly couple to temperature, especially for the small temperature increases presented here, an increase in coupling is suspected. Taking the resonance at ~ 1588 nm and plotting the loaded Q factors as a function of heater power, there is a clear downward trend in Figure 3.10 (a), which matches well an increase in coupling (of $\sim 3\%$), plotted in Figure 3.10 (b). To completely decouple tuning of wavelength and cross-coupling, future designs will need to better isolate the evanescent coupling region from the temperature shifts due to the wavelength couplers.

3.3.2 Coupling tuning

Using Ohm's Law and Joule's Law as before, a coupling micro-heater resistance of $0.82 \text{ k}\Omega$ is calculated, from which the power dissipation is calculated and plotted in Figure 3.11. The lower resistance of this heater reflects its shorter length - approximately 0.16 times that of the wavelength tuning micro-heater.

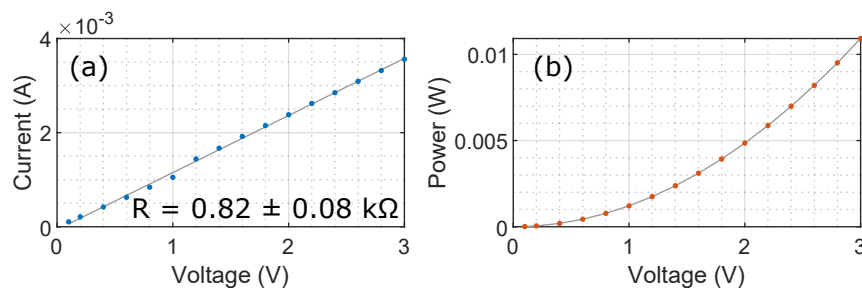


FIGURE 3.11: (a) Current and (b) power plots for increasing voltage applied to coupler micro-heater.

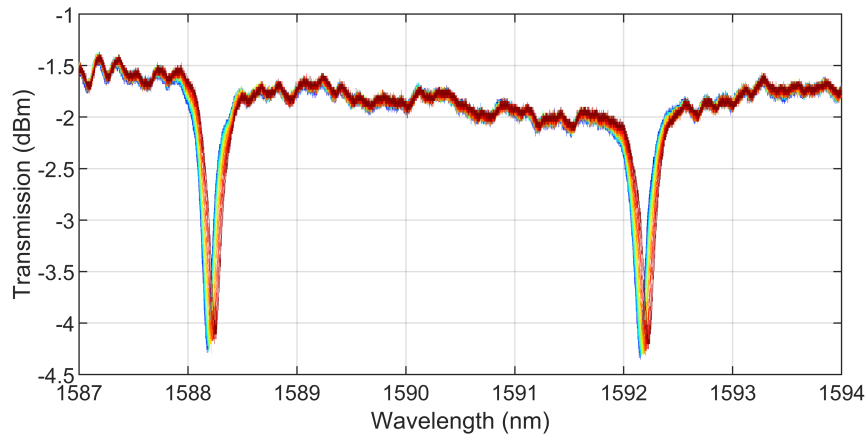


FIGURE 3.12: Spectra taken for increasing voltages applied to the coupler micro-heater.

The associated spectrum is included in Figure 3.12, where a maximum shift in resonance wavelength of 74.9 pm is observed. If the centre wavelengths are plotted against the power dissipated in the heater, as in Figure 3.13 (a), an effective (parasitic) wavelength tuning efficiency can be calculated.

The operation of these tunable couplers requires that the resonator be over-coupled in its initial state, so that the phase mismatch in the evanescent coupling section induced by the thermal gradient across bus and racetrack waveguides reduces the coupling towards critical-coupling [28]. While these resonators are definitely over-coupled, with power cross-coupling fractions, $\kappa \sim 0.145$, and distributed losses of $\sim 3 - 5$ dB/cm, no downward trend in κ is observed in Figure 3.13 (b), instead a $\sim 1\%$ increase is observed. Furthermore, the parasitic wavelength tuning efficiency of 7.24 pm/mW is only moderately smaller than the efficiency of the actual wavelength tuners. It seems likely that any tuning of the coupling - which should have a minimal effect on the position of a resonance - is instead being dominated by unwanted tuning of the wavelength. Further optimisation of these couplers is needed, beginning with adjustments of the lateral offset

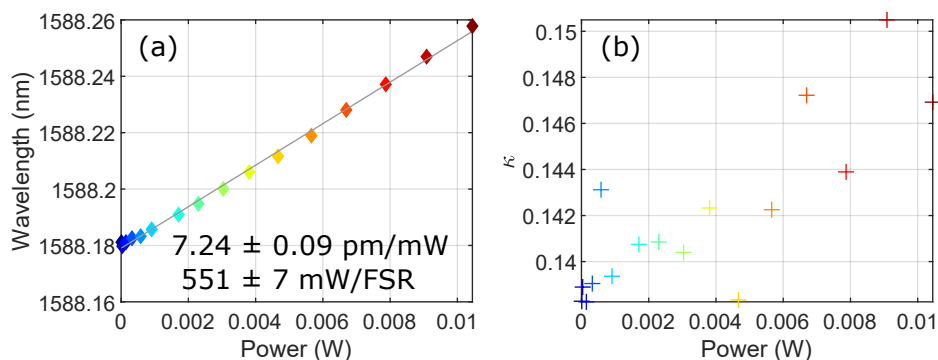


FIGURE 3.13: (a) Wavelength tuning. (b) Power cross-coupling, κ for increasing heater power.

of the heater with respect to the underlying bus waveguide. Finally, the relatively high thermal conductivity of the underlying sapphire substrate in comparison to the silica cladding (~ 20 times greater [37]) may also be exacerbating thermal crosstalk between the wavelength and coupling tuners.

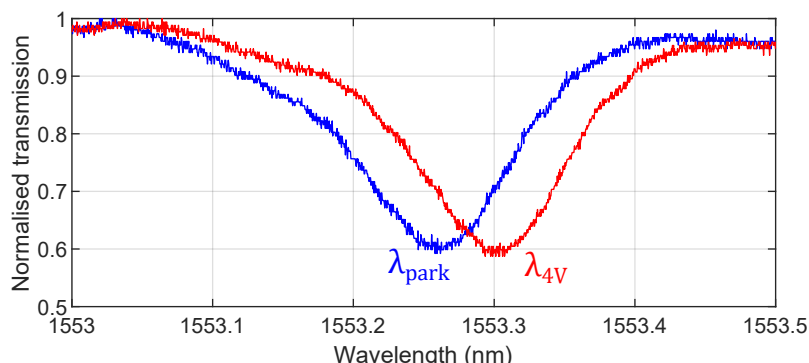


FIGURE 3.14: The peak used as the optical switch for bandwidth measurements.

3.4 Bandwidth measurements

The response times and full peak switching bandwidth were measured by first taking a transmission spectrum as before. A resonance peak was chosen, in this case at a wavelength around 1553 nm, and the laser parked on this value, at the centre of the resonance. A constant laser output power of 1 mW was selected. A square wave input generated by the 20 MHz function generator was then passed through the wavelength tuners, with a 4 V voltage swing (Figure 3.14). For a 0.5 Hz square wave, the electrical input and optical throughput signals are shown in Figure 3.15. Optical signals were measured with a variable gain detector (Thorlabs PDA10CS-EC), operated at 50 dB

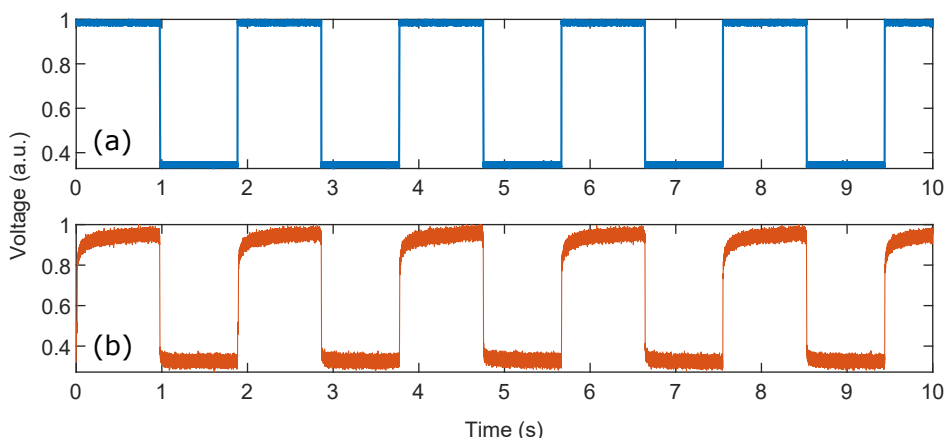


FIGURE 3.15: (a) Trace of the 0.5 Hz square wave input to the wavelength tuning micro-heater. (b) Trace of the modulated optical throughput incident on the detector.

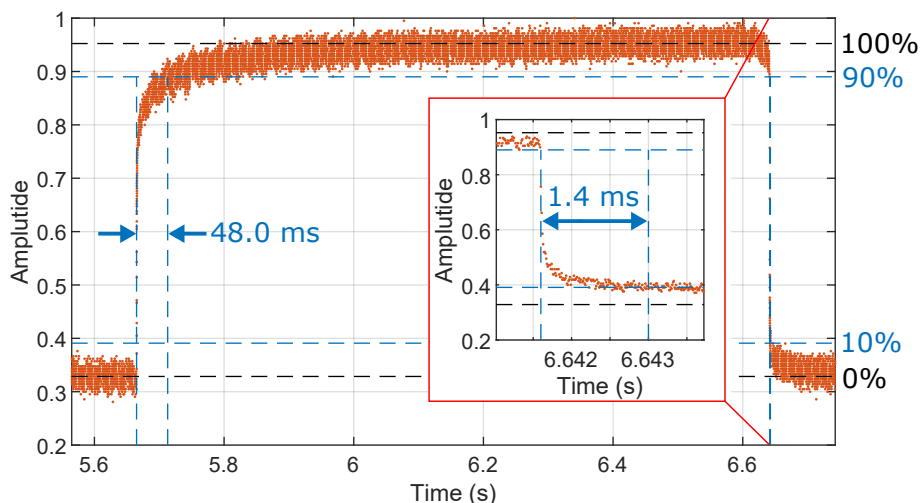


FIGURE 3.16: Resonator thermal switching response time, with an inset detailing the fall time, which is 34 times shorter than the rise time.

gain, corresponding to a detector bandwidth of 90 kHz. The otherwise steady optical throughput is modulated at the same frequency as the electrical input by the action of the micro-heaters changing the resonance wavelength of the racetrack.

From this, the resonator response time can first be calculated. Figure 3.16 focuses on one portion of the wave output of Figure 3.15. The response time is typically defined in a similar fashion to the rise time in electronics: the time interval for the signal to change from 10% to 90% of its maximum value.

A response time of 48.0 ms is extracted for the increase in heater power, and a much shorter time of 1.4 ms is extracted for the decrease in heater power. Therefore thermal energy in the resonator dissipates 34 times faster than it accumulates. A possible

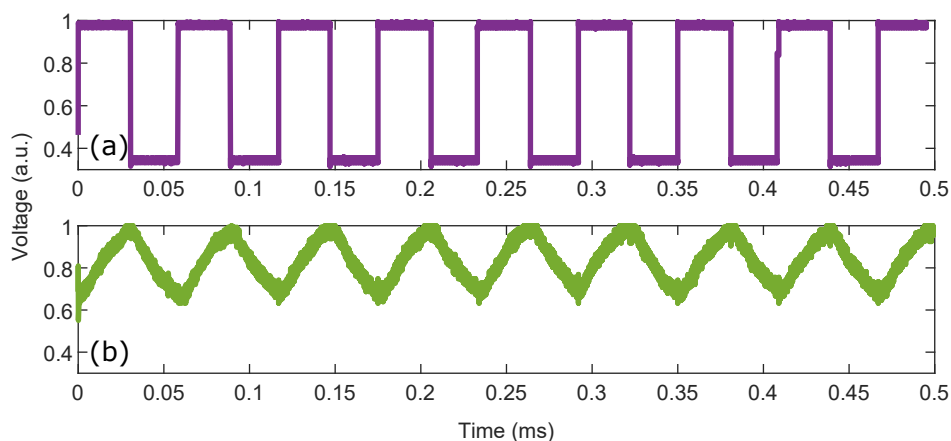


FIGURE 3.17: (a) Trace of a 17 kHz square wave input to the micro-heaters. (b) Corresponding optical throughput trace.

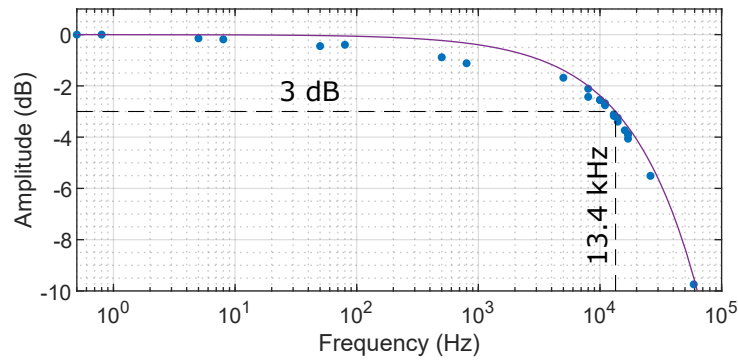


FIGURE 3.18: Peak-to-peak amplitude, referenced against the initial low frequency value.

explanation for such a drastic difference is the large thermal capacity of the silica top cladding, and relatively high thermal conductivity of the sapphire substrate in comparison to the silica cladding (~ 20 times greater [37]). In the previous tuning results, this was postulated as a source of thermal crosstalk between the wavelength and coupling tuners. Here, the thermal capacity of the cladding is increasing the time it takes to bring the GaN waveguide to a steady state temperature, while the high conductivity sapphire is dramatically decreasing the time it takes for that temperature to drop to its base level.

Finally, to evaluate the full peak switching bandwidth of the device, square waves of increasing frequency are passed through the micro-heaters. Limitations in the tuning response time mean there is a certain frequency beyond which the device cannot adequately recreate the electrical square wave input, and the modulated optical signals begins to look more like a sawtooth function, as in Figure 3.17, which was taken for a 17 kHz square wave input. A useful metric for the maximum operational frequency of the device is the 3 dB bandwidth, which in this instance refers to the point at which the peak-to-peak extinction of the optical throughput drops to -3 dB of its initial (low frequency) value. The peak-to-peak extinctions are noted for increasing heater switching frequencies, up to a maximum of 59 kHz, and are plotted in Figure 3.18, and a 3 dB bandwidth of 13.4 kHz is extracted, beyond which the typical sharp drop off in performance is observed.

3.5 Summary

This chapter presented tunable GaN racetrack resonators, which at time of writing, constitute the first effort towards a thermally tunable integrated micro-resonator in this material. The principle behind, and applications of, such devices were highlighted. In

particular, a tunable resonator in GaN could be beneficial for integration with diamond colour centres, whose single photon emissions typically require resonant tuning. A full characterisation of the tunable racetrack was performed, and tuning efficiencies of 11.66 pm/mW (342 mW/FSR) were calculated - values which reflect the lower thermo-optic coefficient of this material with respect to silicon photonics, but are improvements over other recent efforts in other relatively novel integrated optics platforms. An attempt was made to demonstrate tunable coupling from bus to racetrack waveguides, but the high thermal conductivity of the sapphire substrate is limiting factor to the performance of these tuners, because it reduces the thermal isolation in the GaN waveguide core. Finally, the response time and bandwidth of the racetrack modulator was calculated, with rise and fall times of 48 ms and 1.4 ms respectively, and a 3 dB bandwidth of 13.4 kHz.

These values may be improved by decreasing the thickness of the silica cladding, whose high thermal capacity increases the time it takes to heat the GaN. However, reducing the cladding increases the optical losses coming from modal overlap with the metal heaters. Alternatively, partially etched rib waveguides may be fabricated, so that the heaters may be deposited directly on the GaN itself, either side of the waveguide.

References

- [1] Daniel K. Sparacin, Ching-yin Hong, Lionel C. Kimerling, Jurgen Michel, John P. Lock, and Karen K. Gleason. Trimming of microring resonators by photo-oxidation of a plasma-polymerized organosilane cladding material. *Optics Letters*, 30(17):2251, sep 2005.
- [2] J. Schrauwen, D. Van Thourhout, and R. Baets. Trimming of silicon ring resonator by electron beam induced compaction. *ECIO'08 Eindhoven - Proceedings of the 14th European Conference on Integrated Optics and Technical Exhibition, Contributed and Invited Papers*, 16(6):367–370, mar 2008.
- [3] Sam Johnson, Philip R. Dolan, and Jason M. Smith. Diamond photonics for distributed quantum networks. *Progress in Quantum Electronics*, 55(May):129–165, 2017.
- [4] P. R. Dolan, S. Adekanye, A. A. P. Trichet, S. Johnson, L. C. Flatten, Y. C. Chen, L. Weng, D. Hunger, H. C. Chang, S. Castelletto, and J. M. Smith. Robust, tunable, and high purity triggered single photon source at room temperature using a nitrogen-vacancy defect in diamond in an open microcavity. *Optics Express, Vol. 26, Issue 6, pp. 7056-7065*, 26(6):7056–7065, mar 2018.
- [5] Xuefeng Jiang and Lan Yang. Optothermal dynamics in whispering-gallery microresonators. *Light: Science and Applications*, 9(1):1–15, feb 2020.
- [6] Georgios Sinatkas, Thomas Christopoulos, Odysseas Tsilipakos, and Emmanouil E. Kriezis. Electro-optic modulation in integrated photonics. *Journal of Applied Physics*, 130(1):010901, jul 2021.
- [7] G. T. Reed, G. Mashanovich, F. Y. Gardes, and D. J. Thomson. Silicon optical modulators. *Nature Photonics*, 4(8):518–526, jul 2010.
- [8] Ying Guo, Huaiyin Su, Yundong Zhang, Kaiyue Qi, Fuxing Zhu, Changqiu Yu, and Guo Yi. Strain-based tunable hollow-peanut-shaped optical microresonator. *Optics and Laser Technology*, 139:106762, jul 2021.
- [9] Carlos Errando-Herranz, Alain Yuji Takabayashi, Pierre Edinger, Hamed Sattari, Kristinn B. Gylfason, and Niels Quack. MEMS for Photonic Integrated Circuits. *IEEE Journal of Selected Topics in Quantum Electronics*, 26(2), mar 2020.
- [10] John Heebner, Rohit Grover, and Tarek Ibrahim. Optical microresonator theory. *Springer Series in Optical Sciences*, 138:71–103, 2008.
- [11] Larry Dalton and Stephanie Benight. Theory-guided design of organic electro-optic materials and devices. *Polymers*, 3(3):1325–1351, aug 2011.
- [12] Sebastian Koeber, Robert Palmer, Matthias Laueremann, Wolfgang Heni, Delwin L. Elder, Dietmar Korn, Markus Woessner, Luca Alloatti, Swen Koenig, Philipp C. Schindler, Hui Yu, Wim Bogaerts, Larry R. Dalton, Wolfgang Freude, Juerg Leuthold, and Christian Koos. Femtojoule electro-optic modulation using a silicon-organic hybrid device. *Light: Science and Applications*, 4(2):e255–e255, feb 2015.
- [13] Abu Naim R. Ahmed, Sean Nelan, Shouyuan Shi, Peng Yao, Andrew Mercante, and Dennis W. Prather. Subvolt electro-optical modulator on thin-film lithium niobate and silicon nitride hybrid platform. *Optics Letters*, 45(5):1112, mar 2020.

- [14] Zeyu Pan, Xiaochuan Xu, Chi Jui Chung, Hamed Dalir, Hai Yan, Ke Chen, Yaguo Wang, Baohua Jia, and Ray T. Chen. High-Speed Modulator Based on Electro-Optic Polymer Infiltrated Sub-wavelength Grating Waveguide Ring Resonator. *Laser and Photonics Reviews*, 12(6):1700300, jun 2018.
- [15] Abu Naim R. Ahmed, Shouyuan Shi, Andrew Mercante, Sean Nelan, Peng Yao, and Dennis W. Prather. High-efficiency lithium niobate modulator for K band operation. *APL Photonics*, 5(9):091302, sep 2020.
- [16] Wolfgang Heni, Yasar Kutuvantavida, Christian Haffner, Heiner Zwickel, Clemens Kieninger, Stefan Wolf, Matthias Lauermann, Yuriy Fedoryshyn, Andreas F. Tillack, Lewis E. Johnson, Delwin L. Elder, Bruce H. Robinson, Wolfgang Freude, Christian Koos, Juerg Leuthold, and Larry R. Dalton. Silicon-Organic and Plasmonic-Organic Hybrid Photonics. *ACS Photonics*, 4(7):1576–1590, 2017.
- [17] Andrew J. Mercante, Shouyuan Shi, Peng Yao, Linli Xie, Robert M. Weikle, and Dennis W. Prather. Thin film lithium niobate electro-optic modulator with terahertz operating bandwidth. *Optics Express*, 26(11):14810, may 2018.
- [18] Naoki Watanabe, Tsunenobu Kimoto, and Jun Suda. Thermo-optic coefficients of 4H-SiC, GaN, and AlN for ultraviolet to infrared regions up to 500 °C. *Japanese Journal of Applied Physics*, 51(11), 2012.
- [19] Yasuo Kokubun, Norihide Funato, and Masanori Takizawa. Athermal waveguides for temperature-independent lightwave devices. *IEEE Photonics Technology Letters*, 5(11):1297–1300, 1993.
- [20] Ming Han and Anbo Wang. Temperature compensation of optical microresonators using a surface layer with negative thermo-optic coefficient. *Optics Letters*, Vol. 32, Issue 13, pp. 1800-1802, 32(13):1800–1802, jul 2007.
- [21] Arpana Agrawal, Tanveer A. Dar, J. T. Andrews, Pranay K. Sen, and Pratima Sen. Negative thermo-optic coefficients and optical limiting response in pulsed laser deposited Mg-doped ZnO thin films. *JOSA B*, Vol. 33, Issue 9, pp. 2015-2019, 33(9):2015–2019, sep 2016.
- [22] E. D. Palik. Thermo-Optic Coefficients. *Handbook of Optical Constants of Solids*, pages 115–261, jan 1997.
- [23] Kishore Padmaraju and Keren Bergman. Resolving the thermal challenges for silicon microring resonator devices. *Nanophotonics*, 3(4-5):269–281, aug 2014.
- [24] S. M. Lee, David G. Cahill, and Thomas H. Allen. Thermal conductivity of sputtered oxide films. *Physical Review B*, 52(1):253–257, jul 1995.
- [25] W. Bogaerts, P. de Heyn, T. van Vaerenbergh, K. de Vos, S. Kumar Selvaraja, T. Claes, P. Dumon, P. Bienstman, D. van Thourhout, and R. Baets. Silicon microring resonators. *Laser and Photonics Reviews*, 6(1):47–73, jan 2012.
- [26] Po Dong, Wei Qian, Hong Liang, Roshanak Shafiiha, Dazeng Feng, Guoliang Li, John E. Cunningham, Ashok V. Krishnamoorthy, and Mehdi Asghari. Thermally tunable silicon racetrack resonators with ultralow tuning power. *Optics Express*, Vol. 18, Issue 19, pp. 20298-20304, 18(19):20298–20304, sep 2010.
- [27] Brian S. Mitchell. An introduction to materials engineering and science for chemical and materials engineers. page 954, 2004.

- [28] Piero Orlandi, Francesco Morichetti, Michael John Strain, Marc Sorel, Andrea Melloni, and Paolo Bassi. Tunable silicon photonics directional coupler driven by a transverse temperature gradient. *Optics Letters*, Vol. 38, Issue 6, pp. 863-865, 38(6):863–865, mar 2013.
- [29] L. Liu and J. H. Edgar. Substrates for gallium nitride epitaxy. *Materials Science and Engineering: R: Reports*, 37(3):61–127, 2002.
- [30] J. Komma, C. Schwarz, G. Hofmann, D. Heinert, and R. Nawrodt. Thermo-optic coefficient of silicon at 1550 nm and cryogenic temperatures. *Applied Physics Letters*, 101(4):041905, jul 2012.
- [31] Nicolás Sherwood-Droz, Aleksandr Biberman, Benjamin G. Lee, Howard Wang, Keren Bergman, Long Chen, and Michal Lipson. Optical 4×4 hitless silicon router for optical Networks-on-Chip (NoC). *Optics Express*, Vol. 16, Issue 20, pp. 15915-15922, 16(20):15915–15922, sep 2008.
- [32] Han-Yong Ng, Michael R. Wang, Daqun Li, Xuan Wang, Jose Antonio Martinez, Roberto R. Panepucci, and Kachesh M. Pathak. 4×4 wavelength-reconfigurable photonic switch based on thermally tuned silicon microring resonators. *Optical Engineering*, 47(4):044601, apr 2008.
- [33] Minming Geng, Lei Zhang, Lianxi Jia, Lin Yang, Ping Chen, Tong Wang, and Yuliang Liu. Four-channel reconfigurable optical add-drop multiplexer based on photonic wire waveguide. *Optics Express*, Vol. 17, Issue 7, pp. 5502-5516, 17(7):5502–5516, mar 2009.
- [34] Hui Yu, Marianna Pantouvaki, Sarvagya Dwivedi, Peter Verheyen, Guy Lepage, Roel Baets, Wim Bogaerts, Philippe Absil, and Joris Van Campenhout. Compact thermally tunable silicon racetrack modulators based on an asymmetric waveguide. *IEEE Photonics Technology Letters*, 25(2):159–162, 2013.
- [35] Xiaoyue Liu, Pan Ying, Xuming Zhong, Jian Xu, Ya Han, Siyuan Yu, and Xinlun Cai. Highly efficient thermo-optic tunable micro-ring resonator based on an LNOI platform. *Optics Letters*, Vol. 45, Issue 22, pp. 6318-6321, 45(22):6318–6321, nov 2020.
- [36] Walter Shin, Yi Sun, Mohammad Soltani, and Zetian Mi. Demonstration of green and UV wavelength high Q aluminum nitride on sapphire microring resonators integrated with microheaters. *Applied Physics Letters*, 118(21):211103, may 2021.
- [37] Properties of sapphire wafers, sapphire thermal conductivity. <https://valleydesign.com/sappprop.htm>. Accessed: 08-12-2022.

Chapter 4

Hybrid integration of diamond with GaN PICs

In this chapter, the hybrid integration by micro-transfer printing of diamond micro-disk resonators and platelets with the previously presented GaN PICs is demonstrated. The integration of AlGaAs micro-disk resonators is also presented.

After providing a brief overview of hybrid photonic integration, the specific method used in this work - micro-transfer printing with patterned elastomer stamps - will be explained. An overview of diamond disk fabrication will then be presented. Following this, optical characterisations of the printed devices will be presented, showing successful coupling between the GaN and printed components, as well as high Q resonances in the diamond disk.

4.1 Introduction

4.1.1 The case for hybrid integration

A PIC's target application depends largely on the material characteristics of its waveguide and cladding layers. Properties such as the band gap and transparency window determine the operating wavelengths, while the propagation losses influence the overall device performance, including maximum optical path length and resonator intrinsic Q factors. The potential to incorporate optical gain provides the possibility for direct electrical to optical converters, or on-chip optical pumps. There are also myriad nonlinear processes that may be accessed only in those materials possessing second and third order nonlinearities of appropriate magnitudes. Single photon generation may be achieved by

use of one of these optical nonlinearities (such as $\chi^{(2)}$ spontaneous parametric down conversion or $\chi^{(2)}$ spontaneous four-wave mixing [1]), or by using optically active single photon emitting atomic defects [2] or quantum dots [3]. Other important factors are the refractive index contrast between core and cladding, CMOS compatibility, ease of fabrication, and the cost and availability of good quality material - preferably in large wafers on a low index substrate.

It is clear therefore that with the range of properties laid out above, PICs can in principle be accorded a greater proportion of the technological burden which is usually shared between off-chip components (fibre optics, sources, detectors), and on-chip integrated photonics (waveguides, resonators, directional couplers). An increased emphasis on photonic integration will lead to reductions in device size, cost and power-consumption; and improvements in efficiency and scalability. Perhaps the most important demonstration of the benefits of increased photonic integration is the impact of the hybrid silicon integrated laser on the world's large scale data centres. The incorporation of III-V gain material on a silicon photonic multiplexing chip offers low loss, high bandwidth, direct electrical-optical conversion for integrated optical transceivers, allowing data centres to keep up with the rapid growth of internet traffic and data generation [4-6].

More generally, the central challenge facing increased photonic integration is the fact that the full range of properties laid out above do not tend to exist in a single material,

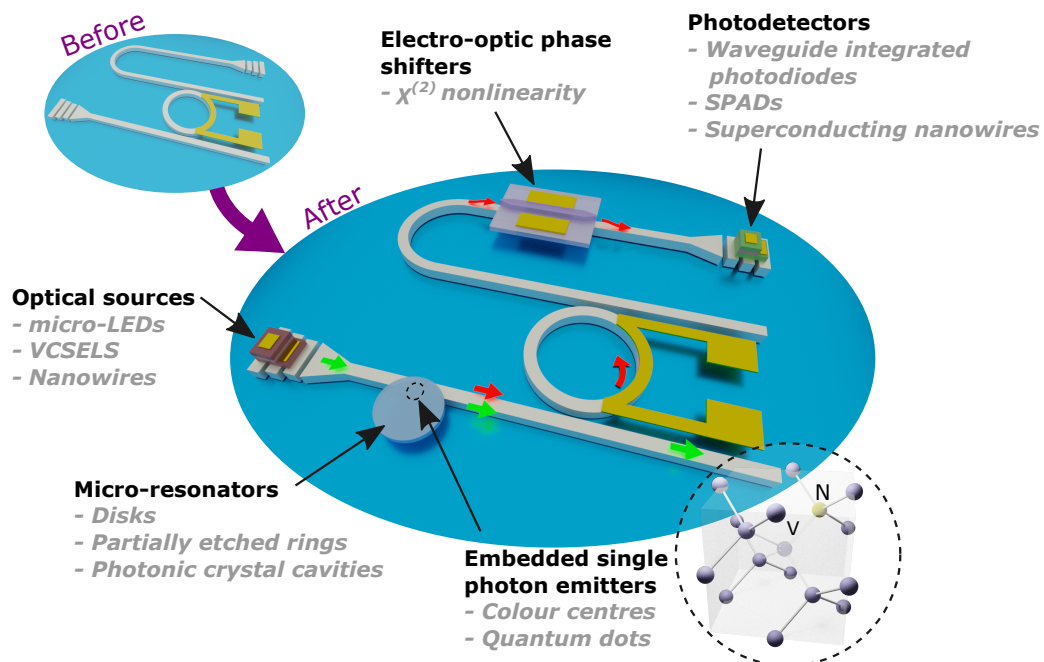


FIGURE 4.1: The hybrid integration of disparate elements, showing multiple pre-fabricated components integrated onto a single PIC.

meaning it is difficult or impossible to integrate the desired functionalities monolithically. Furthermore, a material may possess superlative properties in one area, but significant deficiencies in others which preclude the realisation of high performance devices. Overcoming these limitations is the central motivation for *heterogeneous* and *hybrid* integration - two similar approaches toward having multiple materials performing multiple functions on one host PIC, as in Figure 4.1.

Hybrid integration completely decouples the otherwise incompatible fabrication steps of donor and receiver chips. Here, the *receiver* is the chip (for example a passive photonic circuit) onto which one or multiple *donor* elements/chiplets/dies are to be placed (for example a micro-LED or microdisk resonator). In particular, with micro-transfer printing, devices that would be impossible to fabricate monolithically can be assembled with high accuracy [7], at scale [8], and in close proximity to other printed elements [9]. For example, Figure 4.2(a) shows a section of an array of 64 pre-fabricated GaN micro-LEDs, individually transfer printed onto a CMOS drive chip so that each pixel can be individually controlled [8]. Figure 4.2(b) shows the transfer printing of objects orders of magnitude smaller: nanowire lasers, coupled to polymer waveguides [10]. Figures 4.2(c,d) show waveguide coupled photodetectors fabricated in Ge and GaAs, printed onto Si and SiN waveguides respectively [11, 12]. Finally, Figure 4.2(e) shows a GaAs photonic crystal cavity, containing a strongly coupled InGaAs quantum dot, transfer printed onto a silicon waveguide [13]. Where high alignment accuracy is required (e.g. when targeting critical coupling between a printed resonator and host waveguide), nanoscale alignment protocols exist [7]. In other cases, careful design of donor and receiver chips can allow for alignment-free photonic interconnects between the two [14].

Until recently the terms ‘hybrid’ and ‘heterogeneous’ have been used interchangeably in literature, but there is now an emerging consensus that ‘hybrid’ should be reserved for integration schemes which do not require significant post processing [15]. This includes the integration of fully pre-fabricated LEDs, micro-disk resonators, nanowires, etc. ‘Heterogeneous’ should then refer only to instances where full layers of foreign material are bonded (not heteroepitaxially grown) on the host PIC/substrate, with further fabrication steps required to realise functioning devices.

4.1.2 Diamond integration

Diamond is a perfect example of a material benefiting from hybrid integration. As has been mentioned, many of its intrinsic properties are excellent. Its combination of low phonon density of states and high isotopic purity, makes the diamond lattice especially good at isolating colour centres and their associated electron spins from environmental

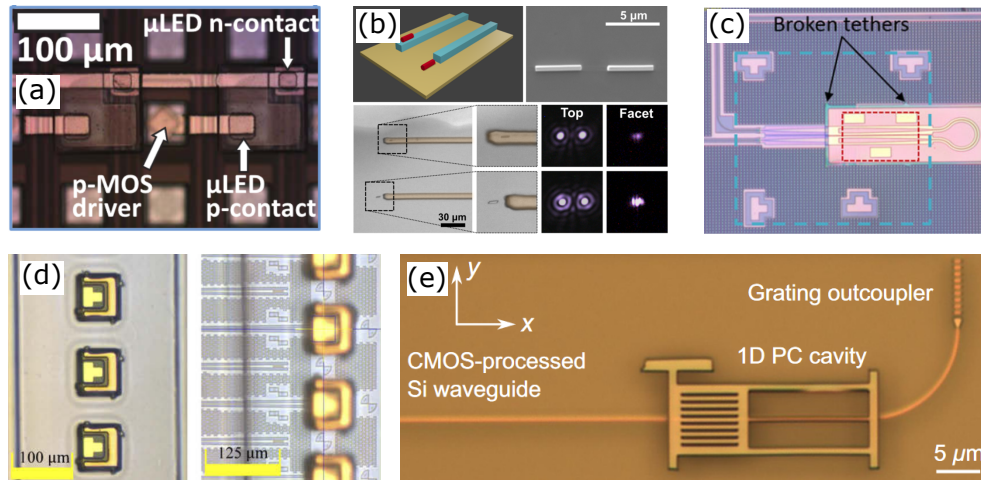


FIGURE 4.2: (a) micro-LEDs transfer printed directly onto CMOS drive chip [8]. (b) Nanowire lasers printed so as to emit into polymer waveguides [10]. (c) A transfer printed germanium photodiode, coupled to a silicon waveguide [11]. (d) A transfer printed GaAs p-i-n photodiode array on SiN waveguides [12]. (e) A transfer printed quantum dot containing GaAs photonic crystal cavity, coupled to a silicon receiver waveguide [13].

(thermal and paramagnetic) decoherence mechanisms. For diamond's NV^- centre, this leads to room temperature coherence times unmatched in the solid state [16], meaning these colour centres are excellent resources in quantum information processing - particularly as an interface between long-lived stationary spin qubits and 'flying' photonic qubits [17–20]. The incredible stiffness of the diamond lattice also gives it an exceptional Raman gain coefficient, useful for integrated Raman lasers [21, 22]. Besides this, its low absorption losses, low thermo-optic coefficient, wide-bandgap, and broad transparency window allow it to operate at high pump powers and over a wide wavelength band, from visible to IR.

However, the fabrication of a PIC designed to utilise these properties in the diamond itself is made difficult by the small area (a few mm^2) of available single crystal diamond platelets - a result of fundamental limitations in diamond homoepitaxy, as outlined in Chapter 1. Furthermore, these platelets are much too thick for single-mode operation at either visible or IR wavelengths; and they are free-standing, meaning there is no low index substrate giving mode confinement in the diamond. Also, diamond's centrosymmetric lattice gives it a vanishing $\chi^{(2)}$ nonlinearity. Contrast this with GaN, which can be heteroepitaxially grown on a low index substrate like sapphire, is available in large area templates, and has respectable $\chi^{(2)}$ and $\chi^{(3)}$ nonlinearities.

Several hybrid and heterogeneous integration methods exist for circumventing the difficulties of diamond micro-fabrication. Notable examples include patterning GaP waveguides out of sheets first bonded atop the diamond [23, 26, 27]. Here the optical mode is

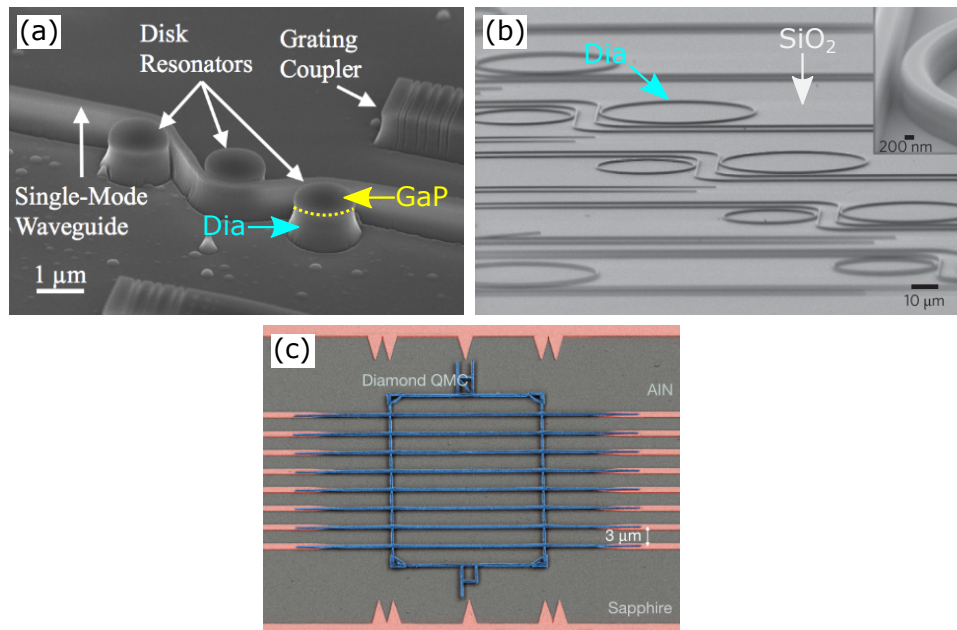


FIGURE 4.3: GaP on diamond disk resonators, with NV centres contained in the diamond pillars beneath the GaP disks [23]. Ultra-high Q-factor (1×10^6) diamond rings patterned on SiO₂ substrates [24]. A suspended array of tapered diamond waveguides, containing single photon source colour centres, pick-and-place integrated onto an AlN PIC [25].

confined and guided in the high-index GaP waveguide layer, and the evanescent fields emanating into the diamond substrate are used to interact with the colour centres therein. Alternatively, to achieve guiding in the diamond itself, it may first be bonded to an SiO₂ substrate, before waveguides are etched into the diamond [21, 22, 24, 28]. Examples of these heterogeneous integration schemes are shown in Figures 4.3 (a) and (b) respectively, and while these works are extremely impressive, they both remain limited by the small area of the available single crystal diamond platelets. Thus, true hybrid integration of pre-fabricated diamond dies/chiplets/resonators onto a separate PIC is likely the best route towards large scale diamond photonic integration. One excellent effort in this direction was carried out by Wan *et al.* [25], whereby diamond micro-chiplets were pick-and-place integrated onto AlN PICs (Figure 4.3 (c)). The diamond chiplets were first pre-screened for germanium vacancy and silicon vacancy colour centres, and after integration into the AlN PIC, a 128 channel defect-free array of waveguide integrated colour centres was created. The large-scale integration of coherent quantum emitters into a PIC is an important milestone in quantum information processing, particularly for multiplexed quantum repeaters [29, 30] and quantum processors [31].

Finally, hybrid donor devices are typically tens to hundreds of microns wide, and $< 10 \mu\text{m}$ thick. Their small size means the weak van der Waals forces are enough to sufficiently bond them to the receiver without a specifically engineered bonding inter-layer. Contrast this with the heterogeneous integration of large area sheets of material,

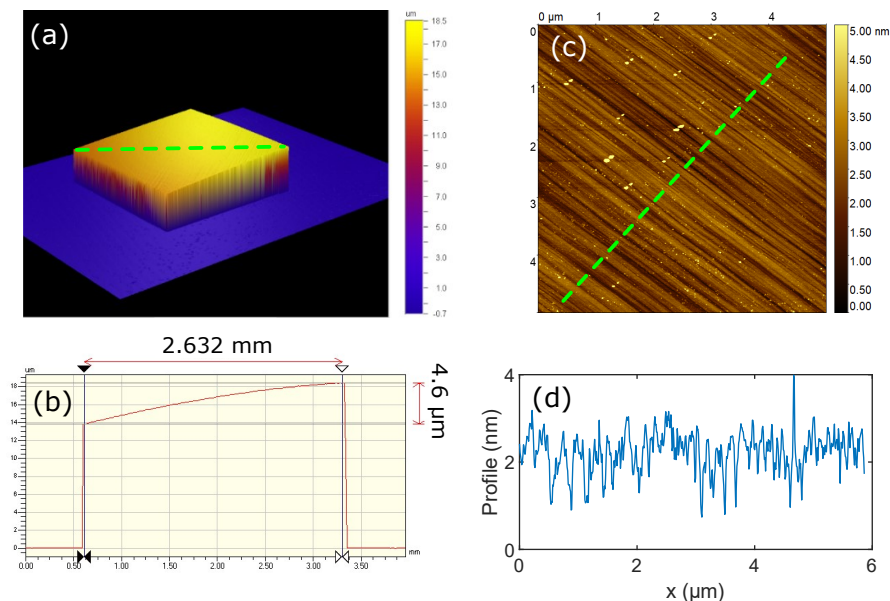


FIGURE 4.4: (a) 3D Optical profile of a whole diamond platelet. (b) Line profile taken across the diagonal, showing a $4.6 \mu\text{m}$ thickness increase over 2.632 mm . (c) AFM scan of an as received diamond platelet, RMS roughness 1.49 nm , showing scarring from the CMP step. (d) A line profile, perpendicular to the scar orientation, showing these scratches are typically around 2 nm deep, and tens of nanometres wide.

which often require careful preparation of each surface to achieve a quality bond [32].

Continuing work carried out in our group [33, 34], in the following we integrate free-standing diamond micro-disk resonators onto a non-native PIC platform (in the present case, GaN on sapphire), using high-accuracy micro-transfer printing with elastomeric micro-stamps. To briefly reiterate the points made in Chapter 1, GaN is an excellent host platform for diamond photonics not only because of the complementary properties laid out above, but also because the two materials have similar refractive indices (which are approximately equal around $630\text{-}640 \text{ nm}$). This greatly eases the optical coupling from one to the other by reducing the index (and phase) mismatch between modes in each material. Interfacial scattering losses, proportional to the square of the index difference, are also minimised [35].

4.2 Diamond disk fabrication

Following the method outlined in Hill *et al.* [34], commercially sourced single crystal electronic-grade CVD diamond was used. These diamonds arrive laser-diced and chemomechanically polished from their as-grown dimension to a $2 \times 2 \text{ mm}^2$ platelet, with thickness of the order of $10 - 30 \mu\text{m}$. Although the polishing step reduces the surface r.m.s. roughness (to around of 1.5 nm), it also imparts a wedged thickness variation across the platelet. These observations, common to all diamonds sourced by this method

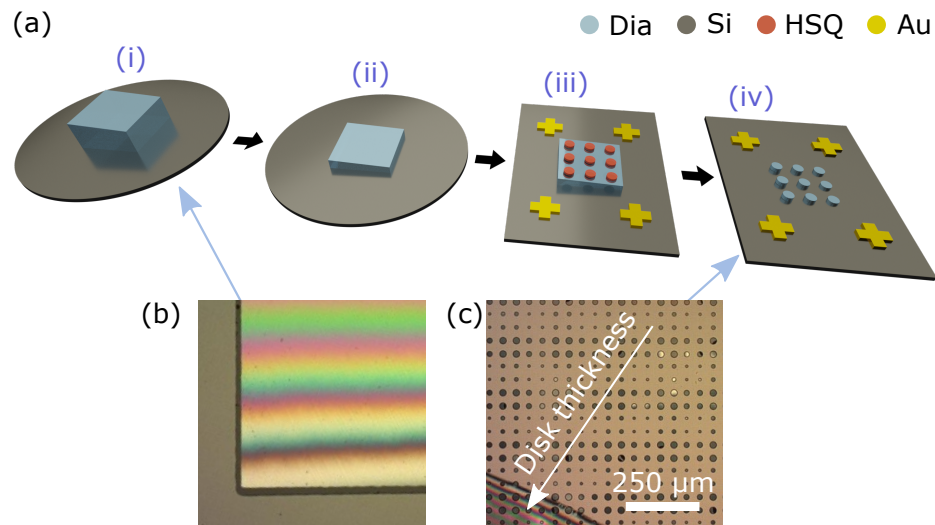


FIGURE 4.5: (a) Diamond disk fabrication steps: (i) After cleaning and initial characterisation, the platelet is placed on a silicon carrier wafer. (ii) ICP etching in Ar/Cl₂ to thin platelet. (iii) Transfer to a second silicon carrier, pre-patterned with alignment markers for electron-beam lithography in HSQ resist. (iv) An Ar/O₂ etch down to the silicon transfers the pattern to the diamond. (b) Optical micrograph of a corner section of an as-received diamond, showing thin-film interference fringes due to the wedged thickness variation of the diamond. (c) Array of fully etched diamond disks, with a portion of partially etched platelet remaining in the bottom corner. Arrow indicates direction of increasing disk thickness.

[36], are shown in Figure 4.4, which details the initial characterisation of a typical diamond as received. Of course, since the ultimate integration method is a pick-and-place one, the wedge in the starting material is not a major issue, and in fact allows us to select disks of certain thickness.

Having visually inspected the diamond quality and characterised its roughness and thickness, the fabrication begins with a 20 minute clean in a piranha mixture of three parts sulphuric acid (H₂SO₄) to one part hydrogen peroxide (H₂O₂). An exothermic reaction which stabilises at 70° C in this ratio, this step thoroughly removes any organic contaminants from the diamond surface. The platelet is thick enough to be handled with tweezers at this stage, but as the diamond is successively thinned, it must be indirectly handled with IPA soaked cleanroom wipes. The diamond was then placed on a silicon ICP carrier wafer for etching in Ar/Cl₂ (Figure 4.5(a-i)). The etch parameters were as follows: Ar 25 sccm, Cl₂ 40 sccm, platen power 100 W, coil power 400 W, pressure 5 mTorr. This chemistry has been shown to smooth the diamond, reducing its surface RMS roughness from 0.53 nm to 0.19 nm after just 10 minutes of etch time [37]. Several 1 hour etches with this chemistry were carried out, and after each the diamond was displaced from the resultant silicon plinth, and its reduced thickness characterised with

white-light vertical scanning interferometry (as in Figure 4.4(a)). This process was repeated until a target thickness of a few microns was achieved at the thickest corner of the diamond. The platelet was transferred to a new silicon carrier piece (Figure 4.5(a-iii)) using an IPA-on-wipe mediated process, and finally direct blowing with an N₂ gun to press the platelet onto the substrate, displacing the liquid between the substrate and the bottom of the diamond. The silicon carrier was pre-patterned with electron-beam alignment markers, so that HSQ could be spun on the entire sample, and disks patterned atop the diamond. Transfer of the pattern to the diamond was achieved with an ICP Ar/O₂ etch, which has previously shown good results for etching diamond with silica hard-masks [38]. The conditions were: Ar 15 sccm, O₂ 40 sccm, platen power 300 W, coil power 800 W, pressure 5 mTorr. This etch has a positive selectivity between diamond and hard-mask of approximately 6:1, with the diamond etching at 150 - 200 nm/min. The high coil power also ensures vertical sidewalls of the disk. The final step, prior to the transfer-printing process detailed below, is to remove the residual hard-mask with a short CHF₃ RIE etch, leaving an array of diamond disks whose thickness increases in the direction of the original platelet wedge (Figure 4.5(c)).

4.3 Hybrid integration by micro-transfer printing

4.3.1 Stamp preparation

Polydimethylsiloxane (PDMS) micro-stamps, patterned with deformable pyramidal features, were used to transfer the diamond disks to the GaN PIC. The stamps are a mixture of pre-polymer base with cross-linking curing agent (Sylgard 184). The ratio of base to agent is an easy way to alter the adhesion properties of a stamp. In addition, changes to the topology of the contacting surface can be targeted during the initial mould fabrication; with pyramidal features [39], rectangular extrusions [40], or basic flat surfaces regularly used [7]. Each have different benefits for printing different donor coupons. To

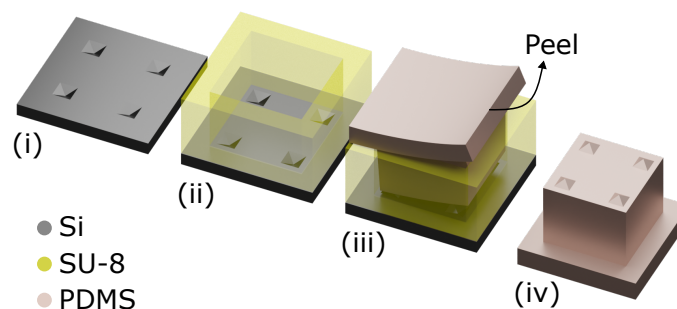


FIGURE 4.6: Simplified process flow for stamp fabrication.

reduce contact between disk and stamp and aid subsequent release, pyramidal features were chosen.

The mould was itself fabricated with traditional photolithography, detailed in Trindade *et al.* [41]. The process begins with PECVD SiO₂ deposition on a piece of Si(100) silicon. Using positive photoresist and a standard photomask, square openings were patterned and etched into the silica in an RIE step. A wet potassium hydroxide (KOH) etch was then used to etch pyramidal features into the silicon through these openings (Figure 4.6(i)), utilising KOH's preferential etching of the Si<100> direction, leaving behind practically unetched Si(111) planes. Indeed, in a 30% concentration of KOH at 80°C, the <111> direction is etched at 0.0063 times the speed of the <100> direction [42]. A thin SiO₂ layer can then be deposited to isolate the exposed rough silicon from the mould. The central body of the stamp was then defined by spinning a thick layer of SU-8 photoresist on the sample (> 100 μm), and opening a large square hole, centred over the four pyramids (Figure 4.6(ii)). The PDMS was poured into the mould, cured, and then removed (Figure 4.6(iii-iv)).

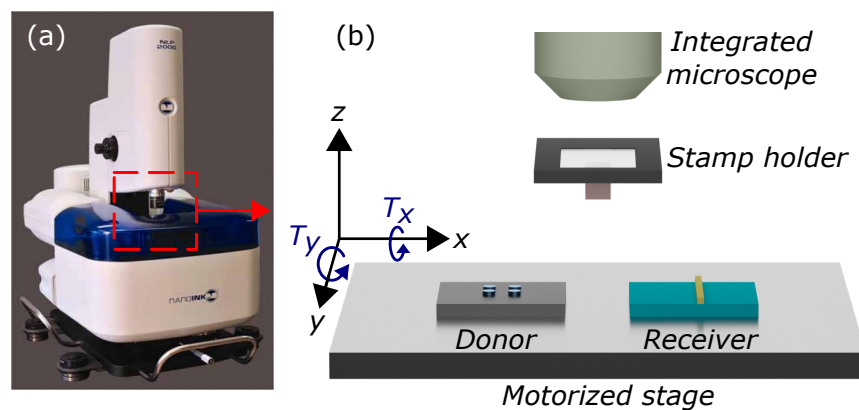


FIGURE 4.7: (a) The NLP 2000 tool used for transfer printing. (b) Detail of the essential components of the tool.

4.3.2 Micro-transfer printing process

The micro-transfer print tool, shown in Figure 4.7(a), is a modified NanoInk Dip Pen Nanolithography system (NLP 2000) [43], where the “pen” has been replaced with a stamp holder consisting of a frame mounted glass slide, onto which the stamp - having been peeled from its mould - is fixed with a border of transparent wax. Since the PDMS is also transparent, we can image the sample through the top of the stamp. The essential components of the transfer-print tool are an integrated microscope column, high accuracy computerized stage, and PC control (Figure 4.7(b)); and the general printing process is shown in Figure 4.8(a). The assembly stage, on which the donor and receiver

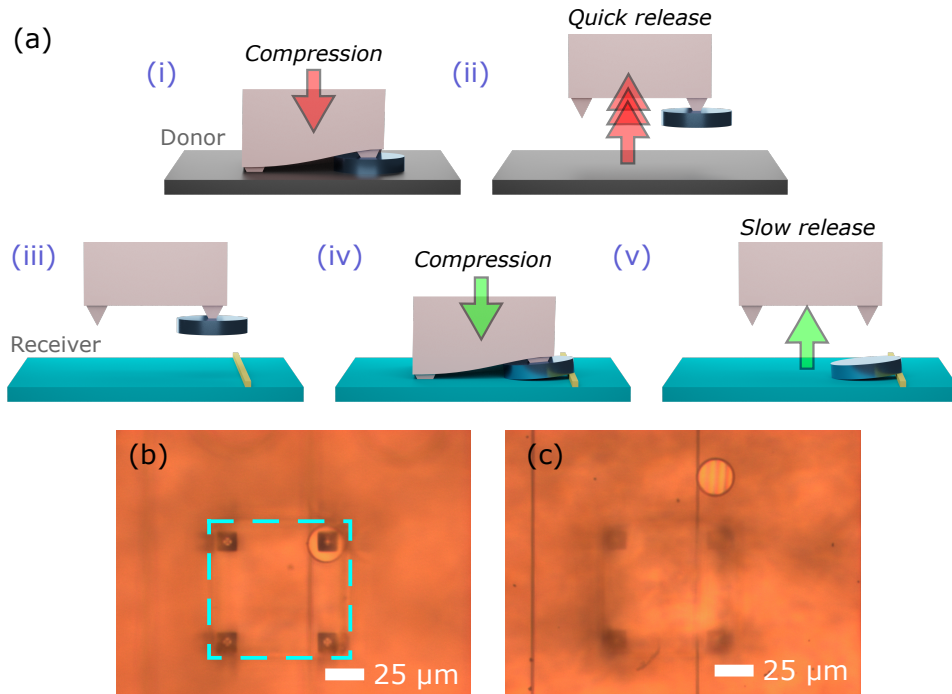


FIGURE 4.8: (a) Micro-transfer printing process: (i) Stamp compressed onto donor disk. (ii) The stage is quickly lowered, releasing the disk. The stamp relaxes, the pyramids decompress, and the stamp-disk contact area is reduced to the pyramid tip. (iii) Alignment over receiver waveguide. (iv) Disk compressed on top of waveguide. (v) Slow retraction of stage, printing the disk onto the waveguide. (b) Image taken during the alignment stage, with the body of the stamp delineated by the dashed square and a waveguide visible beneath. (c) Image taken after a disk is printed and stamp retracted.

chips are mounted side by side, features six axes of motion (x , y , z , two tilt axes T_x , T_y , and rotation about z), and it is the stage that moves while the stamp is fixed in place. Linear translation is piezo driven, with an accuracy of ± 25 nm, while the goniometer driven tilt axes have accuracies of $\pm 0.00025^\circ$.

Retrieval of a target disk is achieved by centring a pyramid over the disk, bringing the stage up slowly, and compressing donor chip into the PDMS so that not only do the pyramids deform, but the “roof” of the PDMS collapses into full contact with the substrate. Then, a rapid release step plucks the diamond from the silicon donor, as in Figure 4.8(a-ii). Free of compressive stress, the PDMS relaxes and the diamond is left with a single PDMS contact area at the tip of the pyramid (Figure 4.8(b)). The magnification and zoom of the microscope is sufficient for easy alignment to waveguides of the order of $1 \mu\text{m}$ wide such as these, though alignment protocols have been developed if greater accuracy is needed [7]. Then, having brought the disk into contact with the GaN, slow retraction of the stamp releases the diamond (Figure 4.8(a-v)), utilising the principle of rate-dependent adhesion of viscous polymers like PDMS - leading to lower energy release rates at smaller separation speeds [44–46].

4.4 Results

4.4.1 Hybrid integration onto GaN PICs

Using the above method, hybrid devices shown in Figure 4.9 were assembled, including diamond disks, diamond membranes, and AlGaAs disks. The diamond membranes were fabricated in a similar fashion to the diamond disks. The AlGaAs disks, whose fabrication is outlined in [47], were patterned in the same way as the disks, but dry-etched in a $\text{SiCl}_4/\text{Ar}/\text{N}_2$ chemistry. Their release was achieved with a selective HF etch of the high aluminium content layer ($\text{Al}_{0.7}\text{Ga}_{0.3}\text{As}$) separating the top $\text{Al}_{0.2}\text{Ga}_{0.8}\text{As}$ layer from the GaAs substrate. Because of its high second and third order nonlinearities, and possibility to integrate optical gain, AlGaAs is another material of great interest for hybrid integration [9, 47].

Figure 4.9(a) shows three diamond components integrated in close proximity on chip. The disks were printed in series (cascaded) with the monolithic GaN on sapphire racetracks, while the membrane was printed on top of the racetrack. In Figure 4.9(b), three (non-resonant) diamond disks of differing radii are shown, and Figure 4.4(c-e) shows diamond and AlGaAs disks printed on two nearby racetrack bus waveguides. The AlGaAs disks were printed with one sitting on top of the waveguide for vertical coupling, and one sitting to the side of the waveguide for edge coupling, showing the control possible even with visual feature defined alignment. Of note in all of the above – and the AlGaAs disks in particular – is the fact that each successive new component was printed onto an area commensurate with the dimensions of the stamp head ($100\ \mu\text{m}$), without disturbing the already printed devices.

The GaN was left air-clad to ensure strong enough optical coupling to printed components as to be seen in transmission measurements. This means disks printed in a vertical coupling geometry, where the underlying waveguide effectively delineates the shortest chord of the disk, are tilted. The SEM image (Figure 4.9(b)) and slowly varying interference patterns visible in the vertically coupled disks (Figures 4.9(d,e)) – which are notably absent in the edge-coupled AlGaAs disk which sits flat on the sapphire – are evidence of this tilt. Without high resolution SEM imaging, it is difficult to fully assess the contact area between diamond and receiver, although the interference pattern in Figure 4.9(d) does seem to transition sharply to a flat area at the top, which would be indicative of full contact with the sapphire. We can reassure ourselves with simple geometric arguments that even in the worst case scenario (where the diamond is completely free of deformation, contacting the substrate only in two points), its large diameter in

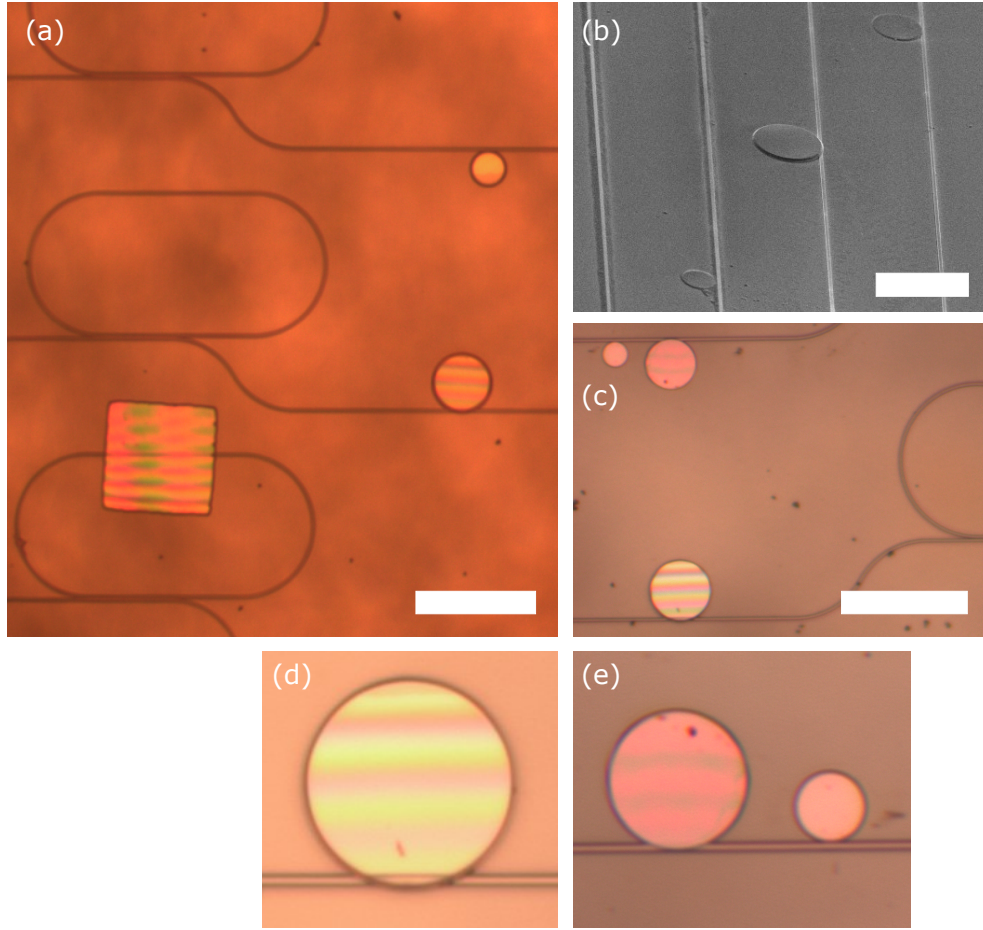


FIGURE 4.9: (a) Optical micrograph of diamond disks and membrane on the air-clad GaN PIC. (b) SEM image of an earlier printing effort of (non-resonant) disks on GaN waveguides. (c) A diamond disk (bottom), and two AlGaAs disks (top), successively printed in an a small area. (d) Close up of the vertically coupled diamond disk (diameter: 25 μm). (e) Close up of the AlGaAs disks, one vertically coupled (diameter: 20 μm), one edge coupled (diameter: 10 μm). All scale bars: 50 μm

comparison to the GaN's height means it is nonetheless in close proximity with the receiver (Figure 4.10). We have the expressions: $\sin(\theta) = 1/c_1$ and $\cos(\theta) = 1/c_2$, and since $c_1 + c_2 = 25$, we have:

$$\theta = \arcsin\left(\frac{1}{25 - c_2}\right) = \arccos\left(\frac{1}{c_2}\right), \quad (4.1)$$

which is solved for c_2 using the trigonometric identity:

$$\sin(\arccos(a)) = \sqrt{1 - a^2}. \quad (4.2)$$

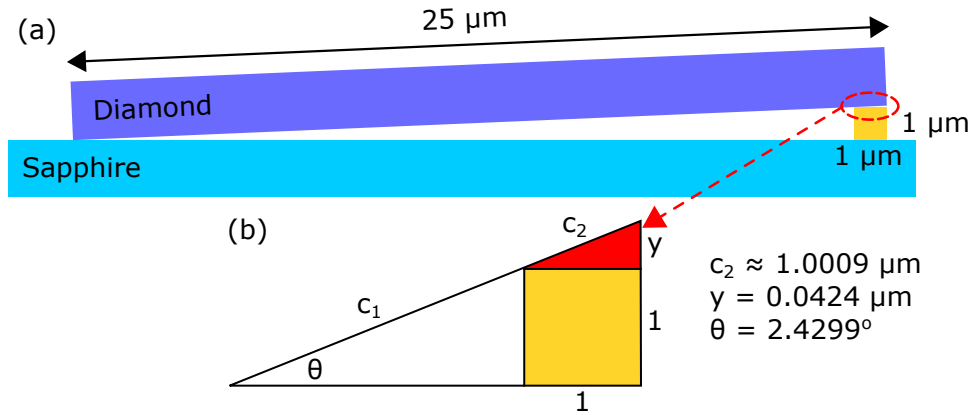


FIGURE 4.10: (a) Rigid diamond disk on a GaN waveguide, angled at 2.4299°. (b) The same, but simplified and at an exaggerated angle to highlight the similar triangles to the left of and above the GaN waveguide.

4.4.2 Disk WGM considerations

Most of the results that follow are for the device shown in Figure 4.9(d) – a diamond disk, thickness: 1.8 μm, diameter: 25 μm, printed in series with a monolithic GaN racetrack. The disk is printed so that the greatest modal overlap and strongest cross-coupling will be to the lowest (radial) order modes, circulating around the inside edge of the disk. Although these modes may suffer the greatest roughness induced scattering losses, their radiation loss is much smaller. For curved open boundary devices the key loss mechanism is tunnelling to outwardly propagating radiative modes, which is directly related to bend loss [48].

To fully appreciate this, it is useful to first highlight the differences between a waveguide based ring/racetrack resonator – in which light is confined by total internal reflection between two dielectric interfaces, with a disk whispering gallery mode (WGM) resonator – in which TIR occurs on one dielectric boundary only. The mode can be said to be confined to an effective radial potential well $(m/nr)^2$ [48], plotted in Figure 4.11(a), with $n = n_{disk}$ for $r < r_{disk}$ and $n = n_{cladding}$ for $r > r_{disk}$. In place of an inner dielectric boundary there is a *caustic radius*, and modes are only bounded in the region between this caustic radius and the outer edge of the disk. Moving toward the centre of the disk, the radial potential approaches infinity (and the phase velocity approaches zero). The caustic radius is the point at which the azimuthal propagation constant exceeds $k_0 n_{disk}$, leading to exponentially decaying evanescent field solutions. Tied to this is an outer radiation boundary, beyond which the azimuthal propagation is smaller than $k_0 n_{cladding}$, leading to unbounded oscillatory field solutions, or radiation modes. The nature of the mode solution in each region is labelled in Figure 4.11(a), including another evanescent region between the disk edge and radiation boundary. This narrow region

where the solution is evanescent separates the circularly propagating bounded modes from the outwardly propagating radiation modes.

Figure 4.11(b-d) plots the field magnitudes, $|E|^2$, for some TM modes of a model WGM resonator. These were calculated from analytical solutions to the Helmholtz wave equation expressed in cylindrical coordinates [48], and neatly demonstrate the importance of radiative loss for modes confined further inside the disk, such as high order radial modes. For such modes, the radiation boundary is pulled towards the edge of the disk so that tunnelling to radiation modes is made easier. Since the azimuthal phase velocity exceeds the speed of light in vacuum beyond this point, the fields then spiral away. Conversely, the maximum distance between disk edge and radiation boundary (and lowest radiation loss) is achieved for the low radial order modes circulating around the disk edge, as in Figure 4.11(b), and it is these modes that are targeted when the disk is printed.

Typically, the main loss mechanisms are WGM radiation loss, and scattering from surface roughness. The former is fundamental and unavoidable, and in the absence of all other

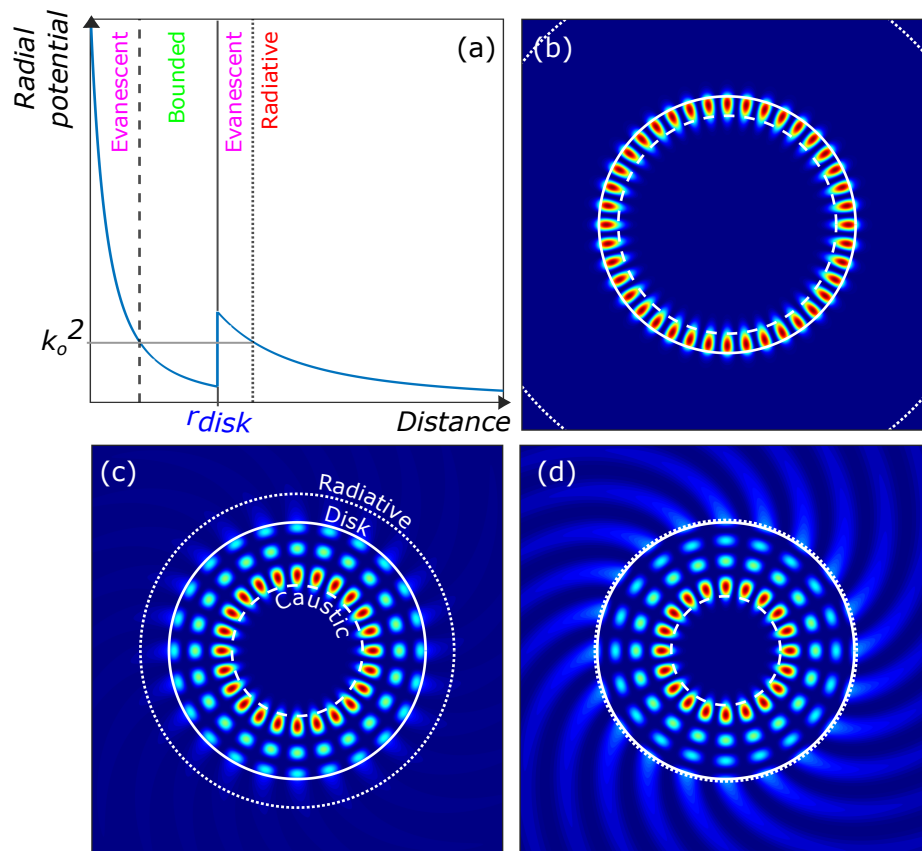


FIGURE 4.11: (a) Example radial potential of a WGM disk resonator. (b) $|E|^2$ for a model WGM resonator (refractive index = 2.4, radius = $2.5 \mu\text{m}$, $\lambda = 1600 \text{ nm}$) of decreasing azimuthal mode number. $m = 20$. (c) $m = 12$. (d) $m = 10$. Solid lines mark the boundary of the disk, dashed lines mark the circle defined by the caustic radius, and dotted lines mark the radiation boundary.

loss is directly related to the intrinsic Q factor of the resonator. The latter can be minimised with optimised fabrication steps, or using devices with larger bend radii, since these devices have better confinement to the disk. If the roughness is found to be too high however, the disk can simply be printed so as to target higher order radial modes, assuming the radiative loss is acceptable. Such control over the coupling, after the disk and receiver are already fabricated, is another benefit of the transfer-print micro-assembly method.

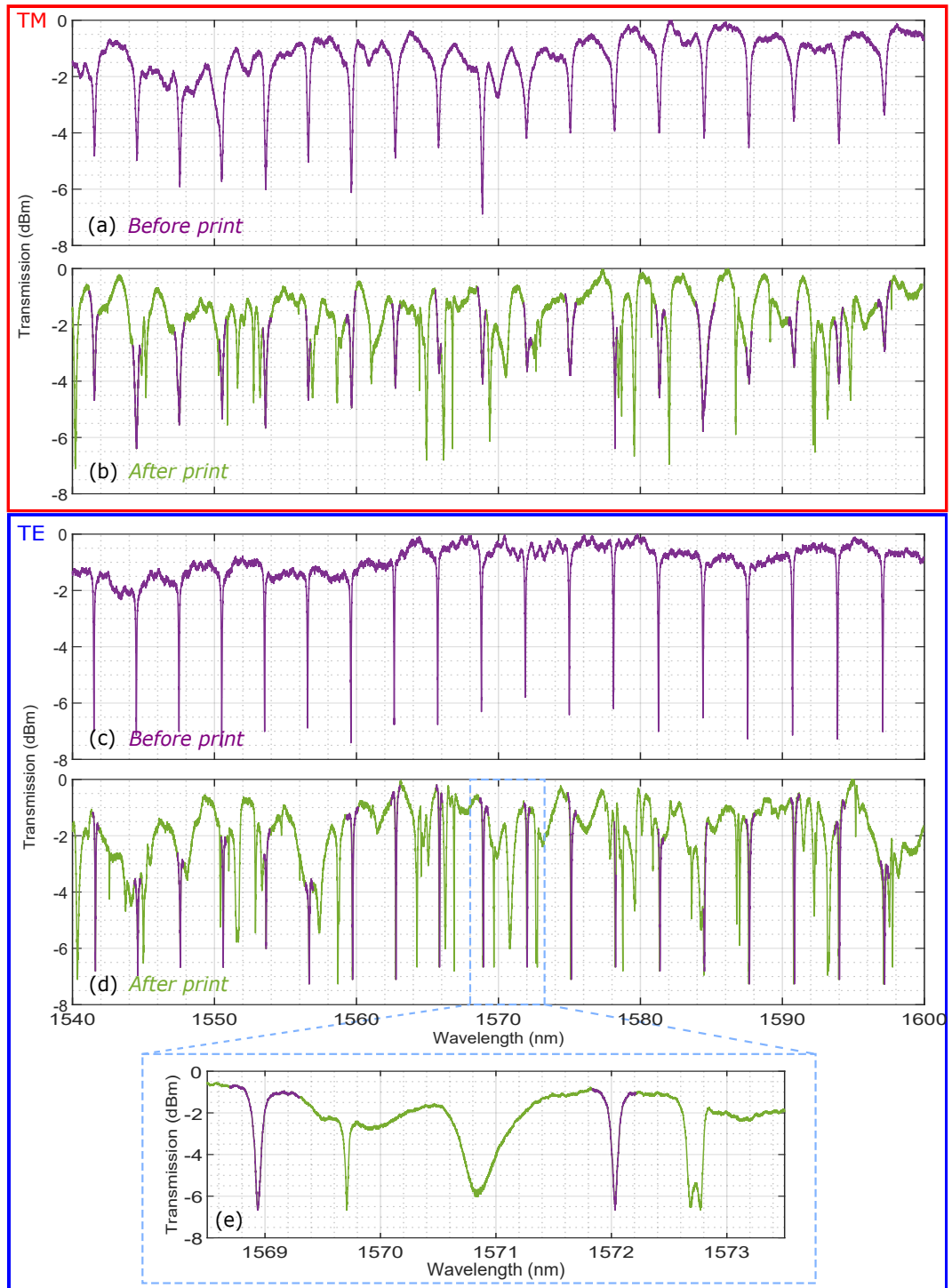


FIGURE 4.12: Transmission spectra, taken before and after printing, for both polarizations.

4.4.3 Transmission measurements

Transmission spectra were taken with the method outlined in previous chapters. They were taken before and after printing the diamond disk, and for both polarisations (Figure 4.12). Before printing, the transmission spectra is that of a simple monolithic GaN racetrack. After printing, there are now two cascaded resonators sharing one bus waveguide (Figure 4.9(c), bottom), measurable in a single transmission sweep. Since the GaN resonances are uniform and are not shifted by the printing process, they can be easily distinguished from the diamond resonances.

Immediately evident in the transmission spectra is the fact that the diamond disk is multimode, with different resonances having drastically different characteristics (Figure 4.12(e)). Deep and shallow resonances, with both sharp and broad linewidths, feature in the spectrum; as well as split resonances where clockwise and counter-clockwise propagating modes are excited. FDE simulations for the cross-sectional field distributions (Figure 4.13) show that this geometry supports high order radial modes (Figure 4.13(e,f)) as well as high order axial modes (Figure 4.13(c,d)). Each of these will be coupled to by the GaN waveguide below with a different cross-coupling coefficient, and each will have differing intrinsic losses based on radiative and scattering contributions. Mode overlap integrals between these diamond modes and the TE/TM

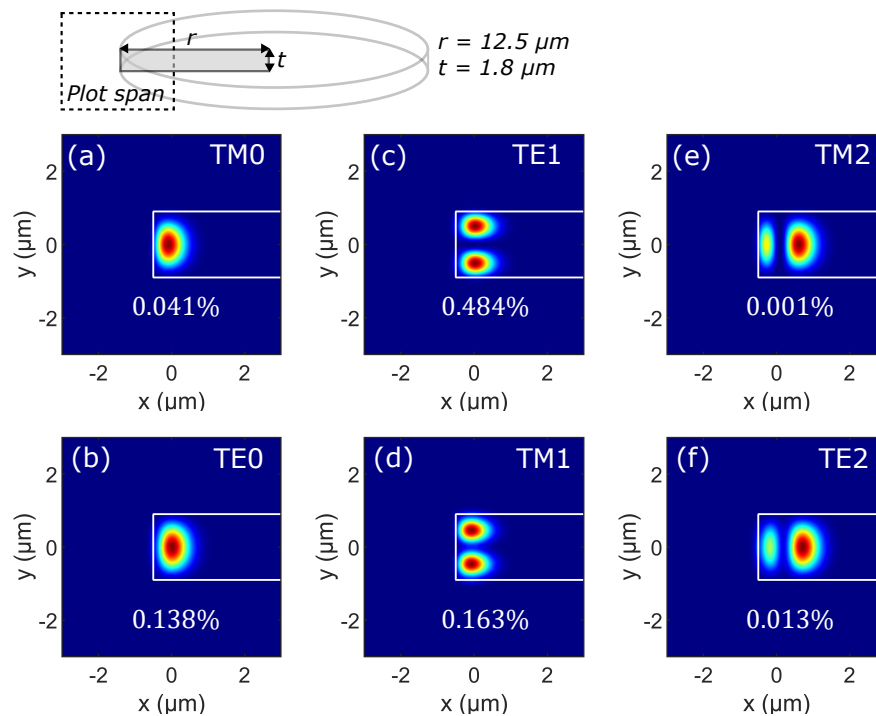


FIGURE 4.13: (a-f) Electric field distributions ($\lambda = 1550 \text{ nm}$) for the first six cross-sectional radial/axial modes of the diamond disk, labelled with their polarisation with respect to the plane of the disk. The modes are also labelled with their respective power coupling percentages from a GaN waveguide (not-pictured) beneath the disk edge.

GaN modes of a waveguide situated in an idealised position beneath the disk edge can be used to give a purely relative analysis of the coupling strengths. We find that the first order axial mode of each polarisation – having a greater overlap with the disk bottom – is coupled to by a far greater fraction than the fundamental modes. The TE₀ mode, having poorer vertical confinement, has a greater coupling fraction than the TM₀ mode. These coupling and loss differences are most likely the origin for the variations of lineshapes in Figures 4.12(b) and 4.12(d).

The resonances are again fitted with the all-pass transmission function detailed in previous chapters, so that their losses, coupling coefficients, and Q factors can be extracted. A selection of such fits is presented in Figure 4.14. Figure 4.14(a) shows the highest loaded Q resonance, equal to 9.05×10^4 , which occurs for TE polarisation. The free parameters in the fit which determine the coupling regime are almost equal, differing only by 0.0029. Thus, this resonance is almost critically coupled. Given its narrow linewidth and the rapidity with which extinction drops off as coupling decreases (recall Chapter 1), we can conclude this resonance is on the under-coupled side of critical coupling. Its distributed loss is then calculated to be 3.60 dB/cm, and its power cross-coupling coefficient is just 0.06%. The characteristics of this resonance in comparison to the others (e.g. Figure 4.14(b,c)) strongly suggests it is likely one of the higher order radial modes, located further inside the disk and away from the bus waveguide underlying the disk edge. Its intrinsic Q factor is calculated to be 9.9×10^4 .

Beyond this, it is difficult to look for definitive trends in the coupling across the spectra because it can't be said with certainty which spatial mode corresponds to which resonance peak. If we instead examine the broadest resonance (Figure 4.14(c)), which

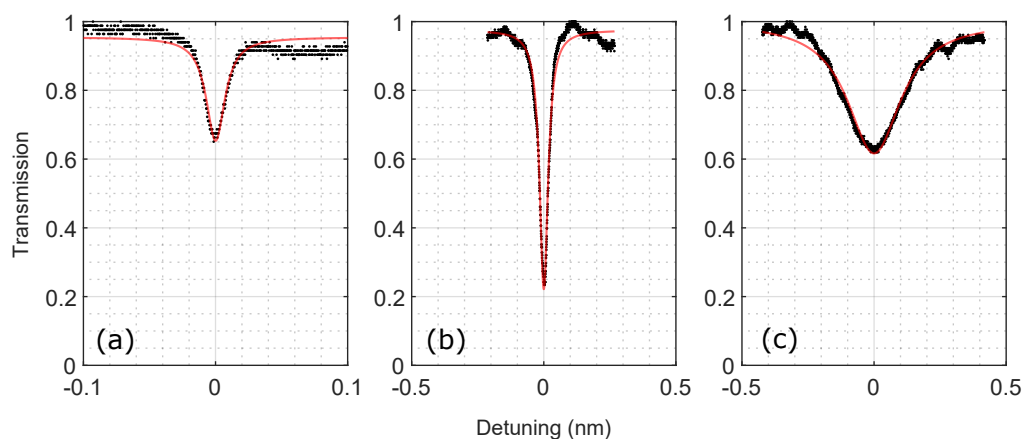


FIGURE 4.14: (a) Highest loaded Q diamond resonance, at $\lambda = 1542.6089$ nm, FWHM = 17.0 pm, $Q = 9.05 \times 10^4$, TE polarisation. (b) Deepest TE resonance, $\lambda = 1566.9018$ nm, FWHM = 38.4 pm, $Q = 4.08 \times 10^4$. (c) Broadest TE resonance, $\lambda = 1591.5548$ nm, FWHM = 227.6309 pm, $Q = 6.99 \times 10^3$.

by similar logic to the above we expect to be over-coupled, we find a loaded (intrinsic) Q factor of 6.99×10^3 (6.90×10^4). A loss of 5.726 dB/cm, and power cross-coupling of 8% is also extracted. (If we treated this resonance as being under-coupled, the distributed loss would take an implausible value of 47.6 dB/cm, further evidence it is over-coupled). Extending this analysis across all fitted diamond peaks, we find an average loss of 4.54 dB/cm; though bear in mind we expect the loss characteristics of the separate modes in Figure 4.13 to be different, which this averaging will ignore. Power cross-coupling fractions can be as low as 0.06% or as high as 8%, depending on which mode is being coupled to. A peak Q_{int} of 1.6×10^5 is recorded, with an average value of 1.02×10^5 over the same set of peaks.

4.5 Conclusion

This chapter highlighted the growing importance of hybrid integration in the field of planar lightwave circuits, and went on to detail why diamond in particular is a material benefiting from hybridisation with other platforms. The fabrication, characterisation, and integration of diamond with a novel GaN platform was presented, showing high Q diamond resonances. Such devices have applications in the resonant Purcell enhancement of colour centre single photon emitters, as well as integrated Raman lasers. In the following chapter, the benefits of having two materials on one chip, probed in one transmission sweep, for photonic thermometry will be elucidated.

It should be noted that after this characterisation effort, the same diamond was reprinted onto the second (thermally tunable) GaN PIC, with results shown in Figure 4.15, with an aim to electronically control the diamond's resonance positions. However, due to an un-optimised fabrication procedure, no coupling to the diamond was observed – largely because of the thickness of silica cladding separating the GaN from the diamond. Nonetheless, the prototyping of a diamond disk in different configurations, without having to go through the full fabrication again, is a final benefit of the hybrid integration procedure.

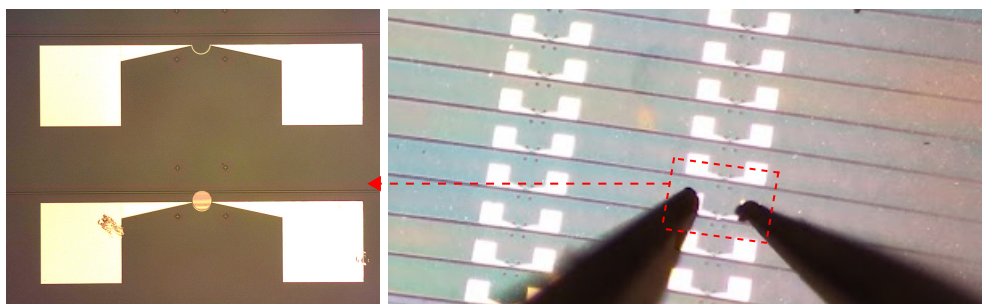


FIGURE 4.15: Diamond disk printed onto thermal tuners.

References

- [1] Lucia Caspani, Chunle Xiong, Benjamin J. Eggleton, Daniele Bajoni, Marco Liscidini, Matteo Galli, Roberto Morandotti, and David J. Moss. Integrated sources of photon quantum states based on nonlinear optics. *Light: Science and Applications*, 6, 2017.
- [2] I. Aharonovich, S. Castelletto, D. A. Simpson, C. H. Su, A. D. Greentree, and S. Prawer. Diamond-based single-photon emitters. *Reports on Progress in Physics*, 74(7):076501, jun 2011.
- [3] Chao Yang Lu and Jian Wei Pan. Quantum-dot single-photon sources for the quantum internet. *Nature Nanotechnology*, 16(12):1294–1296, dec 2021.
- [4] L. Chen, E. Hall, L. Theogarajan, and J. Bowers. Photonic switching for data center applications. *IEEE Photonics Journal*, 3(5):834–844, 2011.
- [5] Chong Zhang and John E. Bowers. Silicon photonic terabit/s network-on-chip for datacenter interconnection. *Optical Fiber Technology*, 44:2–12, aug 2018.
- [6] Cyriel Minkenberg, Nathan Farrington, Aaron Zilkie, David Nelson, Caroline P. Lai, Dan Brunina, Jerry Byrd, Bhaskar Chowdhuri, Nick Kucharewski, Karl Muth, Amit Nagra, German Rodriguez, David Rubi, Thomas Schrans, Pradeep Srinivasan, Yeong Wang, Chiang Yeh, and Andrew Rickman. Reimagining Datacenter Topologies With Integrated Silicon Photonics. *Journal of Optical Communications and Networking*, Vol. 10, Issue 7, pp. B126-B139, 10(7):B126–B139, jul 2018.
- [7] John McPhillimy, Dimitars Jevtics, Benoit J.E. Guilhabert, Charalambos Klitis, Antonio Hurtado, Marc Sorel, and Martin D. Dawson. Automated nanoscale absolute accuracy alignment system for transfer printing. *ACS Applied Nano Materials*, 3(10):10326–10332, oct 2020.
- [8] J. F. C. Carreira, A. D. Griffiths, E. Xie, B. J. E. Guilhabert, J. Herrnsdorf, R. K. Henderson, E. Gu, M. J. Strain, and M. D. Dawson. Direct integration of micro-LEDs and a SPAD detector on a silicon CMOS chip for data communications and time-of-flight ranging. *Optics Express*, 28(5):6909, 2020.
- [9] Dimitars Jevtics, Jack A. Smith, John McPhillimy, Benoit Guilhabert, Paul Hill, Charalambos Klitis, Antonio Hurtado, Marc Sorel, Hark Hoe Tan, Chennupati Jagadish, Martin D. Dawson, and Michael J. Strain. Spatially dense integration of micron-scale devices from multiple materials on a single chip via transfer-printing. *Optical Materials Express*, Vol. 11, Issue 10, pp. 3567-3576, 11(10):3567–3576, oct 2021.
- [10] Dimitars Jevtics, Antonio Hurtado, Benoit Guilhabert, John McPhillimy, Giuseppe Cantarella, Qian Gao, Hark Hoe Tan, Chennupati Jagadish, Michael J. Strain, and Martin D. Dawson. Integration of Semiconductor Nanowire Lasers with Polymeric Waveguide Devices on a Mechanically Flexible Substrate. *Nano Letters*, 17(10):5990–5994, 2017.
- [11] Nan Ye, Grigorij Muliuk, Jing Zhang, Amin Abbasi, Antonio Jose Trindade, Chris Bower, Dries Van Thourhout, and Gunther Roelkens. Transfer Print Integration of Waveguide-Coupled Germanium Photodiodes onto Passive Silicon Photonic ICs. *Journal of Lightwave Technology*, 36(5):1249–1254, 2018.
- [12] Jeroen Goyvaerts, Sulakshna Kumari, Sarah Uvin, Jing Zhang, Roel Baets, Agnieszka Gocalinska, Emanuele Pelucchi, Brian Corbett, and Gunther Roelkens. Transfer-print integration of GaAs p-i-n photodiodes onto silicon nitride photonic integrated circuits. *2020 IEEE Photonics Conference, IPC 2020 - Proceedings*, 28(14):21275–21285, 2020.

- [13] A. Osada, Y. Ota, R. Katsumi, M. Kakuda, S. Iwamoto, and Y. Arakawa. Strongly coupled single-quantum-dot-cavity system integrated on a CMOS-processed silicon photonic chip. *Physical Review Applied*, 11(2):024071, feb 2019.
- [14] Saumil Bandyopadhyay and Dirk Englund. Alignment-free photonic interconnects. *Arxiv*, sep 2021.
- [15] Paramjeet Kaur, Andreas Boes, Guanghui Ren, Thach G. Nguyen, Gunther Roelkens, and Arnan Mitchell. Hybrid and heterogeneous photonic integration. *APL Photonics*, 6(6), 2021.
- [16] S. Bogdanov, M. Y. Shalaginov, A. Boltasseva, and V. M. Shalaev. Material platforms for integrated quantum photonics. *Optical Materials Express*, Vol. 7, Issue 1, pp. 111-132, 7(1):111–132, jan 2017.
- [17] B. Hensen, H. Bernien, A. E. Dréau, A. Reiserer, N. Kalb, M. S. Blok, J. Ruitenberg, R. F. L. Vermeulen, R. N. Schouten, C. Abellán, W. Amaya, V. Pruneri, M. W. Mitchell, M. Markham, D. J. Twitchen, D. Elkouss, S. Wehner, T. H. Taminau, and R. Hanson. Experimental loophole-free violation of a Bell inequality using entangled electron spins separated by 1.3 km. *Arxiv*, aug 2015.
- [18] W. B. Gao, A. Imamoglu, H. Bernien, and R. Hanson. Coherent manipulation, measurement and entanglement of individual solid-state spins using optical fields. *Nature Photonics 2015 9:6*, 9(6):363–373, may 2015.
- [19] Kae Nemoto, Michael Trupke, Simon J. Devitt, Burkhard Scharfenberger, Kathrin Buczak, Jörg Schmiedmayer, and William J. Munro. Photonic Quantum Networks formed from NV centers. *Scientific Reports 2016 6:1*, 6(1):1–12, may 2016.
- [20] Anna Tchebotareva, Sophie L.N. Hermans, Peter C. Humphreys, Dirk Voigt, Peter J. Harmsma, Lun K. Cheng, Ad L. Verlaan, Niels Dijkhuizen, Wim De Jong, Anaïs Dréau, and Ronald Hanson. Entanglement between a Diamond Spin Qubit and a Photonic Time-Bin Qubit at Telecom Wavelength. *Physical Review Letters*, 123(6):063601, aug 2019.
- [21] Birgit J. M. Hausmann, Irfan Bulu, Marko Lončar, Michael J. Burek, Pawel Latawiec, and Vivek Venkataraman. On-chip diamond Raman laser. *Optica*, Vol. 2, Issue 11, pp. 924-928, 2(11):924–928, nov 2015.
- [22] Pawel Latawiec, Vivek Venkataraman, Amirhassan Shams-Ansari, Matthew Markham, and Marko Lončar. Integrated diamond Raman laser pumped in the near-visible. *Optics Letters*, Vol. 43, Issue 2, pp. 318-321, 43(2):318–321, jan 2018.
- [23] Michael Gould, Emma R. Schmidgall, Shabnam Dadgostar, Fariba Hatami, and Kai Mei C Fu. Efficient Extraction of Zero-Phonon-Line Photons from Single Nitrogen-Vacancy Centers in an Integrated GaP-on-Diamond Platform. *Physical Review Applied*, 6(1):1–8, 2016.
- [24] B. J.M. Hausmann, I. Bulu, V. Venkataraman, P. Deotare, and M. Loncar. Diamond nonlinear photonics. *Nature Photonics 2014 8:5*, 8(5):369–374, apr 2014.
- [25] Noel H. Wan, Tsung Ju Lu, Kevin C. Chen, Michael P. Walsh, Matthew E. Trusheim, Lorenzo De Santis, Eric A. Bersin, Isaac B. Harris, Sara L. Mouradian, Ian R. Christen, Edward S. Bielejec, and Dirk Englund. Large-scale integration of artificial atoms in hybrid photonic circuits. *Nature*, 583(7815):226–231, 2020.
- [26] Nicole Thomas, Russell J. Barbour, Yuncheng Song, Minjoo Larry Lee, and Kai-Mei C. Fu. Waveguide-integrated single-crystalline GaP resonators on diamond. *Optics Express*, 22(11):13555, may 2014.

- [27] Michael Gould, Srivatsa Chakravarthi, Ian R. Christen, Nicole Thomas, Shabnam Dadgostar, Yuncheng Song, Minjoo Larry Lee, Fariba Hatami, and Kai-Mei C. Fu. Large-scale GaP-on-diamond integrated photonics platform for NV center-based quantum information. *Journal of the Optical Society of America B*, 33(3):B35, 2016.
- [28] Birgit J.M. Hausmann, Brendan Shields, Qimin Quan, Patrick Maletinsky, Murray McCutcheon, Jennifer T. Choy, Tom M. Babinec, Alexander Kubanek, Amir Yacoby, Mikhail D. Lukin, and Marko Lončar. Integrated diamond networks for quantum nanophotonics. *Nano Letters*, 12(3):1578–1582, mar 2012.
- [29] Sreraman Muralidharan, Linshu Li, Jungsang Kim, Norbert Lütkenhaus, Mikhail D. Lukin, and Liang Jiang. Optimal architectures for long distance quantum communication. *Scientific Reports 2016 6:1*, 6(1):1–10, feb 2016.
- [30] Nicolò Lo Piparo, William J. Munro, and Kae Nemoto. Quantum multiplexing. *Physical Review A*, 99(2):022337, feb 2019.
- [31] C. Monroe, R. Raussendorf, A. Ruthven, K. R. Brown, P. Maunz, L. M. Duan, and J. Kim. Large-scale modular quantum-computer architecture with atomic memory and photonic interconnects. *Physical Review A - Atomic, Molecular, and Optical Physics*, 89(2):022317, feb 2014.
- [32] Lin Chang, Martin H. P. Pfeiffer, Nicolas Volet, Michael Zervas, Jon D. Peters, Costanza L. Manganelli, Eric J. Stanton, Yifei Li, Tobias J. Kippenberg, and John E. Bowers. Heterogeneous integration of lithium niobate and silicon nitride waveguides for wafer-scale photonic integrated circuits on silicon. *Optics Letters*, 42(4):803, feb 2017.
- [33] Paul Hill, Erdan Gu, Martin D. Dawson, and Michael J. Strain. Thin film diamond membranes bonded on-demand with SOI ring resonators. *Diamond and Related Materials*, 88:215–221, sep 2018.
- [34] Paul Hill, Charalambos Klitis, Benoit Guilhabert, Marc Sorel, Erdan Gu, Martin D. Dawson, and Michael J. Strain. All-optical tuning of a diamond micro-disk resonator on silicon. *Photonics Research, Vol. 8, Issue 3, pp. 318-324*, 8(3):318–324, mar 2020.
- [35] F P Payne and J. P.R. Lacey. A theoretical analysis of scattering loss from planar optical waveguides. *Optical and Quantum Electronics*, 26(10):977–986, 1994.
- [36] Ye Tao and Christian Degen. Facile Fabrication of Single-Crystal-Diamond Nanostructures with Ultrahigh Aspect Ratio. *Advanced Materials*, 25(29):3962–3967, aug 2013.
- [37] C. L. Lee, E. Gu, M. D. Dawson, I. Friel, and G. A. Scarsbrook. Etching and micro-optics fabrication in diamond using chlorine-based inductively-coupled plasma. *Diamond and Related Materials*, 17(7-10):1292–1296, jul 2008.
- [38] C. L. Lee, M. D. Dawson, and E. Gu. Diamond double-sided micro-lenses and reflection gratings. *Optical Materials*, 32(9):1123–1129, jul 2010.
- [39] Seok Kim, Jian Wu, Andrew Carlson, Sung Hun Jin, Anton Kovalsky, Paul Glass, Zhuangjian Liu, Numair Ahmed, Steven L. Elgan, Weiqiu Chen, Placid M. Ferreira, Metin Sitti, Yonggang Huang, and John A. Rogers. Microstructured elastomeric surfaces with reversible adhesion and examples of their use in deterministic assembly by transfer printing. *Proceedings of the National Academy of Sciences of the United States of America*, 107(40):17095–17100, oct 2010.

- [40] Benoit Guilhabert, Antonio Hurtado, Dimitars Jevtics, Qian Gao, Hark Hoe Tan, Chennupati Jagadish, and Martin D. Dawson. Transfer Printing of Semiconductor Nanowires with Lasing Emission for Controllable Nanophotonic Device Fabrication. *ACS Nano*, 10(4):3951–3958, apr 2016.
- [41] A. J. Trindade, B. Guilhabert, D. Massoubre, D. Zhu, N. Laurand, E. Gu, I. M. Watson, C. J. Humphreys, and M. D. Dawson. Nanoscale-accuracy transfer printing of ultra-thin AlInGaN light-emitting diodes onto mechanically flexible substrates. *Applied Physics Letters*, 103(25):253302, dec 2013.
- [42] Kazuo Sato, Mitsuhiro Shikida, Yoshihiro Matsushima, Takashi Yamashiro, Kazuo Asaumi, Yasuroh Iriye, and Masaharu Yamamoto. Characterization of orientation-dependent etching properties of single-crystal silicon: effects of KOH concentration. *Sensors and Actuators A: Physical*, 64(1):87–93, jan 1998.
- [43] John McPhillimy, Benoit Guilhabert, Charalambos Klitis, Martin D. Dawson, Marc Sorel, and Michael J. Strain. High accuracy transfer printing of single-mode membrane silicon photonic devices. *Optics Express*, 26(13):16679, jun 2018.
- [44] Matthew A. Meitl, Zheng Tao Zhu, Vipin Kumar, Keon Jae Lee, Xue Feng, Yonggang Y. Huang, Ilesanmi Adesida, Ralph G. Nuzzo, and John A. Rogers. Transfer printing by kinetic control of adhesion to an elastomeric stamp. *Nature Materials 2006 5:1*, 5(1):33–38, dec 2005.
- [45] Xue Feng, Matthew A. Meitl, Audrey M. Bowen, Yonggang Huang, Ralph G. Nuzzo, and John A. Rogers. Competing Fracture in Kinetically Controlled Transfer Printing. *Langmuir*, 23(25):12555–12560, dec 2007.
- [46] Andrew Carlson, Audrey M. Bowen, Yonggang Huang, Ralph G. Nuzzo, and John A. Rogers. Transfer Printing Techniques for Materials Assembly and Micro/Nanodevice Fabrication. *Advanced Materials*, 24(39):5284–5318, oct 2012.
- [47] John McPhillimy, Stuart May, Charalambos Klitis, Benoit Guilhabert, Martin D. Dawson, Marc Sorel, and Michael J. Strain. Transfer printing of AlGaAs-on-SOI microdisk resonators for selective mode coupling and low-power nonlinear processes. *Optics Letters*, 45(4):881, feb 2020.
- [48] John Heebner, Rohit Grover, and Tarek Ibrahim. Optical microresonator theory. *Springer Series in Optical Sciences*, 138:71–103, 2008.

Chapter 5

High precision integrated photonic thermometry utilising a hybrid diamond on GaN chip

This final results chapter presents high precision, dual material, photonic thermometry, enabled by the hybrid integration of a high Q diamond disk resonator with a monolithic GaN on sapphire racetrack circuit. While the previous chapters detailed the fabrication and characterisation of such a photonic platform, this chapter advances an application of the hybrid device, with favourable results in comparison to similar silicon devices.

5.1 Introduction

Photonic thermometry utilises light-matter interactions (usually those causing changes in the transmission characteristics) to measure temperature shifts. The process is similar to the thermally tuned GaN racetracks presented previously, but instead of directly controlling the resonance position with the temperature of a nearby heating element, we allow environmental changes to shift the resonance position by an amount proportional to the temperature change – thus allowing for photonic measurements of temperature.

A metrology application such as this can be viewed in the broader context of the increasingly widespread implementation of PICs in several diverse sensing and measurement fields, such as gas detection [1], bio-sensing [2], and optical coherence tomography (OCT) [3]. In each, the often cited benefits when compared to their fibre-based or free-space equivalents are firstly dramatic reductions in size because of the small form factor of photonic devices. Utilising optical waveguides also increases mechanical stability when

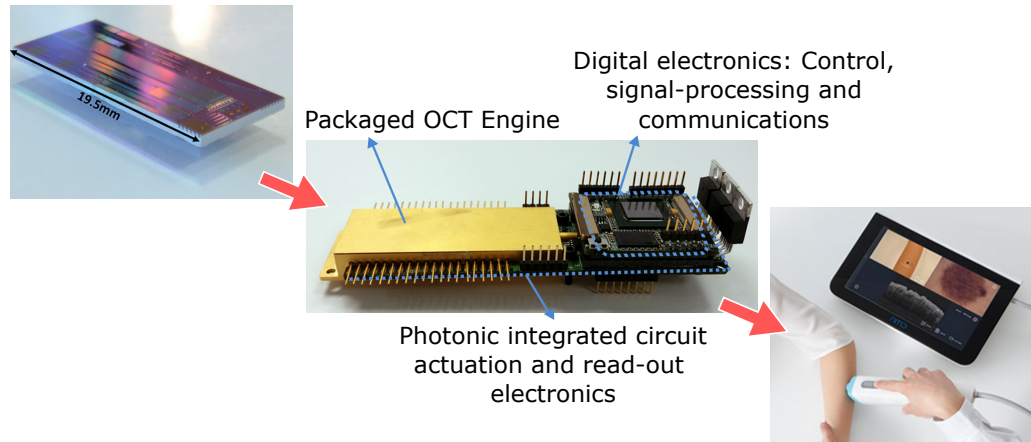


FIGURE 5.1: An example of high-level PIC implementation: a handheld multi-functional skin imaging device, capable of both OCT and epiluminescence microscopy, based on a $19.5 \times 1.1 \text{ mm}^2$ SOI PIC. Adapted from [4].

compared to bulk optics which often require realignment, and the tight optical confinement they offer often leads to improved sensitivity. A highly illustrative example of all of these benefits is shown in Figure 5.1, which demonstrates how an SOI PIC – with appropriate control electronics and layers of integration and packaging – can form the basis of a multi-functional, lightweight, point-of care skin imaging device, replacing expensive and bulky OCT machines [4].

Besides compatibility with the operating wavelengths, the above example utilises silicon because it is the most mature of all materials used for PICs. Many commercial silicon foundries offer application-focused researchers a relatively inexpensive and direct route towards realising their own PIC designs. However, depending on the application, silicon may not always be the most appropriate choice of material.

5.1.1 The general case for chip-scale photonic thermometry

In 1821, Humphry Davy reported to the Royal Society his discovery that the conductivity of copper wire decreased in proportion to its temperature [5]. However, lacking both copper of sufficient purity and even a universally accepted definition of electrical resistance, much of the work on this subject was carried out many years later. It wasn't until 1863 that the Ohm (then “ohmad”) was first adopted as the unit of resistance, following a report to the British Association from a committee comprising Lord Kelvin, J.C. Maxwell, J.P. Joule, et al. [6]. Around the same time, wishing to probe the temperature-dependent degradation of coils of undersea telegraph cables, C.W. Siemens invented the platinum resistance thermometer (PRT) [7], and after some initial problems with contamination and strain induced resistance shifts were solved by H.L. Callendar [8], PRT usage became widespread.

Ubiquitous and inexpensive, standard PRTs and similar resistance based methods have remained largely unchanged since. Nowadays their temperature uncertainties are regularly as low as 50 mK. Recently however, there has been a great deal of work updating this century-old technology with either photonic or optomechanical equivalents. Although less costly, PRTs remain vulnerable to degradation, particularly in harsh environments where chemical contamination, thermal stress, mechanical shock, radiation exposure, or humidity variations can occur ¹. Their robustness is further hampered by their sensitivity to electromagnetic interference. All of these factors incur a resistance drift over time which affects their measurement accuracy and which must be periodically recalibrated for [10]. The recalibration procedure can itself be costly and time-consuming if the PRT is mounted in an inaccessible location. A photonic thermometer by comparison provides a far more stable platform, largely immune to the above hindrances, allowing for more sensitive measurements of temperature [11–15]. Additionally, their low weight and small form factor allows for the multiplexing of several devices to enhance sensitivity further.

For these reasons a photonic thermometer has immediate applications across a number of industries [16], such as manufacturing [17], physiological monitoring [18], and environmental engineering controls [19]; particularly in harsh environments [20, 21]. Besides these, the stability, sensitivity, and micron length scales of these devices also opens up applications in more fundamental physics [15, 22–24]. In particular, as part of the SI units redefinition enacted in 2019, the Kelvin was redefined such that the Boltzmann constant would be exactly 1.380649×10^{-23} J/K [25]. However, self-calibrating primary thermometers based on accurate determinations of Boltzmann’s constant need to operate at cryogenic temperatures for sub-millikelvin resolution, with electrical contacts attached to the sample [26, 27]. Conversely, photonic and optomechanical thermal sensors operating at room temperature are more portable, and do not suffer the limitations inherent with making direct electrical contact with the sample. Therefore in the near term, such sensors could first be used as secondary thermometers (calibrated against bulky lab-based primary thermometers), which can then be easily disseminated, maintaining their calibration. There is also future potential for sufficiently precise photonic devices to themselves be portable indirect primary thermometers, supplanting the need for cryogenics and invasive electrical contacts entirely.

¹A spectacular example of PRT failure once lead to the only example of an in-flight main engine shut-down during a space shuttle flight in 1985. Repeated heating and cooling cycles rendered multiple PRTs unreliable, and their defective readings were suggestive of critical overheating [9].

5.1.2 Device operation

The temperature-dependant resonance wavelength of an ring/racetrack/disk resonator is given by:

$$\lambda_m(T) = \frac{n_{eff}(\lambda, T)L(T)}{m}, \quad (5.1)$$

where n_{eff} is the modal effective index, L is the cavity length, and m is the integer mode number – or number of wavelengths fitting into the resonator optical path length. The effective index is a function of temperature and wavelength through the thermo-optic coefficient and dispersion respectively. The cavity length is only temperature dependent through the thermal-expansion of the cavity itself. A change in temperature, ΔT will induce a wavelength shift, $\Delta\lambda_m$, according to [11]:

$$\Delta\lambda_m = \left(\frac{\left(\frac{\partial n_{eff}}{\partial T} \right) + n_{eff} \left(\frac{\partial L}{\partial T} \right) \left(\frac{1}{L} \right)}{n_g} \right) \lambda_m \Delta T. \quad (5.2)$$

As mentioned in the discussion of thermo-optic resonance tuning in Chapter 3, the cavity length is usually considered constant in these analyses, since for most reasonable temperature shifts its effect on the resonance wavelength is much weaker than the thermo-optic coefficient, $\partial n_{eff}/\partial T$. Setting $\partial L/\partial T = 0$, we recover the same expression as was used previously in Chapter 4 to describe the temperature induced wavelength shift:

$$\Delta\lambda_m = \frac{1}{n_g} \left(\frac{\partial n_{eff}}{\partial T} \right) \lambda_m \Delta T. \quad (5.3)$$

Thus, a temperature shift measurement amounts to the accurate determination of the resonance wavelength shift. The above equation can also be used to determine the material's thermo-optic coefficient $\partial n_{eff}/\partial T$, once the group index, n_g , has been calculated. The group index, which includes the waveguide's dispersion, can be easily extracted from the transmission spectrum FSR with:

$$n_g = \frac{\lambda^2}{FSR \times L}, \quad (5.4)$$

or, in the case of multimode disk resonances where clear FSRs are difficult to extract, it can be estimated through the usual resonance fits and the following [28]:

$$n_g = \frac{(1 - ra)\lambda^2}{\pi L(ra)^{1/2}} FWHM^{-1}, \quad (5.5)$$

where r and a have their usual meanings: power self-coupling and round trip loss fraction respectively.

5.1.3 Material considerations

Much of the work on integrated photonic thermometry has utilised silicon microresonators – both microrings [11, 13, 14] and photonic crystal cavities [12]. Silicon’s relatively large thermo-optic coefficient affords these devices large sensitivities – that is, large wavelength shifts for a given temperature shift. However, this also exacerbates absorption based self-heating of the microresonator, which is already a serious impediment to long-term accuracy and precision. There are two distinct absorption pathways for silicon. These are: two-photon absorption, stemming from silicon’s narrow bandgap; and surface state absorption, facilitated by intra-gap surface states. Both of these absorption pathways have been shown to lead to self-heating [11, 29].

Naturally, it is undesirable for a temperature sensor to self-heat, especially if the relationship between optical intensity and temperature is complex and nonlinear [30]. Ideally, the resonance wavelength should be a function of the target environmental temperature only, and not also of optical intensity. Absorption based self-heating thus reduces both accuracy and precision in single-shot and continuous measurements of resonance wavelength. Here accuracy is understood to mean the closeness of a measured value to the true value, while precision refers to the closeness of measurements to each other.

5.1.4 Hybrid wide-bandgap photonic thermometry

It is beneficial to move towards wide-bandgap materials like diamond and GaN, whose respective bandgaps of 5.4 eV and 3.4 eV are much greater than silicon’s 1.1 eV. These alternative material platforms not only operate over broader transparency windows, but their larger bandgaps lead to greatly reduced absorption based-self heating. Furthermore, since the refractive index of diamond and GaN is smaller than that of silicon, single-mode devices tend to have larger mode volumes for a given wavelength. This

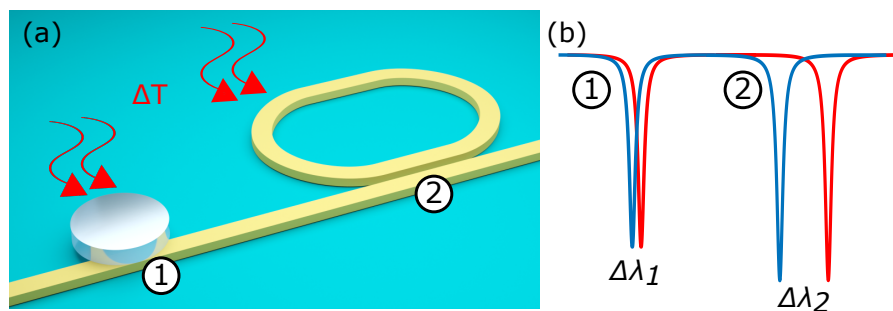


FIGURE 5.2: (a) Schematic of a compact, dual material photonic thermometer. (b) Resulting thermal red-shifting of their cascaded resonances, where resonator 2 has the greater thermo-optic coefficient, leading to $\Delta\lambda_2 > \Delta\lambda_1$

fact, in combination with their smaller thermo-optic response, helps to relieve thermal bistability of resonant modes, which has been observed in some silicon devices [12, 31].

It has been shown in the previous chapter that with high-accuracy micro-transfer printing it is possible to cascade diamond and GaN resonators on a single waveguide bus channel, as in Figure 5.2 (a). Having two materials which can be probed effectively simultaneously and are integrated in such a compact footprint provides further benefits for high precision photonic thermometry. Their thermo-optic coefficients are of course independent, leading to different red-shifts of their respective resonance wavelengths in the cascaded transmission spectrum (Figure 5.2 (b)), each according to Equation 5.3. The magnitude of their shifts will be linearly correlated, and any environmental changes that lead to variations in either material's wavelength response will be highlighted in deviations from this linear correlation. This is an intrinsic benefit of using multiple materials in this way. Furthermore, the cascaded spectrum will feature several temperature-dependent resonant lineshapes, and by tracking multiple shifts of multiple peaks across the two materials, the uncertainty in determining ΔT can be reduced.

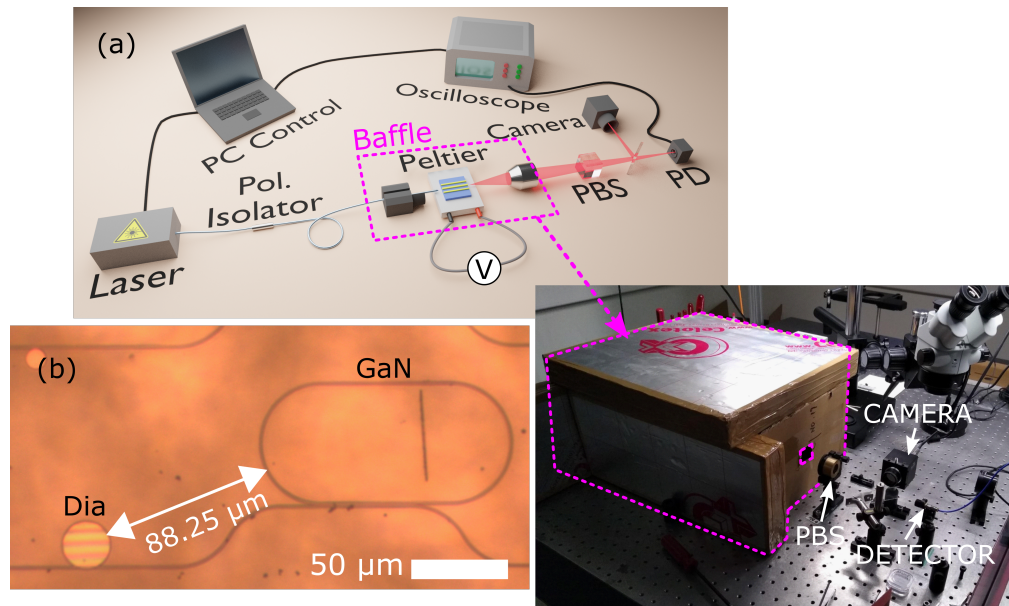


FIGURE 5.3: (a) Schematic and baffle enclosure erected around sample stage of fibre injection rig. (b) Hybrid diamond-GaN device.

5.2 Method

The hybrid device used in the following was fabricated and characterised in the previous chapter. It consists of a monolithic GaN racetrack resonator, and a vertically coupled transfer printed diamond disk resonator, in the configuration shown in Figure 5.3 (b). The physical separation between the two resonators is just 88.25 μm.

The optical set-up, shown in Figure 5.3 (a), is a slightly modified version of the set-up used previously. In this instance, the device was bonded with thermally conductive paste to a Peltier heating element. Once aligned to the waveguide facet, the lensed injection fibre was mechanically locked in place and a baffle enclosure erected around the fibre injection and sample stage apparatus. The baffle minimises airflow across the device and cantilever oscillations of the fibre tip, preventing any modulation of throughput intensity that might otherwise interfere with subsequent wavelength shift measurements. Temperature was measured locally with a resistance thermometer, also bonded to the sample stage. The Peltier, operated in positive bias, allows control of the device global temperature to higher values than the environment (Peltier surface area: 3 cm², GaN chip area: 0.5 cm², GaN/Dia microresonator effective area: 3.13 × 10⁻⁴ cm²), while the optical transmission was probed in the usual way.

5.3 Results

5.3.1 Resonance position determination

Previously, resonance wavelengths have been extracted through nonlinear least-squares fits of peak lineshapes with the all-pass transmission function for a notch filter. This equation is widely used because determination of its free parameters also determines the resonator losses and coupling coefficients. Here however, the sole interest is accurate determination of the resonance wavelength position. This is most easily evaluated by fitting with the following simple modified Lorentzian, which is agnostic to coupling, loss, and effective index:

$$T(\lambda) = T_0 - \frac{I\Gamma^2}{(\lambda - \lambda_{res})^2 + \Gamma^2} \quad (5.6)$$

$T(\lambda)$ is the normalised throughput transmission at wavelength λ , T_0 is the off-resonant baseline intensity, I is the peak height, Γ is the half-width at half-maximum, and finally, λ_{res} is the centre (resonance) wavelength. Since Equation 5.6 is directly a function of the resonance wavelength, using it instead of the previous notch filter function simplifies the procedure of extracting peak positions and their associated fitting errors. Furthermore, where previously initial conditions for the coupling, loss, and effective index have been required for the fitting procedure, here only initial conditions relating to the lineshape itself are required. Since these can be estimated quickly and with little user input, the process of systematically fitting several peaks is greatly simplified.

However, the extracted centre wavelength is also strongly influenced by the span of the fitting window and any asymmetry in the off-resonance background transmission levels.

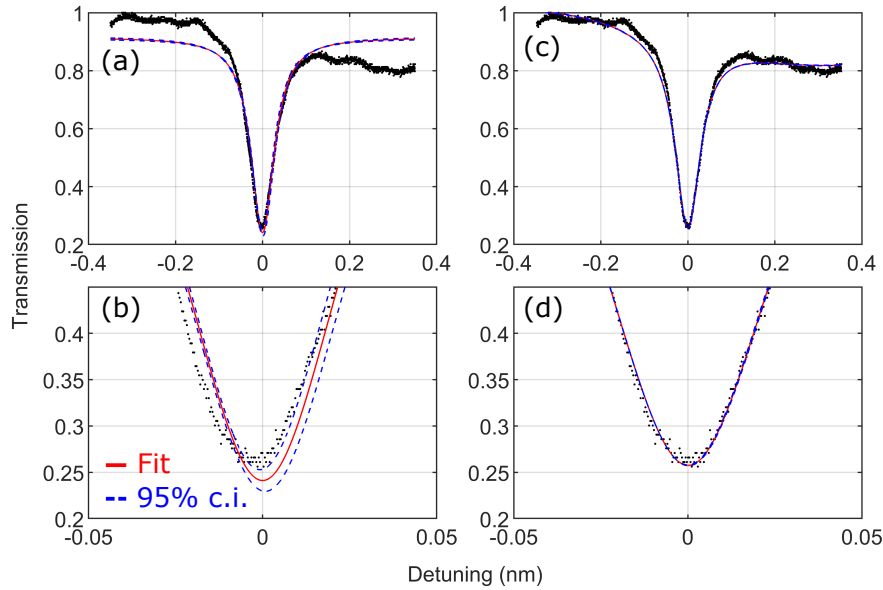


FIGURE 5.4: (a) Lorentzian fitting and 95% confidence intervals of an example diamond peak at 1593.22 nm. (b) Detail around peak minimum. (c) The same peak, but with polynomial background correction. (d) Detail showing a much improved fit around peak centre.

As an example, compare the two fits shown in Figure 5.4 and the marked improvement in the region around the centre wavelength. In Figure 5.4 (c), the fit has been weighted around the middle of the peak, and the off-resonant background is corrected with a third-order polynomial. As a result, the squared norm of the residuals in the region around the centre wavelength (Figures 5.4 (b,d)) is reduced by a factor of 11, and the 95% confidence intervals are much tighter. Therefore, in order to systematically and accurately measure the ‘true’ resonance positions for each peak in Figure 5.5, the order of the polynomial background correction and span of the fitting window are parameterised during the fitting procedure, so that the minimum residual case can be taken.

5.3.2 Simultaneous thermal tuning and thermo-optic coefficient measurement

To begin, transmission spectra for increasing Peltier voltages were taken, with results plotted in Figure 5.5. When the Peltier was off, the ambient temperature reading was 293 K. For all spectra, the laser wavelength was swept at 20 nm/s, meaning a full spectrum takes 3 s to construct.

Two nearby peaks are shown in Figure 5.5 (b), with the left peak belonging to the diamond resonator and the right belonging to the GaN. We can first use the fact that only the single-mode GaN has regularly spaced peaks to disentangle them from the diamond, as was shown in the previous chapter. Additionally, since the thermo-optic

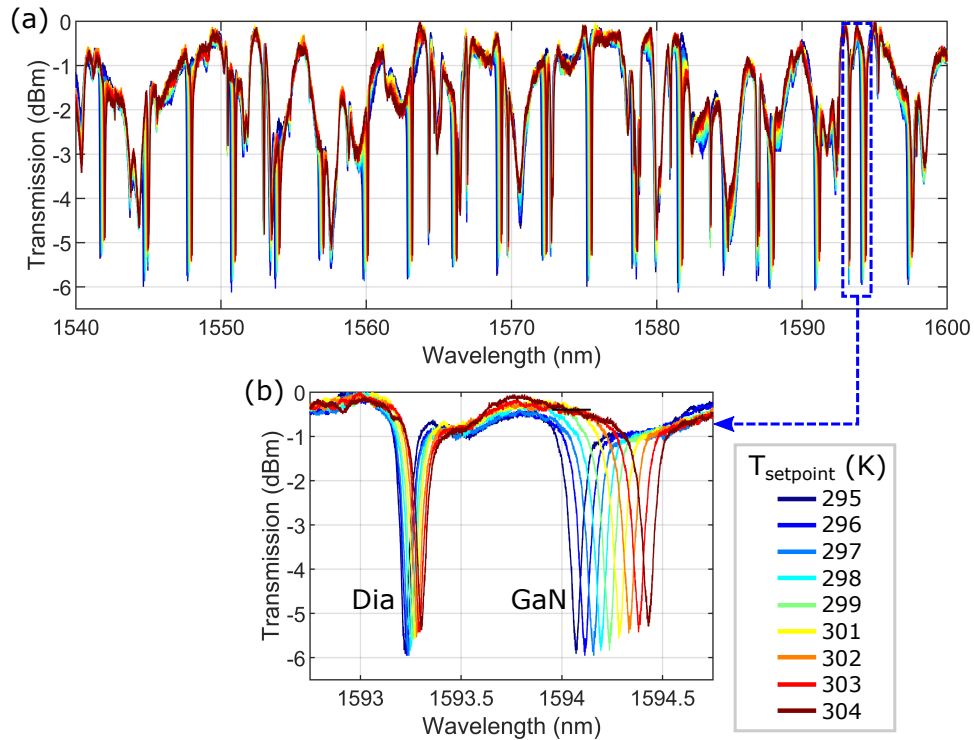


FIGURE 5.5: (a) Thermally tuned cascaded diamond-GaN transmission spectrum. (b) Detail of nearby peaks.

response of diamond is much smaller than that of GaN, the magnitude of the wavelength shift for a given temperature shift also makes it obvious which peaks belong to which material.

It is possible at this point to directly calculate the thermo-optic coefficients of each material by using Equation 5.3 and plotting the normalised wavelength shifts against temperature set-point (Figure 5.6). For small temperature ranges over which the thermo-optic coefficient is constant, this plot should have a slope equal to that material's

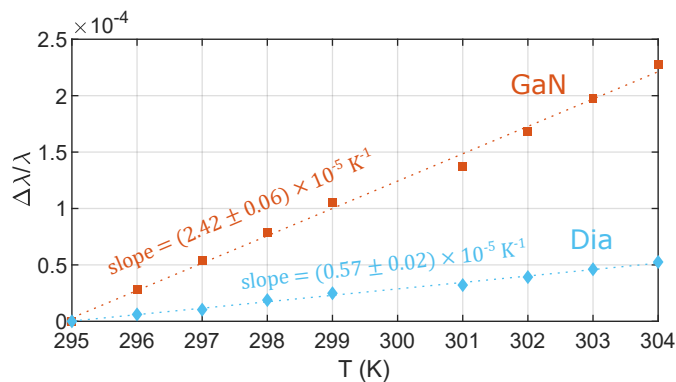


FIGURE 5.6: Thermally induced peak position shifts, with linear fits, for the integrated diamond-GaN device. Each $\Delta\lambda/\lambda$ data point is an average over all peak shifts associated with that material.

TABLE 5.1: Thermo-optic coefficients calculated from the slopes of relative wavelength shift against temperature set-point.

Material	$(\frac{\partial n}{\partial T})$ measured	$(\frac{\partial n}{\partial T})$ literature
GaN	$(6.06 \pm 0.16) \times 10^{-5} K^{-1}$	$6.0 \times 10^{-5} K^{-1}$ [32]
Dia	$(1.44 \pm 0.04) \times 10^{-5} K^{-1}$	$1.5 \times 10^{-5} K^{-1}$ [33]

thermo-optic coefficient divided by its group index, n_g . For the GaN, which has an FSR of 3 nm, we calculate $n_g = 2.503$ using Equation 5.4. For the diamond, using Equation 5.5, we get $n_g = 2.520$. With these, and the slopes of the straight line fits in Figure 5.6, thermo-optic coefficients are calculated and tabulated in Table 5.1. The values found with this method are in relatively good agreement with previously reported literature values [32, 33].

5.3.3 Single-shot temperature error

When calculating the temperature error associated with a resonant wavelength shift, the following analysis is used, in favour of Equation 5.2:

$$\lambda(T + \Delta T) = \lambda(T) + \frac{d\lambda}{dT} \Delta T, \quad (5.7)$$

which is valid over temperature ranges measured here. Here, $d\lambda/dT$ can simply be considered the initial calibration of the device, therefore including the dispersion present in the full analysis of Equation 5.2. A single resonance wavelength shift is simply given by:

$$\Delta\lambda = \lambda_2 - \lambda_1, \quad (5.8)$$

where $\lambda_2 = \lambda(T + \Delta T)$ and $\lambda_1 = \lambda(T)$

The errors add in quadrature, giving the following expression for the standard error in the calculated shift:

$$\sigma(\Delta\lambda) = [\sigma(\Delta\lambda_2)^2 + \sigma(\Delta\lambda_1)^2]^{1/2}, \quad (5.9)$$

where $\sigma(\Delta\lambda_{1,2})$ are respectively the standard errors in the wavelength positions at T and $T + \Delta T$, whatever that T may be. These errors can themselves be obtained after the

resonance fitting procedure on the associated lineshapes using the Lorentzian function (Equation 5.6). As was mentioned earlier, since the centre wavelength is a free parameter in the fit, its error information is either directly accessible as part of the fitting process (e.g. in MATLAB) or from the resulting fit's variance-covariance matrix [34]. An expression for the temperature shift is obtained by rearranging Equation 5.7 for ΔT :

$$\Delta T = \Delta \lambda \left(\frac{d\lambda}{dT} \right)^{-1}, \quad (5.10)$$

where $d\lambda/dT$ is the slope of that resonance's straight line fit calibration measurement. For clarity, call this slope s . Stemming from a linear regression of λ against T (similar to Figure 5.6), it has its own standard error $\sigma(s)$. Now, having expressions for the errors in the calibration measurement and subsequent wavelength shift measurements, we can propagate the errors to find the error in ΔT :

$$\sigma(\Delta T) = \Delta T \left[\left(\frac{\sigma(\Delta \lambda)}{\Delta \lambda} \right)^2 + \left(\frac{\sigma(s)}{s} \right)^2 \right]^{1/2} \quad (5.11)$$

This is the standard error in a single evaluation of temperature shift after measuring initial and final wavelengths. In the above spectrum however, there are several peaks measuring that *same* shift, spread out over both materials. Justification for this is twofold. First, thanks to the capabilities of the hybrid integration procedure, the diamond and GaN resonators are located in close-proximity on chip. The size of the entire chip in comparison to the total area of the Peltier heating element is already small. Here the combined area of diamond and GaN resonator is so much smaller than even that, that they can be thought of as sampling the same local temperature. Second, the transmission spectrum is constructed in 3 s thanks to a rapid sweep speed of 20 nm/s (or a pace of 0.05 s/nm). Since the voltage supplied to the Peltier is steady on this time scale, the diamond and GaN resonators are measuring the temperature effectively simultaneously in this single-shot measurement.

We can thus combine all evaluations from all resonance peak shifts into a single weighted average with the following:

$$\Delta \bar{T} = \frac{\sum_{peaks} \Delta T / \sigma(\Delta T)^2}{\sum_{peaks} 1 / \sigma(\Delta T)^2}, \quad (5.12)$$

whose error, again calculated with propagation of errors, is:

$$\sigma(\Delta\bar{T}) = \left[\frac{1}{\sum_{peaks} \sigma(\Delta T)^{-2}} \right]^{1/2}, \quad (5.13)$$

For the increasing $T_{setpoint}$ values and GaN and diamond peaks shown in Figure 5.5 (b), the errors calculated with Equation 5.11 are plotted in Figure 5.7 (a). We note first that the diamond error is generally smaller than the GaN's, likely due to its smaller thermo-optic coefficient reducing the impact of random errors in the slope determining $d\lambda/dT$ (Equation 5.10). When the weighted average of these two is taken according to Equation 5.13, the combined error is reduced to around 20 mK. Then, expanding the summation in Equation 5.13 over all peaks in the spectrum (GaN and diamond), the error can be reduced even further, as in Figure 5.7 (b).

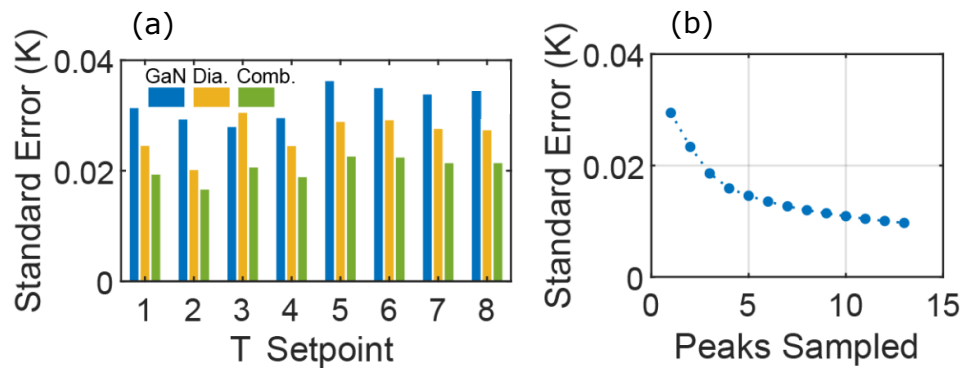


FIGURE 5.7: (a) Standard error in each temperature shift measurement using the single GaN and diamond peaks shown in Figure 5.5. (b) Minimisation of error by averaging over an increasing number of peaks, taken for the second $T_{setpoint}$ in (a).

Finally, the combined response of the hybrid device can be expressed as a single collection of measurements by noting that the correlation between the individual measurements across each material is near unity; as in Figure 5.8 (a), which shows a correlation coefficient $\rho = 0.9997$. Using the slope of 0.2347 as a conversion factor, a single set of wavelength shifts and their associated temperature points and errors can be calculated (according to Equations 5.12 and 5.13 respectively). These data are shown in Figure 5.8 (b) which is well modelled by a second-order polynomial function, whose mean fit residual is 9.2 ± 1.8 mK.

Thus by optimizing the fitting procedure to increase the accuracy of resonant wavelength extraction; using wide-bandgap materials that do not self heat as much; tracking and averaging over multiple peaks; and utilising the strong correlation between independent thermo-optic based measurements of temperature, we have demonstrated a hybrid device

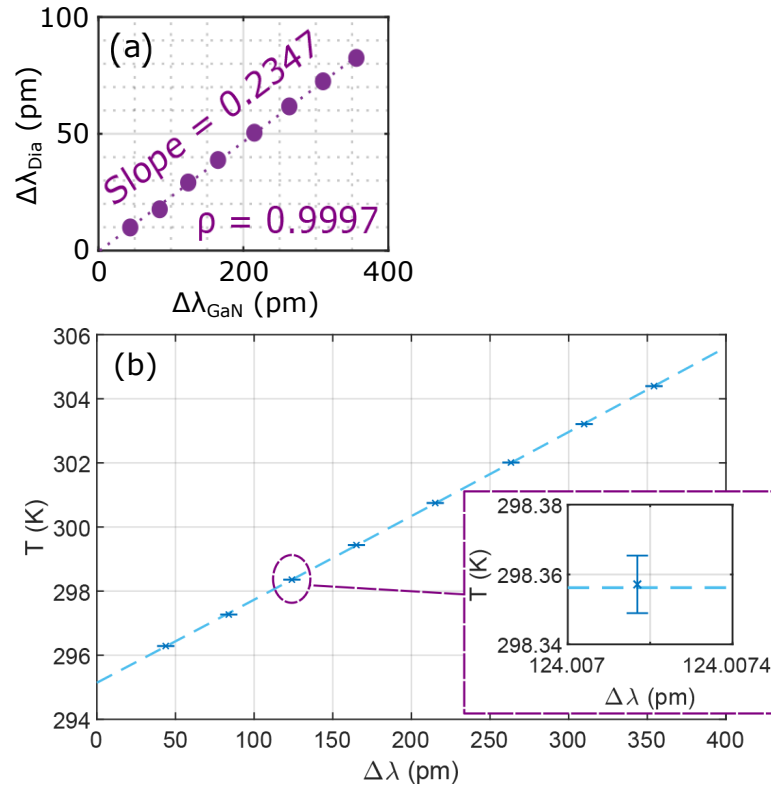


FIGURE 5.8: (a) Correlation between mean diamond and GaN wavelength shifts. (b) Temperature response of the combined hybrid device, with error bars indicating the standard error in each temperature estimate.

with a precision nearly five times improved over similar single peak silicon based devices [12].

5.3.4 Stability measurements

Having characterised the precision in a single-shot temperature shift measurement, the measurement stability with respect to sampling time, which rely on the transient responses of each device, are now analysed. Unlike the preceding results, these measurements do not represent a combined steady-state response.

A transmission spectrum is first taken to identify a suitable resonance. The laser wavelength is then parked on the side of the lineshape, in the high gradient, approximately linear region. The laser is left running, and a time trace of the transmitted light is taken. At this point in the transmission function, temperature fluctuations will give the greatest modulation of the throughput optical intensity, as in Figure 5.9.

A separate silicon chip featuring racetrack resonators of similar size and Q factor (coupling length 60 μm , bend radius 15 μm , waveguide width 500 nm) was used to compare with and benchmark the diamond-on-GaN device. The silicon chip featured a 16.11 dB

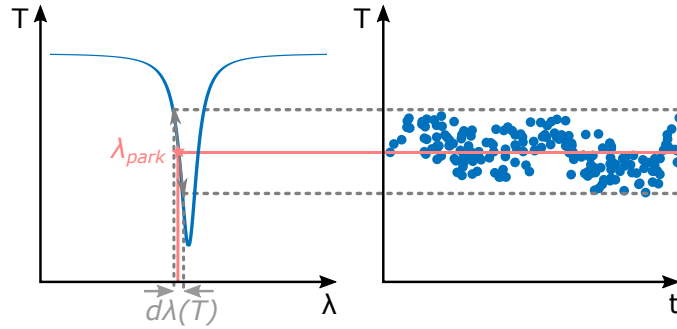


FIGURE 5.9: Time trace acquisition method for stability measurement.

coupling loss improvement over the GaN, and so to ensure equal on-chip optical powers the injected laser power was first attenuated before coupling to the silicon. The equal on-chip power for both chips was $4 \mu\text{W}$, and the Peltier voltage was held at a constant and steady 1 V, reading 303 K.

Time traces, shown in Figure 5.10, were taken for 500 s with a sampling frequency of 4 kHz. Traces were taken for GaN, diamond, and silicon resonances. The trace labelled ‘System’ in Figure 5.10 was generated in the absence of any chip in the beam path, with the lensed injection fibre instead aligned directly to the collection optics. Immediately evident is the long term drift in throughput intensity for the silicon. This drift is weaker for the GaN and diamond and is absent the system throughput trace – meaning the drift is not coming from the measurement system.

The frequency analyses of these time traces are shown in Figure 5.11 (a), and were generated by taking the fast Fourier transform (FFT) of the discrete time traces in Figure 5.10. They show typical $1/f$ pink noise at low frequencies. The system trace sets the noise floor, which includes all those contributions to signal noise that do not

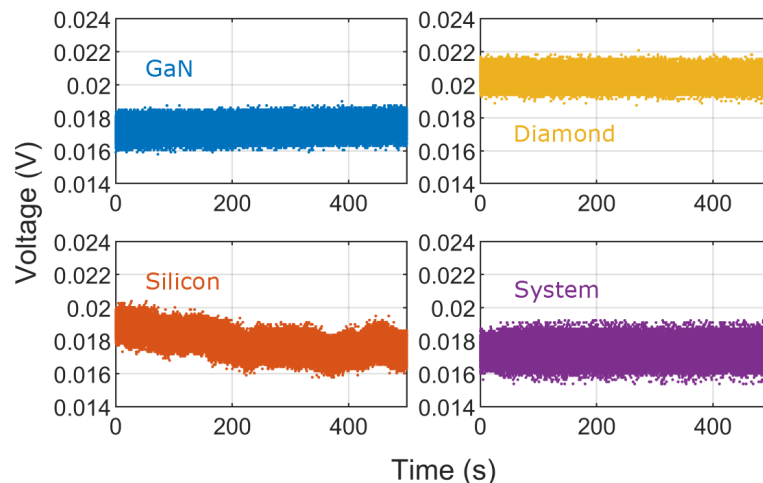


FIGURE 5.10: Time traces of voltage at the detector with the laser parked on the side of a resonance for each material, as well as the system throughput trace for comparison.

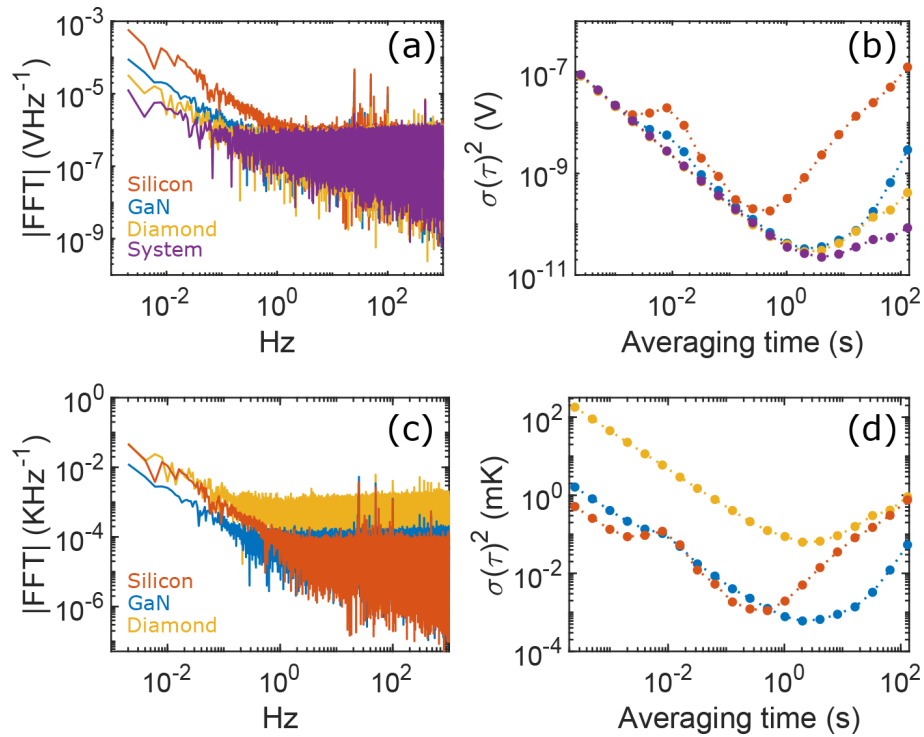


FIGURE 5.11: (a) FFT amplitude spectra of the side-of-peak time traces. (b) Allan variance plots for each trace. (c) Equivalent FFT spectra in temperature units. (d) Allan variance for the temperature traces.

stem from side-of-resonance temperature fluctuations. Laser frequency noise Above this sits the diamond, and above that the GaN. As expected, the silicon performs the worst, having the greatest low frequency noise contribution. The Allan variance (or two-sample variance) of the signals is plotted in Figure 5.11 (b), and is effectively a measurement of the stability of the signal over time – or increasing time averaging/sampling windows. Plotted on a log-log scale, the y-intercept thus corresponds to the noise variance for a single measurement point. As the sampling window is increased, high frequency noise components are averaged out and the Allan variance decreases. This trend continues until a turning point is reached at the minimum Allan variance, beyond which low frequency oscillations begin to dominate and the Allan variance increases again. Looking at Figure 5.11 (b), the diamond and GaN Allan variances share a fourfold improvement in minimum Allan variance averaging times over the silicon, indicating a better performance over longer time scales. The diamond performs the best here, consistently have a smaller Allan variance than the other two materials.

While it may seem that by having the smallest thermo-optic coefficient the diamond provides the most stable environment, and indeed in these like-for-like throughput intensity measurements that seems to be the case. However, when the detector voltage traces (Figure 5.10) are converted to an effective temperature trace, the diamond performs less well. This conversion is done quite simply by taking the intensity trace as the

codomain of a function (the approximately linear side-of-peak lineshape), whose domain is wavelength, or by Equation 5.7, temperature. Consider Figure 5.9. Simply put, we are working backwards from the time trace, projecting the points onto the resonance peak and its temperature dependent wavelength points. Since there is no such lineshape for the system noise trace it must be omitted. Resulting FFT spectra and Allan variance plots are shown in Figure 5.11 (c,d). While the GaN and diamond still share minimum Allan variance averaging times that remain reassuringly four times greater than the silicon, now only the GaN features an improvement in the minimum Allan variance value itself.

Previous work on similar diamond disks printed onto SiO_2 have shown strong confinement of the heat to the diamond disk [35]. Other recent work has shown a significant barrier to thermal transport between Van der Waals bonded diamond and GaN [36]. Of course, these problems will be exacerbated by the presence of an air gap between the diamond and substrate. Subsequently, the transient trapping of heat is likely the reason the diamond performs less well here, especially at shorter averaging times.

5.4 Conclusion

This chapter presented an application of the hybrid diamond-on-GaN photonic device fabricated and characterised in the preceding chapter. A brief overview of the field of photonic thermometry was presented, and the specific advantages of using a dual wide-bandgap platform were outlined. Following descriptions of an updated fitting procedure to accurately and precisely extract resonant wavelengths, it was indeed shown that our hybrid device performs better than narrow-bandgap materials like silicon. Temperature measurement errors of 9.2 mK were found, which represent a nearly fivefold improvement over similar silicon devices [12]. This device was left air-clad, but of course a top-cladding layer of PECVD silica or atomic layer deposited alumina could be used to encapsulate the device. Although transient response times would be reduced, in steady state measurements this would preserve the device performance from long term damage of other environmental changes.

In transient, continuous acquisition measurements, the device performs broadly as expected given the characteristics of each material. For the GaN and diamond, improved averaging times were observed at a point four times greater than a directly comparable silicon device. For the GaN only, an additional improvement in the Allan variance minimum was observed.

References

- [1] Andreas Hänsel and Martijn J.R. Heck. Opportunities for photonic integrated circuits in optical gas sensors. *Journal of Physics: Photonics*, 2(1):012002, jan 2020.
- [2] J. Gonzalo Wangüemert-Pérez, Abdelfettah Hadij-ElHouati, Alejandro Sánchez-Postigo, Jonas Leuermann, Dan Xia Xu, Pavel Cheben, Alejandro Ortega-Moñux, Robert Halir, and Íñigo Molina-Fernández. [INVITED] Subwavelength structures for silicon photonics biosensing. *Optics and Laser Technology*, 109:437–448, jan 2019.
- [3] Elisabet A. Rank, Ryan Sentosa, Danielle J. Harper, Matthias Salas, Anna Gaugutz, Dana Seyringer, Stefan Nevlacsil, Alejandro Maese-Novo, Moritz Eggeling, Paul Mueller, Rainer Hainberger, Martin Sagmeister, Jochen Kraft, Rainer A. Leitgeb, and Wolfgang Drexler. Toward optical coherence tomography on a chip: in vivo three-dimensional human retinal imaging using photonic integrated circuit-based arrayed waveguide gratings. *Light: Science and Applications*, 10(1):1–15, jan 2021.
- [4] Juan Sancho-Durá, Kirill Zinoviev, Juan Lloret-Soler, Jose Luis Rubio-Guvernau, Eduardo Margallo-Balbás, and Wolfgang Drexler. Handheld multi-modal imaging for point-of-care skin diagnosis based on akinetic integrated optics optical coherence tomography. *Journal of Biophotonics*, 11(10):e201800193, oct 2018.
- [5] Humphry Davy. Farther researches on the magnetic phenomena produced by electricity; with some new experiments on the properties of electrified bodies in their relations to conducting powers and temperature. *Philosophical Transactions of the Royal Society*, 111:425–439, 1821.
- [6] L B Hunt. The Origin of the Platinum Resistance Thermometer. *Platinum Metals Rev*, (31):10441–10453, 1980.
- [7] C.W. Siemens. -. *Phil. Mag.*, 21(73), 1861.
- [8] Hugh Longbourne Callendar. On the practical measurement of temperature: Experiments made at the Cavendish laboratory, Cambridge. *Philosophical Transactions of the Royal Society of London. (A.)*, 178:161–230, dec 1887.
- [9] Wayne Hale, H Lane, G Chapline, and K Lulla. *Wings in Orbit: Scientific and Engineering Legacies of the Space Shuttle, 1971-2010*. 2011.
- [10] Gregory F. Strouse. Standard Platinum Resistance Thermometer Calibrations from the Ar TP to the Ag FP. *Special Publication (NIST SP)*, 250(81), jan 2007.
- [11] H Xu, M Hafezi, J Fan, M Taylor, G.F. Strouse, and Z Ahmed. Ultra-sensitive chip-based photonic temperature sensor using ring resonator structures. *Optics Express, Vol. 22, Issue 3, pp. 3098-3104*, 22(3):3098–3104, feb 2014.
- [12] Nikolai Klimov, Thomas Purdy, and Zeeshan Ahmed. Towards replacing resistance thermometry with photonic thermometry. *Sensors and Actuators A: Physical*, 269:308–312, jan 2018.
- [13] Cheng Zhang, G Kang, Yiti Xiong, Tongtong Xu, Linpeng Gu, Yijie Pan, and JiFeng Qu. Photonic thermometer with a sub-millikelvin resolution and broad temperature range by waveguide-microring Fano resonance. *Optics Express, Vol. 28, Issue 9, pp. 12599-12608*, 28(9):12599–12608, apr 2020.

- [14] René Eisermann, Stephan Krenek, Georg Winzer, and Steffen Rudtsch. Photonic contact thermometry using silicon ring resonators and tuneable laser-based spectroscopy. *Technisches Messen*, 88(10):640–654, oct 2021.
- [15] Elias Ferreiro-Vila, Juan Molina, Lukas M. Weituschat, Eduardo Gil-Santos, Pablo A. Postigo, and Daniel Ramos. Micro-Kelvin Resolution at Room Temperature Using Nanomechanical Thermometry. *ACS Omega*, 6(36):23052–23058, sep 2021.
- [16] Hratch G. Semerjian and Ellyn S. Beary. Temperature Metrology and Its Impact on Industry. In *AIPC*, volume 684, pages 1–6. American Institute of Physics Inc., sep 2003.
- [17] Xing Yi Woo, Zoltan K. Nagy, Reginald B.H. Tan, and Richard D. Braatz. Adaptive Concentration Control of Cooling and Antisolvent Crystallization with Laser Backscattering Measurement. *Crystal Growth and Design*, 9(1):182–191, jan 2008.
- [18] M R Pinsky, L Brochard, J Mancebo, and G Hedenstierna. *Applied Physiology in Intensive Care Medicine*. Springer, 2006.
- [19] Herbert Stanford III. *HVAC Water Chillers and Cooling Towers: Fundamentals, Application, and Operation*. CRC Press, 2006.
- [20] Alberto Fernandez, F Berghmans, B Brichard, M.C. Decreton, A.I. Gusarov, O Deparis, P Megret, M Blondel, and A Delchambre. Multiplexed fiber Bragg grating sensors for in-core thermometry in nuclear reactors. In *Proceedings Volume 4204, Fiber Optic Sensor Technology II*, 2001.
- [21] Shinzo Saito, Toshiyuki Tanaka, and Yukio Sudo. Design of high temperature Engineering Test Reactor (HTTR), 1994.
- [22] Stephan Briauudeau. Photonic and Optomechanical Sensors for Nanoscaled and Quantum Thermometry: The EU Project PhotOQuanT. *CPEM 2018 - Conference on Precision Electromagnetic Measurements*, oct 2018.
- [23] Cyriaque Genet, Astrid Lambrecht, and Serge Reynaud. Temperature dependence of the Casimir effect between metallic mirrors. *Physical Review A*, 62(1):012110, jun 2000.
- [24] E. Gil-Santos, D. Ramos, V. Pini, J. Llorens, M. Fernández-Regúlez, M. Calleja, J. Tamayo, and A. San Paulo. Optical back-action in silicon nanowire resonators: bolometric versus radiation pressure effects. *New Journal of Physics*, 15(3):035001, mar 2013.
- [25] B. Fellmuth, J. Fischer, G. MacHin, S. Picard, P. P.M. Steur, O. Tamura, D. R. White, and H. Yoon. The kelvin redefinition and its mise en pratique. *Philosophical Transactions of the Royal Society A: Mathematical, Physical and Engineering Sciences*, 374(2064), mar 2016.
- [26] Haiying Fu, Hanan Baddar, Kerry Kuehn, Melora Larson, Norbert Mulders, Anton Schegolev, and Guenter Ahlers. A High-Resolution Thermometer for the Range 1.6 to 5 K. *Journal of Low Temperature Physics* 1998 111:1, 111(1):49–71, 1998.
- [27] J. F. Qu, S. P. Benz, H. Rogalla, W. L. Tew, D. R. White, and K. L. Zhou. Johnson noise thermometry. *Measurement Science and Technology*, 30(11):112001, sep 2019.
- [28] W. Bogaerts, P. de Heyn, T. van Vaerenbergh, K. de Vos, S. Kumar Selvaraja, T. Claes, P. Dumon, P. Bienstman, D. van Thourhout, and R. Baets. Silicon microring resonators. *Laser and Photonics Reviews*, 6(1):47–73, jan 2012.

-
- [29] Francesco Morichetti, Stefano Grillanda, Marco Carminati, Giorgio Ferrari, Marco Sampietro, Michael J. Strain, Marc Sorel, and Andrea Melloni. Non-invasive on-chip light observation by contactless waveguide conductivity monitoring. *IEEE Journal on Selected Topics in Quantum Electronics*, 20(4), jul 2014.
- [30] Ted V. Tsoulos and Giulia Tagliabue. Self-induced thermo-optical effects in silicon and germanium dielectric nanoresonators. *Nanophotonics*, 9(12):3849–3861, sep 2020.
- [31] Qianfan Xu and Michal Lipson. Carrier-induced optical bistability in silicon ring resonators. *Optics Letters*, 31(3):341–343, feb 2006.
- [32] Naoki Watanabe, Tsunenobu Kimoto, and Jun Suda. Thermo-optic coefficients of 4H-SiC, GaN, and AlN for ultraviolet to infrared regions up to 500 °C. *Japanese Journal of Applied Physics*, 51(11), 2012.
- [33] Richard P Mildren. *Intrinsic Optical Properties of Diamond*. 2013.
- [34] G.A. Seber and C.J Wild. *Nonlinear Regression*. John Wiley and Sons, Ltd, 2003.
- [35] Paul Hill, Charalambos Klitis, Benoit Guilhabert, Marc Sorel, Erdan Gu, Martin D Dawson, and Michael J Strain. All-optical tuning of a diamond micro-disk resonator on silicon. *Photonics Research*, 8(3):318–324, mar 2020.
- [36] WM Waller, JW Pomeroy, D Field, EJW Smith, PW May, and M Kuball. Thermal boundary resistance of direct van der Waals bonded GaN-on-diamond. *Semiconductor Science and Technology*, 35(9):095021, aug 2020.

Chapter 6

Conclusion and outlook

Presented in this thesis were efforts to develop a novel wide-bandgap platform for hybrid integration with non-native diamond microresonators. The chosen platform was GaN on sapphire – itself a relatively underutilised material for photonic integrated circuitry. Thus, details of the initial fabrication and characterisation of the GaN platform were outlined, and monolithic GaN resonators were found to have good Q factors (loaded: 2.91×10^4 , intrinsic: 1.22×10^5). Furthermore, despite known difficulties with GaN on sapphire epitaxy, microresonator losses were found to be as low as 3.13 dB/cm. Considering this is for an air-clad, fully etched waveguide, this excellent initial result shows great promise for future optimisation of the platform.

The first example of actively (thermally) tunable GaN microresonators was shown, with tuning efficiencies of 11.658 pm/mW measured. Naturally, this value is smaller than similar silicon resonators – because of silicon’s larger thermo-optic coefficient – but compares favourably to other wide-bandgap materials like AlN or LiNbO₃. For quantum applications utilising room temperature single photons emitted by diamond colour centres, a tunable wavelength filter such as this is especially important for actively filtering the spectrally indistinguishable single photons emitted without the mediation of an unknown quanta of lattice vibrations [1].

A diamond disk resonator was then integrated onto the GaN chip by high accuracy micro-transfer printing; targeting vertical coupling from the GaN waveguide. In this way, two cascaded resonators sharing one bus waveguide – one hybrid diamond and one monolithic GaN – could be probed simultaneously. After the initial characterisation of the performance of this device, an application was demonstrated in high precision photonic thermometry. By using two wide-bandgap materials which present independent responses to temperature shifts, a nearly fivefold improvement in single-shot accuracy was observed over similar silicon devices, with a precision of 9.2 ± 1.8 mK.

6.1 Future work

Attempts were made to characterise these GaN chips at visible (635 nm) wavelengths, as in Figure 6.1. However, it was obvious that leakage into the sapphire substrate was too great. This may be coming from point scattering on defects along the propagation length of the GaN waveguide, or from modal mismatch on injection at the GaN facets between the guided mode and the spot projected by the coupling lensed fibre.

There are obvious routes forward around these obstacles however. Firstly, future fabrication runs could target partially etched waveguides as opposed to the fully etched guides presented here. At the expense of larger devices (larger mode areas, larger bend radii, increased bend losses), waveguides with almost all of the optical power contained in the GaN can be in principal be fabricated. Figure 6.2(a) shows the fundamental TE mode for a single mode GaN rib waveguide, on the usual 350 nm AlN buffer, on sapphire. Two benefits arise: improved mode matching with the output of lensed fibres, reducing the amount of light getting into the substrate on injection; and reduced scattering from the buffer layer defects and dislocations, which was previously postulated as a source of loss in the IR.

Another possibility is to target GaN devices released from a silicon substrate by KOH underetching. In this case, small photonic devices (Figure 6.2(b)) on membranes of GaN can be integrated onto another platform, such as foundry-accessible SiN. Here GaN is changing roles from receiver to donor.

Wide-bandgap materials like diamond and GaN represent the current frontier of research in integrated optics. Silicon has long dominated at infrared wavelengths, but the emergence of applications operating below its transparency window necessitate the development of new material platforms. Diamond and GaN are excellent candidates because of their high refractive indices and complementary properties. For example,

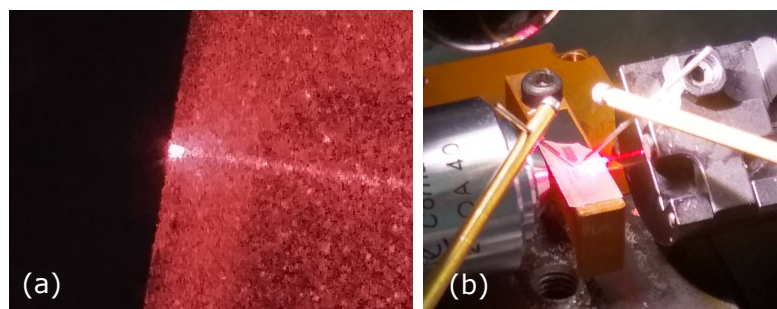


FIGURE 6.1: (a) Plan view of the collection facet of a GaN slab waveguide (50 μm). (b) Attempted optical and electrical probing of tunable GaN resonators at 635 nm.

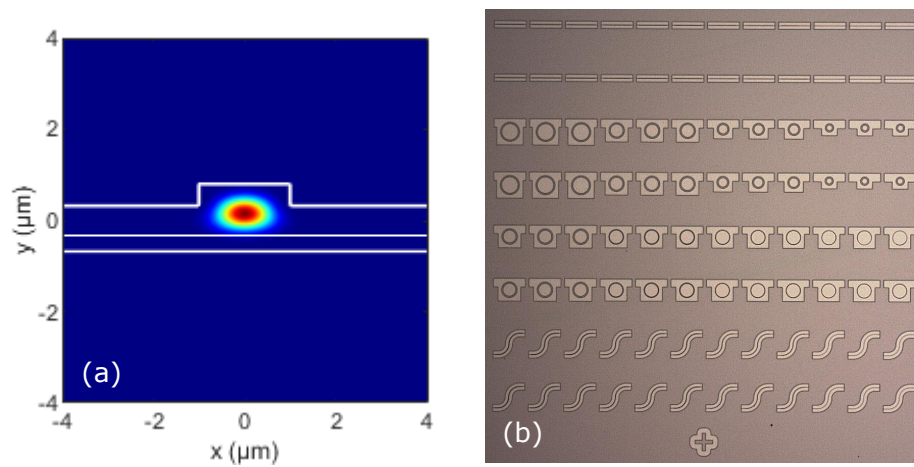


FIGURE 6.2: (a) TE mode of a single mode GaN partially etched waveguide. (b) Ongoing work on miniature photonic devices for membrane fabrication.

GaN's scalability and linear electro-optic modulation capabilities; and diamond's unrivalled room temperature single photon sources. Difficulties in diamond growth, and issues in GaN on sapphire device fabrication, can in both cases be neatly circumvented by micro-transfer printing. The work detailed in this thesis showed the feasibility of the hybrid platform, and forwarded an application uniquely suited to a hybrid wide-bandgap approach.

References

- [1] Sam Johnson, Philip R. Dolan, and Jason M. Smith. Diamond photonics for distributed quantum networks. *Progress in Quantum Electronics*, 55:129–165, sep 2017.

Appendix A

Dielectric waveguide theory

A.1 General waveguide equation

Some common waveguide geometries are shown in Figure A.1. The confinement of optical power to these waveguide is predicated on their possessing a greater refractive index than their surroundings. The larger this index contrast, the more the light is confined to the high index region. The cross-sections in Figure A.1 represent the boundaries under which Maxwell's equations must be solved to find the allowed modes of propagation.

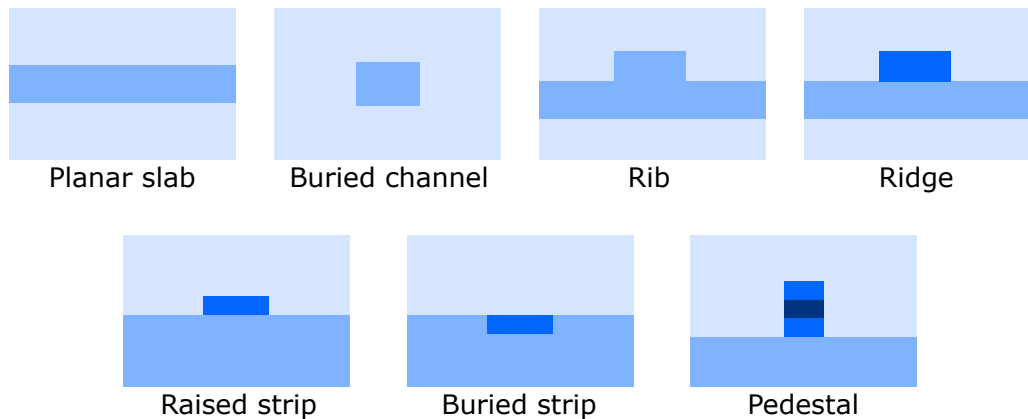


FIGURE A.1: Names of various waveguide geometries, where darker regions represent greater refractive indices. The direction of propagation is into the page. *Adapted from: [1]*

Maxwell's curl equations in a dielectric medium with permittivity, ϵ , are:

$$\nabla \times \mathbf{E} = -\mu_0 \frac{\partial \mathbf{H}}{\partial t} \quad (\text{A.1})$$

$$\nabla \times \mathbf{H} = \varepsilon \frac{\partial \mathbf{E}}{\partial t}, \quad (\text{A.2})$$

where μ_0 is the vacuum permeability. In general, dielectrics with linear responses in their displacement and magnetic fields \mathbf{D} and \mathbf{H} respectively obey the constitutive relations:

$$\mathbf{D} = \varepsilon \mathbf{E} + \mathbf{P} \quad (\text{A.3})$$

$$\mathbf{H} = \frac{\mathbf{B}}{\mu} \quad (\text{A.4})$$

Plugging equation A.4 into equation A.2 results in:

$$\nabla \times \left(\frac{\mathbf{B}}{\mu} \right) = \varepsilon \frac{\partial \mathbf{E}}{\partial t}, \quad (\text{A.5})$$

and by simplifying, taking taking the curl of both sides, and using the vector calculus identity for the curl of the curl of a vector, we obtain:

$$\nabla \times (\nabla \times \mathbf{B}) = \nabla (\nabla \cdot \mathbf{B}) - \nabla^2 \mathbf{B} = \mu \varepsilon \frac{\partial}{\partial t} (\nabla \times \mathbf{E}) \quad (\text{A.6})$$

Since there are no magnetic monopoles, the divergence $\nabla \cdot \mathbf{B} = 0$. Finally plugging equation A.1 into the right hand side of equation A.6 results in:

$$\nabla^2 \mathbf{H} = \frac{n^2}{c^2} \frac{\partial^2 \mathbf{H}}{\partial t^2}, \quad (\text{A.7})$$

where we have introduced the refractive index n , given by $n = (\mu_r \varepsilon_r)^{1/2}$ with μ_r and ε_r the relative permeability and permittivity respectively; and the speed of light in vacuum c , given by $c = (\mu_0 \varepsilon_0)^{-1/2}$ with μ_0 and ε_0 the vacuum permeability and permittivity. The ∇^2 Laplace operator is: $\nabla^2 = \partial^2/\partial x^2 + \partial^2/\partial y^2 + \partial^2/\partial z^2$. By an identical method to the above, starting instead with equation A.1 and using the fact there are no free charges in a dielectric ($\nabla \cdot \mathbf{D} = 0$), we arrive at:

$$\nabla^2 \mathbf{E} = \frac{n^2}{c^2} \frac{\partial^2 \mathbf{E}}{\partial t^2} \quad (\text{A.8})$$

These two wave equations describe the propagation of electric and magnetic waves, travelling though the medium with velocity $1/v^2 = n^2/c^2$, or $v = c/n$.

The following is applicable to both wave equations, so consider just the electric field wave equation. To arrive at the paraxial waveguiding equation, we assume the electric field is harmonic in time, propagating in the positive z direction, and has time independent transverse components (i.e. mode profiles $\mathbf{E}(x, y)$):

$$\mathbf{E}(x, y, z, t) = \mathbf{E}(x, y)e^{i(\omega t - \beta z)}, \quad (\text{A.9})$$

where ω is the radian angular frequency and β is a propagation constant. With this separation of variables, it is easy to plug equation A.9 into equation A.8 and get:

$$\nabla_T^2 \mathbf{E}(x, y) + (k_0^2 n^2 - \beta^2) \mathbf{E}(x, y) = 0, \quad (\text{A.10})$$

where $\nabla_T^2 = \partial^2/\partial x^2 + \partial^2/\partial y^2$ represents the transverse components of the Laplace operator only. We have also introduced the free-space wavenumber, k_0 , given by $k_0 = 2\pi/\lambda = \omega/c$. Note that equation A.10 is equivalent to the time-independent Schrödinger equation. It can only be solved analytically for the planar slab waveguide, where either $\partial/\partial x = 0$ or $\partial/\partial y = 0$. All other geometries listed in Figure A.1 require either approximations like Marcatili's method, the effective index method, or beam propagation methods [2]; or they require numerical finite difference or finite element solvers.

However, some important concepts and properties common to all waveguides can be highlighted just by considering the case of the planar slab.

A.1.1 The asymmetric planar slab

The planar slab consists of a region of high refractive index, sandwiched between two regions of lower index, all of which extend to infinity in one of the transverse directions, meaning either $\partial/\partial x = 0$ or $\partial/\partial y = 0$. Setting $\partial/\partial y = 0$, which is also a valid simplification for rectangular waveguides very much larger in one cross-sectional dimension than the other, equation A.10 reduces to:

$$\frac{\partial^2}{\partial x^2} E_y(x, y) + (k_0^2 n_i^2 - \beta^2) E_y(x, y) = 0, \quad (\text{A.11})$$

where n_i is the refractive index in the region being solved for. For the geometry described in Figure A.2, equation A.11 thus describes three differential equations with n_1 , n_2 , and n_3 .

Equation A.11 admits several solutions, but not all are guided modes. Solving for E_y is a process of finding the propagation constants β for which the electric field is continuous across the dielectric interfaces. However, the essential nature of the solutions can be stated just by inspecting the sign of the $(k_0^2 n^2 - \beta^2)$ term. Neglecting constants, if $\beta > k_0 n_i$, equation A.11 describes a function whose second partial derivative is equal to itself – an exponential function. When $\beta < k_0 n_i$, the electric field’s second partial derivative is equal to its own negative – a sinusoidal function.

Take $n_2 > n_3 > n_1$. If $k_0 n_3 < \beta < k_0 n_2$, the solution is sinusoidal in the n_2 region, and exponentially decaying in the n_1 and n_3 cladding regions. This describes a guided mode, where optical power is confined to the waveguide as a plane wave oscillating with angular frequency ω , and decays exponentially with tangential distance from the waveguide edge as an *evanescent* wave. This is how light can be guided over great distances, without diffraction or (in the ideal case) loss. Two such guided modes are shown in Figure A.2. If $k_0 n_1 < \beta < k_0 n_3$, the solution is sinusoidal in the guide and the substrate (region n_3), while decaying exponentially in region n_1 . This corresponds to

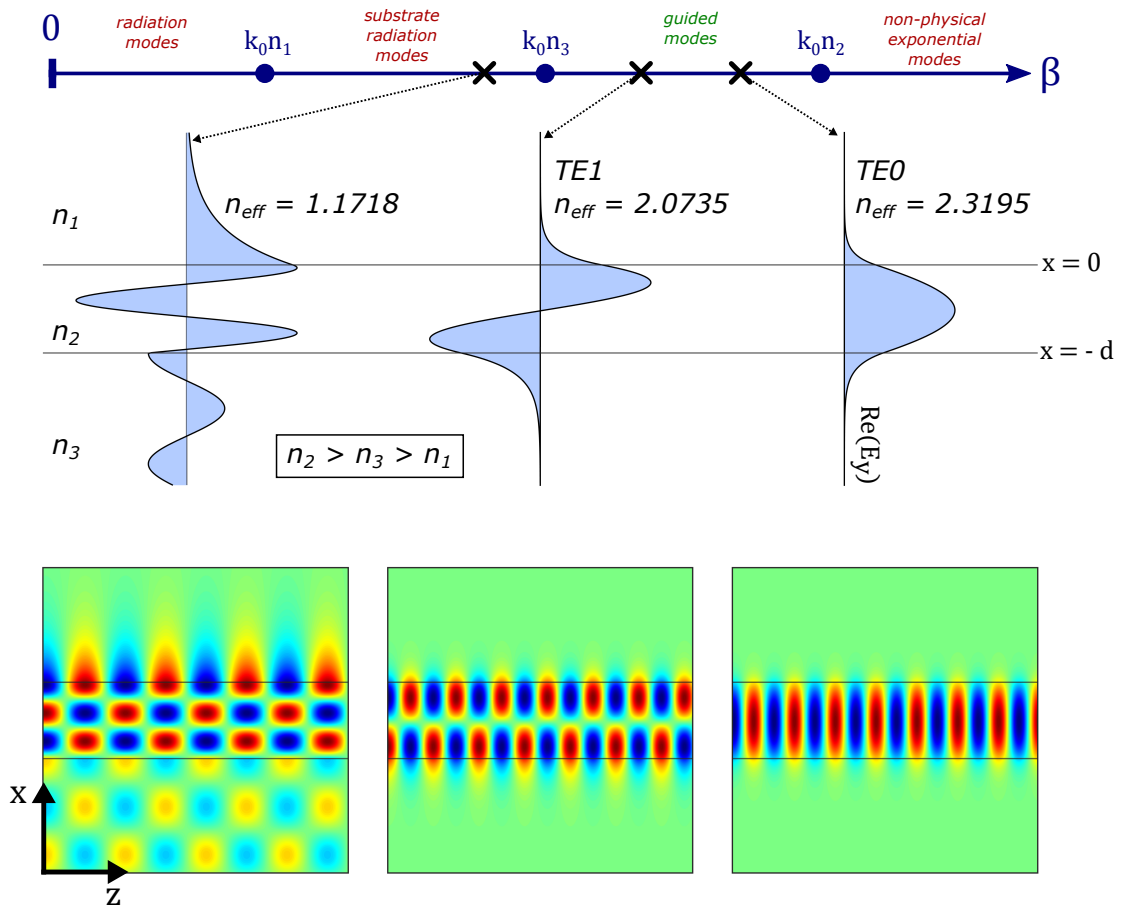


FIGURE A.2: Transverse electric (TE) field solutions for an asymmetric slab waveguide, with line profiles and corresponding field patterns taken along the propagation length, z .

a non-guided *substrate radiation mode*, characterised by the continuous loss along the propagation length of light to the substrate. An example substrate radiation mode is also shown in Figure A.2.

Each mode has an *effective index* given simply by $n_{eff} = \beta/k_0$, and modes are only confined if n_{eff} is greater than a *cut-off* value, equal to n_3 in this case. As n_{eff} approaches n_2 , the optical confinement to the waveguide region increases. For example, note how the TE0 mode in Figure A.2 has a greater effective index, and smaller evanescent tails extending into the cladding regions, than TE1.

In order to calculate the β values that correspond to guided modes, we start with equation A.11 . A general solution for a field propagating in z , and where $\partial/\partial y = 0$, is given by [3]:

$$E_y(x, y, z) = A_y(x)e^{-i\beta z} \quad (\text{A.12})$$

$A_y(x)$ is the transverse field profile, given by:

$$A_y(x) = \begin{cases} C \exp(-qx) & 0 \leq x < \infty \\ C(\cos hx - \frac{q}{h} \sin hx) & -d \leq x \leq 0 \\ C(\cos hd + \frac{q}{h} \sin hd) \exp[p(x+d)] & -\infty < x \leq -d \end{cases} \quad (\text{A.13})$$

where C is constant chosen to maintain 1 unit of power in the waveguide; and h , q , and p are intermediate propagation constants, calculated by plugging equation A.12 into equation A.11:

$$\begin{aligned} h &= \sqrt{n_2^2 k_0^2 - \beta^2} \\ q &= \sqrt{\beta^2 - n_1^2 k_0^2} \\ p &= \sqrt{\beta^2 - n_3^2 k_0^2} \end{aligned} \quad (\text{A.14})$$

Continuity of $A_y(x)$ and its derivative at the interfaces $x = 0$ and $x = -d$ leads to:

$$\tan hd = \frac{p+q}{h(1-pq/h^2)}, \quad (\text{A.15})$$

Equations A.14 allow the expression of A.15 in terms of β only. The intercepts of $\tan hd$ and $(p+q)/h(1-pq/h^2)$ can then be found. In the range $k_0 n_3 < \beta < k_0 n_2$, these

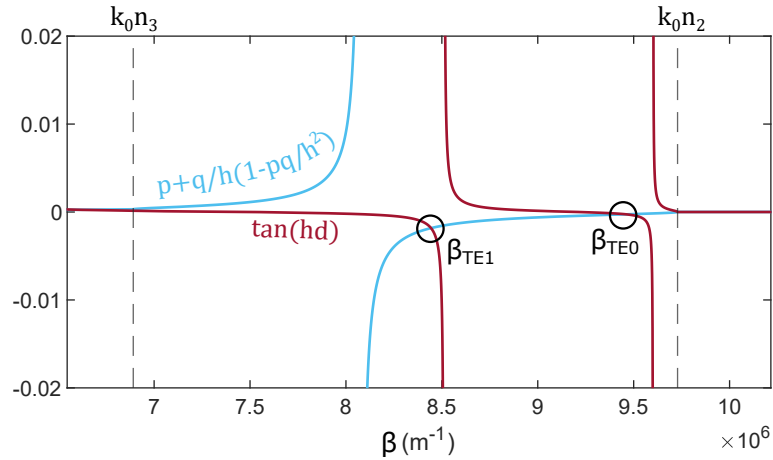


FIGURE A.3: Allowed propagation constants for the above geometry. Only two guided modes are supported at this wavelength.

intercepts correspond to the values of β that simultaneously satisfy the left and right hand sides of equation A.15. The fields plotted in Figure A.2 are for a guide of dimension $d = 1 \mu\text{m}$, $n_2 = 2.4$, $n_3 = 1.7$, $n_1 = 1.0$, and $\lambda = 1500 \text{ nm}$; and their allowed β values were taken from Figure A.3. Note also in Figure A.3 for $\beta > k_0 n_2$ and $\beta < k_0 n_3$, the two curves tend to each other, implying a continuum of non-guided solutions to equation A.11 for these propagation constants. Not shown in Figure A.2 are the field patterns for these two extreme cases, where either $\beta > k_0 n_2$ or $0 < \beta < k_0 n_3$. In the former case, the electric field is exponential in all three regions. Continuity conditions at the boundary mean the field must be exponentially increasing in one or both of the regions of index n_1 and n_3 , and so such a solution is non-physical. In the latter case, the solution is sinusoidal in all three regions, and is thus termed a *radiation mode*.

References

- [1] John Heebner, Rohit Grover, and Tarek Ibrahim. Optical microresonator theory. *Springer Series in Optical Sciences*, 138:71–103, 2008.
- [2] K S Chiang. Review of numerical and approximate methods for the modal analysis of general optical dielectric waveguides. *Optical and Quantum Electronics*, 26:3–134, 1994.
- [3] Amnon Yariv. *Optical Electronics*. Saunders College Publishing, 1991.

List of Publications

Journals

- [1] Jack A. Smith, Paul Hill, Charalambos Klitis, Lukas Weituschat, Pablo A. Postigo, Marc Sorel, Martin D. Dawson, Michael J. Strain, *High precision integrated photonic thermometry enabled by a transfer printed diamond resonator on GaN waveguide chip*. Optics Express, 29(18), 29095-29106. <https://doi.org/10.1364/OE.433607> (2021)
- [2] Dimitars Jevtics, Jack A. Smith, John McPhillimy, Benoit Guilhabert, Paul Hill, Charalambos Klitis, Antonio Hurtado, Marc Sorel, Hark Hoe Tan, Chennupati Jagadish, Martin D. Dawson, Michael J. Strain *Spatially dense integration of micron-scale devices from multiple materials on a single chip via transfer-printing*, Optics Materials Express 11, 3567-3576 (2021)

Conferences

- [3] Jack A. Smith, Charalambos Klitis, Paul Hill, Marc Sorel, Erdan Gu, Martin D. Dawson, and Michael J. Strain, *Heterogeneous Integration of Diamond Disk Resonators with Gallium Nitride Photonics*. OSA Advanced Photonics Congress (AP) 2020 (IPR, NP, NOMA, Networks, PVLED, PSC, SPPCom, SOF), L. Caspani, A. Tauke-Pedretti, F. Leo, and B. Yang, eds., OSA Technical Digest (Optica Publishing Group, 2020), paper ITu2A.5.
- [4] Jack A. Smith, Paul Hill, Charalambos Klitis, Marc Sorel, P. A. Postigo, Lukas Weituschat, Martin D. Dawson, and Michael J. Strain, *High Precision Diamond-on-GaN Photonic Thermometry Enabled by Transfer Printing Integration*, OSA Advanced Photonics Congress 2021, B. Yang, F. Leo, A. Tauke-Pedretti, S. Arafin, M. Clerici, L. Caspani, L. Busse, M. Kats, J. Fan, W. Ming (Steve) Lee, D. Caplan, N. Parsons, W. Freude, C. Tremblay, D. Hillerkuss, K. Igarashi, H. Elgala, N. Guerrero Gonzalez, R. "Patty" Stabile, K. Jaeger, R. Saive, H. Aziz, and H. Tan, eds., OSA Technical Digest (Optica Publishing Group, 2021), paper IM1A.4.